Investigation of the Kinetics and Dynamics of Structural Changes in Organic Hybrid Lead Halide Perovskite Materials

Von der Universität Bayreuth
zur Erlangung des Grades eines
Doktors der Naturwissenschaften (Dr. rer. nat.)
genehmigte Abhandlung

von

Christopher Reiner Greve

aus Naila, Deutschland

1. Gutachter: Prof. Dr. Eva M. Herzig
2. Gutachter: Prof. Dr. Dr. h.c. Frank Schreiber

Tag der Einreichung: 11.06.2024
Tag des Kolloquiums: 01.10.2024

Deutsche Zusammenfassung

Eine der vielversprechendsten neuen Halbleiterklassen ist die Klasse der Metallhalogenid-Perowskite. Während Perowskit-Solarzellen kurz vor der Kommerzialisierung stehen, zeigen Metallhalogenid-Perowskite auch vielversprechende Eigenschaften für den Einsatz in anderen optoelektronischen Geräten, wie Röntgendetektoren oder neuromorphen Geräten. Eine anwendungsübergreifende Herausforderung ist die Stabilität dieser Materialien, die oft mit der Tatsache zusammenhängt, dass in Metallhalogenidperowskiten viele dynamische Strukturprozesse gleichzeitig ablaufen. Die Dynamik und Kinetik der strukturellen Veränderungen während und nach der Materialbildung sind noch nicht gut verstanden, und die grundlegenden Mechanismen bleiben unklar. Ziel dieser Arbeit ist es daher, das grundlegende Verständnis der kinetischen und dynamischen Strukturprozesse in Bleihalogenidperowskiten zu erweitern und weitere Möglichkeiten zur Messung dynamischer Prozesse zu schaffen.

Aus diesem Grund konzentriert sich diese Arbeit zunächst auf die Entwicklung eines detaillierten Verständnisses der Verarbeitung von Bleihalogenidperowskiten aus der Lösung in Kapitel 4. In diesem Kapitel habe ich die Kristallisationsprozesse während der Spin- und Slot-Die-Beschichtung von $MAPbI_3$ mit unterschiedlichen Verdampfungsraten untersucht. Der Perowskitbildungsprozess wird durch gleichzeitige in-situ Photolumineszenz-, Lichtstreuungs- und Absorptionsmessungen untersucht. Verfolgt man die zeitliche Entwicklung der optischen Parameter, so zeigt sich bei beiden Prozessierungsmethoden zunächst die Bildung von Lösungsmittel-Komplex-Strukturen, gefolgt von der Perowskit-Kristallisation. Die Kristallisation erfolgt bei der Spin-Beschichtung in zwei Stufen, während bei der Slot-Die-Beschichtung nur eine Kristallisationsphase stattfindet. Aus der Verfolgung der optischen Parameter auf einer relativen Zeitskala lässt sich ableiten, dass die Dauer der zweiten Perowskit-Kristallisation bei der Spin-Coating-Beschichtung mit steigenden Verdampfungsraten zunimmt, was darauf hindeutet, dass die zweite Kristallisation aufgrund von Unterschieden in den anfänglich gebildeten Lösungsmittel-Komplex-Phasenmorphologien begrenzt erscheint.

Im anschließenden Teil der Arbeit (Kapitel 5) wird die Kinetik der Halogenidwanderung in einer physikalischen Mischung aus trocken prozessierten $MAPbI_3$- und $MAPbBr_3$-Pulvern untersucht. Mit Hilfe der Röntgenbeugung zur Verfolgung der Halogenidwanderung habe ich den thermisch getriebenen Halogenid-Mischprozess unter Lichtausschluss und die Bildung von $MAPbI_{3-x}Br_x$ Mischkristallen untersucht. Außerdem wurde die ionische Flüssigkeit $BMIMBF_4$ zu den reinen Halogenid-Perowskitpulvern hinzugefügt. Ionische Flüssigkeiten wie $BMIMBF_4$ werden gemischten Halogenidperowskiten zugesetzt, um die Entmischung der Halogenidphasen zu verhindern und die Phasenstabilität zu erhöhen. Die genauen Mechanismen, die die Halogenidkinetik verändern, sind derzeit noch unklar. Meine Ergebnisse zeigen, dass die Halogenidmigration durch den Zusatz von $BMIMBF_4$ im Vergleich zu additivfreien Mischungen erheblich beschleunigt wird. Dies wird auf die flüssigkeitsähnliche Dynamik von $BMIMBF_4$ bei erhöhten Temperaturen zurück-

geführt, wodurch Defektstellen an Perowskit-Grenzflächen freigesetzt werden. Die Röntgenbeugungsexperimente zeigten außerdem, dass die Aktivierungsenergie für die Bromidwanderung halidspezifisch ansteigt.

Im nächsten Teil (Kapitel 6) der Dissertation wird die kohärente Streumethode Röntgenphotonenkorrelationsspektroskopie (XPCS) auf dünne Filme von $MAPbI_3$ angewandt, um die Dynamik auf der Nanometer- bis Mikrometerskala im Inneren des Dünnfilms zu messen. Für die Messung dünner Filme wird XPCS bei streifendem Einfall (GI) gemessen, was zu einer Überlagerung von Signalen aufgrund von Reflexions- und Brechungseffekten führt, die aus dem Störungsansatz der Bornschen Näherung (DWBA) bekannt sind. Durch gleichzeitige Messung von XPCS bei transmittiertem streifendem Einfall und XPCS bei streifendem Einfall kann ich die Auswirkungen dieser Effekte experimentell bestimmen. Dazu vergleiche ich die experimentellen Ergebnisse im Rahmen der vereinfachten DWBA und beziehe den nichtlinearen Effekt der Refraktion mit ein, um Bereiche auf dem Detektor zu identifizieren, die hauptsächlich durch einen einzelnen Streuungsbeitrag dominiert werden. Der vorgestellte Analyseansatz ermöglicht es, experimentelle Bedingungen zu identifizieren, sodass die analysierten Daten so nah wie möglich an unverzerrte Transmissions-XPCS Ergebnisse herankommen.

Im letzten Teil meiner Dissertation (Kapitel 7) habe ich die Auswirkungen von Reflexion und Brechung in XPCS-Experimenten unter streifendem Einfall weiter untersucht. Durch die Simulation eines Systems von Partikeln in ballistischer Bewegung und die Analyse der Dynamik direkt aus den Partikeltrajektorien, aus berechneten Transmissions-XPCS und berechneten XPCS im streifenden Einfall konnte ich den Effekt von überlappenden Streusignalen bei XPCS im streifenden Einfall quantifizieren. Um den Ursprung der Verzerrungen zu ermitteln, habe ich den in Kapitel 6 vorgestellten Ansatz angewandt und gezeigt, dass die Verzerrungen für das ausgewählte Partikelsystem hauptsächlich auf Brechungseffekte zurückzuführen sind. Dieses Ergebnis konsolidiert den auf den experimentellen Ergebnissen aus Kapitel 6 basierenden Ansatz zur Identifikation von experimentellen Bedingungen, die möglichst wenig Verzerrungen bei XPCS-Experimenten im streifenden Einfall produzieren. Zusammen eröffnen Kapitel 6 und 7 ein weiteres Instrument zur Messung der Dynamik im Inneren von Bleihalogenid-Perowskit-Dünnschichten.

English Abstract

One of the most promising new classes of semiconductors is the class of metal halide perovskites. While perovskite solar cells are on the verge of commercialisation, metal halide perovskites also show promising properties for use in other optoelectronic devices, such as X-ray detectors or neuromorphic devices. A cross-application challenge is the stability of these materials, often associated with the fact that many dynamic structural processes take place simultaneously in metal halide perovskites. The dynamics and kinetics of structural changes during and after material formation are still not well understood and fundamental mechanisms remain unclear. Therefore, the aim of this thesis is to extend the basic understanding of kinetic and dynamic structural processes in lead halide perovskites and to provide further possibilities to measure dynamic processes.

For this reason, this thesis will first focus on the development of a detailed understanding about lead halide perovskite processing from solution in Chapter 4. In this chapter I investigated the crystallization processes during spin and slot-die coating of $MAPbI_3$ with different evaporation rates. The perovskite processing is investigated by simultaneous in-situ photoluminescence, light scattering, and absorption measurements. By following the time evolution of the optical parameters, both processing methods initially show the formation of solvent-complex structures, followed by perovskite crystallization. The crystallization takes place in two stages for spin coating, while for slot-die coating only one crystallization phase occurs. By following the optical parameters on a relative time scale it is deduced that the duration of the second perovskite crystallization in spin coating increases with increasing evaporation rates, an indicator that the second crystallization appears restricted due to differences in the initially formed solvent-complex phase morphologies.

In the subsequent part of the thesis (Chapter 5) the halide migration kinetics in a physical mixture of dry-processed $MAPbI_3$ and $MAPbBr_3$ powders are investigated. By using X-ray diffraction to follow the halide migration I investigated the thermally driven halide mixing process under dark conditions and the formation of solid solutions of $MAPbI_{3-x}Br_x$. Furthermore, the ionic liquid $BMIMBF_4$ was added to the pure halide perovskite powders. Ionic liquids, such as $BMIMBF_4$, are added to mixed halide perovskites to prevent halide phase segregation and increase phase stability. However, the exact mechanisms changing the halide kinetics are currently unclear. I conclude from my experiments that halide migration is significantly accelerated with the addition of $BMIMBF_4$ compared to additive-free mixtures. This is attributed to liquid-like dynamics of $BMIMBF_4$ at elevated temperatures, liberating defect sites at perovskite interfaces. The X-ray diffraction experiments further showed that a halide specific increase of the activation energy for bromide migration is seen.

In the next part (Chapter 6) of the thesis the coherent scattering method X-ray photon correlation spectroscopy (XPCS) is applied to thin films of $MAPbI_3$ to measure dynamics on the nanometer to micrometer scale in the thin film bulk. In measuring thin films, XPCS is applied in grazing incidence (GI), which leads

to a superposition of signals due to reflection and refraction effects, known from the distorted-wave Born Approximation (DWBA). By simultaneously measuring grazing incidence transmission and grazing incidence XPCS, I can experimentally determine the impact of these effects. For this I compare the experimental results in the framework of the simplified DWBA and include the nonlinear effect of the refraction to identify areas on the detector, which are mainly dominated by a single scattering contribution. The presented analysis approach allows the identification of experimental conditions that can be chosen to run the data analysis as close as possible to undistorted transmission XPCS.

In the final part of my thesis (Chapter 7) I further investigated the impact of reflection and refraction in grazing incidence XPCS experiments. By simulating a system of particles under ballistic motion and analyzing the dynamics directly from the particle trajectories, from calculated transmission XPCS and calculated grazing incidence XPCS the effect of overlapping scattering signals in grazing incidence XPCS is quantified. To identify the origin of the distortions I applied the approach presented in Chapter 6 and showed that the distortions for the chosen particle system are mainly connected to refraction effects. This result further consolidates the approach based on the experimental results from chapter 6 to identify experimental conditions that minimise distortions in grazing incidence XPCS experiments. Together, chapters 6 and 7 provide another tool to measure the dynamics inside lead halide perovskite thin films.

Contents

1 Introduction

1.1 Motivation

In the course of advancing global warming, the demand for renewable and locally available energies is growing and solar cells are now an important cornerstone of the world's energy supply.[1, 2] In the last decades silicon-based photovoltaics (PVs) emerged as a pillar of renewable energy supply and are currently dominating the market.[1, 3] This is mainly due to an energy return on energy invested (EROI) of 10 and an energy pay-back time (EPBT) of around one year, [1, 3] which leads to acceptable an performance for a lifetime of several years. However, it has been shown that the power conversion efficiency (PCE) of silicon solar cells can be further increased by combining the active silicon layer with a second layer, e.g. in a tandem-cell design. In such a tandem configuration two solar cells with different band gaps are stacked on top of each other to extend the spectral coverage of the solar cell into the blue and green spectral range.[4, 5] Therefore, materials are of interest which have a band gap suitable for silicon and can be processed onto a prefabricated solar cell with low energy expenditure and low processing costs.[4, 6]

One material class satisfying these requirements are metal halide perovskites (MHP). In tandem cells with monolithic silicon a PCE of 33,9% was recently achieved,[7] but also MHP single-junction solar cells reach impressive PCE levels. While the first MHP solar cells had efficiencies of 3.8% in 2009,[8] the PCE increased to 26.1% in the course of less than two decades.[7] This is a level previously achieved only by single crystal silicon solar cells and thus outperforms the most widely used polycrystalline silicon solar cells.[7] Additionally, compared to silicon solar cells, MHP solar cells require thinner active layers and can be deposited on mechanically flexible substrates.[9] This combination of substrate flexibility and light weight allows for the opportunity to extend the field of application to e.g. aerospace and wearable electronics applications.[10] Furthermore, recent research demonstrated that MHP also perform well as X-ray detectors,[11–13] in LEDs,[14–16] in lasers[17–19] and in neuromorphic devices, i.e. artifical synapses and memristors.[20–22]

However, although MHP materials deliver impressive results for many applications, there are issues that stand in the way of widespread commercialization. With a focus on solar cell devices these issues primarily include problems with the transition to industrially relevant module sizes (lab-to-fab transition) and the still low device stability.[23–25] In respect to the lab-to-fab transition, the perovskite crystallization from the precursor solution during film formation is highly sensitive to factors such as the precise precursor stoichiometry or the solvent used.[26, 27] Depending on the solvent used, the crystallization route and rates and thus the resulting film quality and structure will change.[27–29] But even after film formation, dynamic processes continue to take place in MHPs.[30] For instance, the comparatively mechanically soft lattice structure in MHPs in combination with lattice defects leads to diffusion of mobile ionic species.[30, 31] Such ionic diffusion can result in pronounced hysteresis in measured

J-V-curves or even lead to phase segregation for mixed halide perovskites.[32, 33] Phase segregation alters the previously tuned optoelectronic properties of the perovskite and is therefore detrimental in applications.[33–35]

All these phenomena I mentioned are related to the fact that organic hybrid lead halide perovskites are a highly dynamic system, during and after processing.[30] The dynamic processes, such as the movement of ions and the associated changes in defects, take place continuously in a fully processed film.[31] As a result the kinetics of many material properties change, such as the ion migration rates or phase transformation rates.[45] Consequently, the material properties of a perovskite thin film can be better understood by quantifying its dynamics and kinetics, e.g. by measuring the dynamics of ionic motion and the kinetics of the respective ion migration rates.

Earlier approaches in MHP processing mostly ignored these dynamic processes but focused on optimizing the film morphology by finding suitable processing parameters resulting in promising perovskite films, but without yet understanding the underlying mechanism of film formation.[36, 37] Such trial-and-error approaches are on the one hand labor-intensive and on the other hand error-prone, since the perovskite crystallization pathway depends on various parameters which are often not considered in the optimization approaches.[38, 39] In addition, the influence of other processing variables, such as ambient temperature, humidity or variances in purchased precursors, is often not taken into account when optimizing perovskite processing routes. Consequently, there are significant differences in MHP properties between laboratories.[39]

To transition from an error-prone trial-and-error optimization approach to a more systematic approach of optimizing perovskite processing routes, it is necessary to study and to increase the understanding of the perovskite film formation and subsequent dynamical processes. Such an understanding would allow to selectively affect the perovskite crystallization and the associated film formation and identify routes to hinder subsequent film degradation.

Suitable methods to study the kinetics of perovskite formation and subsequent dynamic processes and changes to the kinetics of material properties in MHP materials are various *in situ* methods. Optical *in situ* spectroscopy and *in situ* X-ray scattering have proven to be particularly suitable and popular.[40–42] Optical *in situ* spectroscopy capitalizes on the knowledge that the optoelectronic properties of the perovskite are strongly affected by the structure of the perovskite,[43, 44] whereas *in situ* X-ray scattering allows direct time-resolved structural characterization.[45, 46] However, only the structural changes with time can be resolved by X-ray scattering, and the direct observation of dynamic processes such as ionic diffusion is only possible if they result in structural changes.[45] One X-ray based method for direct observation of dynamics and disorder that has gained prominence in recent years is X-ray Photon Correlation Spectroscopy (XPCS).[47, 48] However, as geometric effects are known to distort the extracted dynamics for thin films, XPCS is not yet standard practice for most thin films.[49] For surface-sensitive measurement geometries these effects can be avoided,[50] but not for the bulk-sensitive XPCS measurements of interest for perovskites.[49]

1.2 Objective

In the motivation it was outlined that still numerous gaps in the knowledge of perovskite film formation and the subsequent dynamic processes remain. As a result optimizing perovskite materials is still labor-intensive and key steps for the transition to stable large scale PVs are not well understood.

The aim of the presented thesis is to investigate the kinetics and dynamics of key structural processes of organic hybrid lead perovskite materials. The hereby investigated structural processes include the initial kinetics of perovskite film formation from solution and the kinetics of halide migration in fully formed organic hybrid lead halide perovskite materials. Furthermore, a new approach to extend dynamic XPCS measurements to perovskite thin films is presented, broadening the available tools to track dynamics in perovskite materials. For that reason, the thesis is structured in three parts that are introduced in the following and which are schematically depicted in Figure 1.1.

As mentioned in the Introduction, the transition from small scale lab devices to large scale fab devices encounters ongoing problems in the organic hybrid lead halide perovskite community and the underlying mechanisms are not well investigated and understood. In general, devices produced via continuous coating techniques tend to result in lower PCE than comparable spin coated devices, associated with differences in the perovskite film properties. In the first part of my thesis (Chapter 4) I investigate this open question by examining the kinetics of structure formation of organic hybrid lead halide perovskite thin films with optical *in situ* spectroscopy. To elucidate the origin of these variations in film properties the crystallization kinetics during slot-die and spin coating of perovskite thin films are investigated. As a model system the probably best-investigated MHP methylammonium lead iodide ($CH_3NH_3PbI_3$ or $MAPbI_3$) is chosen. The thin films are processed for both coating techniques in a one-step synthesis, as such conceptually more simple syntheses are more relevant in an industrial context, i.e. for roll-to-roll processing. To ensure comparability in the duration of film formation between the coating techniques, the solvent evaporation rates are adjusted by means of an air knife in the case of slot-die coating and via the rotation speed in the case of spin coating.

Even after the material formation organic hybrid lead halide perovskite are a highly dynamic material class. They tend to phase segregate into halide species-rich domains in working PV devices, significantly hindering the commercialization of these materials. The underlying mechanism of ionic diffusion and how to alter it is currently under debate and various possible origins are discussed. To contribute to this ongoing field of research, the second part of my thesis (Chapter 5) focuses on investigations of the kinetics of the formation of solid solutions in mixed halide lead perovskites via *in situ* X-Ray Diffraction. One popular approach to alter ionic diffusion and therefore phase stability is to add ionic liquids (ILs), but the exact mechanisms how ILs are changing halide kinetics are unclear. Here, perovskite powders ($MAPbI_3$ and methylammonium lead bromide, $MAPbBr_3$) with and without the IL 1-butyl-3-methyl-imidazolium tetrafluoroborate ($BMIMBF_4$) of comparable morphology are physically mixed. These physical mixtures are heated to temperatures between 55 °C and 90 °C and the kinetics of halide diffusion are extracted from the reduction of neat $MAPbI_3$ and $MAPbBr_3$ phases, showing that the addition of $BMIMBF_4$ leads to accelerated ionic diffusion for both halide species, but resulting in a more pronounced

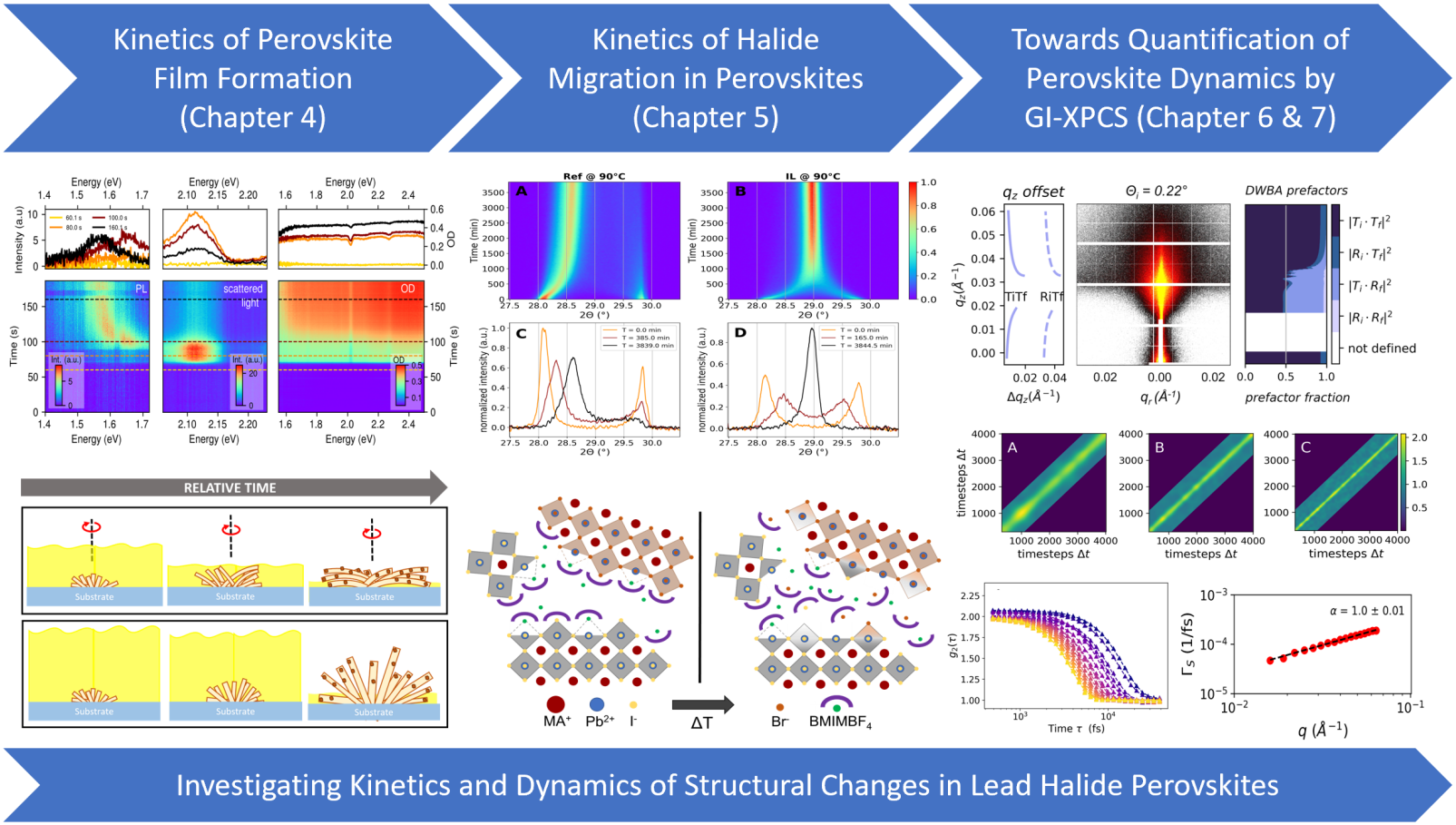

Figure 1.1: Overview of the topics covered within the thesis. The overarching aim of the work is to contribute to the unterstanding of dynamic processes in lead halide perovskites and broaden the available tools to track these dynamics. Therefore, the work is split into three parts. First, established optical spectroscopic methods are used to investigate how the processing techniques spin coating and slot-die coating influence the kinetics of film formation in MHPs. In the next step, time-resolved X-ray diffraction is used to investigate the kinetics of solid solution formation in mixed halide MHPs and how this can be modified by the addition of ionic liquids. In the last part of the work, experiments and simulations are used to determine the origin of distortions in bulk-sensitive GI-XPCS measurements on MHP thin films and how such distortions can be avoided.

acceleration for Bromide.

In the last part I analyzed via experiments (Chapter 6) and simulations (Chapter 7) the angle-dependent geometry and reflection effects in bulk-sensitive grazing incidence X-Ray Photon Correlation spectroscopy (GI-XPCS) measurements. By the GI-XPCS measurements of $MAPbI_3$ thin films and further GI-XPCS simulations I could deduce how the distortions of extracted bulk-dynamics due to geometry and reflection effects arise and how such distortions may be avoided. To quantify the effect of these distortions, at first theoretical calculations on the influence of refractive and reflective effects of X-ray scattering within a thin film are presented. These calculations are then taken into consideration when comparing distortion-reduced grazing incidence transmission (GT)-XPCS measurements to the distorted, but easily available, GI-XPCS measurements. The comparison allows to identify regions in reciprocal space, which are expected to minimize the GI geometry-related distortions in XPCS. Further, it will be analyzed how the identified reciprocal space regions change with sample parameters, such as the film thickness and the material composition. However, since even in the less distorted GT geometry the distortions are not completely eliminated and transmission XPCS measurements for thin $MAPbI_3$ films are not possible, another approach is used to further quantify the influence of distortions in the GI geometry. For this quantification ballistic particle motion in a liquid-like melt is simulated via Molecular Dynamics (MD) simulations. Based on the derived time-resolved particle positions time-resolved X-ray scattering images in a reflection and refraction-free transmission geometry and in the GI-geometry are calculated. Particle dynamics are extracted from the time-resolved scattering images in both geometries and compared to the dynamics calculated from the MD-derived particle trajectories, showing that increased distortions are present within the GI derived dynamics with increasing incidence angle. The incident angle dependence of the distortions is further analyzed to identify the main origin of the distortions. By applying a refraction correction during the recalculation of the time-resolved GI scattering images the calculated transmission XPCS dynamics are nearly reproduced, establishing that for the presented particle motion the main origin of the distortions is connected to refraction effects.

The remaining chapters cover the theoretical background (Chapter 2) and the applied characterization methods and the details on employed material and sample preparation procedures (Chapter 3). The thesis concludes with a summary discussing the results of the presented work and remaining open questions are raised (Chapter 8).

2 Theoretical Section

This chapter covers the theoretical background for the topics dealt within the thesis. First, a brief history of the material class 'perovskite' is given in section 2.1. The focus in this section is put on the perovskite structure including the structural tunability and how different material morphologies, such as crystals, powders and thin films, may influence material properties. Section 2.2 focuses on the optical properties of lead halide perovskites. The section provides the necessary background to follow the structural evolution of lead halide perovskites via photoluminescence and UV-Vis absorption measurements. The chapter continues with an introduction to X-ray scattering and its application to lead halide perovskites in section 2.3. The section covers the basic principle of X-ray scattering, its application in grazing incidence measurement geometries and the use of coherent X-rays for scattering. The chapter concludes with an introduction to solid state Nuclear Magnetic Resonance spectroscopy in section 2.4, covering its application to lead halide perovskite materials.

2.1 Lead Halide Perovskite Background

In general, the term perovskite refers to a material that has an ABX_3 structure (see Figure 2.1). After its first description in 1839, the material class was named after the Russian mineralogist Lev Perovski.[51] Although there are many minerals of the eponymous structure,[52, 53] the term perovskite is used synonymously with metal halide perovskites (MHPs) in the MHP research field. This will also be the case for the presented thesis. For MHP the A-site is populated by cations (e.g. MA^+ or FA^+), while the B-site is populated by a metal (e.g. Pb^{2+} or Sn^{2+}) and the X-site by halide anions (e.g. I^- or Br^-).[54, 55] Since for MHP the A-site cation is an organic molecule, these types of perovskites are referred to as hybrid organic-inorganic perovskites (HOIP).[55] Though first investigated in 1978,[56, 57] the first solar cell with HOIP as the active layer was produced in 2009.[8] While initially power conversion efficiencies of around 3.8% were reported,[8] the research on MHPs increased tremendously in the following years and nowadays MHP single junction solar cells reach power conversion efficiencies above 26%.[7] MHP have also established themselves as active layers in other application areas. Today, they are used in LEDs[14–16] and X-ray detectors[11–13], but also in neuromorphic devices such as artificial synapses and memristors.[20–22] The popularity and rapid growth of MHP-related research is partly due to the comparatively simple synthesis and processing, not requiring specialized laboratory equipment.[58] In addition, the material properties of MHPs can be easily tuned to the respective application,[59] resulting in a tremendous increase in the number of related publications over the years from research groups of varying backgrounds.[60]

One of the most frequently studied and best understood lead halide perovskites is methylammonium lead iodide ($MAPbI_3$),[61] which can be either orthorhombic, tetragonal or cubic in crystal structure, depending on the temperature.[62] $MAPbI_3$

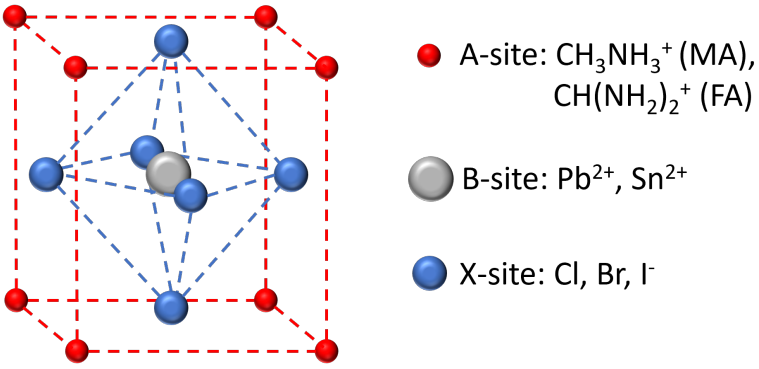

Figure 2.1: Perovskite crystal structure. For MHP the A-site is populated by cations (e.g. MA^+ or FA^+), while the B-site is populated by a metal (e.g. Pb^{2+} or Sn^{2+}) and the X-site by halide anions (e.g. I^- or Br^-).

exists in the tetragonal phase at room temperature ($\approx 160\,\mathrm{K} < T < 330\,\mathrm{K}$) but undergoes a rearrangement to an orthorhombic crystal structure at low temperature ($T \approx 150\,\mathrm{K}$) and a cubic crystal structure at high temperature ($T \approx 330\,\mathrm{K}$).[62] However, the exact transition temperatures depend on the respective sample morphology. For example, $MAPbI_3$ single crystals show well-defined phase transition temperatures for the tetragonal to cubic phase transition (327 K).[63] In contrast, a wide range of temperatures was reported in thin films (310 K to 333 K).[64–67] This is partly due to the polycrystalline sample structure of thin films, as each individual $MAPbI_3$ crystal within the thin film has its own transition temperature, depending on crystal size, strain and crystal defects.[68–70] Recent results have shown that the transition temperature can even be lowered to room temperature (297 K) by means of strain engineering.[71]

2.2 Optical Properties of Lead Halide Perovskites

The basic optical properties of metal halide perovskites are similar to those of other crystalline classical semiconductors, such as silicon or gallium arsenides, and can be described using the basic theory of solid state physics.[72, 73] However, there are also differences to conventional semiconductors. For example, the lead halide perovskites considered in this work feature a soft ionic crystal structure, which contains a heavy lead atom.[31, 74, 75] These differences to conventional semiconductors lead to minor differences in the optical and electrical properties of lead halide perovskites, the origins of which are still being debated.[76]

Absorption of Lead Halide Perovskites: As in conventional inorganic semiconductors, the optical absorption of lead halide perovskites is determined by the band-to-band transition from the valence band maximum (VBM) to the conduction band minimum (CBM). Depending on whether the transition from VBM to CBM takes place at the same position in reciprocal space, i.e. a vertical transition, or takes place at different positions, the band gap is direct or indirect, respectively .[77] In the case of an indirect band gap, the transition from VBM to CBM is supported by phonons. These phonons are responsible for the necessary change in momentum of the excited charge carrier. Because the indirect transition is a two-particle process,

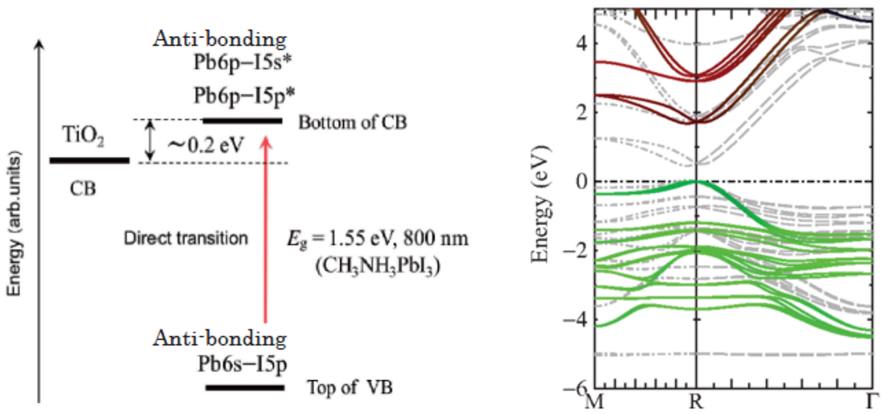

Figure 2.2: Band gap structure and energy landscape of $MAPbI_3$. The right side shows the band gap structure for the quasiparticle self-consistent GW approximation. Zero denotes VBM. Green solid lines, red solid lines, and gray dotted lines depict bands of I 5p, Pb 6p, Pb 6s, respectively. Points denoted M and R are zone-boundary points. Reprinted with permission from Brivio et al.,*Phys. Rev. B* 2014, 89, 155204,[82] (Copyright 2014 by the American Physical Society) and Miyasaka, *BCSJ*, 2018, 7,1058+. [83]

its probability is lower than for a direct transition, resulting in a weaker absorption compared to a direct transition. In addition, the probability for an indirect transition depends on the phonon population, which results in a temperature dependence of the absorption strength.[77]

In the case of approximation of parabolic bands (valid near the extrema), the absorption coefficient $\alpha(E)$ for a direct band gap can be calculated proportional to $\sqrt{E - E_g}$, [78] while for an indirect band gap the absorption coefficient $\alpha(E)$ is proportional to $(E - E_g \pm E_{ph})^2$.[79] Here E_g is the energy of the band gap and E_{ph} is the energy of the phonons involved in the indirect transition. For lead halide perovskites the width of the band gap is defined by the lead and halide orbitals, as both the conduction and valence bands consists of these orbitals,[80–82] as depicted in Figure 2.2.

Another characteristic of absorption, which is not only known for lead halide perovskites, but also for other materials, for example solid state and organic semiconductors, is tail state absorption, consisting of absorbing states below the band gap.[84–87] If the absorption coefficient has a spectral dependence below the band gap of the following form

$$\alpha(E) = \alpha_0 \exp\left(\frac{E - E_0}{E_u}\right), \tag{2.1}$$

these absorbing tail states are called Urbach tail with α_0 and E_0 being fitting parameters with dimensions of inverse length and energy, respectively, and E_U is the so-called Urbach energy.[88] The absorption within the Urbach tail is related to exciton-phonon and electron-phonon interaction plus structural and thermal disorder.[84, 86, 89] As such, the urbach absorption can therefore be used to investigate disorder in perovskite samples. Thereby it is common practice to split the Urbach Energy into two contributions steming from thermal and structural disorder, as depicted in the following formula:[86, 87, 90, 91]

$$E_U(T, X) = K(\langle U^2 \rangle_T + \langle U^2 \rangle_X) \tag{2.2}$$

In Eq. 2.2 $\langle U^2 \rangle$ is the contribution of the respective disorder (T: thermal, X: structural) to the average square displacement of atomic positions from the equilibrium position and K is a constant.[90, 92]

Photoluminescence of Lead Halide Perovskites: Various transitions contribute to photoluminescence after prior photoexcitation. One of these possible transitions is the recombination of free electrons in the conduction band (CB) with free holes in the valence band (VB). This recombination of excess holes and electrons is known as band to band or bimolecular recombination, which is dependent on the concentration of free electrons n and holes p that are generated during photoexcitation.[93] In the case of equal free hole and electron concentrations, the change in the free carrier concentration can be expressed by the rate constant of bimolecular recombination k_2.[93, 94] The rate constant k_2 is an intrinsic material characteristic, which can be related via the Roosbroeck-Shockley relation to the absorption coefficient in the case of thermal equilibrium.[95]

Another transition that may contribute to photoluminescence is the recombination of excitons. Such excitons - electrons bound to holes via Coulomb interaction [93] - are in general divided into Wannier and Frenkel excitons, depending on their spatial extent, which is related to their binding strength. While Wannier-excitons tend to have a high spatial extent (occurring in lead halide perovskites and inorganic semiconductors,[93, 96] Frenkel-excitons have a smaller spatial extent and appear in e.g. organic semiconductors.[96] Excitons are further divided into bound and free excitons. While the term 'bound exciton' refers to an electron-hole pair that is bound to a material defect (e.g. impurities or lattice-defects), a 'free exciton' may travel freely through the material.[93] Due to the extra binding energies of bound excitons compared to free excitons, the photoluminescence of bound excitons generally occurs at lower energies. In addition, bound excitons have significantly greater oscillator strength ('giant' oscilattor strength) compared to free excitons,[97–99] which, with the large spatial extent of Wannier excitons, leads to efficient trapping of excitons at impurities and defects and to a stronger PL in comparison to free excitons.[93, 99]

Additionally, photoluminescence after excitation can also be generated by point defects in the material. Such point defects, which include impurities, interstitials, anti-site occupations and vacancies, lead to a, compared to excitons, broader PL spectrum and are especially relevant at low excitation energies.[100, 101]

Based on the short introduction on photoluminescence above, the photoluminescence of $MAPbI_3$ for its tetragonal phase (up to room temperature) and its cubic phase (at elevated temperatures) is discussed below. Figure 2.3 shows exemplary temperature-dependent PL spectra measured on $MAPbI_3$) thin films.[66, 102] Starting with the orthorombic phase at 160 K the PL spectrum consists of a single well-defined PL peak at around 790 nm, associated with bimolecular band-to-band recombination of free carriers.[66, 94, 103–105] Upon heating to room temperature the PL peak shifts from greater wavelengths to a characteristic wavelength of around 775 nm (1.55 eV).[66, 102] Additionally, the PL peak becomes broader and less intense, as indicated by the change from low to high fluence in Figure 2.3A and the increase in counts in 2.3B. This decrease in intensity is related to a decrease in bimolecular recombination rate k_2 with increasing temperature.[72] When further increasing the

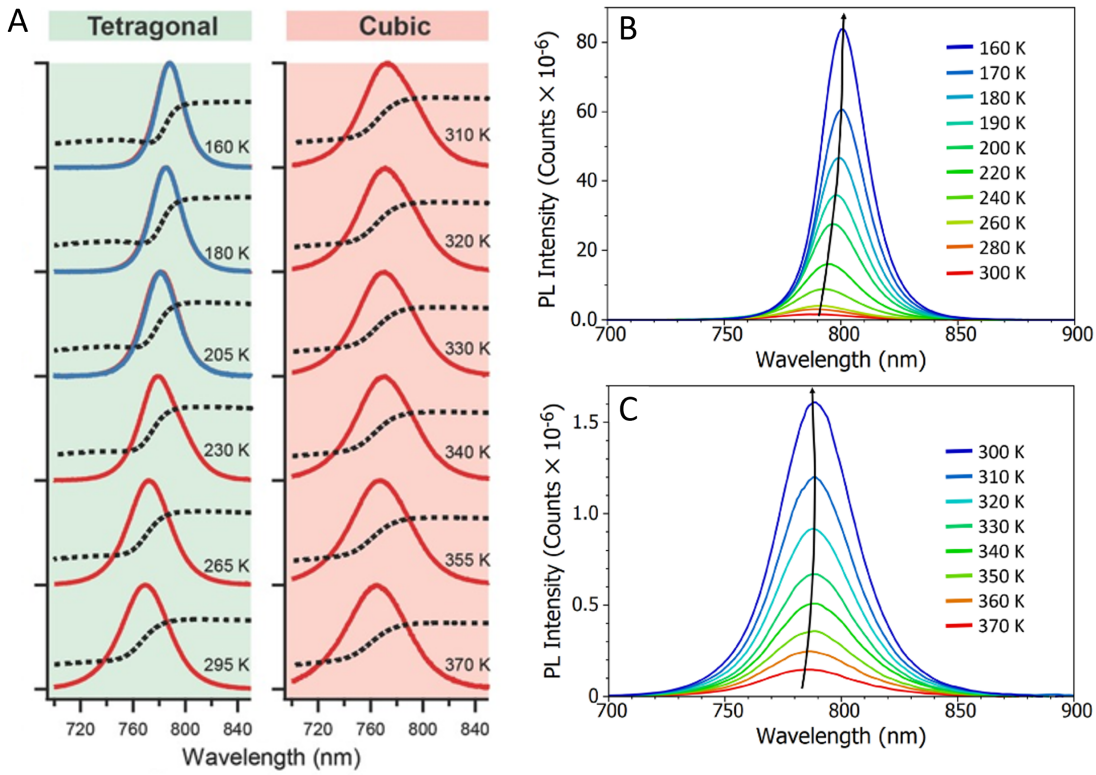

Figure 2.3: A: Normalized PL of a $MAPbI_3$ thin film from between 160 K to 370 K at high (red line) and low fluence (blue line). The black dashed line shows the transmittance indicating the absorption onset. Adapted from Milot et al. 2015[66] under a Creative Commons Attribution 4.0 Licence, Copyright 2015 The Authors. B,C: Diminishing PL intensity of a $MAPbI_3$ thin film from 160 K to 370 K. The black arrows indicate a shift of the PL peak position with temperature. Reproduced with permission from Thomson 2018.[102]

temperature a change to a cubic crystalline phase occurs, which leads to a shift in PL peak position to greater wavelengths around 785 nm due to a sudden change in overlapping orbitals,[66, 106] which is again followed by a change to shorter wavelengths for more elevated temperatures.

To be quite thorough it must be noted that the presented PL features within the tetragonal and cubic crystal phases are mainly related to bimolecular recombination. Features related to the above mentioned excitonic- and defect-related PL are mainly relevant for the PL spectrum of the low temperature orthorombic crystal phase. As these features are highly dependent on the experimental conditions and the quality and nature of the sample, their occurance and their respective intensities vary highly between publications.[66, 106–108]

Influences of Stoichiometry and Morphology on Lead Halide Perovskites: As mentioned in the introduction, metal halide perovskites have the beneficial property that the optoelectronic properties can be easily tuned. This can be done, for example, by replacing the constituents or mixing different constituents, e.g. different halogens or different organic molecules.[109–113] In particular, the possibility of changing the bandgap to a level suitable for various applications, e.g. in memristors, photodetectors

or solar cells, is a major advantage.[11, 12, 20, 21, 114–116] The selection of the possible components, however, is limited by their respective size, which is expressed in the so-called Goldschmitt rule:[117]

$$\alpha = \frac{r_A + r_X}{\sqrt{2}(r_B + r_X)} \tag{2.3}$$

In Eq. 2.3 r_i denotes the ionic radii for the ions located at the A-, B- and X-sites, which result in the Goldschmitt tolerance factor α. For stable perovskites, the tolerance factor α assumes values between 0.8 and 1.0.[117] While the empirical Goldschmitt rule was developed for oxide perovskites it retains its validity for metal halide perovskites.[117, 118] However, it is not only the respective ionic radii that determine whether a perovskite structure is formed, but the electrical charge of the unit cell must also be neutral. Materials such as iodide (I^-), bromide (Br^-) and chloride (Cl^-), as well as methylammonium (MA, $[CH_3NH_3]^+$) and formamidinium (FA, $[NH_2(CH)NH_2]^+$) are often used in lead-based metal halide perovskites, as they fulfill both criteria.[119]

As introduced in the beginning of this chapter, the band gap and thus the PL of lead halide perovskites depends mainly on the lead and halide orbitals.[80–82, 120] Thus, the optoelectronic properties can easily be influenced by the exchange of the halide species. As introduced above, $MAPbI_3$ shows a band gap of 1.55 eV at room temperature,[45, 109, 121] whereas the exchange of iodide to bromide increases the band gap to 2.35 eV for $MAPbBr_3$.[45, 122, 123] Proportional mixtures of the halide anions at the X-side are possible, resulting in an almost continuous shift of band gap energies from 1.55 eV to 2.35 eV when substituting increasing amounts of iodide with bromide.[45, 124] The almost continuous increase in the band gap energy is associated with a similar reduction in the unit cell lattice parameter, accompanied by a transition from the tetragonal to the cubic crystal phase at room temperature.[124] At higher temperatures (above $\approx$ 330 K) both $MAPbI_3$ and $MAPbBr_3$ are within a cubic crystalline phase and no phase transition with increasing bromide content takes place.[125] Figure 2.4 exemplarily shows the absorbance, PL, band gap energy and unit cell lattice parameter for varying mixtures of $MAPbI_{3-x}Br_x$ with x ranging from 0 to 3. Furthermore, the figure shows that, depending on the evaluation method, the band gap energies vary by several tens of meV. This constitutes one of the reasons for variations in reported band gap energy values between various research groups.[113, 126]

One effect occurring in mixed-halide perovskites is the so-called light-induced phase segregation.[127, 128] In this process, the halide anions migrate within the material under light irradiation and separate in regions with an excess of a single halide species, altering the optoelectronic properties.[129, 130] PL spectroscopy is an established tool to track illumination-induced halide demixing, allowing to link the change in the PL peak position to the present halide compositions.[128, 130] However, problems arise when quantifying the respective composition quantities, as charge carrier funneling occurs from high-bandgap to low-band gap halide perovskite compositions.[131] For example, a 1:1 mixed bromine iodine halide perovskite shows a disproportionately intense $MAPbI_3$-associated PL peak after demixing, as charge carrier funneling from $MAPbBr_3$-rich regions to $MAPbI_3$-rich regions takes place.[45, 130, 132]

In addition, the optoelectronic properties depend on the sample morphology. For example, differences in the optical properties occur between a single-crystalline sample, a polycrystalline thin film or a powder sample. These differences are related

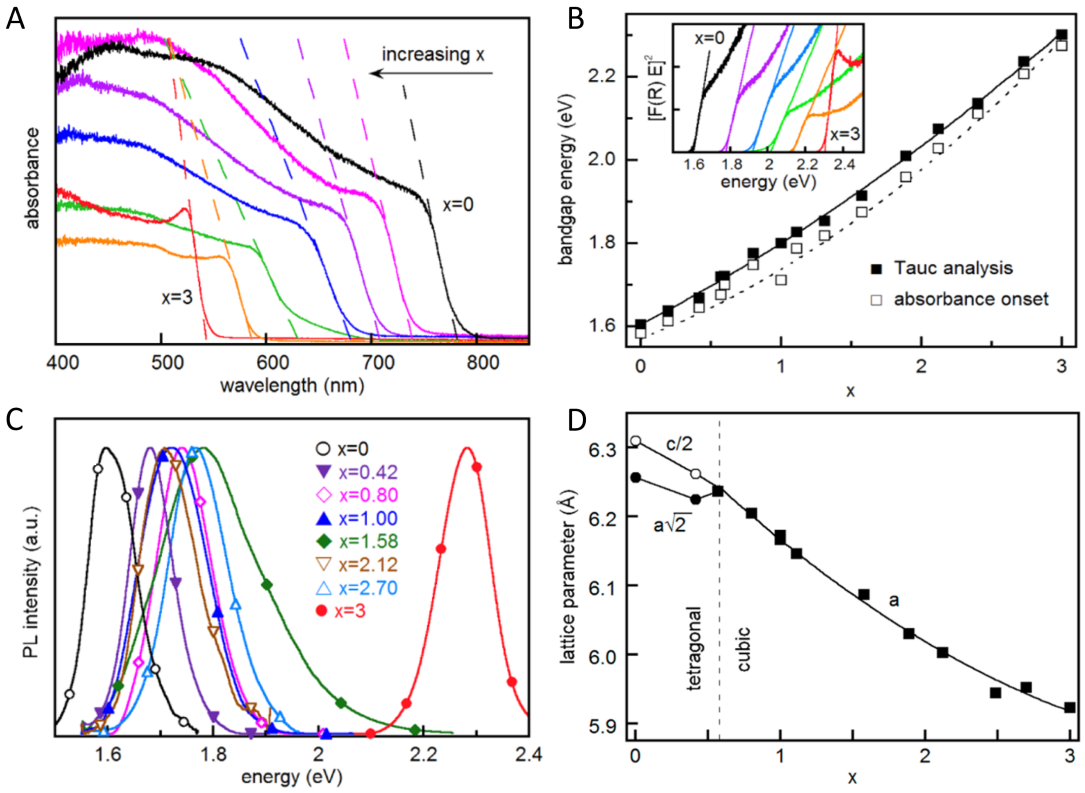

Figure 2.4: A: Absorption spectra, B: band gap energy (determined via Tauc analysis and absorbance onset), C: PL intensity spectra and D: lattice parameter of $MAPbI_{3-x}Br_x$ thin films with varying bromine content x. Adapted with permission from Fedeli et al. [124], Copyright 2015 American Chemical Society.

to changing degrees of crystallinity and, for example, the influence of the underlying substrate in the case of thin films. A large proportion of the differences that occur can be attributed to differences in defect densities. In general, solution-processed thin films have a higher density of bulk defects, whereas single crystals have fewer due to their comparatively more controlled and slower growth.[112, 133, 134] In addition, thin films have a significantly higher surface-to-bulk ratio in comparison, which means that there are more grain boundaries, which are known to have an increased defect density.[112, 135] The greatly increased defect density in polycrystalline thin films results in a trap-dependent reduced excited state lifetime and photonluminescence quantum yield (PLQE) compared to single crystals.[136–139]

Another proportion of the occurring differences in the optical properties can be related to external factors, such as stress and strain within perovskite grains. In combination with the above mentioned variances in defect densities thin films, single crystals and powders show different optical signatures during structural phase transitions. An example is the transition from the orthorombic to the tetragonal $MAPbI_3$ phase. For thin film samples, this transition occurs over a range of tens of Kelvin,[44, 106, 140, 141] whereas for powder samples of the same material, the transition temperature is much more narrowly defined.[62, 142] This is related to the fact that in polycrystalline perovskite samples such as the thin films and powders mentioned, each crystalline grain has an individual phase transition temperature which depends on the defect density of the grain,[143] but is also influenced by stress and strain, i.e.

caused by any substrates in the case of thin films.[142] However, this dependence of phase transition temperatures on strain and defect densities can lead to advantages in sample stability, and strain engineering is now an established subfield of stability research in metal halide perovskites.[144, 145] As a result, the cubic phase of $MAPbI_3$ has been stabilized at room temperature, revealing insights into the structure-dependent changes in optoelectronic properties going from the tetragonal to the cubic crystal phase.[71]

2.3 X-Ray Scattering for Lead Halide Perovskites

As introduced in the section before a structure-optoelectronic property relationship exists in metal halide perovskites, and as such the sample morphology plays a crucial role. Two separate length scales are of special interest. First, the local ordering on the scale of the crystalline unit cells has a strong impact on the optoelectronic properties such as the PL peak position and PLQE. Second, larger morphological features such as crystalline grains or phase separations in mixed halide perovskites play a crucial role for its functionality.

To link the morphology of MHP sample with their optoelectronic properties X-ray scattering techniques are a non-destructive tool enabling the investigation of the volume morphology on different length scales. In this section, the general concept of X-ray scattering is introduced, followed by its application to X-Ray diffraction measurements and measurements in grazing incidence geometries. The section concludes on how the usage of coherent scattering allows the extraction of structural dynamics.

X-ray Scattering Principle: X-ray scattering is based on the interaction of an incident electromagnetic wave with the electrons of the sample being analysed. The incident photons of wave vector $k = |\vec{k}_i| = \frac{2\pi}{\lambda}$ with λ being the wavelength are described by an electromagnetic field vector:[146]

$$\vec{E}(\vec{r}) = \vec{E}_0 \cdot \exp(i\vec{k}_i\vec{r}) \tag{2.4}$$

With $\vec{r}$ being the position vector and the vector $\vec{E}_0$ provides information about the amplitude and polarisation of the incident photons. The propagation of $\vec{E}(\vec{r})$ through a medium is described by the Helmholtz equation, which connects the refraction index $n(\vec{r})$ of the medium with the incident electric field:[146]

$$\Delta\vec{E}(\vec{r}) + k^2 n^2(\vec{r}) \cdot \vec{E}(\vec{r}) = 0 \tag{2.5}$$

The refractive index $n(\vec{r})$ is defined as follows:

$$n(\vec{r}) = 1 - \delta(\vec{r}) + i\beta(\vec{r}) \tag{2.6}$$

and depends on the dispersion δ and absorption β. Both dispersion and absorption are wavelength-dependent material properties resulting in the case of X-rays in refractive index values slightly smaller than unity. The dispersion and absorption are calculated as follows:

$$\delta(\vec{r}) = \frac{\lambda^2}{2\pi}\rho(\vec{r}), \quad \beta(\vec{r}) = \frac{\lambda}{4\pi}\mu(\vec{r}) \tag{2.7}$$

depending on the scattering length density $\rho(\vec{r}) = r_e\rho_e(\vec{r})$ (ρ_e: electron density; r_e: electron radius) and the linear absorption $\mu(\vec{r})$. In the case of X-rays and photon energies away from material-specific absorption edges,[147] typical values of the dispersion δ are in the range of 10^{-6}, whereas the absorption β is one to two orders of magnitude smaller.[147] Considering the differences in the refractive index of two different materials, an expression for the scattering strength can be given, which is referred to as contrast:

$$\Delta\delta^2 + \Delta\beta^2 = (\delta_1 - \delta_2)^2 + (\beta_1 - \beta_2)^2 \tag{2.8}$$

The contrast indicates how strongly scattering occurs at the interface of the materials due to differences in scattering length density, i.e. the respective electron densities.

As the refractive index n is smaller than unity total external reflection (TER) occurs. For a homogeneous medium with no spatial variance of $n(\vec{r})$, the critical angle α_c for TER can be estimated via Snell's law, resulting in the following expression:

$$\alpha_c = \sqrt{2\delta} \tag{2.9}$$

This material-dependent critical reflection angle is important in scattering experiments. Yoshikazu Yoneda was the first to show that anomalous surface scattering from thin films in grazing incidence X-ray scattering exhibits an intensity enhancement when emerging at the critical angle.[148] This phenomenon allows the material-specific investigation of individual materials in, e.g. material blends or phase segregating ones.

X-ray Scattering for X-Ray Diffraction (XRD) measurements: The most widely used X-ray scattering technique is X-ray diffraction (XRD), a technique to probe the crystalline structure of a sample. By using a monochromatic X-ray beam, the scattering from different lattice planes (hkl) within the sample is investigated. Figure 2.5A shows an example of parallel impinging X-rays being diffracted at two parallel crystalline lattice planes with the distance d_{hkl}. As a result the outgoing X-rays have a path length difference of Δs. Depending on the path length difference and therefore the incident angle Θ of the scattered beams constructive or destructive interference is observed. Under the Bragg condition,[149]

$$n\lambda = 2d_{hkl}sin(\Theta) \tag{2.10}$$

constructive interference occurs. Introducing the scattering vector $\vec{q} = \vec{k_f} - \vec{k_i}$, which is an expression of the momentum transfer between incoming wave vector $\vec{k_i}$ and outgoing wave vector $\vec{k_f}$, the Bragg condition can be expanded to the Laue condition in three dimensions. The Laue condition states that if the difference between the incoming wave vector and the scattered wave vector is equal to a reciprocal lattice vector ($\vec{q} = \vec{G}$), constructive interference occurs.[150] A common visualization depicting which scattering vectors $\vec{q}$ can satisfy the Laue condition is the Ewald sphere, which is depicted in Figure 2.5B.[151] In the case of elastic scattering with momentum conservation ($|\vec{k_i}| = |\vec{k_f}|$) the Ewald sphere has a radius of $|\vec{k_i}|$, depicting from the overlap of the shell and the reciprocal lattice points for which scattering vectors diffraction patterns are observed.

A common approach to the application of the Bragg condition in XRD is to take measurements within the Bragg-Brentano geometry.[152] Within the Bragg-Brentano measurement geometry the X-ray source and the downstream placed X-ray detector are moved in parallel on a semispherical arc around the sample. As a result, the scattered light is detected under the specular condition, i.e. $\Theta_i = \Theta_f$. This is advantageous because the detected intensity is maximized under the specular condition. The detected intensity patterns in XRD are commonly plotted against the scattering angle 2Θ. The Bragg-Brentano-geometry for XRD is depicted in

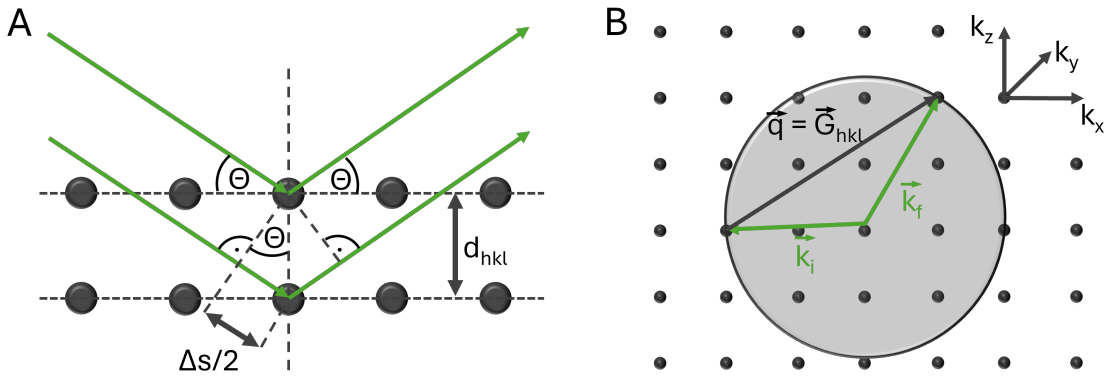

Figure 2.5: A: Illustration of the Bragg conditions. Two parallel beam paths (green) impinge under angle Θ on crystalline lattice planes with distance d_{hkl}. The scattered beams exit under angle Θ and interfere constructively if the path difference Δs is an integer multiple of the wavelength. B) Illustration of the Ewald sphere. Constructive interference occurs for the intersections of the reciprocal lattice (dots) with the shell defined by the radius of $|\vec{k_i}|$.

Figure 2.6. The illustration also shows an important limitation of XRD. XRD is only sensitive to crystalline planes that are perpendicular to the surface normal of the sample. This is related to the momentum transfer in XRD only occurring along the q_z direction, due to the specular detection. In order to be able to characterize samples, XRD samples are often prepared as powders so that all possible sample orientations are isotropically distributed in it.[152]

Consequently, powdered XRD samples show a plethora of scattering peaks. These diffraction peaks allow to extract different characteristics of the crystalline domains of the sample. As already stated above, the peak position in reciprocal space is inversely proportional to the distance d_{hkl} between lattice planes within the crystalline domains. Furthermore, the amplitude provides information about the amount of crystalline domains, while via the Scherrer equation the spatial expansion of crystallites within the sample can be determined. For this purpose, the Scherrer equation links the full width half maximum (FWHM) $\Delta(2\Theta_{hkl})$ of a diffraction peak at a scattering angle $2\Theta_{hkl}$ with a lower limit of the crystallite size D_{hkl}:[153]

$$D_{hkl} = \frac{K\lambda}{\Delta(2\Theta_{hkl}) \cdot cos(\Theta_{hkl})} \tag{2.11}$$

In Eq. 2.11 K is the Scherrer constant and λ is the wavelength. Typical values for K are cited to be around 0.9,[154] while the original publication state it to be 0.93.[153] It is important that only for average crystallite sizes below 100 nm to 200 nm a sample-related FWHM widening is expected, which is why values for D_{hkl} can only be extracted below this size.[155]

Based on this, XRD has developed into a valuable tool for the phase characterization of perovskites as powders, but also for thin films. Typical applications are the determination of crystallite size and crystalline phases,[40, 156] the determination of phase purity of precursors for mixed halide perovskites, as well as the detection of crystalline degradation products,[45, 156, 157] but also the time-resolved tracking of mixing and demixing processes based on material changes due e.g. halide ion

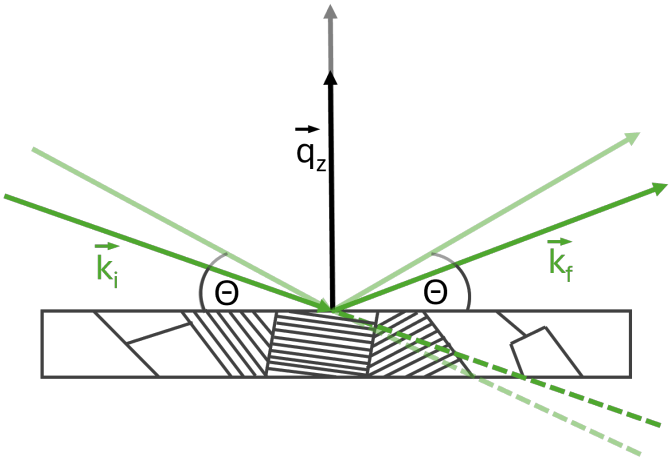

Figure 2.6: Illustration of the Bragg-Brentano geometry in XRD measurements. The wave vector $\vec{k_i}$ (green) impinges under angle Θ and scatters on a powder sample, showing various crystalline orientations. The exiting wave vector is detected under specular conditions at angle Θ, detecting scattering at an effective angle of 2Θ. The resulting q_z-vector of scattering is orientated perpendicular to the surface normal. The transparent representations of impinging and exiting wave vectors and q_z show that XRD only generates scattering sensitive to the structure along the surface normal.

migration.[45, 158] In addition, XRD can be used to characterize effects such as stress and strain in thin films,[159] a prerequisite for strain enginnering in metal halide perovskites.[70, 145]

Grazing Incidence X-ray Scattering (GIXS) measurements: While in the XRD community it is common to express experimental data in the scattering angle 2Θ, the scattering vector q is more commonly applied for other scattering techniques, such as in grazing incidence X-ray scattering (GIXS) techniques. Herein, an X-ray beam impinges on the sample under a shallow angle $\Theta_i < 1°$. The shallow angle results in a large footprint on the sample and a large scattering volume, respectively. In contrast to XRD where point or line detectors are applied in GI the diffuse scattering is captured on an area (2D) detector. For each pixel on the detector the scattering angles Θ_f and Ψ_f can be assigned, with Θ_f being the scattering angle introduced for XRD and Ψ_f being the scattering angle out of the plane, spanned by impinging and specular beam. Thus, for grazing incidence geometries the scattering vector q can be expressed as:

$$\vec{q} = \begin{pmatrix} q_x \\ q_y \\ q_z \end{pmatrix} = \frac{2\pi}{\lambda} \begin{pmatrix} cos(\Psi_f)cos(\Theta_f) - cos(\Theta_i) \\ sin(\Psi_f)cos(\Theta_f) \\ sin(\Theta_i) + sin(\Theta_f) \end{pmatrix} \tag{2.12}$$

Two cases of GIXS are discussed in more detail below, namely grazing incidence wide angle X-ray scattering (GIWAXS) and grazing incidence small angle X-ray scattering (GISAXS). These GIXS techniques differ primarily in terms of the sample-detector distance (SDD) used and thus the resulting q range, with a higher and lower covered q range, respectively.

Firstly, GIWAXS, also known as GIXD on a 2D detector, is discussed. GIWAXS is mainly measured in a SDD of several mm to about 300 mm and the concepts of the Ewald sphere and the Bragg scattering condition introduced for XRD are retained. Further analyses, e.g. of strain, are less meaningful for GIWAXS measurements as the q range is reduced compared to XRD. With regard to crystallite sizes, there are no restrictions. However, the Scherrer equation given in Eq. 2.11 must be transferred to q space, which results in the Scherrer equation in reciprocal space, depending on the reciprocal space FHWM Δq_{hkl}:

$$D_{hkl} = \frac{2\pi K}{\Delta q_{hkl}} \tag{2.13}$$

A closer look at the Ewald construction in Figure 2.5B shows an important limitation in GI geometries. For an incident wave vector $\vec{k_i}$, the scattered wave vector cannot contain a k_z component without also having components within the $k_{x/y}$ plane. In GIWAXS measurements this is always the case, where scattering within the specular plane ($k_y = 0$) is a combination of k_z and k_y. As a consequence, part of the q range along the q_z direction is not accessible. The inaccessible q_z region is referred to as the 'missing wedge', when the 2D detector image is projected in a $q_{x/y}$ vs q_z representation.[160]

While GIWAXS is sensitive to the intramolecular distance, such as the crystalline lattice planes in metal halide perovskites, GISAXS is sensitive to bigger real space distances, such as crystalline domain and grain sizes. This larger real space distance corresponds to a lower q range and smaller exit angles Θ_f. These smaller exit angles lead to pronounced effects of reflection at the sample and substrate surface, as well as to refractions at the vacuum-sample and sample-substrate interface. A distinction must be made between two grazing incidence small angle geometries: the more commonly applied grazing incidence (GI) geometry and the grazing incidence transmission geometry (GT) geometry. Both geometries are shown in Figure 2.7. The figure shows that the refraction at the interfaces results in a difference between the real scattering vector Q_z (labelled intrinsic scattering vector Q_z) and the scattering vector q_z measured at the detector. It should be noted that the change between intrinsic Q_z and detector q_z is only relevant for the small exit angles observed in SAXS.[161] Furthermore, for the transformation of the $q_{x/y}$ component the difference between intrinsic and detector reciprocal space along the z axis is negligibly small.[161] The figure further shows that GISAXS is measured above the horizon ($\Theta_i > 0$) and GTSAXS is measured below the sample horizon ($\Theta_i < 0$).

For both, GISAXS and GTSAXS the reflection and refraction events need to be adressed to fully understand the diffraction signal observed on a 2D area detector. A well established approach to account for the occurence of reflections is the distorted wave Born approximation (DWBA), a first-order perturbation approach, which calculates the exiting diffuse scattering as a combination of the direct scattering and scattering from reflection events.[162, 163] The relevant scattering contributions within the DWBA are shown in Figure 2.8, starting from left to right with direct scattering to various sequences of reflection and scattering events. As the intensity on the detector is derived from the combination of scattering and reflection events the intensity $I_d(q_z)$ is calculated in the DWBA as follows:

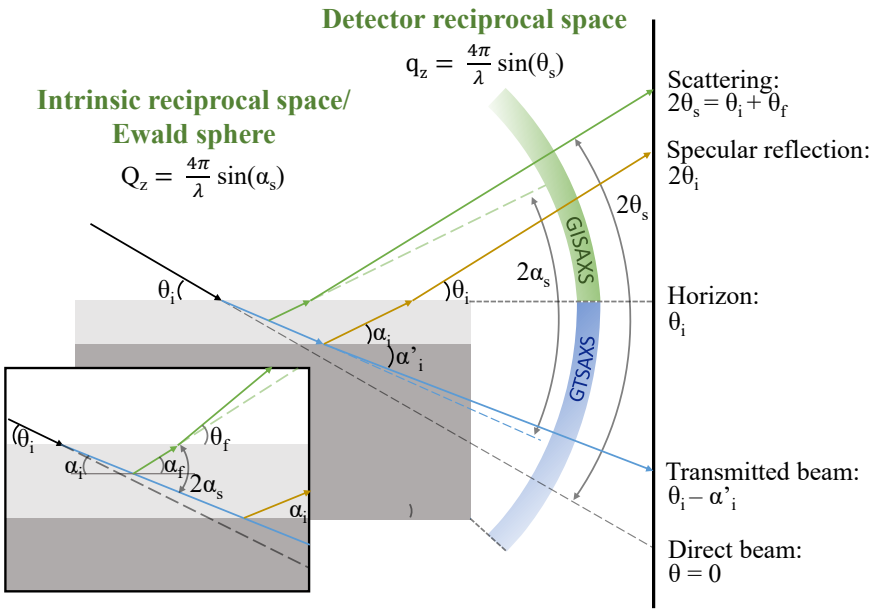

Figure 2.7: The schematic diagram depicts the X-ray scattering geometry for grazing incidence experiments. An incident beam (solid black line with incident angle Θ_i) is first refracted at the air-film interface and a second time at the film-substrate interface for grazing transmission (GT)-SAXS experiments. The refraction events alter the exit angle of the transmitted beam (blue line) relative to the direct beam at $\Theta = 0$. A similar refraction sequence applies to the scattered X-rays (dark green line) while the beam leaves in the grazing incidence (GI)-SAXS region. Due to refraction the scattering occurs in the thin film under an angle of $2\alpha_s = \alpha_i + \alpha_f$ (in intrinsic sample reciprocal space Q_z) and is projected to the detector at a different scattering angle $2\Theta_s = \Theta_i + \Theta_f$, resulting in an altered detector reciprocal space q_z.

$$\begin{aligned} I_d(q_z) = &|T(\alpha_i)T(\alpha_f)F(+Q_{z1}) + T(\alpha_i)R(\alpha_f)F(-Q_{z2}) + \\ &R(\alpha_i)T(\alpha_f)F(+Q_{z2}) + R(\alpha_i)R(\alpha_f)F(-Q_{z1})|^2 \end{aligned} \tag{2.14}$$

Herein $F(\pm Q_{z1/2})$ is the scattering strength of the form factor, capturing the sample scattering for the intrinsic $Q_{z1/2}$ vectors. The vectors $Q_{z1/2}$ take into account the beam direction within the film. As such Q_{z1} corresponds to the refracted classical definition of q_z introduced in Eq. 2.12, while

$$Q_{z2} = ksin(\alpha_i) - ksin(\alpha_f) \tag{2.15}$$

represents a shift of the associated scattering along q_z caused by a single reflection events. $R(\alpha_i)$ and $R(\alpha_f)$ are the angle dependent Fresnel reflectivity coefficients and $T(\alpha_i)$ and $T(\alpha_f)$ are the respective Fresnel transmissivity coefficients, which can be calculated by following the multilayer matrix formalism.[164, 165]

After expansion, Eq. 2.14 consists of 16 terms, in which most are complex valued cross terms describing interference effects between the DWBA contributions shown in Figure 2.14. For polydisperse samples these cross terms can be neglected as they are comparatively small only result in high-frequency modulations seen near the materials critical angle and small $q_{x/y}$.[166–168] As a result the full DWBA is often

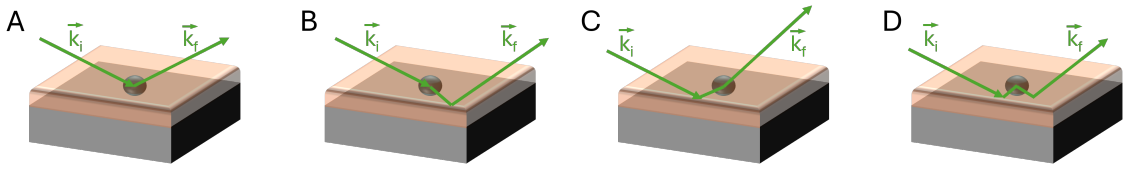

Figure 2.8: Schematic illustration of the contributions within the DWBA. A: Directly scattered incident beam. B: First scattered then reflected beam. C: First reflected then scattered beam. D: Sequence of reflection, scattering and reflection of the incident beam.

simplified to the 4 main contributing terms, describing the intensity due to the independent scattering terms considered in Figure 2.8. The result is referred to as the simplified DWBA (sDWBA):[161]

$$\begin{aligned} I_d(q_z) =& |T(\alpha_i)T(\alpha_f)|^2|F(+Q_{z1})|^2 + |T(\alpha_i)R(\alpha_f)|^2|F(-Q_{z2})|^2 + \\ & |R(\alpha_i)T(\alpha_f)|^2|F(+Q_{z2})|^2 + |R(\alpha_i)R(\alpha_f)|^2|F(-Q_{z1})|^2 \end{aligned} \tag{2.16}$$

Several analysis programs for grazing incidence scattering data are based on the sDWBA and allow to simulate 2D scattering patterns.[169–171]

Since GTSAXS was previously introduced as GISAXS with exit angles below the sample horizon $\Theta_i < 0$, the exit angle restriction has a strong impact on the required sDWBA scattering terms. Scattering from a reflection after the scattering event results in an exit angle above the sample horizon and cannot contribute to a GTSAXS signal. As a consequence, only the following sDWBA terms are relevant for GTSAXS:[172]

$$I_d(q_z) = |T(\alpha_i)T(\alpha_f)|^2|F(+Q_{z1})|^2 + |R(\alpha_i)T(\alpha_f)|^2|F(+Q_{z2})|^2 \tag{2.17}$$

further simplifying the necessary calculations for scattering events compared to GISAXS. As $R(\alpha_i)$ is often vanishing for high incidence angles α_i, GTSAXS is often referred to as 'surface scattering within the Born approximation'.[172]

Both GIWAXS and GISAXS are commonly applied methods to characterize metal halide perovskite thin films. With the help of GIWAXS, the film formation mechanisms for several MHP systems could be resolved and some of the relevant precursor complexes were identified.[46, 173] In addition, GIWAXS is a suitable tool for tracking degradation processes and the associated phase transitions in metal halide perovskite thin films.[174, 175] GISAXS supplements this information with longer length scales and thus allows, for example, the formation of nuclei to be correlated with typical distances between them in order to create a complete picture of film formation mechanisms.[176, 177]

X-ray Photon Correlation Spectroscopy: Another scattering technique, which is not only sensitive to the samples crystalline structure, but can also probe its dynamics, is X-ray photon correlation spectroscopy (XPCS). XPCS probes the dynamics present in bulk materials as well as at their surfaces and interfaces.[178] The extracted dynamical properties may be for example the diffusivity and sub- or super-diffusive behaviour of a colloidal system or the time between dejamming steps in a system of decomposing emulsion.[179–181] XPCS can either be measured in a

standard transmission geometry, i.e. applied in SAXS measurements, or in a grazing incidence scattering geometry (either GISAXS or GTSAXS). In general, in all possible measurement geometries the measurement approach is identical to a time-resolved scattering measurement in which a series of subsequent scattering images on a 2D detector is recorded.[182] In contrast to classical SAXS or GISAXS measurements, where non-coherent X-ray beams are utilized, for XPCS highly coherent X-ray beams are used. As such the time-resolved scattering images in XPCS show speckle patterns, arising from scattering due to the time-dependent structural arrangement of electron density differences within the material present in the illuminated coherence volume.[183] The time on which the correlation function derived from the intensity of the evolving speckle pattern decorrelate offers a measure to quantify the dynamical properties of the sample in the illuminated coherence volume.[184] The measurement procedure for a transmission geometry is shown in Figure 2.9. In this geometry XPCS is foremost applied to liquid samples, such as colloidal solutions, creams and emulsions or even protein solutions.[179, 181, 185, 186] But also for non-liquid and more jammed-like systems, more similar to perovskite thin films, XPCS can be applied. Typically applied thin film systems currently include curing of epoxy resins, confined polymers and following the thin film growth for various materials ranging from polymers, small molecules to metallic nitrides.[187–190]

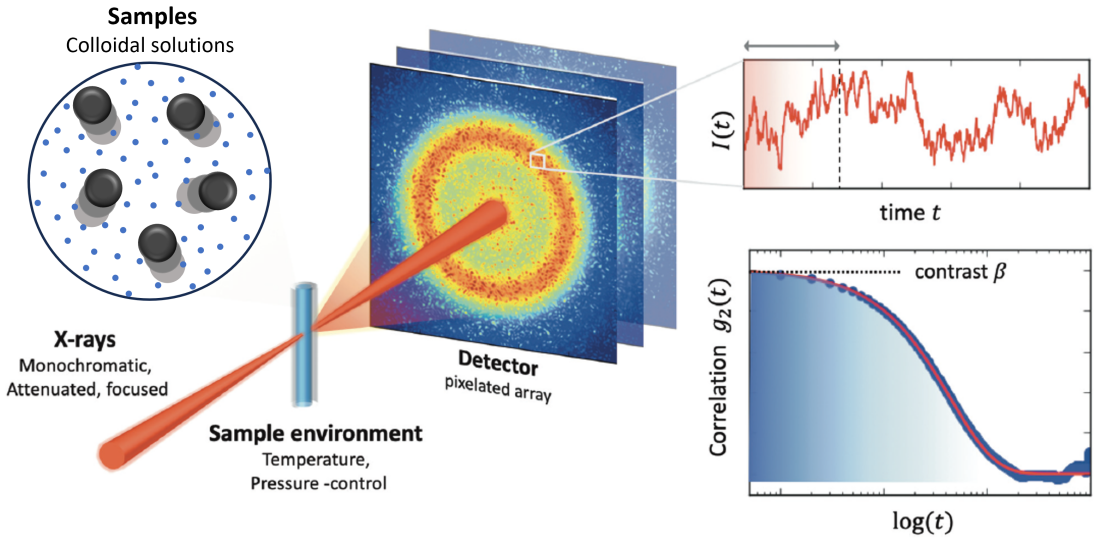

Figure 2.9: Illustration of an experimental setup of X-ray Photon Correlation Spectroscopy (XPCS) of colloidal solutions. A coherent, monochromatic X-ray beam impinges on the sample, producing a time series of speckled scattering pattern on a pixelated 2D area detector. The scattering intensity (upper right hand panel) fluctuates as a function of time. Calculating the intensity correlation function g_2 (lower right hand panel) from the fluctuating intensity $I(t)$ gives a measure about the present dynamics. The characteristic decay time on which g_2 decays to 1/e reflects the timescale of the present colloidal motion at the momentum transfer q at which $I(t)$ was calculated. Adapted from Perakis and Gutt 2020[185] under a Creative Commons Attribution-Noncommercial 3.0 Unported Licence.

For equilibrium systems the dynamics of the scatterers can be extracted from the detected speckle patterns via the calculation of the one-time correlation function g_2

(1TCF), which is calculated as follows:[179, 191]

$$g_2(q,\tau) = \frac{\langle I(q,t)I(q,t+\tau)\rangle}{\langle I(q)\rangle^2} \tag{2.18}$$

In Eq. 2.18 $I(q,\tau)$ is the intensity measured at wave vector q at lag time τ. The average $\langle\cdot\rangle$ is taken over the whole time series of possible t. Two limits for small and large delay times are reached for $g_2(q,t)$, $\langle I^2(q)\rangle$ and $\langle I(q)\rangle^2$ respectively.[191] As such $g_2(q,t)$ reaches unity for $t \to +\infty$ and $1+\beta$ for $t \to 0$, with β being the optical contrast. For perfectly coherent light sources β equals unity, while for partially coherent X-rays, describing the conditions in typical XPCS experiments, values between 0 and 1 are reached.[191] An example of g_2 can be seen in the lower right hand panel of Figure 2.9.

If the systems shows non-equilibrium dynamics, such as jamming, freezing or evolving structures, which result in changed velocities of scatterers Eq. 2.18 only shows an average of the dynamics, but is not reproducing its evolution with time. For such non-equilibrium systems the dynamics can be characterized by two-time correlation functions (2TCF):

$$C(q,t_1,t_2) = \frac{\langle I(q,t_1)I(q,t_2)\rangle}{\langle I(q,t_1)\rangle\langle I(q,t_2)\rangle} \tag{2.19}$$

The calculation results in a symmetric 2D map showing the intensity correlation between times t_1 and t_2 in the measured time series. As expected $C(q,t_1,t_2)$ reaches a maximum for $t_1 = t_2$ (selfcorrelation) and decays as a function of the lag time τ, which is defined as $\tau = |t_1 - t_2|$ in the case of 2TCF[191]. From the 2TCF it is possible to characterize steady-state dynamics within the non-equilibrium dynamics by extracting 'aged' 1TCF $g_2(q,\tau)$ at deterioration time $\bar{t} = \frac{t_1+t_2}{2}$:[191]

$$g_2(q,\tau) = \left\langle \frac{\langle I(q,\bar{t}-\frac{\tau}{2})I(q,\bar{t}+\frac{\tau}{2})\rangle}{\langle I(q,\bar{t}-\frac{\tau}{2})\rangle\langle I(q,\bar{t}+\frac{\tau}{2})\rangle} \right\rangle_{\bar{t}\pm\Delta\bar{t}} \tag{2.20}$$

In Eq. 2.20 the average $\langle\cdot\rangle_{\bar{t}\pm\Delta\bar{t}}$ indicates that g_2 is extracted over a range of deterioration times $2\Delta\bar{t}$ around $\bar{t}$ in which the extracted 1TCF are invariant. For full disclosure it should be mentioned that the 1TCF is connected to the intermediate scattering function $g_1(q,\tau)$ (ISF) and can be calculated via the Siegert relation from it.[192]

One approach to analyze the extracted 1TCFs from a XPCS experiments is to approximate its form via a stretched exponential fit of the following form:

$$g_2(q,\tau) = \beta \cdot \exp(-2(\Gamma\tau))^\gamma + g_\infty \tag{2.21}$$

As introduced above β is equivalent to the optical contrast, also labelled as Siegert factor, and is defined by the setups geometry, the sample and the coherence properties of the impinging X-ray beam.[191] γ is the Kohlrausch-Williams-Watts (KWW) exponent [193] of the stretched exponential and Γ its characteristic decay frequency. The offset g_∞ is known as the ergodicity plateau, which is reached for $\tau \to \infty$. Often equivalent forms of Eq. 2.21 are applied, e.g. using the characteristic decay time $\tau_0 = 1/\Gamma$. Following such a fitting approach is well-known for soft matter systems and glass-formers, which mainly show purely diffusive and hyper diffusive dynamics.[185, 194–196] But also for jammed systems and rapidly evolving systems the presented approach keeps its validity. [179, 197–199]

2.4 Solid-State Nuclear Magnetic Resonance Spectroscopy for Lead Halide Perovskites

As introduced in the prior sections optoelectronic and structural information relevant to the functionality of MHP in various applications can be accessed by either optical spectroscopy or X-ray scattering. Another versatile and non-destructive tool to gather further information is solid-state Nuclear Magnetic Resonance (ssNMR) spectroscopy. In ssNMR spectroscopy experiments the resonance frequencies of nuclear spins of a nucleus species are examined in an external oscillating magnetic field. From the measured resonance frequencies the chemical nature, geometry, and topology of the surroundings of the examined atomic nuclei species can be deduced. Through the time-resolved measurement of ssNMR spectra the structural dynamics of nuclei surroundings in materials can be examined, without prerequisites for crystallinity, size, or composition of the sample.[200, 201] This allows e.g. insights into defect chemistry, defect dynamics, as well as ion mobilities and static disorder on the nanoscale of the sampled nuclei.[201–205] The section starts with a general introduction to the principles behind ssNMR spectroscopy and looks at various ways in which the nuclear spin can be influenced and how external electromagnetic fields are used for this purpose, e.g. in magic-angle spinning (MAS) and in Nuclear Quadrupole Resonance (NQR) spectroscopy. The general introduction is followed by paragraphs focusing on the various constituents of lead halide perovskites, starting with ^{207}Pb, followed by A-side cations probed by $^{1/2}$H, ^{13}C and $^{14/15}$ ssNMR spectroscopy and concluding with halide sensitive ssNMR and ssNQR.

Nuclear Magnetic Resonance Spectroscopy Principle: In solid-state NMR spectroscopy, the spin energy transitions of atomic nuclei with a spin are studied. These spin energy transitions are highly chemical-element-specific and allow to sample the chemical nature, geometry, and topology of the surrounding of atomic nuclei as well as the structure dynamics in materials.[200, 201] These spin energy transitions can be derived from the Zeeman effect, which describes the shift of individual spin energy levels in an external magnetic field (covered by the Zeeman interaction H_Z).[206] The Zeeman splitting is described by the Larmor frequency ω_0, which is different for each isotope. This results in an isotope specific frequency range within the ssNMR signals. These frequencies are further influenced by other interactions of the probed nuclei with e.g. other nuclear or electron spins or charge-related electromagnetic fields. These spin energy-related frequency alterations are covered by the dipolar coupling interaction (H_{DD}) and the J-coupling interaction (H_J). Further influences to the spin energies are deviations of the local magnetic fields from the applied fields due to chemical shielding effects related to neighbouring nuclei and their respective spins (H_{CS}). Another influence to the respective spin energy transitions for nuclei with spins $>1/2$ is related to their non-spherical charge distribution, which leads to an electric quadrupole moment. The nuclear electric quadrupole moment couples with surrounding electric field gradients generated by surrounding charges, leading to an alteration of spin energies via the quadrupole interaction (H_Q).[200]

All these possible interactions are governed into the spin interaction H_{spin} shown in Eq. 2.22:

$$H_{spin} = H_Z + H_J + H_{DD} + H_{CS} + H_Q \tag{2.22}$$

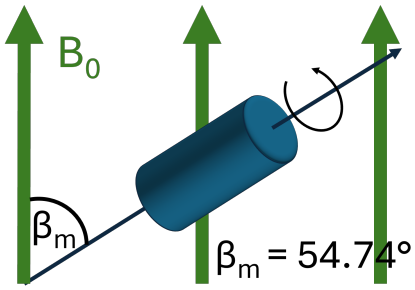

Figure 2.10: Schematic illustration of magic angle spinning (MAS) in solid-state Nuclear Magnetic Resonance (ssNMR) spectroscopy measurements. The ssNMR probe is tilted by $\beta_m = 54.74°$ and spun rapidly to average anisotropic spin interactions, leading to a reduction of line broadening.

As H_{spin} covers a plethora of spin interactions various insights can be derived from ssNMR spectra. For example gives the strength of H_{DD} insights about interatomic distances, H_{DD} about connectivity and H_{CS} and H_Q both about the chemical specific geometry by magnetic and electric interactions. As H_{spin} is sensitive to all these interactions the signals within a NMR spectrum are affected by all of the interactions in Eq. 2.22 through the shift of the resonance frequency, signal broadening and further shape distortion.[200, 201] A detailed in-depth discussion of the expression H_{spin} including the mathematical expressions for the covered interactions can be found in the respective literature.[207, 208]

In contrast to solution NMR, which produces very narrow linewidths due to averaging of anisotropic NMR interactions, the linewidths and spectra are broad in solid-state NMR, as the full effects of orientation-dependent interactions are captured in the spectrum. One possibility to measure high resolution solid-state NMR spectra is the use of magic angle spinning (MAS),[209] in which the NMR probe is tilted by $\beta_m = 54.74°$ ('magic' angle) with respect to the external magnetic field and spun rapidly around the probe axis (see Figure 2.10). The spinning frequency hereby must be above the static spectral linewidth, which can reach tens of kHz. By spinning around the 'magic angle' at these high spin rates anisotropic interactions leading to line broadening are averaged and vanish within the spectra, leading to a reduction of line broadening due to the dipolar interaction H_{DD}.[210]

While ssNMR spectroscopy works well for most lead halide perovskite constituents, heavier halides possessing quadrupole moments (such as ^{35}Cl, ^{79}Br and ^{127}I) are challenging to measure. This is related to their high quadrupole interaction H_Q, which symmetry and interaction strength is governed by the asymmetry η_Q and quadrupole coupling constant C_Q. The quadrupole coupling constant scales with the quadrupole moment of the nuclear spin and the combination of large quadrupole moments for halide spins and large reported values for electric field gradients in lead halide perovskites leads to large reported values C_Q.[211, 212] This poses a problem in conventional ssNMR measurements, as magnetic field strengths that are greater than or comparable to C_Q are required to measure Larmor frequencies ω_0, which are frequently not achievable in commercial devices (e.g. for ^{127}I).[200] Nuclear Quadrupole Resonance (NQR) spectroscopy, a comparable zero-field method, has become established for measuring the halides concerned with excessive C_Q values.[213]

^{207}Pb ssNMR Spectroscopy of Lead Halide Perovskites: One major component studied by ssNMR in lead halide perovskites is ^{207}Pb. As ^{207}Pb shows a large chemical shift range of around 20000 ppm it is highly sensitive to structural changes in the vicinity of the nucleus, including changes up to the third coordination shell.[200] Especially in mixed halide lead halide perovskites such as $MAPbI_xBr_{3-x}$ the wide chemical shift range of ^{207}Pb is used to study halide dynamics and halide structuring, as studies showed that seven distinct lead environments of PbI_xBr_{6-x} (x = 0–6) can be distinguished by ssNMR.[214, 215] The seven distinct lead environments span the chemical shift range linearly spaced between their two monohalide counterparts.[214, 215] Further Karmakar et al.[216] could show that within the quantitative spectra, the relative occurrence of each environment could be determined. This proved that the incorporation of the halide ions is random (i.e. solid solutions are formed), as the integral values follow a binomial distribution. Comparable studies showed, that such solid solutions differ by the applied synthesis route resulting in different degrees of homogeneity and halide miscibility as well as crystallinity, distinguishable from the observed line widths and the distribution of the signal integrals.[214–217] It is even possible to distinguish phases, not seen from classically applied characterization methods, e.g. XRD. So showed Rosales et al.[215] that they could observe two distinct phases of $MAPbIBr_2$ and $MAPbBr_3$ in solution-grown $MAPbI_{1.5}Br_{1.5}$, but only $MAPbIBr_2$ was distinguishable by XRD. This indicates that the $MAPbBr_3$ was either low in crystallinity or localized as a thin layer around $MAPbIBr_2$ grains. Another interesting application is the study of decomposition products by ^{207}Pb ssNMR. For example showed Askar et al.[218] that the water-induced decomposition pathways of $MAPbI_3$ can be tracked. They could distinguish the formation of $MAPbI_3$ mono- and dihydrate complexes in the ^{207}Pb ssNMR spectra and that at RT and 80 % relative humidity $MAPbI_3$ slowly converts to its monohydrate.[218] This allows ^{207}Pb ssNMR to track the formation of degradation products simultaneously with other lead-based processes.

A-side ssNMR Spectroscopy of Lead Halide Perovskites: Solid-state NMR further offers the possibility to access A-side cations such as Methylammonium (MA) or Formamidium (FA) via $^{1/2}$H, ^{13}C or $^{14/15}$N ssNMR and allows the screening of cation environments and their dynamics.[204, 219–221] Studies showed that for MA its motion differentiates between a fast cone-shaped gyration and a flip of the C-N axis. In $MAPbI^3$ these motions occur on a timescale of several hundred fs and 3 ps, respectively.[222] Consequently, because of the comparatively fast dynamics ^{1}H and ^{13}C ssNMR spectra of $MAPbX_3$ exhibit narrow linewidths with similar chemical shifts across different halides X.[220, 221, 223] Furthermore, by analyzing the linewidths in ssNMR the dynamic and static disorder of cations can be distinguished from homogenous and inhomogeneous line broadening. While this is not unique to NMR, e.g. PL line widths are also affected by temporal and spatial disorder,[224, 225] in NMR the structural moieties can be easily connected to present chemical structures.[219, 226, 227] In addition, $^{1/2}$H, ^{13}C or $^{14/15}$N ssNMR provides information on the dynamics and coordination of organic additives used in lead halide perovskites.[228–230]

Halide ssNMR and ssNQR Spectroscopy of Lead Halide Perovskites: As mentioned in the paragraph to the introduction of the NMR principle, possess the lead halide perovskite forming halides high quadrupole moments (e.g. ^{79}Br and ^{127}I). These quadrupole moments complicate the measurement of ssNMR spectra, which is why ssNQR spectroscopy is chosen instead.[200, 231] As with ssNMR, general information about the chemical environment of the halide nuclei can be obtained from ssNQR spectra. For example, structural defects within the lead halide perovskite lattice can be investigated.[200] Such structural defects are seen as line broadening generated by the distribution of chemical surroundings, which form a continuous distribution of overlapping resonance frequencies.[200] Consequently, earlier studies correlated measured line widths in $MAPbI_3$ powders with their respective powder quality.[202, 204] The full-width half-maximum (FWHM) of resonance lines is an established measure for the static disorder in lead halide perovskites.[232, 233]

3 Experimental Section

Within this thesis various aspects of dynamic and kinematic phenomena in metal halide perovskites are investigated. The special focus is hereby to correlate structural properties and (opto)electronic properties. For this end, various (*in situ*) characterization methods are employed. This chapter first introduces the employed techniques, starting with the structural characterization methods (3.1.1), followed by the spectroscopic characterization methods (3.1.2). The sections deal with the instruments used, the basic setups, as well as the respective data analysis.

The investigated and discussed films and powders are produced from various solutions and precursors and on different substrates, depending on the measurement requirements of the applied characterization methods described in Section 3.1. As the materials, processing and final morphology differ between the chapters of the thesis, the following Section is divided accordingly. Starting with the materials and sample processing in Section 3.2 for Chapters 4 to 6.

Within the last Section (3.3) of the present Chapter molecular dynamics simulations and associated calculations of time-resolved SAXS and GISAXS detector images are described, which are examined in Chapter 7.

3.1 Characterization Methods

Chapter 3 first introduces and describes the in-situ characterization methods used within the thesis. A distinction is made between structural characterization methods presented in Section 3.1.1 and spectroscopic characterization methods presented in Section 3.1.2.

3.1.1 Structural Characterization

The aim of the presented thesis is to contribute to the understanding of dynamic processes in metal halide perovskites and broaden the available tools for studying these processes. In the course of this, the sample morphology has to be analyzed on different length scales, which requires the application and combination of complementary measurement methods. The methods used can be divided into real space and reciprocal space methods. As real space techniques optical microscopy (OM, section 3.1.1), scanning electron microscopy (SEM, section 3.1.1) and profilometry (section 3.1.1) are used to image surfaces on various length scales. As a reciprocal space scattering technique x-ray diffraction (XRD, section 3.1.1) is applied, allowing the extraction of characteristic real space distances on an atomic scale from the measured momentum space data. As some of the techniques used were employed in more than one project of the dissertation and on more than one setup, the respective experimental subsections are subdivided chapter-wise.

Optical Microscopy

Chapter 4

Images of the processed films to determine the final morphologies were taken with a Leica DM 2700M using Leica N Plan EPI objectives (20x/0.40 BD and 100x/0.85 BD) in combination with a charged coupled device (CCD) camera (Leica MC170HD). The recorded images are processed with Fiji.[237] Real-space distances are calculated from the images according to the respective objective magnifications (20x, resulting in pixel sizes of (0.7 ± 0.1) µm; 100x, resulting in pixel sizes of (0.2 ± 0.1) µm).

Scanning Electron Microscopy

Chapter 4

The film samples were sputtered with platinum (2 nm using a Cressington HR208 sputter coater and a Cressington mtm20 thickness controller) prior to SEM imaging. The platinum-coated film samples were mounted on a standard sample holder via a conductive adhesion graphite-pad (Plano) and examined with a Zeiss Ultra plus equipped with a field-emission cathode using an In-lens secondary electron detector and an accelerating voltage of 3.0 kV.

Chapter 5

SEM measurements were conducted by placing the parent powders on a standard sample holder with the help of conductive adhesion graphite-pads (Plano). The thusly prepared powders were sputtered with 2 nm of platinum (using a Cressington HR208 sputter coater and a Cressington mtm20 thickness controller). Measurements were conducted on a Zeiss Leo 1530 instrument (FE-SEM with Schottky-field-emission cathode, In-lens detector and SE2 detector) using accelerating voltages between 3.0 kV to 20 kV.

Profilometry

Chapter 4

Height profiles of the final films to determine the final film thickness and roughnesses were taken on a Veeco 150 Dektak with an applied stylus force equivalent to a weight of 1 mg and a line scan length of 500 µm. For each film 3 measurements with a distance of 250 µm between each line scan were taken, to sample the mean thickness and roughness within a region equivalent to the approximated area of the focal spot of PL and absorption measurements.

X-Ray Diffraction

Chapter 5

The powder XRD patterns were recorded on a Bragg-Bretano-type diffractometer (Empyrean, Malvern Panalytical BV, Netherlands) equipped with a PIXcel-1D detector using Cu-K_α radiation ($\lambda = 1.5419$ Å). The halide mixing measurements were taken under inert atmosphere (N_2) in a temperature controlled XRK 900 reactor chamber (Anton Paar, Austria).

Three in-situ halide mixing experiments were performed at temperatures of 60 °C, 75 °C and 90 °C for both $MAPbI_3$:$MAPbBr_3$ mixtures with and without $BMIMBF_4$ and one experiment at 90 °C for a $BMIMPF_6$ containing $MAPbI_3$:$MAPbBr_3$ mixture. The integration time for a single XRD pattern in the angular range of 27.5 degree to 30.5 degree (located around the expected positions of the $(200)_c$ peak positions for the parent phases) was set to 3.5 min for all temperatures and compositions with a 2Θ step size of 0.0016°. The complete experimental time per measurement temperature and mixture was between 2.5 days to 3.5 days each.

For pre-characterization measurements of the 1:1 physical mixed parent powders of $MAPbI_3$ and $MAPbBr_3$ with and without the ionic liquid $BMIMBF_4$ and $BMIMPF_6$ containing samples at RT the same setup was used. The integration time was set to 30 min with a 2Θ step size of 0.007° over a angular range of 10° to 50°.

3.1.2 Spectroscopic Characterization

Within the thesis various spectroscopic techniques are employed. While Photoluminescence and UV/Vis absorption (PL/UVVis, section 3.1.2 are utilized to measure the (opto)electronic properties, Nuclear Magnetic Resonance (NMR, section 3.1.2 gives insight into the molecular properties depending on the measured element. X-Ray Photon Correlation Spectroscopy (XPCS, section 3.1.2) is applied in grazing incidence and grazing incidence transmission geometry to quantify variation in electron densities on the lengthscale of tens to hundreds of nanometers.

Photoluminescence (PL) Spectroscopy and UV/Vis Spectroscopy

Chapter 4

In situ optical spectra during spin coating were recorded with the setup described in Buchhorn et al. [238], custom-built at the Chair of Soft Matter Optoelectronic (Experimental Physics II, University Bayreuth UBT). The setup consists of a custom-built spin-coater with a hole in the middle to allow for transmission white light from a white-light LED placed beneath. A laser diode (405 nm) in combination with focusing optics and a diaphragm are placed above the spin-coater to excite the sample for PL measurements. An LED emitting at 490 nm is placed next to the laser, whose scattered light can be detected (referred to as scatter-LED). White-light and excitation laser are turned on and off alternatingly, so that either transmission or PL is probed. Transmitted light, PL and the light from the scatter-LED are collected with a single optical fiber, coupled to a detection system measuring a full spectrum. PL/scattered light and absorption are then recorded alternating frame by frame, with a frame rate (for pairs of PL/scattered light and absorption) of 7.5 Hz for spin coating at 500 rpm, and with a frame rate of 11.6 Hz for spin coating with faster spin speeds (i.e., 600 – 2000 rpm). For slot-die coating the setup was adapted to be fitted on a slot-die coater system. The optical fiber for signal collection and the laser diode were mounted on the printer head. The white-light LED was placed underneath the substrate, to align the final optical fiber position mounted to the print head with the white-light LED used for transmission measurements. No scatter-LED was implemented as the sufficiently strong room light was used as a scatter source. The optical fiber was connected to the same detection system as used while spin coating.

In the case of slot-die coating the spectra were detected with a frame rate (for pairs of PL/scattered light and absorption) of 7.5 Hz as used for spin coating at 500 rpm.

Chapter 5

Photoluminescence (PL) spectra were measured by Markus Griesbach by placing the 1:1 physical mixtures in a round quartz cuvette (inner diameter: 5 mm) and compressing the mixtures with approximately 500 kPa. The cuvette was placed in a cryostat under nitrogen atmosphere (Oxford Instruments) and heated to either 52 °C, 68 °C, 80 °C or 90 °C. Optical excitation was applied with a pulsed nitrogen laser (MNL 100, LTB) with a wavelength of 337.1 nm, a pulse width of 2.5 n sec and a frequency of 20 Hz. The low excitation frequency was chosen to prevent photo-induced demixing. The emitted photoluminescence was filtered trough a long pass filter (band edge 400 nm) and detected via a monochromator (Shamrock SR-303i-B, Andor Technology) with a silicon CCD camera (Andor iDus DU420A-OE).

Nuclear Magnetic Resonance (NMR) Spectroscopy

Chapter 5

Solid state NMR spectra were measured by Helen Grüninger on a Bruker Avance HD III spectrometer at a magnetic field strength of 14.1 T (600 MHz) using a Bruker 3.2 mm HXY MAS NMR probe.

Lead nitrate ($Pb(NO_3)_2$), with a chemical shift -3494 ppm, was used as reference for ^{207}Pb and the samples were spun at a spinning frequency of 5 kHz for magic angle spinning with dry air. The temperature of the air flow was varied for each experiment, and calibrated using $Pb(NO_3)_2$. A spin echo sequence (8.33 µ sec) was used to suppress ringing, with a recycle delay of 0.5 sec and the measurements were performed at a B_1 field strength of approximately 150 kHz with a transmitter offset of 125.66 kHz. As such, series of 1D ^{207}Pb NMR spectra were recorded in timesteps of 10 min at temperatures of 55 °C, 68 °C, 80 °C and 90 °C.

For ^1H MAS NMR spectra taken at the same temperatures as before the spinning frequency was set to 20 kHz using a single-pulse sequence with a B_1 field strength of approximately 100 kHz and a recycle delay of 95 s (sample with $BMIMBF_4$) and 65 s (sample with $BMIMPF_6$). Adamantene (1.85 ppm) was used as a secondary reference for the ^1H chemical shift at room temperature, while adjustments to the temperature-induced shifts were done with the signal position of the methylammonium of the perovskites (3.3 ppm and 6.3 ppm).

^{19}F MAS NMR spectra were recorded at 5 kHz spinning frequency using a single-pulse sequence (B_1 field strength of approximately 90 kHz) at temperatures ranging from 45 °C to 90 °C with a temperature-optimized recycle delay of 20 s to 30 s (sample with $BMIMBF_4$) and 10 s (sample with $BMIMPF_6$). The ^{19}F chemical shift was referenced using NaF (-221 ppm) as secondary reference at room temperature. The BF_4^- or PF_6^-resonances were used to adjust for temperature-induced shifts.

^{79}Br and ^{127}I ($3/2 \rightarrow 5/2$) NQR spectra were recorded with the probe head placed far away from the magnet. The NQR frequencies were 164.09 MHz ($3/2 \rightarrow 5/2$; equatorial Iodine in tetragonal $MAPbI_3$) and 70.45 MHz (^{79}Br) at room temperature. As the T_1 relaxation was extremely short (around 30 µ sec) a fast recycle delay of

0.1 sec was used with 2048 scans using a Hahn-echo experiment with as short delays (8.33 µ sec) as possible.

Grazing Incidence (Transmission) X-Ray Photon Correlation Spectroscopy

Chapter 6

Simultaneous GT-GI-XPCS experiments were conducted at the 11-ID Coherent Hard X-Ray (CHX) beamline at the National Synchrotron Light Source II (NSLS II) at the Brookhaven National Lab. The photon energy was fixed to 9.65 keV (wavelength $\lambda = 1.285$ Å) with a beam size of 10 µm x 10 µm defined by slits. Intensity patterns were captured using an Eiger X 4M detector with a sample detector distance of 13 m and a pixel size of 75 µm. To induce dynamics in a static $MAPbI_3$ sample 13 s of unattenuated beam were administered to the sample under grazing incidence with incident angles of $\Theta_i = 0.22°$ and 0.30° ($\Theta_i > \Theta_c$, bulk-sensitive) for which 600 detector images with an exposure time of 0.2 s and a frame rate of 5 Hz were recorded. The resulting footprints were 2.6 mm and 1.9 mm respectively, but halved for the requirement for edge-near measurements in GT geometry (moved beam center to the substrate edge). With an unattenuated flux of 5×10^{11} ph/s for the beam the respective photon flux on the sample were 1.9×10^7 ph/s/µm^2 and 2.6×10^7 ph/s/µm^2. The administered 120 s of unattenuated beam is 240 times higher than the measured threshold for beam damage of 0.5 s (measured to be 1.0×10^7 ph/µm^2) at an incident angle of 0.30° and induced degradation within the thin film. The chosen flux was I) necessary to gather sufficient photon statistics within the GT-region of the detector and II) allowed to induce beam damage-driven dynamics in the sample. To circumvent build-up of X-ray dose in measurement spots the sample was translated by a minimum of two times the beam size between measurements for subsequent measurements. Subsequent measurements of $\Theta_i = 0.22°$ and 0.30° were taken on the same $MAPbI_3$ sample. The calculation of autocorrelation functions was performed using the computing infrastructure and Python code provided by the CHX beamline staff (see NSLS II on Github).[239]

3.2 Sample Preparation

The present Section presents the materials and sample processing steps applied within the thesis chapter-wise, following the structure of the thesis.

Chapter 4

For the experiments described in chapter 4 two steps are necessary for sample preparation: 1) preparing precursor solutions and 2) processing thin films on pre-cleaned substrates via spin and slot-die coating.

Materials: Precursor solutions for spin coating and for slot-die coating were prepared by dissolving Methylammonium iodide (MAI, Dyesol) and Lead(II) iodide (PbI_2, 99%, Acros) were dissolved in Dimethylformamide (DMF, >99.5%, Fisher Chemical) with a concentration of 0.7 M. The precursors were used as received.

Thin Film Preparation: The ITO substrates were cleaned in an ultrasonic bath with isopropanol (IPA, analytical grade (VWR)) followed by O_2 plasma treatment prior to use. Spin coated perovskite films were prepared using a custom-built spin coater with spin speeds of 500 rpm to 2000 rpm in a one-step processing approach. 70 µl of precursor solution were spin coated on ITO substrates at RT. Slot-die coated perovskite films were prepared using a nRad slot-die coater system (nTact) on ITO substrates with a coating speed of 40 mm s^{-1}, a gap distance of 60 µm and a solvent dispensing rate of 70 µl s^{-1} at RT. An air knife (Super Air Knife, Exair) was directed parallel to the printed precursor film with air pressure between 0.5 bar to 4.0 bar. Both coating techniques were performed in ambient air with a relative humidity in the range of 50 % to 60 %.

Chapter 5

For the experiments described in chapter 5 two steps are necessary for sample preparation: 1) synthesizing metal halide perovskite powders and 2) mixing the powders to obtain the final samples used in the study.

Synthesis: The $MAPbBr_3$ and $MAPbI_3$ powders used for mixing experiments were synthesized by Philipp Ramming and Markus Griesbach by employing a mechanochemical approach by ball milling in a Fritsch 'Pulverisette 5/4' planetary ball mill [240]. The reactants (Methylammonium iodide, MAI; Methylammonium bromide, MABr; Lead(II) iodide, PbI_2; Lead(II) bromide, $PbBr_2$; 1-butyl-3-methylimidazolium tetrafluoroborate, $BMIMBF_4$ and 1-butyl-3-methylimidazolium hexafluorophosphate, $BMIMPF_6$) were weighed to the desired stoichiometry (see Table 3.1) and transferred into an 80 ml stabilized ZrO_2 milling jar, containing stabilized ZrO_2 milling balls with 10 mm diameter. Then, 8 ml cyclohexane was added as a milling agent. The powders were milled at 400 rpm for 5 min. Then milling was paused for 20 min to cool the milling jar. The procedure was repeated until the desired milling time was reached and differed between 50 min to 90 min (see Table 3.1). Subsequently, the cyclohexane was evaporated by opening the milling jar and leaving it at room temperature in air for 15 min. As a last step the so dried powders were sieved with a 63 µm sieve. PbI_2 (Purity >99.8 %) was purchased from Arcos, while $PbBr_2$

(Purity >98 %), $BMIMBF_4$ (Purity >98 %) and $BMIMPF_6$ (Purity >98.5 %) were purchased from Sigma-Aldrich. The reactants MAI and MABr were synthesized following the approach presented in Leupold et al.

	MAI/MABr (g)	PbI_2/$PbBr_2$ (g)	ionic liquid (μL)	Time (min)
$MAPbI_3$, neat	1.90	5.50	-	90
$MAPbBr_3$, neat	1.80	5.90	-	80
$MAPbI_3$, $BMIMBF_4$	1.90	5.50	11.2	50
$MAPbBr_3$, $BMIMBF_4$	1.80	5.90	15.0	80
$MAPbI_3$, $BMIMPF_6$	1.90	5.50	12.3	50
$MAPbBr_3$, $BMIMPF_6$	1.80	5.90	16.5	80

Table 3.1: Stoichiometric weight-ins with and without ionic liquids for the used reactants for perovskite powder synthesis with their respective milling times.

Physical Mixtures: The 1:1 physical mixtures of $MAPbBr_3$ and $MAPbI_3$ powders used for mixing experiments were prepared by Philipp Ramming and Markus Griesbach in a N_2 glovebox by weighing in 1:1 mixtures in a 1 ml milling jar. The contents within the milling jar were then milled with a *Spex Certiprep 6750-115 Freezer Mill* at a temperature of 77 K for 2 min with a frequency of 2 Hz. The mill was cooled via liquid nitrogen. To avoid halide exchange before *in situ* experiments the as-prepared 1:1 mixtures were stored under N_2 atmosphere at 255 K in the dark.

Chapter 6

For the experiments described in chapter 6 two steps are necessary for sample preparation: 1) preparing precursor solutions and 2) processing thin films on precleaned silicon substrates via slot-die coating.

Materials: Materials for thin films of a metal halide perovskite solar cell were used as received. Methylammonium iodide (MAI) was bought from Greatcell Solar and Lead(II) iodide (PbI_2, 99,99% trace metal basis) was obtained from Tokyo Chemical Industry. Solvents used for precursor dissolution were Tetrahydrofuran (THF), stabilised, purchased from BerndKraft and Methylamine, 33% in absolute Ethanol acquired from Aldrich. Solvents used to clean the silicon substrates (SiegertWafer, 1000± 20 µm, PIB, $\langle 100 \rangle \pm 0.5°$) were deionized (DI) H_2O, H_2O_2 (30%, stabilised, VWR) and H_2SO_4 (95% - 97%, for analysis, Merck).

Thin Film Preparation: Thin films of Methylammonium lead iodide ($MAPbI_3$) were produced on silicon substrates by slot-die coating in a one-step process. The

cleaved silicon substrates were first cleaned 15 min in an acid bath (54 ml of DI water, 84 ml of H_2O_2 and 198 ml of H_2SO_4), heated to 80 °C. After rinsing with DI water and drying with pressurized nitrogen, the silicon substrates were functionalized with O_2 plasma (Plasma Technology GmbH, 0.1 bar, 5 min). For thin film preparation metal halide precursors (MAI and PbI_2) were dissolved in a solution of Methylamine in Ethanol and THF (1:1 volume ratio) to get a final precursor concentration of 0.5 mol. The prepared $MAPbI_3$ precursor solution was used to slot-die coat thin films with a custom-built setup under ambient atmosphere [241] on the prepared silicon substrates. The slot-die parameters were as follows: 200 µm gap distance between slot-die head and substrate, 20 mm s^{-1} coating speed, 30 mm s^{-2} coating acceleration and 50 °C substrate bed temperature. After a resting time of approximate 30 s after the finished slot-die coating process, the thin films were transferred to a heat plate and annealed for 10 min at 140 °C. Finished films were around 800 nm thick (as measured by Dektak 150, Veeco) and cleaved to 2 cm x 1 cm size to produce clean edges for simultaneous GI-GT-XPCS experiments. The cleaved films were stored until use in a nitrogen filled glovebox at RT.

3.3 Simulations

In this section the parameters for the presented MD simulations of Chapter 7 and the following time-resolved SAXS and GISAXS calculations, including the calculation of correlation curves are given.

MD Model: The chosen model consists of freely moving particles with a uniform size, similar to a simple liquid melt system, which interactions are well captures by a Lennard-Jones (LJ) potential. This model system was selected, because of readily available results for comparison and simulation software.[242] The MD simulation is carried out using the LJ potential implemented via LAMMPS[242], which has been shown to provide an accurate description for interatomic interactions.[243–245] The LJ potential V_{LJ} is implemented as follows:

$$V_{LJ} = 4\epsilon[(\frac{\sigma}{r})^{12} - (\frac{\sigma}{r})^{6}] \tag{3.1}$$

with ϵ being the reduced energy units, σ being the reduced distance units and r the reduced interparticle distance. The LJ potential is implemented with a cut-off at 2.5 σ. Pair coefficients between the single particle species in the model was set to 0.5 ϵ at 0.1 σ. As the exact characteristics of the simulated melt is of no interest for the comparison of the extracted dynamics from calculated time resolved SAXS pattern and time resolved GISAXS pattern, the MD simulations are done in the reduced LJ units.[242] The MD simulation box is set to be a cube with length L = 20 σ, containing 32000 particles. The initial particle positions are populated on a fcc lattice (0.0884 σ) with lattice spacing 3.5632 σ. From the initial position the particles relax to a local energy minimum for a reduced LJ temperature of 6 K^* over a time of 4 τ (timesteps $\Delta t = 0.001\tau$) using the NVE ensemble. X,Y,Z particle coordinates for scattering calculations are dumped every 10 timesteps.

Time-resolved SAXS and GISAXS: Simulated time-resolved scattering images for XPCS calculations were calculated from the simulated box with its particles for an energy of 10 keV (λ = 1.2398 Å) and a sample detector distance (SDD) of 4 m. The scattering was simulated on a detector with 512 x 512 pixels and a quadratic pixel size of 100 µm. To convert the unitless coordinates from LAMMPS the coordinates and the box size used in scattering calculations are scaled with a factor of 196. This scaling factor ensures that scattering related to the atomic motion is projected to the simulated detector. The calculations of the scattering images is based on a discrete Fourier transformation (DFT) of the particle positions and its squared absolute. This approach is equivalent to scattering within the Born Approximation (BA). GISAXS images are calculated within the simplified distorted wave Born Approximation (sDWBA) [162, 246]. The necessary Fresnel propagation coefficients are calculated via the standard approach propagated by Rauscher et al. and Lazzari et al. [163, 246]. For the given energy (10 keV) the refractive index was calculated to be n = 5.138e-06 + i*4.183e-07 [147] for $MAPbI_3$, resulting in a critical angle $\Theta_c = 0.18°$. GISAXS images were calculated on the detector q space and on the intrinsic Q space (comparable to the transmission q), as such the standard calculation of q_z introduced in Eq. 2.12 was adjusted to include refraction effects based on Liu et al..[161]

Calculations of Correlation Curves: XPCS One-Time Correlation Functions (1TCF) and Two-Time Correlation Functions are calculated from the simulated SAXS and GISAXS image series with a multi tau correlator. The multi tau correlator is implemented in the Python scikit-beam package developed at NSLS-II. Scikit-beam provides a 1-time multi tau correlator based on Lumma et al. [247] for the calculation of 1TCF, as well as a 2-time multi tau correlator based on Fluearasu et al. [248] for the calculation of 2TCF.

4 Kinetics of Structure Formation in Slot-die and Spin coated $MAPbI_3$ Thin Films

As stated in the Introduction in Chapter 1 the majority of highly efficient PSCs are manufactured on a small laboratory scale, typically measured in millimeters, using spin coating.[23, 24, 58, 249–252] However, when moving to large scale manufacturing, i.e. slot-die coating, the efficiencies of larger-scale PSCs tend to be lower compared to those produced through spin coating,[24, 249, 252] often attributed to variations in the final perovskite film properties, stemming from a complex film formation process.[23, 252, 253] Extensive research has been conducted to investigate the perovskite formation process and its kinetics through the utilization of various in-situ characterization methods.[24, 173, 254–258] These include scattering techniques[42, 259–263] as well as optical spectroscopy.[41, 264–266] For instance, absorption and photoluminescence (PL) measurements have been performed simultaneously during the processing of halide perovskites from a solution.[264, 267] Furthermore, the combination of scattering and optical spectroscopy has provided valuable insights into the intricate perovskite formation process and its kinetics.[268, 269] Through these investigations, various structural dynamics and their connected kinetics have been identified, particularly during the initial stages of solution processing, preceding the actual crystallization of the perovskite.[28] In the instance of coating the halide perovskite methylammonium lead iodide ($MAPbI_3$) from a dimethylformamide (DMF) solution, an intermediate phase was observed, attributed to formation of $(MA)_2(DMF)_2Pb_2I_6$ solvent-complex structures.[29] These solvent-complexes are known to crystallize in needle-like structures, which are also observed in the final film.[24, 29] The appearance of these needle-like structures are attributed to perovskite crystallization originating from within the solvent-complex structures, while retaining their needle-like morphology during the conversion process. As such, the needle-shaped solvent-complexes act as a blueprint for the subsequent perovskite crystallization. Such needle-like solvent-complex morphologies often leads to incomplete film coverage, known to be detrimental to the efficiency of final devices.[24]

Consequently, various strategies have been devised in the past to prevent the formation of needle-like film morphologies during perovskite processing. These strategies involve incorporating additional processing steps, such as solution engineering or heating stages.[133, 270–272] However, the implementation of such supplementary steps can be labor and time-consuming, particularly in industrial-scale techniques like role-to-role applications used for slot-die and blade coating.[273] As a result, it is a highly desired goal in the field to achieve a successful transition of one-step solution processing of halide perovskites from spin to slot-die coating.[274]

In order to realize the transition, it is important to be able to monitor the individual stages of film formation in both processing methods so that conclusions

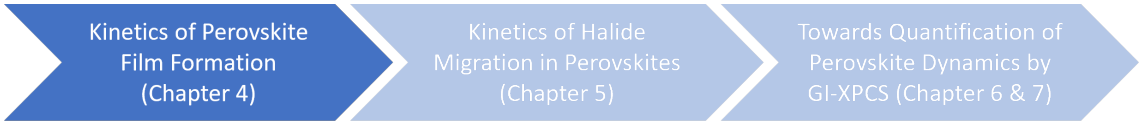

Figure 4.1: Schematic overview of thesis showing the topic of the following chapter: The present chapter describes how to quantify and influence the kinetics of lead halide perovskite thin film formation during one-step processing from a precursor solution. The chapter focuses on a comparison of spin vs slot-die coating, elucidating similarities and differences of the thin film formation of both processing techniques.

can be drawn about similarities and differences. As these similarities and differences define the final film structure and thus the function of final devices. For one-step processing, two phases of structure formation in particular define the final film and its structural properties. The structural properties include the grain sizes of the perovskite crystallites on nanometer lengthscales, but also the surface structure, i.e. the surface roughness on the micrometer lengthscale. 1) The first phase of film formation, which is regarded as decisive for the final film structure, is the formation of crystalline solvent-complexes from the wet precursor solution. The formation of solvent-complexes is crucial because the subsequent perovskite crystallization takes place within the formed crystalline structure of the solvent-complexes and thus defines the final structure of the film. Consequently, by monitoring this first aspect of film formation while varying external influences, such as the drying conditions, the influence of different solvent-complex structures on the subsequent perovskite conversion can be adjusted. 2) Further, the evolution of the subsequent perovskite crystallization from the solvent-complex structure needs to be explored. As such we need to monitor the perovskite crystallization within the solvent-complex structures to understand how the perovskite crystallization kinetics are influenced when the solvent-complex morphologies are changed. Consequently, the first step in the thesis is a comparison of one-step processing of $MAPbI_3$ from DMF by spin and slot-die coating and the monitoring of the evolving stages of their respective film formation and its kinetics for varying drying conditions (Figure 4.1).

The subsequent chapter is based on the publication "Understanding Differences in the Crystallization Kinetics between One-Step Slot-Die Coating and Spin Coating of $MAPbI_3$ Using Multimodal In Situ Optical Spectroscopy", Advanced Optical Materials, 2021, 9, 2101161.[275] The experiments were done within an ongoing collaboration with Konstantin Schötz and Fabian Panzer from the perovskite subgroup located at the Chair of Soft Matter Optoelectronic of Anna Köhler (Experimental Physics II, University Bayreuth UBT), in which Konstantin Schötz and I monitored the film formation during spin-coating and Fabian Panzer during slot-die coating. The analysis of the measurements was done by Konstantin Schötz and myself.

For monitoring the stages of film formation during the one-step processing of $MAPbI_3$ from DMF by spin and slot-die coating an in-situ setup for simultaneous photoluminescence (PL), light scattering and absorption (OD) measurements is applied. By measuring scattered light the formation of solvent-complexes during the initial phase of film formation can be monitored, as the appearance of these photo-inactive structures leads to trackable variances in the reflected intensity of an external light source. The simultaneous PL and OD measurements allow to track the structural and optoelectronic properties of the subsequent formation of

perovskite crystallites within the monitored thin film. The combination of these three optical measurements therefore allows for monitoring the complete film formation from the first emergence of complex-structures in the drying precursor solution to the fully formed perovskite thin film. By varying drying times between the two processing methods an overlap of comparable formation times of the solvent-complexes is achieved, which serves as a starting point for a quantitative comparison between spin and slot-die coating. The *in situ* optical measurements are subsequently complemented by reflected optical microscopy and scanning electron microscopy measurements in order to draw conclusions about the final film morphology from the film formation kinetics.

Details about the experimental procedure are given in section 3.1.2. The section describes sample preparation, the used setups for *in situ* PL, light scattering and absorption measurements, and for *ex situ* reflected optical and scanning electron microscopy measurements. In section 4.1 the film formation of $MAPbI_3$ from spin coating is followed via *in situ* optical measurements and the film formation kinetics are extracted from the measured time-resolved optical properties for various spin speeds to vary the observed drying kinetics. These measurements serve to establish a baseline for the subsequent comparison between spin and slot-die coating. Section 4.2 follows the same approach as the previous section and applies it to slot-die coating of $MAPbI_3$. By varying the drying kinetics through application of an air-knife an overlap of drying times between the two applied processing methods is achieved. Based on these comparable drying times, a quantitative comparison of the two processing methods can be made. In section 4.3 the extracted kinetics are compared on a normalized time scale based on the appearance of the solvent-complexes and perovskite crystallization times, allowing identification of independent parameters to systematically compare the perovskite formation kinetics between spin and slot-die coating. The systematic comparison enables us to identify that the duration of the solvent-complex formation is decisive for the final structure, but also that the perovskite crystallization within the solvent-complex structures takes place differently in both processing methods. The chapter concludes with section 4.4, which summarizes the experimental results and proposes how differences in the drying kinetics of the two processing methods results in differences in the perovskite crystallizations and in the final film morphologies.

4.1 Film Formation of $MAPbI_3$ via Spin Coating

In order to quantify the origin of differences in the film properties of spin coated and slot-die coated $MAPbI_3$ thin films the film formation process of $MAPbI_3$ during one-step spin coating from solution is monitored. To monitor the film formation process the setup described in section 3.1.2 was used. The in-situ setup allows to simultaneously track the PL signal, to calculate the OD density from the transmission signal and to follow the evolution of the scatter LED signal during the film formation process. After preparation of the precursor solution by myself (following the procedure described in section 3.2), Konstantin Schötz and I spin coated the precursor solutions at ambient conditions with rotation speeds ranging from 500 to 2000 rpm. Exemplary data for PL, scattered light and OD during the film formation process is shown in Figure 4.2. The film was processed at 2000 rpm and the figure shows the first 125 s from the start of the spin coating (t = 0) of the optical properties as heat maps in

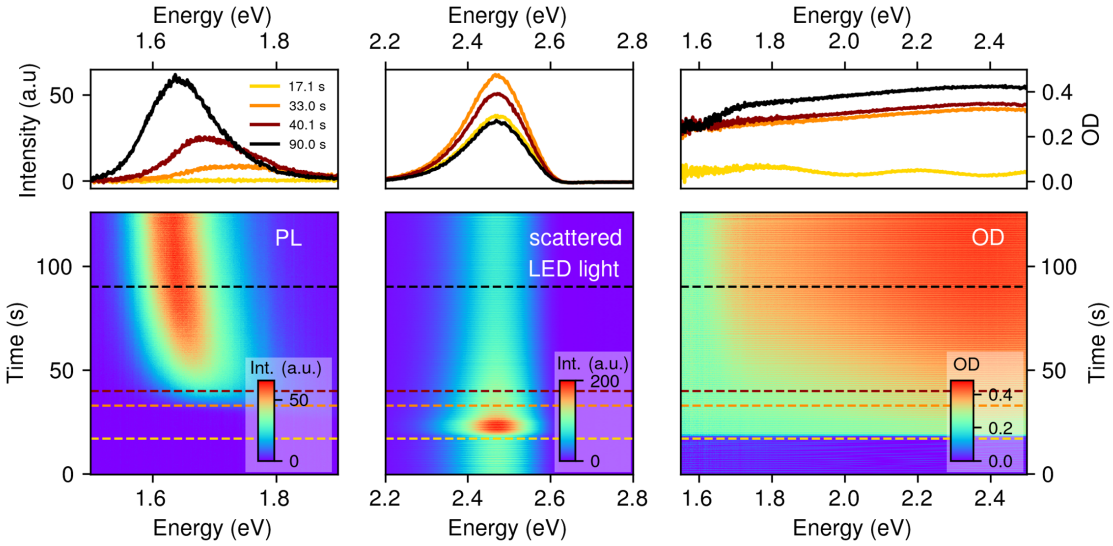

Figure 4.2: Spectra extracted at various times (top) and heat maps (bottom) of photoluminescence (PL, left), light scattering (middle), and optical density (OD, right) measurements during the one-step spin coating of a $MAPbI_3$ film at 2000 rpm. Dashed lines along the heat maps indicate the time at which spectra in the top row were extracted.

the bottom row. The top row shows spectra at selected times after the start of the spin coating process.

Examing the different heat maps in Figure 4.2 from left to right shows that within the first 17 s no PL signal is detected, while a constant signal from the scatter-LED is measured. We attribute this time-invariant scattered light to light scattering from the setup, such as the substrate holder and sample interfaces (solution-air and solution-substrate). Within this time range the OD shows wavelike oscillations as a result of thin film interference.[276, 277] Based on the distance of adjacent intensity maxima in the OD the layer thickness can be calculated from the refractive index:[278, 279]

$$d = \frac{\lambda_1 \lambda_2}{2(\lambda_1 n_2 - \lambda_2 n_1)}. \tag{4.1}$$

In Eq. 4.1 λ_x is the wavelength of the OD peak position x, having the refractive index n_x. Before the evolution of solvent-complexes within the precursor solution the refractive index is mainly governed by the refractive index of the solvent. For the presented case DMF has a refractive index of n = 1.43 at room temperature.[280] By assuming that the refractive index n is constant over the observed spectral range Eq. 4.1 can be converted to the used energy scale in Fig. 4.2:

$$d = \frac{hc}{2n\Delta E}. \tag{4.2}$$

To extract the energetic difference ΔE of adjacent maxima the oscillations in the OD were fitted with a sine function. An exemplary plot of the fitting procedure and the extracted time-resolved layer thickness d is presented in Figure 4.3.

The calculations show that the first detectable wet film thickness is around 5 µm. Within the first 20 s of spin coating the film thickness drops to around 1 µm, after

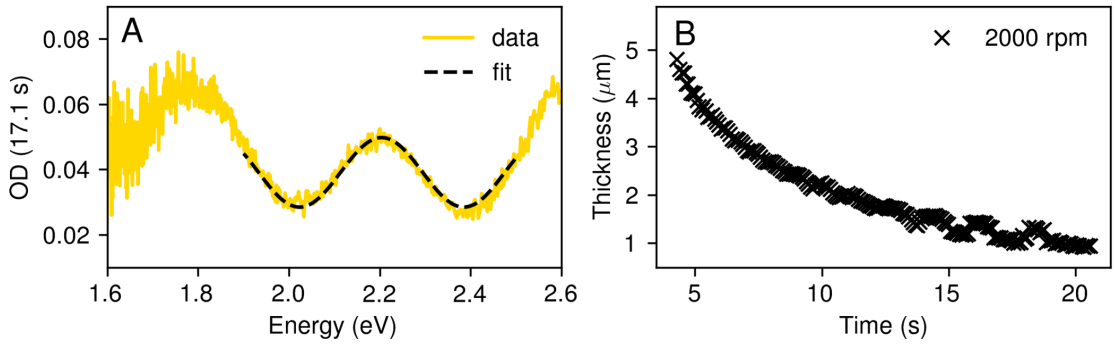

Figure 4.3: A: Zoom-in to the sinusoidal modulation within the OD at t = 17.1 s presented in Figure 4.2 for spin coating at 2000 rpm. The modulation is fitted with a sinusoidal function (black) to extract the energetical distance ΔE of adjacent extrema. B: Thickness d of the solution layer as a function of time extracted from the energetical distance ΔE of adjacent maxima in the white light interference modulations for spin coating at 2000 rpm.

which the oscillations vanish and no thicknesses can be extracted anymore. Up to around 30 s still no PL signal is present, while the scattered light intensity increases twofold. Simultaneously, an increase of the OD from around 0.0 to 0.2 is detected, while the OD spectrum flattens with regard to the earlier observed thin film interference oscillations. The increase in scattered light and OD indicates the appearance of structures, scattering light from the Scatter-LED and white light LED. Along with the missing onset of a $MAPbI_3$ related absorption edge and PL signatures, we suggest that the formation of the scattering centers is related to evolving solvent-complex structures. These solvent-complex structures are known to appear during one-step processing of $MAPbI_3$ from DMF, having the form $(MA)_2(DMF)_2Pb_2I_6$.[24, 29, 276, 278] The onset time for complex-formation is called $t_{0,complex}$. The near constant lift of the OD spectrum after $t_{0,complex}$ related to the light scattering from solvent-complexes, indicates that the evolving structures already reached sizes larger than 500 nm (> wavelength of the Scatter-LED).[281] At around 33 s a broad, asymmetric PL peak appears, located at around 1.7 eV, with the low-energy flank showing a steeper slope. The PL peak, attributed to the nuclei of $MAPbI_3$,[276] undergoes a redshift and narrows in width. Coinciding with the rise of the $MAPbI_3$ PL intensity, the detected intensity from the Scatter-LED decreases by approximately 30 % from its maximum value within a span of 5 s. The decrease in scattered light intensity indicates a reduction in the number of scattering structures within the evolving film. Between the appearance of the PL signal (33 s) and 40 s, the OD remains essentially unchanged except for a slight increase in OD above 2.0 eV. Beyond 40 seconds (t > 40 s), the PL intensity further increases, accompanied by a reduction in peak width. The downward shift in the PL peak position continues, ultimately reaching approximately 1.62 eV by the end of the spin coating process. During this time interval from 40 s to 125 s, the scattered light intensity continuously decreases, albeit at a slower rate in comparison to the decline observed between 30 s to 35 s. The simultaneous occurrence of an increase in PL intensity and a reduction in scattered light intensity indicates a phase transition of solvent-complex structures into $MAPbI_3$. Evidence for the formation of $MAPbI_3$ is further supported by the onset of absorption by $MAPbI_3$ in the OD spectra, visible as an increase in intensity above 1.6 eV for t > 40 s.[80, 281] In contrast

to the expected continuous increase of the absorption coefficient above 1.6 eV,[282] the OD appears still flat, indicating that the resulting perovskite film is not covering the whole substrate.[281] The partially covered substrate allows a fraction of the white light to pass the sample without being absorbed. Consequently, the transmitted minimum intensity establishes an upper threshold for the detectable OD. As a result when approaching the upper threshold for the detectable OD, the absorption spectrum is distorted, displayed as gradual flattening.[281]

As described above the evolution of the optical spectra during spin coating indicate the presence of nucleation and growth processes, both for the formation of the solvent-complex and perovskite phase. To quantify the crystallisation kinetics of the solvent-complex and perovskite phases the time evolution of the introduced optical parameters is extracted and analyzed in detail. For the further analysis the OD and the scattered light time traces are smoothed by application of a Savitzky-Golay filter. The smoothing minimizes the influence of an aliasing effect stemming from the frequency mismatch between spin coater rotation and data acquisition,[275] hence significantly reducing the noise compared to the as-measured time traces.

To obtain information on the growth of perovskite crystallites and the phase conversion from dissolved precursors, to solvent-complexes, to perovskite phase, we extract the time traces of the following optical parameters from the spectra shown in Figure 4.2: 1) The PL peak position , 2) the integrated scattered light intensity, 3) the OD at 1.8 eV and 4) the difference in OD at 1.8 eV and 1.575 eV, which are shown in Figure 4.4A-D. To extract the time evolution of the PL peak position (Figure 4.4A, orange line), we fit an asymmetric hyperbolic secant to the detected perovskite PL spectra. This approach allows to simultaneously extract the PL peak positions and the spectral positions where the PL has dropped to 1/e of the peak intensity. As such, we marked the resulting peak widths as shaded areas, allowing us to follow the evolving asymmetry and peak width reduction. To extract the time traces of the light scattering we integrated the intensity of the scattered light between 2.2 eV and 2.75 eV. The integrated intensity is further on referred to as $I_{Scatter}$, shown in Figure 4.4B. Moreover, the time traces of the OD at 1.8 eV ($OD_{1.8eV}$) are extracted (Figure 4.4C). At a photon energy above the bandgap energy of $MAPbI_3$ of about 1.6 eV this time evolution is sensitive to the emergence of $MAPbI_3$, but also contains contributions due to light scattering effects related to the formation of solvent-complexes, acting as a precursor phase to the emerging $MAPbI_3$. As such, we further extracted the time evolution of the difference in OD at 1.8 eV and 1.575 eV ($\Delta OD = OD_{1.8eV} - OD_{1.575eV}$), which is shown in 4.4D. In here, ΔOD is a measure for the pure perovskite-associated absorption. This assumes that an increase in $OD_{1.575eV}$, which is energetically located below the band gap of $MAPBI_3$, is solely related to light scattering. Due to the weak energy dependence of the scattering in the OD this is a valid approximation to the absorption of the perovskite. Further, we minimized the influence of the scattering energy dependence by choosing energies close to each other, located below and above the $MAPbI_3$ bandgap.

To understand the various crystallization stages and their transition into each other during the spin coating process, we will further analyze the temporal evolution of the optical parameters shown in Figure 4.4A-D. One characteristic time identified in Figure 4.2 is the formation of solvent-complexes at $t_{0,complex}$, which is reflected by the initial increase of $I_{Scatter}$ and of $OD_{1.8eV}$. Initially both signals increase, followed by a saturation time interval with an ensuing rapid decrease in the intensity of $I_{Scatter}$.

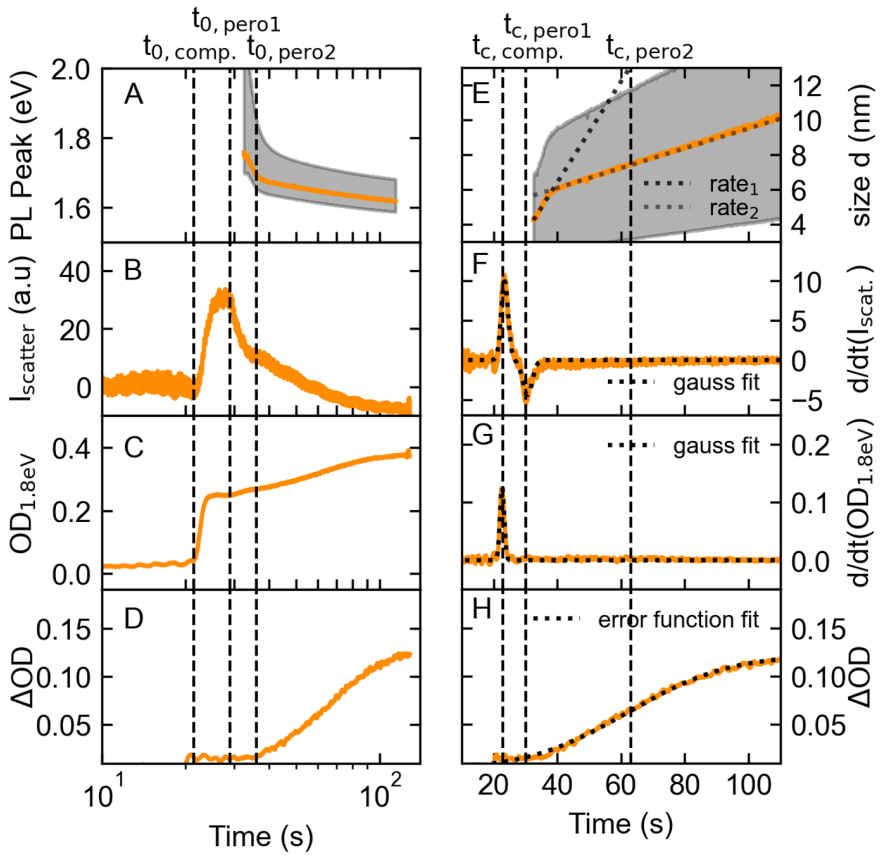

Figure 4.4: A-D: Time evolution of different optical parameters for spin coating at a spin speed of 2000 rpm. A: PL peak position, the gray shaded area indicates the spectral range where the PL intensity is above 1/e of the peak intensity. B: Integrated intensity $I_{Scatter}$ of the scattered light. C: OD at 1.8 eV. D: ΔOD, difference in the OD at 1.8 eV and at 1.575 eV. Vertical dashed lines indicate the onsets t_0 of the different crystallization processes. E-H: Analyses of the optical parameters shown in A-D. E: Average crystallite size calculated from the PL peak position using Eq. 4.3. The shaded area indicates possible upper and lower limit sizes depending on the value of parameter b in Eq. 4.3. Dotted lines are linear fits used to extract growth rates of perovskite crystallites. F: Time derivative of $I_{Scatter}$. G: Time derivative of $OD_{1.8eV}$. The dotted lines in F and G show Gaussian fits used to extract critical times of occurring phases. H: ΔOD fitted with an error function (dotted line). Dashed vertical lines indicate the critical times t_c of the different crystallization processes extracted by the in section 4.1 introduced fits.

The time at which $I_{Scatter}$ starts to rapidly decrease we will from now on refer as $t_{0,pero1}$. The reduction in $I_{Scatter}$ can be attributed to two possible factors: a decrease in the number of scattering structures or an increased absorption at the wavelength of the scatter LED. Taking into account the simultaneous increase in $OD_{1.8eV}$ we can exclude the decrease in the number of scattering structures. Rather, the increase seen in OD for t = 40.1 s at higher photon energies indicates that an additional contribution to the OD spectra after $t_{0,pero1}$ occurs. This contribution could stem from Rayleigh scattering at structures significantly smaller than the wavelength range of the white light, which would be the case for forming perovskite nuclei. These initial nuclei are expected to exhibit a quantum confinement effect, shifting the corresponding bandgap to higher energies.[283] As such, we do not capture absorption from perovskite nuclei in the chosen ΔOD, but from the rapid decrease in $I_{Scatter}$ and the ongoing increase in $OD_{1.8eV}$ we can conclude that at $t_{0,pero1}$ the first nano-sized perovskite crystals form. The suggested initial formation is further supported by the appearance of the first perovskite PL, which is detected shortly after. This PL peak is initially located at higher energies and exhibits a shallower high-energy edge, compared to the expected bulk PL spectra of $MAPbI_3$.[275] The red-shifted PL peak position, combined with a broadened PL confirms that the PL exhibits a quantum confinement effect due to nano-sized perovskite nuclei. According to the detected PL peak position the crystallite size is below the quantum confinement limit for $MAPbI_3$, which was found to be around 20 nm to 30 nm.[283–287] Following the time traces of the PL peak position, $I_{Scatter}$ and ΔOD further with time, a decrease in the PL peak position shift rate, a decrease in the $I_{Scatter}$ decrease rate and an increase in ΔOD is seen. We associate this with a second and on-going perovskite formation process. Thus, the film formation during spin coating proceeds in the order of: 1) formation of solvent-complexes, 2) formation of perovskite nanograins and 3) second perovskite formation process. We refer to the 3 phases as 'solvent-complex phase', 'perovskite phase 1' and 'perovskite phase 2', respectively.

In a next step we will analyze the optical parameters shown in Figure 4.4A-D in more detail. Based on the nanoconfinement effects associated with the decrease in the PL peak position in 4.4A an average crystallite size d can be extracted. Literature suggests that this average crystallite size d depends on the PL peak position E_{PL} by:

$$E_{PL} = E_g + \frac{b}{d^2}. \tag{4.3}$$

E_g is the PL peak position for bulk $MAPbI_3$ and b an empirically determined constant.[288] Based on Equation 4.3 and the PL peak position in Figure 4.4A the evolution of the average $MAPbI_3$ crystal size is calculated as a function of time. In literature the constant b is reported to be in the range of 1 eV nm^{-2} to 5 eV nm^{-2} $MAPbI_3$. Based on this range an average value of 3 eV nm^{-2} is used with a bulk PL position value E_g = 1.59 eV.[275] The results are shown in Figure 4.4E. The indicated upper and lower limits shown as a gray shaded area are based on the suggested values for b and are calculated with b = 1 eV nm^{-2} and b = 5 eV nm^{-2}, respectively. In the time range from 32 s to 38 s the average perovskite crystal size d (orange line) increases fast from 4 nm to 6 nm. After this initial fast increase the average crystal size increases more slowly and reaches 10 nm after 110 s. To extract the average growth rates $rate_1$ and $rate_2$ linear fits are applied in the time range of the fast (black dotted line) and slow increase (gray dotted line), resulting in $rate_1$ =

$(0.319 \pm 0.006)\,\mathrm{nm\,s^{-1}}$ and $\mathrm{rate_2} = (0.059 \pm 0.001)\,\mathrm{nm\,s^{-1}}$.

In order to accurately interpret the average sizes of crystallites and consequently the extracted rates it is necessary to take into account that the most significant contribution on the overall confinement effect originates from the shortest length present within a crystal.[287] This leads to detectable quantum confinement effects, even if only one direction of the crystal is below the confinement limit. As such, not all dimensions of crystal growth during 'perovskite phase 2' need to be impeded, but at least the growth direction of the smallest length scale.

Based on the optical parameters shown in Figure 4.4B-D we identified the onset times of the solvent-complex phase, perovskite phase 1 and perovskite phase 2. To provide a more comprehensive analysis of the kinetics involved in the various crystallization stages, we examine the temporal evolution of the optical parameters.

To examine the temporal evolution an approach reported by Chauhan et al.[276] is applied. Chauhan et al.[276] analyzed the kinetics associated with recrystallization processes of $MAPbI_3$ during solution-based two-step processing. To identify the emergence of solid $MAPbI_3$ from a liquid precursor phase Chauhan et al.[276] calculated the derivative of the OD at 1.66 eV. By fitting a Gaussian function to the resulting derivative the transition time t_T could be identified. t_T is a measure for the point in time at which the greatest change in OD can be observed due to the formation of $MAPbI_3$, while the FWHM of the Gaussian function was interpreted as the duration of the recrystallization process.

In this regard, we generalized the approach by computing the time derivatives of $\mathrm{I_{Scatter}}$ and $\mathrm{OD_{1.8eV}}$ using the data from Figure 4.4B,C, respectively. The resulting derivatives are measures for the emergence of solvent-complexes and perovskite phase, respectively. Consequently, the resulting peaks and dips in the derivative plots align with the times at which the distinct crystallization stages occur. Following the approach by Chauhan et al. [276] we fit the peaks and dips within the derivatives by Gaussian functions. From the peak position in time of the Gaussian functions the critical phase formation times t_c are extracted. While the extracted widths $w = 2\sigma$ are a measure for the duration of the respective crystallization processes.

The resulting time evolutions of $\mathrm{dI_{Scatter}/dt}$ and $\mathrm{dOD_{1.8eV}/dt}$ shown Figures 4.4F,G show clear peak signatures, associated with the solvent-complex phase. The extracted values are: $\mathrm{t_{c,comp.}} = (23.5 \pm 0.1)$ s with $\mathrm{w_{c,comp.}} = (3.1 \pm 0.1)$ s. Furthermore, a dip to negative values is seen in $\mathrm{dI_{Scatter}/dt}$, which stems from a reduction in the number of scattering solvent-complexes. Shortly afterwards, the first $MAPbI_3$ crystals with sizes on the scale of individual nanometres are detected. Since these grow from even smaller nucleation centers, we associate the dip in $\mathrm{dI_{Scatter}/dt}$ with the appearance of perovskite phase 1. The extracted values are: $\mathrm{t_{c,pero1}} = (30.7 \pm 0.1)$ s and $\mathrm{w_{c,pero1}} = (4.4 \pm 0.1)$ s. In contrast, no distinct feature is present to identify $\mathrm{t_{c,pero1}}$ from $\mathrm{dOD_{1.8eV}/dt}$, as the noise level obscures the related feature. Furthermore, in both $\mathrm{dI_{Scatter}/dt}$ and $\mathrm{dOD_{1.8eV}/dt}$, the noise obscures any signature attributed to the perovskite phase 2. To still be able to extract the critical time and duration of the perovskite phase 2 the time evolution of ΔOD is directly examined, by fitting the ΔOD with an error function. As the error function is the integral of the Gaussian function, it is ensured that a comparable measure to the widths w extracted from the Gaussian approximation can be calculated. The fit shown in Figure 4.4H allows to quantify the second perovskite formation process and the following time and width are extracted: $\mathrm{t_{c,pero2}} = (62.7 \pm 0.7)$ s and $\mathrm{w_{c,pero2}} = (52.2 \pm 1.1)$ s.

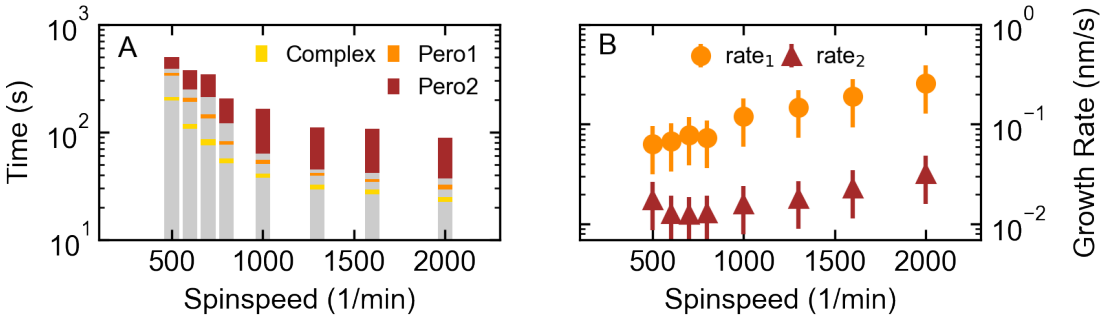

Figure 4.5: A: Color bar representation of the critical times t_c and widths of the crystallization phases present during spincoating. B: Fast and slow perovskite growth rates as a function of spin speed. The rates were extracted from the evolution of average crystal size with time during as exemplified in Figure 4.4E.

Overall, we are not only able to extract the onset times t_0, but also to quantify the critical times t_c and the corresponding time widths w for the earlier identified phases of solvent-complex formation, formation of perovskite nanograins and the second perovskite formation process present while spin coating.

The same measurements were repeated to track the evolving PL intensity, the intensity of the scattered LED light and the evolving optical density for spin speeds between 500 and 1600 rpm. The heat maps corresponding to the presentation of Figure 4.2 are shown in the Appendix (Figures 8.3 and 8.4), with the approximated wet layer thicknesses from OD oscillations in Figure 8.7. Figure 8.6 in the Appendix displays a selection of the optical parameters presented in Figure 4.4A-D for spin speeds between 500 to 2000 rpm. The Figure shows that the optical parameters proceed in the same qualitative manner with spin coating time, but the overall times for the appearance of solvent-complexes and perovskite phase is retarded with decreasing spin speeds. The presented analysis approach for a spinspeed of 2000 rpm was further applied to the other spin speeds of 500 to 1600 rpm and the extracted values are shown in Figure 4.5 as a function of the spin speed.

The resulting critical times and widths for the three identified phases of film formation are shown in Figure 4.5A in the form of a bar plot. The occurring crystallization processes are color-coded. In the chosen bar plot, the temporal position and width of the colored areas correspond to the extracted t_c and their associated width w respectively, i.e. each colored area covers the time range $t_c \pm w$. From the bar representation it is visible that t_c and corresponding widths for all crystallization stages decrease with increasing spin speed due to the accelerated solvent evaporation, i.e., all crystallization stages occur earlier and faster with increasing rpm. Figure 4.5B shows the extracted perovskite growth rates as a function of spin speed. The growth rates are in average about one order of magnitude higher at earlier times ('$rate_1$') compared to the extracted rates ('$rate_2$') at later times, while both rates increase with increasing rpm.

Thus far, an analytical approach to identify and quantify the various occurring crystallization phases during the spin coating process is established. In the next section, this analysis approach is applied to the slot-die coating process to examine the similarities and differences in the occurring crystallization stages.

4.2 Film Formation of $MAPbI_3$ via Slot-Die Coating

In order to achieve comparable data and as such identify the occurring similarities and differences in crystallization kinetics Fabian Panzer, in a co-operation with the Holst Centre (Eindhoven, Netherlands), processed $MAPbI_3$ thin films by slot-die coating using the same precursor solutions and ambient conditions as for spin coating. Further, he applied the same in-situ optical spectroscopy setup, but had to replace the scatter LED due to technical obstacles. Instead the ambient room light is used during the slot-die coating process and its scattered intensity is measured to monitor the scattering related to solvent-complexes. However, in contrast to the scatter LED, the room light is also present during the OD measurement. Consequently, when the initial scattering centers form, the applied background correction recorded before the coating process is invalid. This can result in the appearance of room-light related features appearing in the OD. However, these can be distinguished from the optical signatures of solvent-complexes and $MAPbI_3$ due to the distinct spectral positions of room light sources.

To enhance the control on the drying process during slot-die coating an air knife was mounted above the substrate carrier to generate an air-flow parallel to the substrate. The air flow was adjusted by changing the air pressure through the air knife from 0.5 bar to 4 bar, as such increasing the solvent evaporation with increasing air pressure.

Figure 4.6 shows the initial analysis of the evolution of optical properties prepared by Konstantin Schötz and myself. The presented optical properties were measured during slot-die coating using an air pressure of 4 bar (see Appendix Figure 8.2 for other 2D maps ranging from 0.5 bar to 2 bar). Analogous to Figure 4.2 the Figure shows the PL (left), the scattered room light (middle), and the OD (right) as a 2D heat map (bottom panel), together with individual spectra at selected processing times (top panel). The time axis was chosen so that t = 0 coincides with the moment the slot-die head reaches its final position after dispensing the precursor solution on the substrate.

Figure 4.6 shows that within the first 70 s of processing, no optical signatures of both perovskite and complex structures are detectable. Further, the observed periodic modulations in the OD spectra for spin coating are absent. The lack of modulation in the OD spectra indicates that the height of the solvent layer, which leads to the observed interference effect, is larger than the coherence length of the detected light. Taking into consideration, that the first detectable spectral modulations during spin coating were related to approximate film heights on the scale of 10 µm (see appendix Figure 8.7) and that the same white light LED was used in both experiments, the absent modulations in the OD suggest that the solvent level at the moment of the initial complex phase formation was above 10 µm. From 70 s to 90 s optical signatures of growing solvent-complex structures appear, indicated by a significant increase in scattered light intensity. Simultaneously, a shift in the OD from 0.0 to 0.3 appears, almost independent from the photon energy. As expected earlier, the increased scattered room light intensity leads to distinct spectral features in the OD spectra, here located around 2.0 eV, before any PL or OD signatures related to the formation of $MAPbI_3$ are yet detectable.

After approximately 90 s a PL signature appears at 1.7 eV, shifting to lower energies with longer times. The PL peak reaches its final position at 1.59 eV after

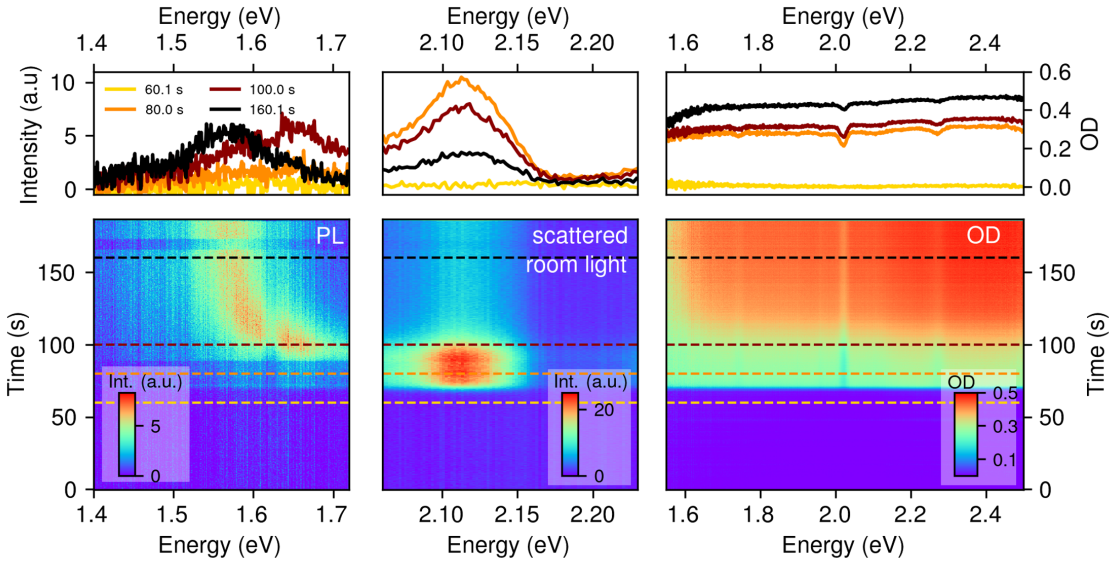

Figure 4.6: Spectra extracted at various times (top) and heat maps (bottom) of photoluminescence (PL, left), light scattering (middle), and optical density (OD, right) measurement during the one-step slot-die coating of a $MAPbI_3$ film at an air-knife pressure of 4 bar. Dashed lines along the heat maps indicate the time at which spectra in the top row were extracted. The drop seen for PL around 160 s to 170 s is related to a power fluctuations in the excitation laser.

160 s, reaching the expected PL peak position for bulk $MAPbI_3$.[275] Following the PL intensity in Figure 4.6 the intensity appears to be lower compared to the spin coating data presented in Figure 4.2. This diminished intensity is associated with a reduced sensitivity for light detection of the used measurement setup (optimized and developed for a spin coater geometry) when implemented into the available slot-die coating setup. Concomitantly with the appearance of the PL signature, the scattered light intensity decreases. After 120 s a constant scattered light intensity is reached, which indicates the transition from complex to perovskite phase as also seen in the spin coating case. Simultaneously with the PL peak appearance and scattered light intensity decrease a first increase in the OD at around 100 s is seen, while the characteristic absorption edge of $MAPbI_3$ at 1.65 eV emerges. Up to 160 s the OD increases further and the absorption edge becomes more pronounced. As for the spin coating case before, the OD shape remains flat above the absorption edge, indicating that also for slot-die coating the substrate is incompletely covered.[278]

As for Figure 4.4 the time evolution of different optical parameters was extracted from Figure 4.6. The analogous results of PL peak position, $I_{Scatter}$, $OD_{1.8eV}$ and ΔOD for slot-die coating at an air-knife pressure of 4.0 bar are presented in Figure 4.7.

The results from Figure 4.7A show that the PL peak position shifts from 1.7 eV to 1.59 eV and reaches the expected bulk $MAPbI_3$ PL peak position.[275] As before, a PL signal shifted to higher photon energies than typically observed for the corresponding bulk value is indicative for quantum confined perovskite nuclei. These crystallites grow continuously in size, indicated by the shift of the PL peak position to lower energies. From the final PL peak position at the energy of the bulk material we conclude that the final perovskite crystallites length scales in all directions must

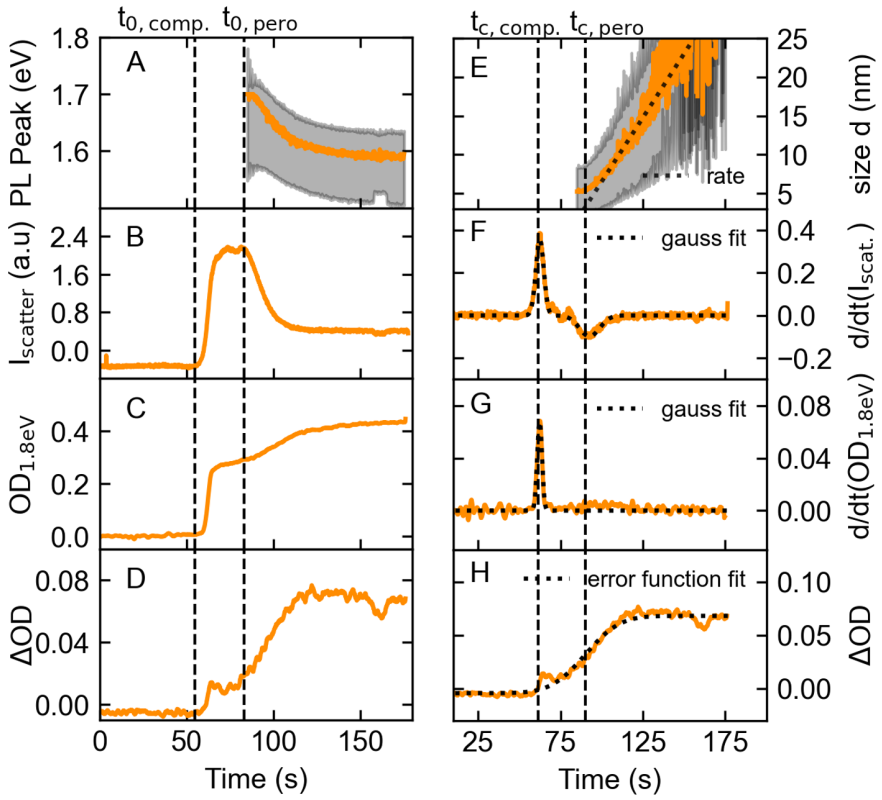

Figure 4.7: A-D: Time evolution of different optical parameters for slot-die coating at an air-knife pressure of 4 bar. A: PL peak position, the gray shaded area indicates the spectral range where the PL intensity is above 1/e of the peak intensity. B: Integrated intensity $I_{Scatter}$ of the scattered light. C: OD at 1.8 eV. D: ΔOD, difference in the OD at 1.8 eV and at 1.575 eV. Vertical dashed lines indicate the onsets t_0 of the different crystallization stages. E-H: Analyses of the optical parameters shown in A-D. E: Average crystallite size calculated from the PL peak position using Eq. 4.3. The shaded area indicates possible upper and lower limit sizes depending on the value of parameter b in Eq. 4.3. Dotted line indicates a linear fit used to extract the growth rate of perovskite crystallites. F: Time derivative of $I_{Scatter}$. G: Time derivative of $OD_{1.8eV}$. The dotted lines in F and G show Gaussian fits used to extract critical times of occurring phase formations. H: ΔOD fitted with an error function (dotted line). Dashed vertical lines indicate the critical times t_c of the different crystallization stages extracted by the earlier introduced fits.

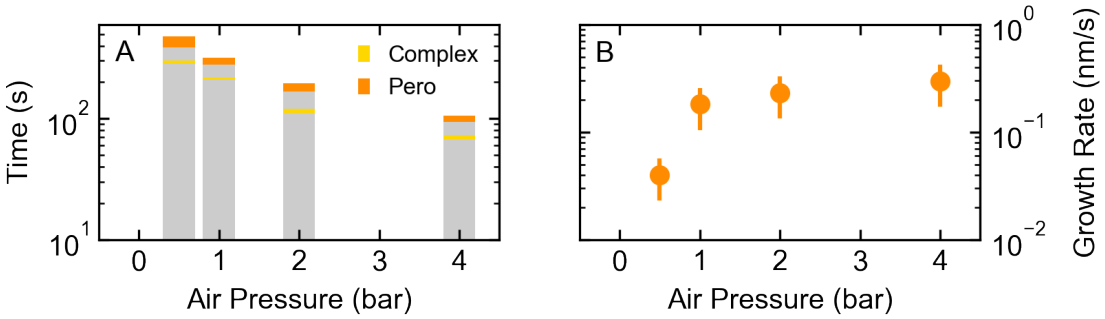

Figure 4.8: A: Color bar representation of the critical times t_c and widths of the crystallization phases present during slot-die coating. B: Perovskite growth rates as a function of air-knife pressure. The rates were extracted from the evolution of average crystal size with time during as exemplified in Figure 4.7E.

be above around 20 nm to 30 nm as seen in Figure 4.7E. This confinement limit of around 20 nm to 30 nm is an experimentally derived value above which no quantum size effects on the PL peak position are observed.[286, 289] Further, combining the information from $I_{Scatter}$ in Figure 4.7B, showing an increase, followed by a plateau and a single decrease to a constant background at the time at which the first perovskite PL peak is detected, with the two-step increase seen in the time evolution of $OD_{1.8eV}$ in Figure 4.7C and the related behaviour in ΔOD in Figure 4.7D, we can attribute the first OD increase to the solvent-complex phase formation and the second OD increase to the appearance of perovskite phase. Contrary to spin-coating this implies that only a single perovskite formation process takes place when slot-die coating.

To follow the approach established in section 4.1 to quantify the phase formation kinetics Konstantin Schötz and I extract the critical times t_c and their corresponding widths w as presented in Figure 4.7F-H. The approach exemplified in Figure 4.7 was further applied to the other measured air-knife pressures of 0.5 bar, 1 bar and 2 bar. The resulting critical formation times and their widths are shown in Figure 4.8A with air-knife pressure for the complex-phase formation (orange) and perovskite phase (blue). As earlier in Figure 4.5 the results are presented on a logarithmic time scale.

As expected, as solvent evaporation accelerates with increasing air knife pressures, complex and perovskite formation occur at earlier times and their time widths are reduced. Interestingly, the width of the perovskite phase formation compared to the width of the complex-phase formation is not increasing with increasing evaporation rate/air-knife pressure but remains unchanged. Similar behaviour of a constant relative width of perovskite phase formation was earlier observed for the first perovskite phase during spin coating, but is in contrast to the increasing relative widths of the second perovskite crystallization seen in spin coating in Figure 4.8A.

To conclude the approach to quantify the phase formation kinetics established in section 4.1 we extract growth rates for perovskite crystallites from the calculated time evolution of average perovskite crystallite sizes (exemplified for 4 bar in Figure 4.7E). Figure 4.8B shows the extracted growth rates as a function of air-knife pressure. We find the growth rate to increase with air knife pressure, with growth rates in a similar range as those extracted during the first identified perovskite crystallization phase for spin coating ($rate_1$ in Figure 4.5B).

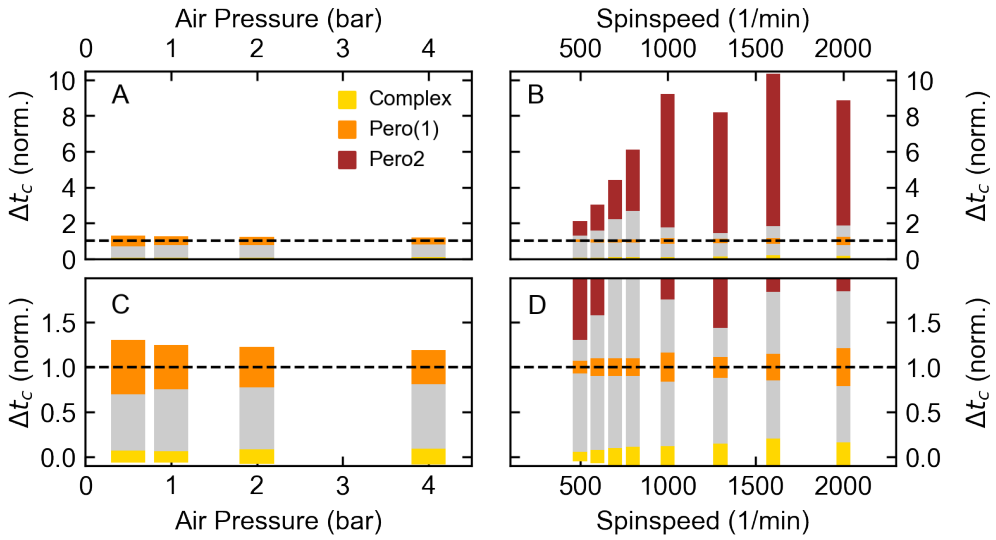

Figure 4.9: Bar chart of critical phase formation times t_cc and widths w extracted from slot-die coating (A,C) and spin coating (B,D), normalized to $\Delta t_c = t_{c,pero}–t_{c,complex}$, so that $t_{c,inter} = 0$ and $t_{c,pero} = 1$. C,D: zoom-in versions of A,B. Vertical dashed line located at $t_{c,pero} = 1$.

To conclude, we applied the analysis approach to quantify the crystallization stages during slot-die coating established in section 4.1. Based on the findings from spin coating qualitative similarities and differences in the two processing methods were identified and are used in the following section to achieve a systematic and quantitative comparison of crystallization processes in spin and slot-die coating.

4.3 Comparison of Film Formation in Spin and Slot-die Coating

To compare the various crystallization stages in a quantitative manner, we aim to find a suitable normalization, in which systematic similarities and differences are accessible. Based on this necessity the influence of the crystallization mechanisms is considered. If the crystallization mechanisms remain unchanged, an increase in the evaporation rate through increasing rotation speeds or air-flows would simply lead to shorter crystallization durations and reduced time differences between them. Consequently, it is expected that by applying an appropriate normalization to the data, the relative crystallisation durations should be independent of the evaporation rate. Thus, the extracted durations of the different crystallization stages from Figure 4.8A and Figure 4.5A are considered relative to each other. As during slot-die coating the film formation proceeds in only two stages, we first consider the normalization of this process, by normalizing the width and times from Figure 4.8A to the time difference $\Delta t_c = t_{c,pero} - t_{c,complex}$. For this the complex formation time $t_{c,complex}$ is subtracted from all formation times, so that $t_{c,complex}$ is the baseline set at $t_{c,complex} = 0$. We further divide all extracted times and widths by the absolute value of Δt_c, so that for slot-die coating $t_{c,pero}$ is normalized to 1 (see Figure 4.9A).

A zoom-in of Figure 4.9A reveals that the widths of the complex formation and perovskite formation are nearly independent of the applied air-knife pressure (Figure 4.9C). This finding provides support for the hypothesis that an increase of the air-knife pressure leads to an accelerated film formation, however, the mechanisms of the crystallization processes do not change in the case of slot-die coating.

Analogous to the normalization presented in Figure 4.9A, the widths and times for the various crystallization stages in spin coating are normalized, which is presented in Figure 4.9B. In the chosen representation Δt_c is calculated with the crystallization time of the first perovskite formation $t_{c,pero1}$, as the growth rates during this phase formation were most comparable to the ones derived during slot-die coating. Figure 4.9B shows that on the chosen relative time scale the second perovskite formation accounts for a large fraction of the overall film formation time. Furthermore, the width and critical times of the second perovskite formation increases with increasing spin speed, while the relative widths of the solvent-complex phase formation (yellow) and the first perovskite phase formation are mostly independent with spin speed (Figure 4.9D), when compared to the significant changes seen for the second perovskite formation phase. Interestingly, the relative widths of solvent-complex and first perovskite formation for spin coating and slot-die coating are similar as seen from Figure 4.9C,D. The comparable widths indicate that the crystallization mechanisms of solvent-complex formation and the following first perovskite crystallisation are also comparable in spin and slot-die coating. However, for spin coating the crystallization process of the second perovskite formation phase differs from the other observed perovskite crystallization processes.

As the results from Figure 4.9 suggest that the mechanism of solvent-complex formation appears to be independent of the processing method, $t_{c,complex}$ or width $w_{complex}$ are most suitable to function as independent parameters for a systematic comparison of the perovskite formation kinetics in spin and slot-die coating. Since the time zero can be difficult to extract with precision the derived time of $t_{c,complex}$ may also be. Consequently, for a quantitative comparison we chose $w_{complex}$ as a parameter for comparison, which does not depend on the time zero. Figure 4.10A,B shows $\Delta t_c = t_{c,pero} – t_{c,complex}$ and w_{pero} as a function of $w_{complex}$ for the perovskite crystallization phases taking place in spin and slot-die coating.

Following Δt_c in Figure 4.10A a linear increase with increasing $w_{complex}$ is seen. This linear increase with $w_{complex}$ corresponds to a decrease in the spin speed and air-knife pressure. Interestingly, the values for the first perovskite crystallisation phase in spin coating (red circles, pero1) and single perovskite crystallisation in slot-die coating (black squares, pero) exhibit nearly the same increase with w_{pero}. This further supports the earlier assumption that the mechanisms of these two perovskite crystallisation stages are similar. In comparison, Δt_c increases more steeply for the second perovskite crystallisation during spin coating (blue circles, pero2), which means that for a shared width $w_{complex}$ the second perovskite crystallisation during spin coating occurs considerably delayed compared to the perovskite formation in slot-die coating. Further, the different slopes for the first perovskite crystallisation in spin coating (black dashed line, slot-die coating respectively) and the second perovskite crystallisation (blue dashed line) in spin coating, indicate that the mechanism of the second perovskite crystallization in spin coating differs from the corresponding mechanism of the first one (and from the one in slot-die coating respectively).

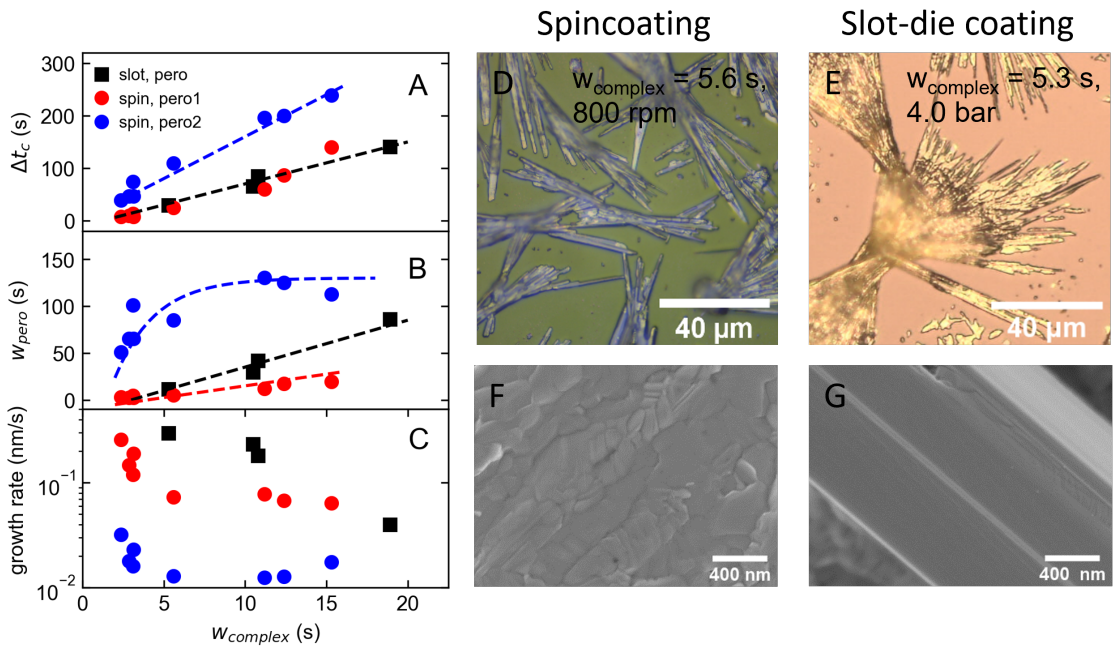

Figure 4.10: A: $\Delta t_c = t_{c,pero} – t_{c,complex}$, B: width of the perovskite phase formation w_{pero} and C: growth rates as a function of the width of the complex phase formation for spin coating (first perovskite formation pero1, red circles; second perovskite formation pero2, blue circles) and slot-die coating (pero, black squares). D,E: Reflected Optical Microscopy images of (D) spin coated and (E) slot-die coated thin films with comparable complex-phase formation duration ($w_{complex}$). Both microscopy images show bundles of needle-like structures with empty regions between. F,G: Scanning Electron Microscopy images of a spin-coated $MAPbI_3$ thin film (F) and a film obtained by drop casting (G).

Furthermore, the suggested difference in the crystallization process is also present in the behaviour of w_{pero} with $w_{complex}$ (Figure 4.10B). For slot-die coating ($w_{slot,pero}$) and the first perovskite crystallization in spin coating ($w_{spin,pero1}$) both increase linearly with $w_{complex}$, with comparable slopes. In contrast, $w_{spin,pero2}$ shows non-linear behaviour with increasing $w_{complex}$, exhibiting an initial steep increase, followed by a flattening towards larger $w_{complex}$, while always at values higher than for $w_{slot,pero}$ and $w_{spin,pero1}$.

Following the perovskite growth rates in Figure 4.10C extracted from the PL peak shifts as introduced above as a function of $w_{complex}$, the rates from slot-die coating and the first perovskite phase in spin coating have a similar magnitude, and decrease in a comparable manner with increasing $w_{complex}$. The growth rates associated with the second perovskite formation phase in spin coating are in contrast diminished by about an order of magnitude. This further supports the earlier assumption, that the first perovskite formation phase in spin coating and the perovskite formation in slot-die coating evolve with a similar perovskite crystallization process, while the second perovskite formation during spin coating appears restricted in comparison.

To investigate the impact of the presumed different crystallization mechanisms on the large scale film morphology, reflected optical microscopy images of the final films were taken. Figure 4.10D,E shows exemplary films processed by spin and slot-die coating, which have comparable $w_{complex}$. In the present case this is a $w_{complex}$ =

5.6 s for spin coating at 800 rpm and a $w_{complex} = 5.3$ s for slot-die coating with an air-knife pressure of 4 bar. Both films show needle-like structures with incomplete film coverage, as expected from the earlier identified phases of complex formation and flat OD spectra. In addition the needles appear to be arranged in bundles, oriented along a preferential direction. However, the bundles in slot-die coating appear wider, indicating that the degree of orientation of the bundles are less pronounced in the slot-die coated film than in the spin-coated film. The dark areas inside the needles in both films are associated with formed perovskite phase,[290] indicating that the latter forms within the solvent-complex structures. Comparing more microscopy images (Appendix Figure 8.8) from both spin and slot-die coating, it is observed that with faster drying kinetics the needle structures become smaller and the film coverage becomes more homogenous.

Furthermore, the microscopy image reveal differences in the vertical expansion of the films. In the slot-die coated film, the yellow out-of-focus areas demonstrate that the needles in the center of the bundle are outside the focal plane of the microscope. This indicates needle growth in vertical direction in the center of the bundles. In contrast, in the case of spin coating such needles outside of the focus plane are only observed at higher magnifications (associated with a smaller depth of field) or at slower rotation speeds (see Appendix Figure 8.9).

The differences in vertical needle growth in spin coating was further quantified by profilometry measurements. Table 4.1 shows the maximum and minimum mean height captured within the approximated excitation area from PL and UV-Vis measurements. The given error corresponds to the standard deviation within a single line measurement and serves as a measure to compare film roughness. The results from the profilometry measurements show that with increasing rpm the mean height of the thin film, as well as the film roughness, decreases. Combined with the out-of-focal plane microscopy in slot-die coating these results suggest that the needle morphology in spin coating is flatter than in slot-die coating.

rpm	**Maximum mean height (μm)**	**Minimum mean height (μm)**
2000	0.60 ± 0.36	0.56 ± 0.34
1600	0.64 ± 0.40	0.53 ± 0.42
1300	0.75 ± 0.37	0.54 ± 0.37
1000	1.1 ± 0.52	0.84 ± 0.52
800	1.3 ± 0.97	1.2 ± 0.87
700	2.2 ± 1.7	1.7 ± 1.4
600	3.7 ± 2.7	1.7 ± 1.1
500	7.0 ± 5.9	4.6 ± 4.6

Table 4.1: Maximum and minimum mean height of spin coated $MAPbI_3$ thin films measured by Dektak profilometry. For both the maximum and minimum mean height dependence with rpm an increase in thin film height with increasing rpm is captured. The given error corresponds to the standard deviation and is used as a measure for the film roughness.

To further investigate the impact of the presumed different crystallisation mechanisms on the single needle morphology, Scanning Electron Microscopy (SEM) of the final films were taken. Figure 4.10F,G shows exemplary films processed by spin coating at 2000 rpm and drop casting, a comparable method to slot-die coating at

an air-knife pressure of 0 bar. The change in preparation method was necessary, as Fabian Panzer wasn't able to prepare SEM-ready samples during his stay at TNO. Consequently, I prepared samples by dropcasting in Bayreuth, which were suitable for SEM measurements. Both films showed needle-like structures with incomplete film coverage as expected from reflected optical microscopy measurements (see Appendix Figure 8.10). The zoom-in to the formed needle-like structures shows that differences in the needle-like structures surfaces exist. While in the case of spin coating (Figure 4.10F) a magnified view of the needle surface structure morphology reveals a rough surface, a much smoother surface surface structure is seen in the case of dropcasting (Figure 4.10G). The much rougher surface for spin-coating is indicating the presence of many small crystallites, while the smoother surface for dropcasting shows no such evidence for crystallite boundaries. Instead, crystallite sizes seem to be well above 1 µm.

The comparison made in this section suggests, that despite similar complex phase formation kinetics, differences are evident in the final film morphology between spin and slot-die coating. Because the perovskite phase forms and grows within the needles of the complex phase it is reasonable to assume that differences in solvent-complex phase morphology not resolved by reflected optical microscopy result in the differences seen in perovskite growth between both processing methods.

4.4 Summary and Discussion

The results obtained provide the necessary preliminary knowledge to obtain a thorough picture of the differences between the crystallization stages in spin and slot die coating. These distinctions between spin and slot-die coating will be discussed in the present section. Figure 4.11 shows an illustration of the evolution of the crystallization stages, normalized to the duration of complex phase formation, as earlier introduced in Figure 4.10A-C.

Deduced from the temporal increase in OD, $I_{Scatter}$ and reflected optical microscopy in both spin and slot-die coating initially needle-like solvent-complexes crystallize (Figure 4.11A).[28] Following the suggestion by Fong et al.[255], the solvent-complex formation results from a supersaturation-induced heterogenuous nucleation and growth process and appears to be independent from the processing method. From their first detection at $t_{0,complex}$ the solvent-complex structures already have lengths on the μm-scale, as suggested by the independence with photon energy of their scattering contribution. Furthermore, for both processing methods the needles increase to sizes above about 50 µm in the final film (Figures 8.9 and 8.8).

Albeit, in the case of spin coating, the modulations in the OD spectra from white light interference around $t_{0,complex}$ indicates that the solvent level has already dropped to a few μm (Figure 4.3B). Therefore, one can conclude that for spin coating the growth of the needles is limited by a decreasing solvent level from a certain point in time. Further, for increasing rpm we observed that the complex phase formation accelerates, as indicated by a decreasing $w_{complex}$ (Figure 4.5A). This suggests that for increasing rpm, the decreasing solvent level influences the growth of the complex phase needles over a longer relative time span. Furthermore, as the flat needle morphology can be explained by the diminishing solvent levels, shear forces from the substrate rotation during spin coating might not influence the growth directions of the needles significantly.

In contrast, due to the missing oscillations in the OD spectra (Figure 4.6) for slot-die coating the solvent level just before $t_{0,complex}$ could only be estimated to be at least 10 µm (Figure 8.7). This may indicate that in slot-die coating the solvent-complex formation is not or only weakly limited by the solvent level (Figure 4.11B). This assumption fits well with the needle-like structures shown in Figure 4.10D,E, which in the case of slot-die coating protrude significantly upwards, while for spin coating a more flat needle morphology is observed.

Following the complex structure formation, the perovskite phase evolves within the solvent-complex structures (Figure 4.11C), which one can determine from the temporal evolution of optical parameters and static reflected optical microscopy images of the final film (e.g. Figure 4.10D,E). As indicated by similar Δt_c and growth rates for comparable $w_{complex}$(Figure 4.10A-C) the first perovskite crystallization stage for slot-die coating and spin coating shows similar initial perovskite crystallization kinetics (Figure 4.11D). However, in the case of slot-die coating a second phase of perovskite crystallization emerges. This second phase is associated with a significant reduction in perovskite growth rate in at least one spatial direction and occurs when perovskite crystallites exceed average crystallite sizes of 5 nm to 7 nm (Figure 4.4E). Compared with the perovskite formation in slot-die coating and the first one in spin coating, the reduction and the associated size limit suggest a restricted crystallization mechanism for the second perovskite formation during spin coating.

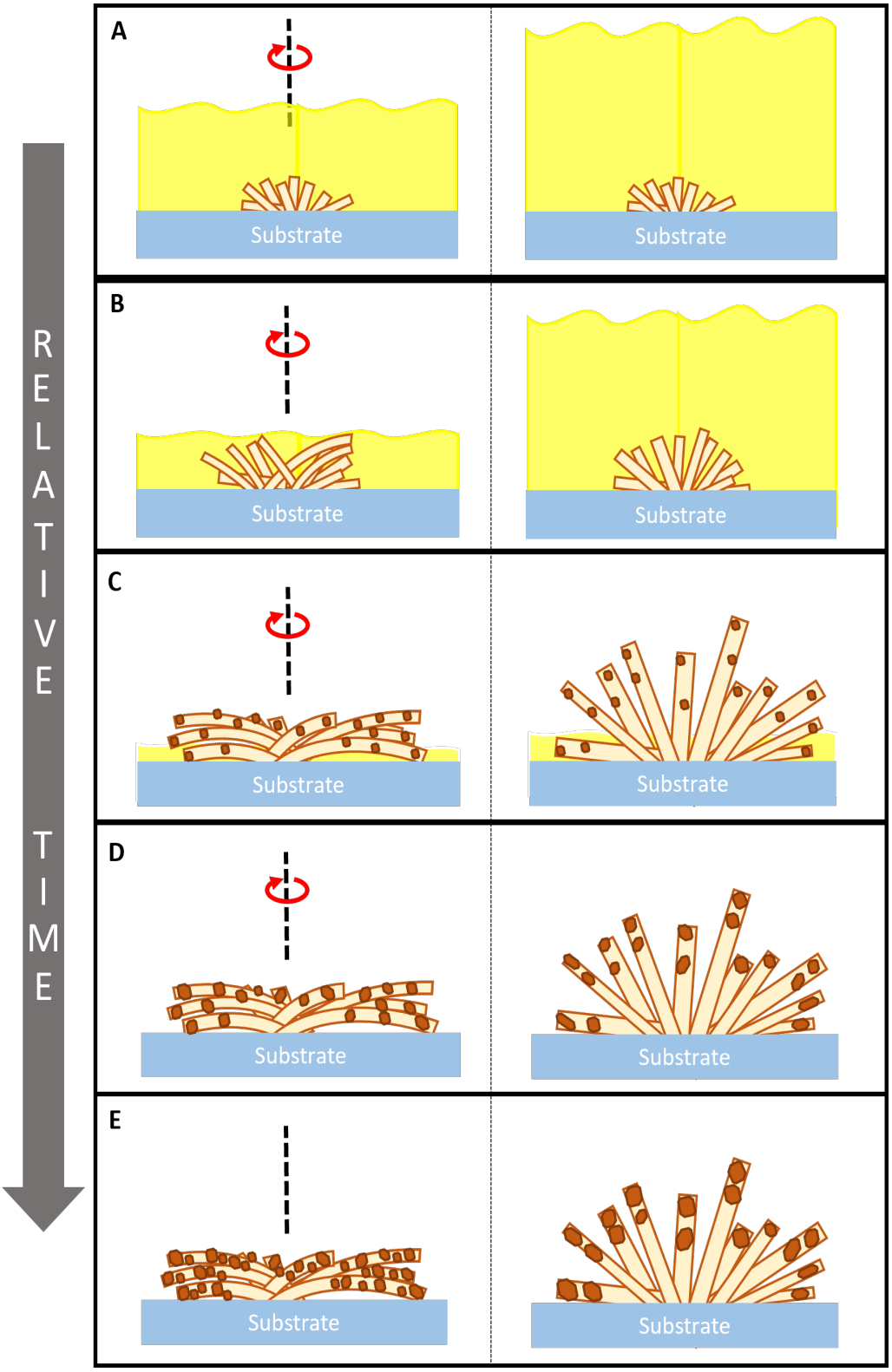

Figure 4.11: A-E: Illustration of the crystallization processes occurring during spin- (left) and slot-die coating (right) on a relative time axis, which is normalized to the duration of the complex phase formation. Supersaturated precursor solution leading to the initial solvent-complex phase nucleation is depicted in yellow, while solvent-complexes are in beige and perovskite nuclei in brown.

Taking further into account that the second perovskite formation phase appears over a longer relative time span compared to the first one (Figure 4.10B), the results suggest that the change in crystallization kinetics of the second perovskite formation is related to the flatter needle morphology of the complex phase observed in spin coating. Furthermore, all growth rates observed in Figure 4.10C are significantly lower in comparison to values reported for direct perovskite synthesis routes in solution (no solvent-complex intermediate phases), ranging from about 10 nm up to 1 µm.[238, 291–293] This reduction in perovskite growth suggests that the perovskite formation from solvent-complexes is considerably restricted compared to direct perovskite formation from the precursor solution. Consequently, it stands to reason to presume that the needle-like morphology of the solvent-complex phase significantly influences the perovskite formation mechanism and its kinetics. This supports the earlier assumption that the different crystallization kinetics of the second perovskite formation phase are a result of the altered solvent-complex phase morphology.

One possibility for such a restriction in the perovskite crystallization might be an increase in polycrystallinity of the solvent-complexes. We speculate that an increased bending of the needles during growth, or growth along non-preferred orientations parallel to the solvent-air interface could lead to defects during growth. These defects result in evolving crystallite boundaries, which increase the polycrystallinity in the formation of solvent-complex needles. Hence, when perovskite nuclei grow these will be restricted when reaching a solvent-complex phase crystallite boundary, resulting in overall smaller perovskite crystallites. In contrast, when the solvent-complex growth is less restricted, the perovskite phase can form more unrestricted. This seems to be the case for slot-die coating, in which the final PL position (Figure 4.6) indicates that the perovskite crystals exceed the confinement limit (Figure 4.11E). This expectation is supported from the Scanning Electron Microscopy (SEM) images of the final film morphology (Figure 4.10F,G), showing that differences in crystallite size exist. While for spin coating (Figure 4.10F) a magnified view of the needle surface structure morphology reveals a rough surface indicative of many small crystallites, the much smoother needle surface structure from a comparative processing to slot-die coating (Figure 4.10G) shows no evidence of crystallite boundaries, but grain sizes above 1 µm.

In summary, it was possible to achieve a thorough picture of the different crystallisation processes during spin and slot-die coating, based on the knowledge gained from the detailed analyses applied to the multimodal optical in-situ spectroscopy and microscopy methods. Further, the presented analysis highlights the sensitivity of perovskite crystallization kinetics on changes of the properties of the precursor phase and its solvent-complex structures from which the perovskite phase evolves. Thus, the presented results and the presented application of the analysis may be an important step to advance the general understanding of the crystallization processes occurring during halide perovskite evolution, independent of the specific solution-based coating method.

5 Kinetics of Thermally Induced Halide Mixing in $MAPbI_3$:$MAPbBr_3$ Powders

In the past years, mixed halide perovskites have become a candidate for application in tandem solar cells due to the tunability of their band gap.[294, 295] Though, halide migration in the bulk of perovskite grains, along the grain surface and across the particle boundaries of solid films leads to phase segregation of halides upon light illumination and consequently degrades the optoelectronic performance.[127–130] Therefore, considerable efforts have been made to study halide diffusion, which drives halide demixing processes under external stimuli such as light irradiation,[127, 296, 297] heat treatment [298–300] and electrical bias.[35, 301] These different studies have shown that the observed light irradiation-induced halide segregation is I) dependent on the administered light intensity and the ambient temperature,[298, 300, 302] II) localized at the grain boundaries[303] and III) reversed under dark conditions. [127, 298] The latter, the reversed halide (re)mixing process, is accelerated by annealing, resulting in 'solid solutions' of mixed halide perovskites,[304] i.e. a homogeneous distribution of two halide species witinh a single perovskite crystal structure, such as $MAPbI_{3-x}Br_x$. The temperature and light-induced mixing and demixing is outlined in equation 5.1 for a mixture of methylammonium lead bromide ($MAPbBr_3$) and methylammonium lead iodide ($MAPbI_3$), where the formation of intermediate halide compositions is indicated.

$$MAPbI_3 + MAPbBr_3 \overset{\Delta T}{\rightarrow} MAPbI_{3-x}Br_x + MAPbI_xBr_{3-x} \underset{h\nu}{\overset{\Delta T}{\rightleftarrows}} 2MAPbI_{1.5}Br_{1.5} \tag{5.1}$$

Phase segregation under illumination results in stable intermediate compositions of iodide-rich phases of $x \approx 0.6$, while the less stable bromide-rich phases are highly distributed.[45, 127] Further, halide diffusion in hybrid perovskites, thus also the halide segregation and mixing process outlined in Equation 5.1, is defect-mitigated[296, 304] via bulk and surface ionic defects.[305, 306] Hence, a particular halide composition influences the underlying mechanism for ion migration.[307] In addition, the halide migration is also influenced by the overall perovskite morphology and the present defect landscape. Since the mechanism of halide diffusion is influenced by such a plethora of material properties, a high variation of activation energies for iodide and bromide migration is found in literature, with values ranging between $7.7\,\mathrm{kJ\,mol^{-1}}$ to $57.9\,\mathrm{kJ\,mol^{-1}}$.[298, 302, 305, 308, 309] Further it was demonstrated that in solid thin films of mixed $MAPbI_{1.5}Br_{1.5}$ the activation energies for remixing are higher in comparison to induced segregation by prior light-irradiation,[298] which could be correlated to charge carrier generation under light-irradiation, resulting in lattice expansion and emerging strain.[310, 311]

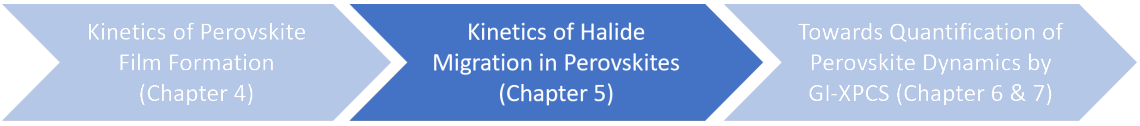

Figure 5.1: Schematic overview of thesis showing the topic of the following chapter: The present chapter describes how to quantify and influence the kinetics of thermally induced halide migration in mixed halide perovskite powders via the addition of ionic liquids. The chapter focuses on a comparison of the thermally induced formation of solid solutions in additive-free and ionic liquid containing physical mixtures of lead halide perovskite powders.

As phase separation is not desired for solar cell applications, multiple approaches have been developed to prevent ion migration, thus countering halide segregation upon illumination and inhibiting the evolution of heterogeneities in halide composition. One prominent approach is the use of additives, known to hinder ion migration by reducing defect densities in bulk,[303, 310] and modifying interfaces in perovskite thin films.[312–314] One additive class used in perovskite materials are ionic liquids. These ionic liquids consist of an anion and a cation and are known to stabilize halide perovskite materials against ambient humidity[315, 316], foster grain growth[317, 318], facilitate film processing[319, 320] and passivate surface and interface trap states.[321–323] In particular, the imidazolium-based super halogen ionic liquid $BMIMBF_4$ (1-Butyl-3-methylimidazoliumtetrafluoroborate) is reported to enhance the thermal stability in $MAPbI_3$ and mixed halide perovskite thin film solar cells under illumination and suppresses the ion migration in $MAPbI_3$ powder thick films.[323–325] But studies that elucidate the exact role of the ionic liquid $BMIMBF_4$ for halide migration and its interaction with the perovskite are still missing.[326] As such the next step in this thesis is to gain a deeper understanding of the kinetics governing the material evolution after the formation process which was examined earlier in chapter 4 as depicted in Figure 5.1.

This chapter is based on the publication "To Stop or to Shuttle Halides? The Role of an Ionic Liquid in Thermal Halide Mixing of Hybrid Perovskites", ACS Energy Letters 2023, 8, 12, 5041–5049.[125] It presents in-situ XRD diffractograms measured by myself, in-situ photoluminescence spectra measured by Philipp Ramming and Markus Griesbach and in-situ NMR spectra measured by Helen Grüninger of the mixing kinetics of a physical mixture of methylammonium lead iodide ($MAPbI_3$) and methylammonium lead bromide ($MAPbBr_3$) perovskite powders without and with the influence of the ionic liquid 1-Butyl-3-methylimidazoliumtetrafluoroborate ($BMIMBF_4$). The experiments were done within an ongoing collaboration with Philipp Ramming and Markus Griesbach from the group of Anna Köhler (Experimental Physics II) and Helen Grüniger (Anorganic Chemistry III), both located at University Bayreuth (UBT). The combination of different in-situ methods allowed us to extract the mixing kinetics on various length scales and sensitive to various chemical compounds within the examined mixed iodine-bromine lead perovskite powders. In this way, the ion migration of iodide near the sample surface can be measured with high sensitivity via PL due to charge carrier funneling into iodide-rich phases. In contrast, NMR not only offers the possibility of measuring the average bromide ion distribution in the bulk with high accuracy, but also provides information about the ionic liquid used via ^1H NMR measurements. In combination with XRD,

which provides information about both halide species and the solid solutions formed in the sample bulk, quantitative conclusions can be drawn about changes in the halide migration kinetics and their origins.

Details about the experimental procedure are given in section 3.1, 3.1.2 and 3.2. The sections describe sample preparation, the used setups for in-situ XRD, PL and NMR. The subsequent sections present first the characterization of the parent powders in section 5.1, ensuring that comparable powder defect densities, purities and sizes are present, with and without added ionic liquids. Second, the changes from the initial 1:1 physical mixture of pure $MAPbI_3$ and $MAPbBr_3$ powders to the final solid solution are examined in section 5.2. To understand the differences seen in the final solid solution state between samples containing $BMIMBF_4$ and samples without the ionic liquid (further called reference samples) the kinetics of the mixing are extracted from the XRD diffractograms and PL and NMR spectra, which enables the analysis of changes in activation energies of the involved halide species due to the addition of $BMIMBF_4$ in section 5.3. The following section 5.4 analyzes the influence of temperature to the mobility of the ionic liquid $BMIMBF_4$ by NMR. To conclude the chapter, section 5.5 combines the experimental results and proposes a mechanism how the addition of $BMIMBF_4$ accelerates the mixing kinetics of a 1:1 physical mixture of $MAPbI_3$ and $MAPbBr_3$ powders and contextualizes the previously presented results to the current literature on halide mixing and demixing.

5.1 Characterization of Parent Powders

To ensure that the changes seen in the halide mixing kinetics are related to the addition of the ionic liquid $BMIMBF_4$ the parent powder morphologies and defect densities need to be comparable with and without addition of $BMIMBF_4$. To test for the comparability of powder morphologies SEM and XRD measurements of $MAPbI_3$ and $MAPbBr_3$ with and without $BMIMBF_4$ are taken. Additionally the defect densities are tested by calculating the Urbach energy from PL measurements and by calculating the FWHM of ^{79}Br and ^{127}I in NQR measurements. The experimental details for each measurement technique are given in section 3.1 and 3.1.2.

Scanning electron microscopy (SEM): The SEM measurements presented in this paragraph were conducted by Simon Biberger (Experimental Physics II, UBT) and Nico Leupold (Functional Materials, UBT) by following the approach described in section 3.1.1. The resulting images for the parent powders of $MAPbI_3$ and $MAPbBr_3$ with and without $BMIMBF_4$ can be seen in Figure 5.2. From the presented SEM images pseudoradii of powder grains were extracted as a measure of the individual particle size of parent powders by Markus Griesbach. To extract the pseudoradii the area of individual grains was estimated from the single SEM images (via ImageJ). To calculate the pseudoradius from the area, the root of (the area divided by π) is taken.

The results are presented as a boxplot in Fig. 5.3. On average identical distributions of pseudoradii are observed for the $MAPbI_3$ parent powders with and without the ionic liquid $BMIMBF_4$ (average pseudoradii $\approx 0.2\,\mu m$). For the $MAPbBr_3$ parent powders the pseudoradii are on average slightly larger for the reference sample ($0.5\,\mu m$) compared to the sample with ionic liquid ($0.3\,\mu m$), but still comparable within the given errors of the pseudoradii distribution. Further, within the error

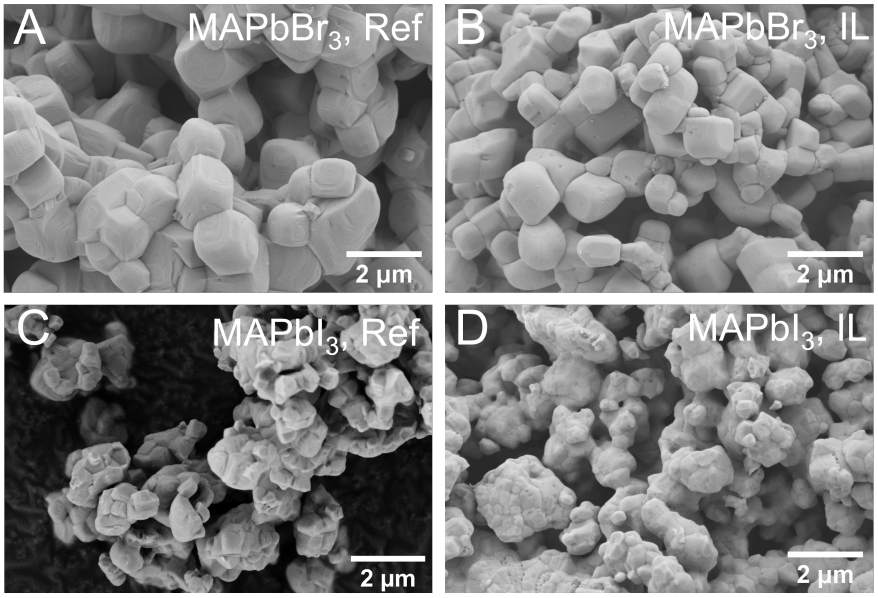

Figure 5.2: Scanning electron microscopy (SEM) images of parent powders of (A,B) $MAPbBr_3$ and (C,D) $MAPbI_3$, synthesized without (A,C: labelled Ref) and with $BMIMBF_4$ (B,D: labelled IL)

margin these differences in particle size are negligible and are not expected to result in strong changes in the observed halide mixing kinetics. Therefore, the morphology, especially particle sizes, of parent powders with and without ionic liquid are comparable from the SEM images.

X-Ray Diffraction (XRD): To determine if the crystallinity as a measure of the powder morphology of the parent powders is comparable between powders with and without ionic liquid I conducted XRD measurements under inert N_2 atmosphere at room temperature.

From Figure 5.4 it is apparent that no differences between the peak positions, peak widths, peak heights and visible diffraction orders are visible for $MAPbI_3$ and

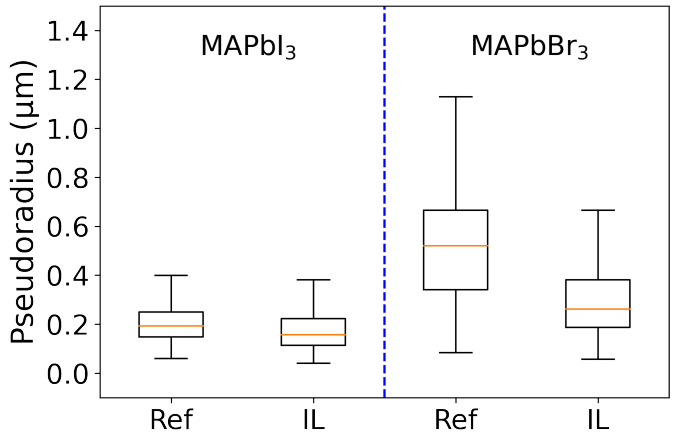

Figure 5.3: Boxplot of parent powders of $MAPbI_3$ (left) and $MAPbBr_3$ (right) , synthesized without (Ref) and with $BMIMBF_4$ (IL).

$MAPbBr_3$ with and without ionic liquid. Further, no scattering signal from the degradation product PbI_2 was observed for either sample, which is expected to appear around 12° and at higher subsequent orders.[327] Therefore we conclude that the crystallinity between $MAPbI_3$ parent powders is comparable, which also applies for the used $MAPbBr_3$ parent powders.

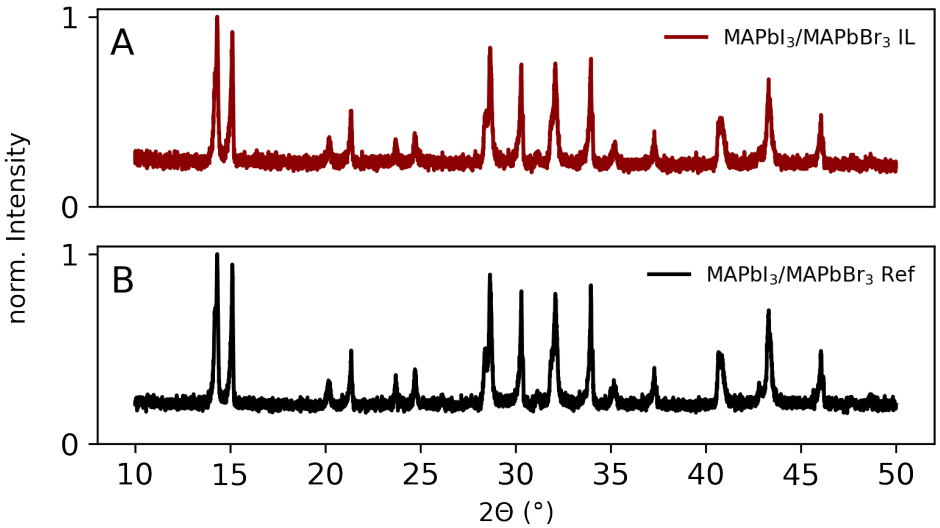

Figure 5.4: Normalized pXRD patterns of 1:1 physical mixtures of parent powders of $MAPbI_3$:$MAPbBr_3$ at room temperature prior to mixing experiments with $BMIMBF_4$ (A, IL, darkred) and without (B, Ref, black).

Urbach energies: To determine if the disorder within the microstructure of the parent powders with and without ionic liquid is comparable, the Urbach energy is extracted from PL measurements performed by Markus Griesbach as described in section 3.1.2. I extracted the Urbach energies by applying an exponential fit to the low energy side of the PL peaks attributed to $MAPbBr_3$ (located around 2.25 eV) and $MAPbI_3$ (located around 1.60 eV) and extracting the slope in this exponential region as seen in Figure 5.5.[91]

I extracted Urbach energies of about $E_U = 20.5\,meV$ for $MAPbBr_3$ with and without ionic liquid, showing that the microstructure disorder in both $MAPbBr_3$ powders is comparable. The same applies to the $MAPbI_3$ parent powders, in which I calculate an Urbach energy of $E_U = 14.8\,meV$ with and without ionic liquid. In hybrid perovskites these low Urbach energies indicate that the disorder within the microstructure is low and a high degree of crystallinity is present.[328]

Nuclear quadrupole resonance (NQR): To determine if the defect density of the parent powders with and without ionic liquid is comparable, NQR spectroscopy measurements of the quadrupole of ^{79}Br and ^{127}I halides was performed by Helen Grüninger, following the procedure described in section 3.1.2.

NQR spectroscopy on the quadrupole halides is sensitive to the local environment around the halide nuclei and thus sensitive to defects within the perovskite lattice.[200] Especially the full width-half maximum (FWHM) is an established qualitative

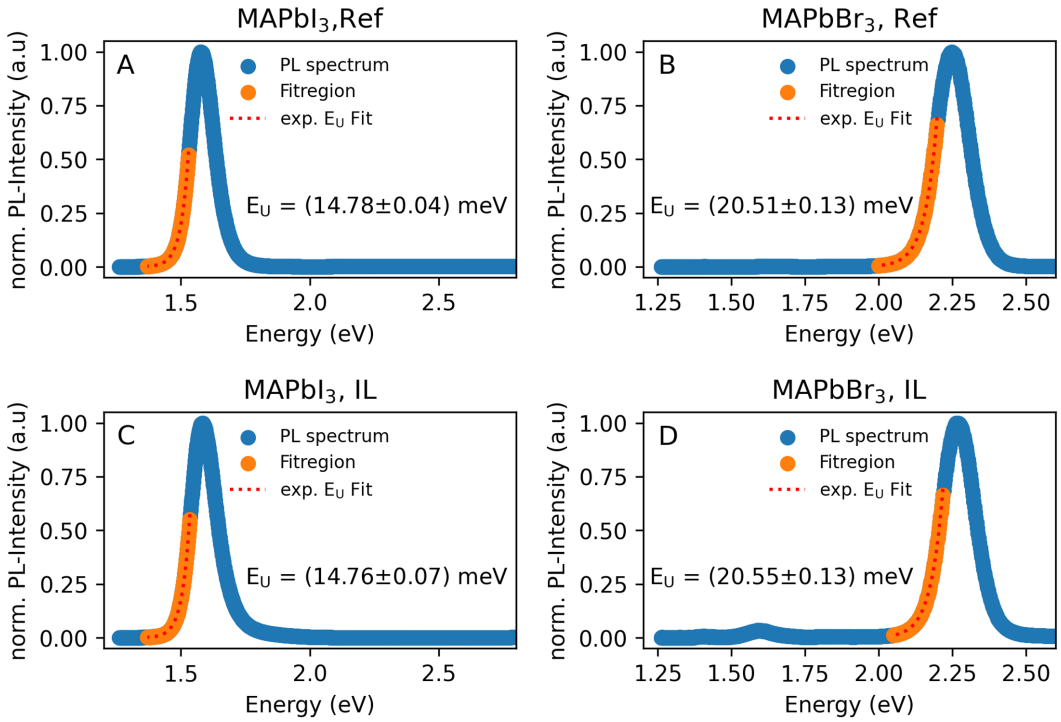

Figure 5.5: PL spectra (blue) of parent powders of (A,C) $MAPbI_3$ and (B,D) $MAPbBr_3$, synthesized (A,B) without (labelled Ref) and (C,D) with $BMIMBF_4$ (labelled IL). The energetic fit range for the exponential Urbach fit (orange), the Urbach fit (red dotted-line) and the extracted Urbach energy E_U are labelled within the spectra. The spectra are normalized to the maximum intensity.

measure for defect densities, but also the absolute signal intensity.[232, 233] The NQR spectra of ^{79}Br for $MAPbBr_3$ with and without ionic liquid and of ^{127}I for $MAPbI_3$ with and without ionic liquid are shown in Figure 5.6. The FWHMs were extracted by approximating the peaks attributed to ^{79}Br and ^{127}I respectively with a Gaussian distribution and calculating the FWHM from the derived standard deviation σ. The values for bromide ($MAPbBr_3$) are: 15.1 kHz (Ref), 17.6 kHz (IL) and for iodide ($MAPbI_3$): 63.7 kHz (Ref), 59.9 kHz (IL). As the absolute intensities as seen from the Figure and extracted NQR FWHMs are comparable for both parent powders ($MAPbBr_3$ with and without ionic liquid, respectively $MAPbI_3$) we infer from the NQR spectra that the bulk defect densities in the corresponding parent powders are also comparable.

Combining the results of XRD, SEM, PL and NQR measurements on parent powders of $MAPbBr_3$ and $MAPbI_3$ with and without the ionic liquid $BMIMBF_4$ I conclude that the defect densities and powder morphologies are comparable for each parent powder species ($MAPbBr_3$ & $MAPbI_3$). Therefore, observed changes in the halide mixing kinetics must be related to the presence of the ionic liquid $BMIMBF_4$ rather than significantly different powder morphologies and/or bulk defect densities in the starting material.

After establishing by XRD, SEM, PL and NQR measurements that the parent powders with and without added ionic liquid have comparable bulk defect densities and powder morphologies, i.e. grain sizes and no degradation related products, in

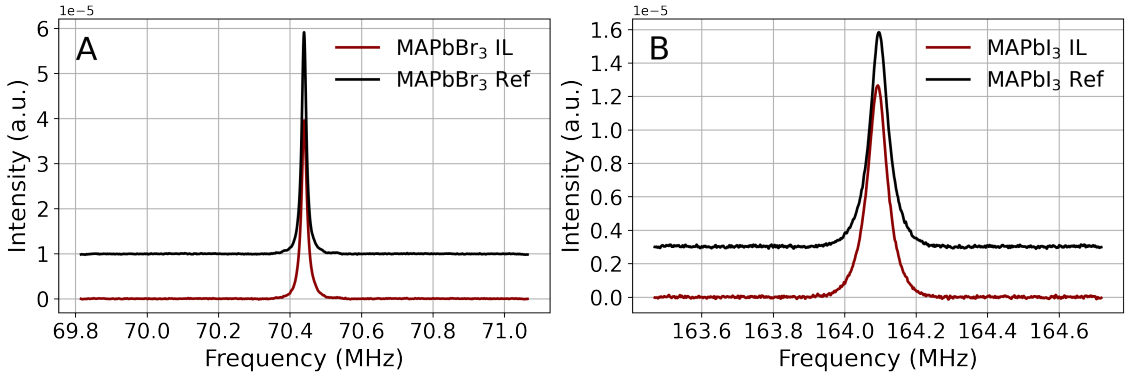

Figure 5.6: (A) ^{79}Br and (B) ^{127}I nuclear quadrupole resonance (NQR) spectra of the physical $MAPbI_3$:$MAPbBr_3$ mixtures without $BMIMBF_4$ (Ref, black) and with $BMIMBF_4$ (IL, red) recorded prior halide exchange experiments. ^{127}I NQR spectra were recorded for the equatorial Iodine atoms in the tetragonal $MAPbI_3$ phase at room temperature due to limitations of the probe to tune to higher frequencies. IL spectra are shifted with respect to reference spectra by a fifth of their maximum height for visibility.

section 5.1, the parent powders are physically mixed in the next section and time-resolved XRD measurements at elevated temperatures are carried out to analyze the effect of $BMIMBF_4$ on the halide mixing.

5.2 In-situ Experiments

To quantify the impact of the ionic liquid $BMIMBF_4$ in-situ XRD experiments of the mixing process at various temperatures are conducted by myself as described in section 3.1.1 for physical 1:1 mixtures of $MAPbI_3$:$MAPbBr_3$ with and without ionic liquid. The XRD measurements provide information on the overall phase distribution of perovskite phases in the bulk. Figure 5.7 shows 2D maps of the time-resolved scattering with and without $BMIMBF_4$ and extracted cuts of normalized intensity for initial, intermediate and final timesteps. The data shown in Figure 5.7 was measured for a mixing temperature of 90 °C.

The 2D scattering maps and extracted 1D diffractograms in Figure 5.7 clearly show that both mixtures start from unmixed parent phases showing reflexes attributed to cubic (200) scattering of $MAPbI_3$ ($2\Theta = 28.1°$) and $MAPbBr_3$ ($2\Theta = 29.8°$).[109, 329] These initial reflexes attributed to the pure parent phases are already asymmetric in shape, indicating the onset of the halide mixing process. With time the initial reflexes are decreasing in intensity, broaden further and shift to intermediate angles 2Θ in between 28.1° and 29.8°. While the reference sample without ionic liquid shows after 3500 min two distinct reflexes, attributed to minority and majority phases of iodide and bromide, a singular reflex at the expected 2Θ position of a fully mixed $MAPbI_{1.5}Br_{1.5}$ is visible already after 1000 min for the ionic liquid containing sample.[330] For even longer retention times at 90 °C the reflex becomes more narrow indicating an increase in crystallinity/average crystal size through annealing. Viewing the 2D maps in Figure 5.7 it also appears that the decrease in intensity of the parent phases appears asymmetric for the reference sample, while almost symmetric decays of the parent phases are observable for the $BMIMBF_4$-containing sample.

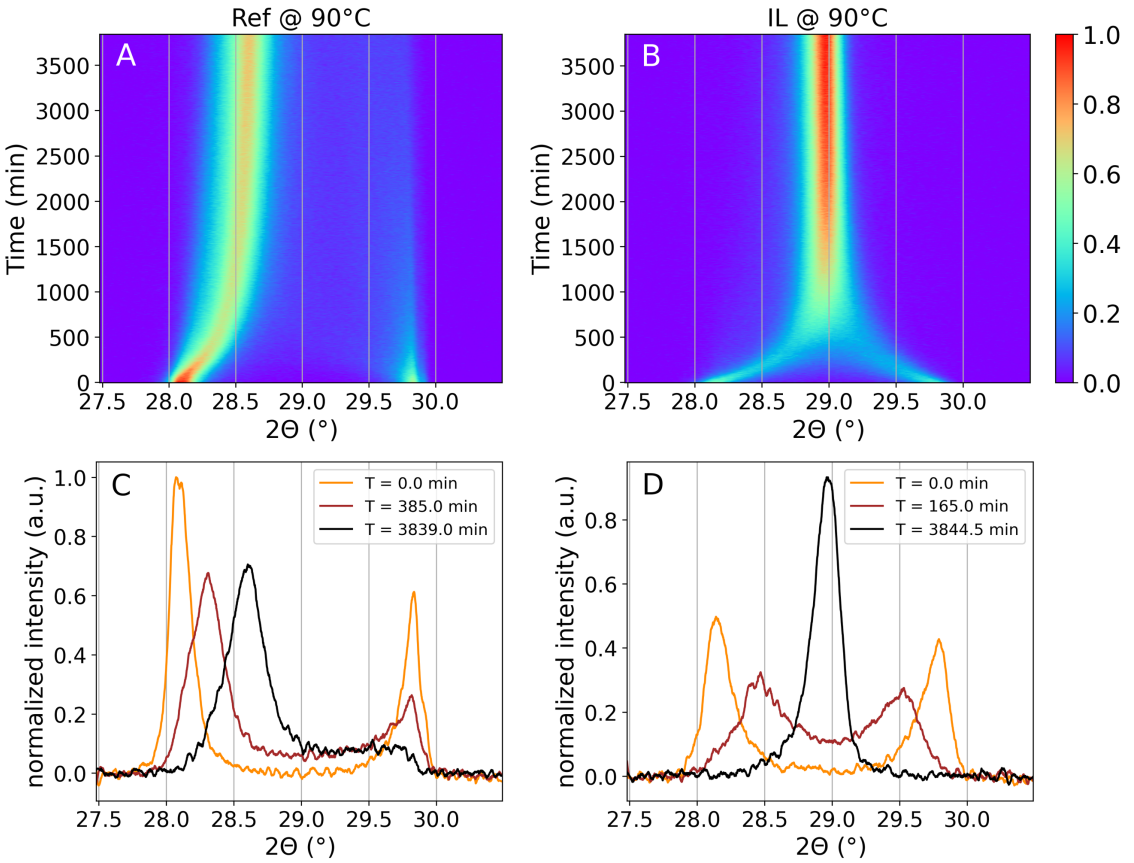

Figure 5.7: (A,B) Temporal evolution of XRD diffractograms as 2D maps for the cubic (200) $MAPbI_3$ and $MAPbBr_3$ peak positions for 1:1 $MAPbI_3$:$MAPbBr_3$ mixtures without (Ref, left column) and with $BMIMBF_4$ (IL, right column) for halide mixing at 90 °C. The color indicates the signal intensities of evolving equivalent phases of differently mixed $MAPbI_{3-x}Br_x$ signals. (C,D) Initial, intermediate and final 1D diffractograms extracted from A,B for the times indicated in the subfigures. The intensities were normalized to the maximum intensity seen in A,B.

After the time-resolved XRD measurements are carried out and commonalities (e.g. starting both from unmixed parent phases) and differences (e.g. single final peak for ionic liquid-containing sample, but two peaks for reference sample) are identified in section 5.2 the findings are used in the next section to establish an analysis approach to extract the kinetics of halide migration from the time-resolved XRD diffractograms.

5.3 In-situ Kinetics

To assess the evolution of iodide and bromide mixing kinetics between powder grains of $MAPbI_3$ and $MAPbBr_3$ the temporal evolution of the powder XRD diffractograms is analyzed. The experimental data are fitted to extract the specific signal integrals of the pure parent phases from the overlapping signals of mixed phases of $MAPbI_{3-x}Br_x$. To extract the signals attributed to the pure parent phases of $MAPbI_3$ and $MAPbBr_3$ from the overlapping signals I apply an approach similar to Suchan et al.[45], in which I approximate the continous phase distribution of $MAPbI_{3-x}Br_x$ by a discrete phase

distribution with 13 different compositions. These 13 compositions are equivalent to phases of $MAPbI_{3-x}Br_x$ with $x = \{0, 0.25, ..., 2.75, 3\}$, whose cubic (200) reflection positions are in good approximation linearly distributed between the parent powders positions due to Vegard's law.[109, 330] The thus discretized phase distribution seen in the evolving diffractograms was followed by fitting Gaussians of fixed width and fixed position to the diffractograms. The fixed peak positions are extracted from a linear extrapolation of the recorded phase's pure cubic (200) $MAPbI_3$ and $MAPbBr_3$ reflections in the initial diffractograms (shown in Figure 5.7). The same initial diffractograms are used to extract a fixed width used for the fitting procedure, as the peak width in the initial diffractograms results from an overlap of the instrumental response, micro strain within the sample and size effects.[153, 331] Consequently, the initial peak widths are a good estimate of sample and instrumental influences to the XRD diffractograms. It is known from literature that for solid solutions around $MAPbI_{1.5}Br_{1.5}$ peak broadening occurs due to lattice distance inhomogeneity,[26, 127, 332] related to either the emergence of micro strain or chemical inhomogeneity, i.e. phase segregation. But the effect of strain is estimated to be negligible, as Suchan et al. showed by analysis of the center of mass of diffraction peaks that for mixed halide perovskite thin films, the peak broadening is governed by their chemical inhomogeneity, while the strain stays constant.[333] As powders tend to have lower micro strain compared to thin films,[334] I deduce that micro strain peak broadening plays no role for the evolving XRD diffractograms and that by applying constant widths based on the initial diffractograms an accurate estimate of the evolving chemical halide inhomogeneity can be extracted. Consequently, I approximate the intensity distribution $I(2\Theta)$ within the diffractograms as a linear combination:

$$I(2\Theta) = \sum_{i=1}^{13} I_i G_i(2\Theta_i) \tag{5.2}$$

with the coefficient I_i corresponding to the intensity of the respective discrete $MAPbI_{3-x}Br_x$ phase approximated by the Gaussian $G_i(2\Theta_i)$ located at $2\Theta_i$. The approach is shown in the Appendix in Figure 8.11 for halide mixing at 90 °C for a $BMIMBF_4$ containing sample to demonstrate the approach. I further tested whether the respective number of intermediate solid solutions can be reduced to 7, equally to the following mixed halide perovskite phases of $MAPbI_{3-x}Br_x$ with $x = \{0, 0.5, ..., 2.5, 3\}$. Following the same approach of phase extraction by using peak widths based on the initial XRD diffractograms of the pure parent phases (as such based on the instrumental response) the respective coefficient of determination R^2 of the fitting procedure is significantly reduced over the whole experiment, as seen from Figure 8.12 in the Appendix. Consequently, the fitting procedure of a linear combination of 13 equidistantly spaced Gaussians with constant peak width introduced earlier is used to extract the respective intensities I_i.

As these intensities I_i are proportional to the respective halide compositions located at $2\Theta_i$ in the diffractograms and to their respective amount in the analyzed powder sample, by normalizing each $I_i(t)$ to the overall sum of intensities of $I_i(t)$ the distribution of mixed halide perovskite compositions can be tracked. The resulting distribution of normalized compositions is shown in Figure 5.8.

Comparing the reference sample at 90 °C in Figure 5.8A with the IL containing sample at 90 °C in Figure 5.8B shows that the initial decay of pure parent phases is faster in the case of the reference sample. Furthermore, the dominant solid

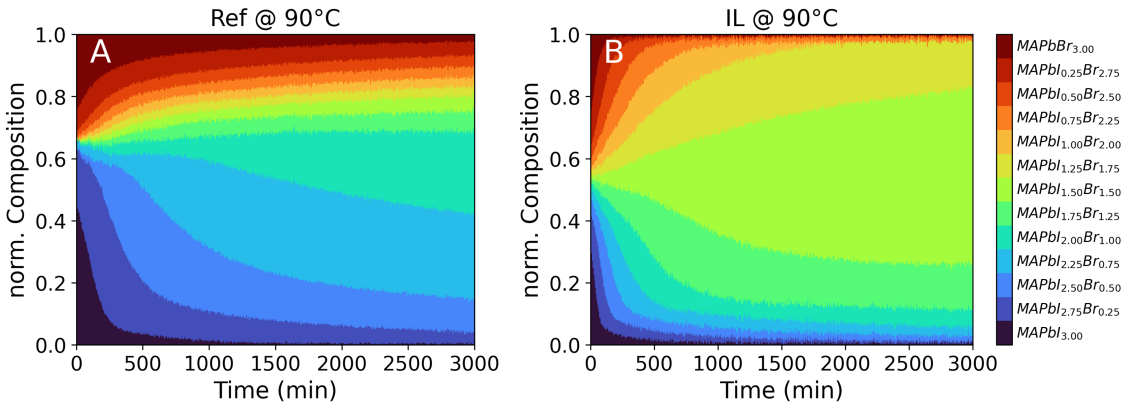

Figure 5.8: Temporal evolution of normalized halide composition distribution extracted from the halide composition attributed intensities I_i introduced in Eq. 5.2. (A) 1:1 physical mixture of $MAPbI_3$:$MAPbBr_3$ retained at 90 °C without ionic liquid (Ref). (B) 1:1 physical mixture of $MAPbI_3$:$MAPbBr_3$ retained at 90 °C with ionic liquid (IL). The color indicates the amount of equivalent phase of differently mixed $MAPbI_{3-x}Br_x$ solid solutions.

solutions after a retention time of 3000 min differ significantly. In the case of the Ref sample, the compositional distribution is dominated by $MAPbI_{2.25}Br_{0.75}$ and $MAPbI_{2.00}Br_{1.00}$, with only low amounts of Br-heavy compositions, whereas in the case of the IL containing sample the final distribution of compositions is mainly defined by $MAPbI_{1.50}Br_{1.50}$ and $MAPbI_{1.75}Br_{1.25}$ with a more symmetric distribution of I- and Br-rich compositions.

The halide migration for intermediate phases is not easy to distinguish from the changing compositions with time, as during the halide mixing process, intermediate solid solutions rich in a single halide species, such as $MAPbI_{2.00}Br_{1.00}$, are not only losing halide ions to perovskite phases with a lower halide ion concentration but also receive halide ions from perovskite phases with a higher halide ion concentration.

In order to further quantify the complex interplay of migrating halide ions, the decay in the intensities of the pure $MAPbI_3$ and $MAPbBr_3$ parent phases is tracked, as halide transport mainly takes place from these perovskite phases. As such, by following the single halide perovskite phase-attributed intensities I_1 and I_{13} with time, it is possible to track the loss in the amount of crystalline $MAPbI_3$ and $MAPbBr_3$ and the migration of their respective halide ions. The resulting decay curves for $MAPbI_3$ and $MAPbBr_3$ are presented in Figure 5.9 for samples with and without ionic liquid at a mixing temperature of 90 °C. The intensity was normalized to the intensity extracted from the initial diffractograms and is presented on a semi-logarithmic scale.

All decay curves, which correspond to a loss of pure parent phase material, show complex kinetics. For all decay curves an initial fast decay is evident, followed by a slower decay in intensity. The transition time marking the change from fast to slow decay regime is earlier for the ionic liquid (IL) containing sample. In the chosen semi-logarithmic plot, the fast and slow decay regimes appear as linear slopes, indicating that at least two first order processes can be identified within the mixing process, changing with time.[335] However, it is realistic that a superposition of several processes influences the observed kinetics. Such as halide migration at grain interfaces and in the crystalline bulk,[336–338] dynamic changes of the defect landscape and the

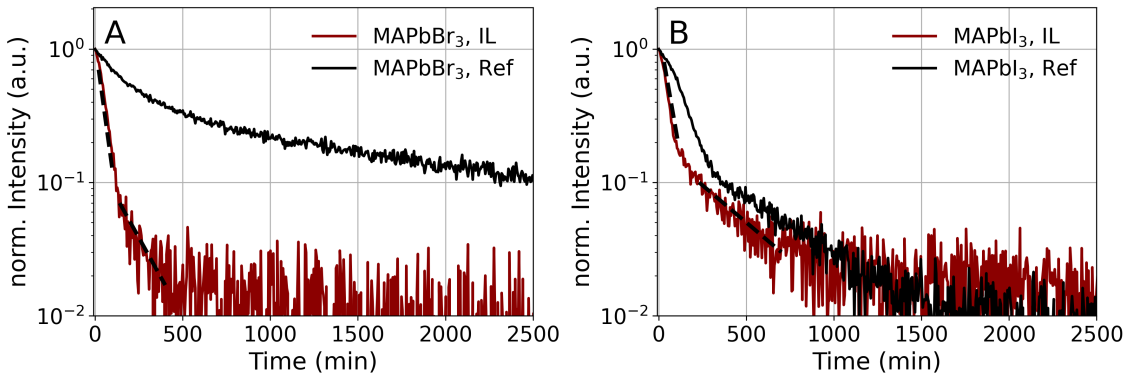

Figure 5.9: Temporal evolution of the normalized intensities I_1 and I_13 attributed to the pure phase of (A) $MAPbBr_3$ and (B) $MAPbI_3$ of a physical 1:1 mixture of $MAPbI_3$:$MAPbBr_3$ powder during thermally induced halide mixing at 90 °C extracted from XRD diffractograms via Eq. 5.2. $BMIMBF_4$ containing mixture labelled IL (red), while reference perovskite powders (Ref, black) were synthesized without IL. The black dashed lines are a guide-to-the-eye indicating changing slopes for the IL containing powder sample.

resulting ion migration pathways during annealing,[339] growth processes of grains [340] and the continuous evolution of the compositional gradient, acting as a driving force for the configurational entropy gain during the formation of a solid solution.[341] Further, comparing the acceleration of decay rates on the mixing kinetics by the ionic liquid (related to the halide species involved), the acceleration is more pronounced for the Br^- migration, whereas only a moderate acceleration of mixing kinetics is seen for I^-. Consequently, the presence of the ionic liquid $BMIMBF_4$ has a stronger influence on Br^- transport than on I^- transport.

To check whether an equivalent acceleration of kinetics is present during the thermally induced halide mixing due to a physical mixture of parent phases on other length scales NMR measurements for tracking Br^- and PL measurements for tracking I^- ions were conducted by Helen Grüninger and Philipp Ramming respectively (described in section 3.1.2). While the chemical shifts followed in ^{207}Pb NMR are sensitive to the halide composition in the local environment of ^{207}Pb and as such to its first octahedral coordination shell,[329] PL is highly sensitive to low-energy emitting sites, due to charge carrier funneling into I-rich domains that have the smallest bandgap,[131, 311] as such being highly sensitive to I-rich domains.[45, 311] Further, NMR spectroscopy is sensitive to the material's bulk, thus providing an average description of both, bulk and surfaces of the powder, whereas PL is highly sensitive to the surface, due to low penetration depth of the exciting light, due to the strong absorption of metal halide perovskites. As such the combination of XRD, NMR and PL measurements can help to derive a full picture of the mixing process, spanning over several length scales and being sensitive to different halide species.

To follow the kinetics from NMR and PL Helen Grüninger and Philipp Ramming applied an equivalent approach as introduced for the in-situ XRD measurements, in which they tracked the change in material attributed to the parental phases from the time-resolved 1D NMR and PL spectra. The time-resolved spectra were approximated similar to equation 5.2 but adjusted to the respective measurement technique.

NMR-kinetics: In ^{207}Pb NMR the derived spectra during mixing initially start with distinct signals at chemical shifts of $\delta = 1450$ ppm and 400 ppm, which are attributed to ^{207}Pb in pure octahedral I^- and Br^- coordination.[216, 233, 329] Evolving within the mixing process, a signal in between the pure parent phase peaks located around $\delta = 1050$ ppm emerges, attributed to a mixture of various halide coordinations of $PbI_{6-x}Br_x$ with $x = \{0, ...6\}$. Consequently, the evolving spectrum is fitted with 7 signals corresponding to the possible Pb-halide environments.[329] As in XRD, fixed positions and a fixed FWHM were used to model the signal, but due to slightly changing lattice constants in different perovskite compositions a slight resonance position variance is needed.[216, 217] Further, the single signal shape was modelled as a pseudo-Voigt with a Gaussian to Lorentzian ratio of 0.9. Within the NMR experiments the resonance from $PbBr_6$ coordination was the best resolved, so this resonance is used to further assess the loss in $MAPbBr_3$ phase during thermally induced halide mixing. However, also in Br-rich mixed phases of $MAPbI_{3-x}Br_x$ (x>2) significant amounts (above 10%) of ^{207}Pb are in full octahedral Br^- coordination. As such, the decay of the $PbBr_6$ resonance will be influenced by these mixed Br-rich phases, causing a flattening of decay curves in comparison to the expected decay curves attributed to the pure $MAPbBr_3$ phase.[125] The resulting intensity decay curves for the $PbBr_6$ resonance are shown in Figure 5.10 for samples with and without ionic liquid at a mixing temperature of 90 °C on a semi-logarithmic scale.

PL-kinetics: In PL the measured spectra during mixing initially start from distinct emissions at 780 nm and 550 nm corresponding to phases of $MAPbI_3$ and $MAPbBr_3$, respectively.[131] Further, despite equal phase ratios of $MAPbI_3$ and $MAPbBr_3$ the intensity from the $MAPbBr_3$ attributed emission is heavily suppressed, due to charge carrier funelling into I-rich material phases.[45, 131] Evolving with the mixing process, the emissions attributed to the parent phases shift to wavelenths in-between their initial peak positions and merge with time until a peak at 718 nm dominates the final spectrum. This peak does not correspond to the expected wavelength for a fully mixed phase of $MAPbI_{1.5}Br_{1.5}$, indicating that the mixing process even for ionic liquid containing samples at 90 °C is not resulting in fully mixed solid solutions of $MAPbI_{1.5}Br_{1.5}$. In these incompletely mixed solid solutions there still exist I-rich domains, which dominate the PL emission due to the earlier-introduced charge carrier funneling into these I-rich domains.[45] Consequently, the PL measurements are dominated by signals attributed to the I-rich phases, such as the $MAPbI_3$ phase. Adopting the approach for the XRD diffractogram analysis Philipp Ramming modelled the time-resolved PL spectra based on the model proposed by myself in Eq. 5.2. He adapted the model by using a linear combination of 7 equally spaced Gaussians located at and in-between the emission wavelengths of the parent phases, as such being equivalent to phases of $MAPbI_{3-x}Br_x$ with $x = \{0, 0.5, ..., 2.5, 3\}$. The fixed center wavelengths and the FWHMs of the single Gaussians were derived from the positions and widths of the initial $MAPbI_3$ and $MAPbBr_3$ PL peaks at t = 0 min. Since the FWHM from the initial PL spectrum was comparatively broader than the peak width of the initial XRD diffractograms, only 7 distinct solid solutions could be extracted due to the limited resolution. Since the emission in PL spectra is dominated by $MAPbI_3$ or other I-rich phases due to charge carrier funneling, the intensity decay corresponding to the $MAPbI_3$ PL emission is used to assess the loss in $MAPbI_3$ phase during thermally induced halide mixing. The resulting intensity

decay curves for the $MAPbI_3$ emission is shown in Figure 5.10 for samples with and without ionic liquid at a mixing temperature of 90 °C on a semi-logarithmic scale.

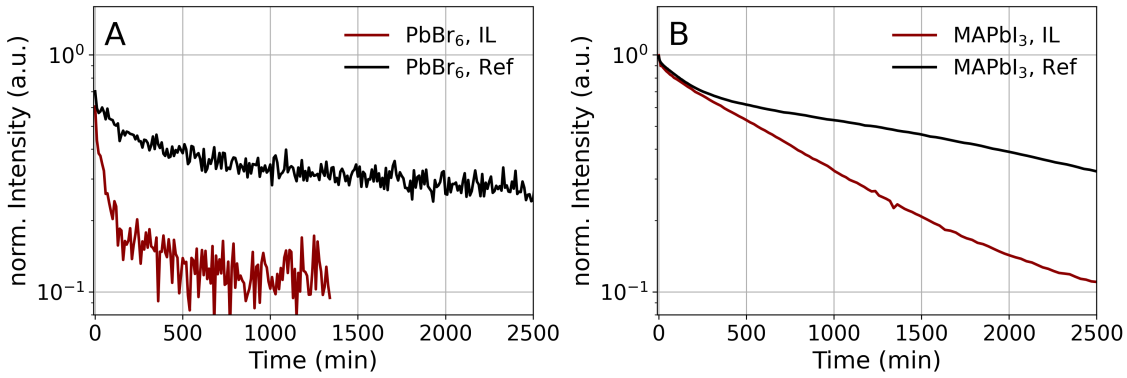

Figure 5.10: Temporal evolution of the normalized intensity attributed to the pure phase of (A) $PbBr_6$ octahedra from NMR measurements and (B) $MAPbI_3$ from PL measurements of a physical 1:1 mixture of $MAPbI_3$:$MAPbBr_3$ powder during thermally induced halide mixing at 90 °C. $BMIMBF_4$ containing mixtures are labelled IL (red), while reference perovskite powders (Ref, black) were synthesized without IL.

Comparing Figure 5.9 and 5.10 it is evident that the decay curves associated with Br^- transport, such as XRD following the decay of $MAPbBr_3$ perovskite phase and NMR, following the decay of $PbBr_6$ octahedra, are qualitatively comparable. Both show the two-step decay identified earlier with comparable transition times between the fast and slow decay regimes. But differences appear for the decay curves associated with I^- migration, such as XRD and PL, following the decay of $MAPbI_3$ perovskite phase. The kinetic curve derived from PL decays significantly slower than the one derived from XRD measurements. The comparatively slower decay in $MAPbI_3$ perovskite phase seen in PL measurements might indicate that at the probed surfaces I-rich domains remain longer compared to the sample bulk probed by XRD measurements. Such I-rich surface domains may appear enhanced in the PL signal compared to their relative proportion due to charge carrier funneling into such domains,[45] while on average over longer length scales as probed by XRD the mixing from parent phases might already appear complete.

To conclude, in section 5.3 I established an analysis approach to extract the kinetics of halide migration from the parent phases in halide mixing experiments via XRD and compared the results qualitatively to comparative thermally induced halide mixing experiments of PL and NMR. For the three compared methods of XRD, PL and NMR an acceleration of halide migration with the addition of the ionic liquid is seen. The extracted kinetics are quantitatively analyzed in the subsequent section and possible origins of differences in the kinetics of samples with and without ionic liquid are explored.

5.4 Origin of Change in Halide Kinetics

To further investigate the influence of the ionic liquid $BMIMBF_4$ on the mixing kinetics and why its presence has a greater impact for Br^- migration compared to I^- migration the decay curves from Figure 5.9 are further analyzed.

As a measure for the migration of Br^- and I^- ions I extract the decay rates from the slopes in the semi-logarithmic decay curves shown in Figure 5.9.[335] Since intensity decays in Figure 5.9 show a recognizable transition region between regions of linear slopes, the decay rates are extracted using a biexponential fit on a logarithmic time scale of the subsequent form: $I(t) = A_1 \cdot \exp(-t \cdot k_1) + A_2 \cdot \exp(-t \cdot k_2) + \text{offset}$. Here A_x and k_x are the amplitude and decay rate of the single exponentials and the offset is a constant necessary to account for incomplete conversions of the parent phase and variations in noise. As a result, the transition regions are not neglected and both the initial (fast) decay rate k_1 and the second (slow) decay rate k_2 for the linear slopes seen earlier can be extracted. However, it is important that the original data set was recorded on a linear time axis. In order to not overweigh data points on the logarithmic time axis for higher decades (times above 10^3 min), the time axis is rescaled to a logarithmic scale. The time axis is resampled with 8 data points per decade and data points on the linear time axis between consecutive logarithmic timesteps are averaged to increase statistic power. The resampled data set of Figure 5.9 with the described biexponential fit is shown in the Figures 8.15 and 8.16 (top row) in the Appendix. Until now only data sets for thermally induced mixing experiments at 90 °C were discussed, but further experiments for intermediate temperatures of 60 °C and 75 °C were conducted (see experimental details in section 3.1.1). These temperatures ensure that both parent phases of $MAPbI_3$ and $MAPBBr_3$ are within their cubic crystalline phases for the halide exchange experiments.[62, 123] For all measured temperatures and physical mixtures (Ref and IL) the decays of the parent phases of $MAPbI_3$ and $MAPbBr_3$ are extracted and fitted with the biexponential decay model. The fits and resampled decays are shown in the Figures 8.15 and 8.16 (middle and bottom row) in the Appendix. The extracted fit parameters are shown in Tables 8.2 and 8.1. The semi-logarithmic resampled decays and their respective extracted fit parameters show that in most cases the chosen biexponential model is sufficient to describe the decay curves. But in some cases, such as for the decays of the $MAPbI_3$ at 90 °C a stretched exponential may be a better approximation. Such a stretched exponential is an indicator that a distribution of decay rates is present.[342] Nevertheless, the approximation by a biexpoential model is sufficient to identify two dominant decay rates within the investigated decays. Further, in some cases only a single decay rate could be extracted, before the intensities decayed to a flat regime. These single decays were only detected for kinetics related to iodide migration from the $MAPbI_3$ phase. Here, the single extracted decay rate was interpreted as a fast decay rate k_1. The obtained fast and slow decay rates k_1 and k_2 follow an Arrhenius-type behaviour and are presented consequently as an Arrhenius plot in Figure 5.11. Figure 5.11 presents the dominant decay rates, i.e. only full temperature data sets of 60 °C to 90 °C are depicted when: I) the respective amplitudes A_x are above 0.05 and II) the decay rates k_1 and k_2 are different. The dominance criterion ensures that biexponential fits resulting effectively in single exponentials are not depicted twice in separate Arrhenius plots, resulting only in the dominance of the decay rates k_1.

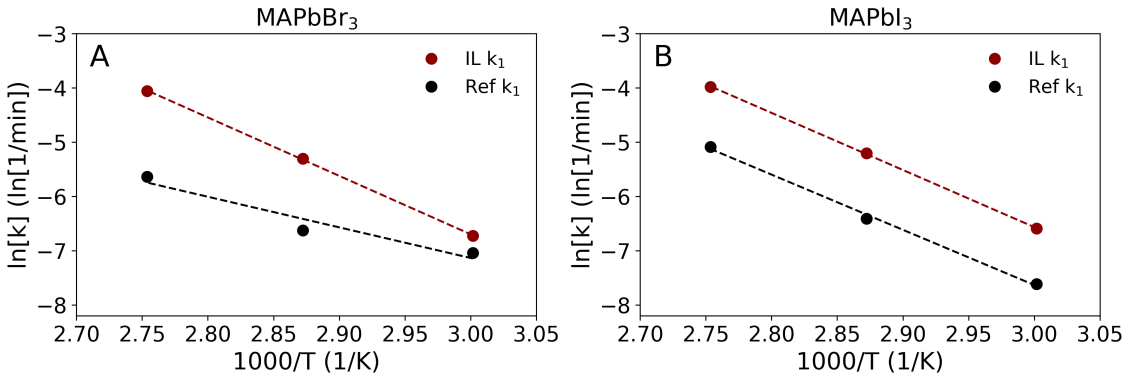

Figure 5.11: Arrhenius plot of decay rates obtained via XRD from phase evolution of $MAPbBr_3$ (A) and $MAPbI_3$ (B) in a physical 1:1 mixture of $MAPbI_3$:$MAPbBr_3$ powder during thermally induced halide mixing with (IL, red) and without $BMIMBF_4$ (Ref, black). The dashed lines mark linear fits to the decay rates to extract activation energies E_a.

When comparing the behaviour of reference samples without added ionic liquid (black) and their counterpart with added ionic liquid (red) Figure 5.11 shows that the extracted decay rates are up to an order-of-magnitude higher if the ionic liquid $BMIMBF_4$ is added during the thermally induced mixing. As identified earlier, the effect is more pronounced for Br^- ions compared to I^- ions. Further, the plot shows that the addition of $BMIMBF_4$ nearly equalizes the decay rates k_1 for Br^- at 60 °C with the reference data set, while for I^- a near-constant increase in k_1 for IL additions is seen for all temperatures. To further quantify the impact of $BMIMBF_4$ the activation energies E_A for halide migration are extracted from the slope of the linear fits within the Arrhenius plot (dashed lines). One can see that the bromide migration is impacted more strongly by the addition of the ionic liquid, which is reflected in the steeper slope for the fast decay rates k_1 of $MAPbBr_3$ compared to the reference. The steeper slope is equivalent to a two-fold increase in activation energies from $E_{A,Br,Ref} = (0.49 \pm 0.13)\,\mathrm{eV\,mol^{-1}}$ to $E_{A,Br,IL} = (0.93 \pm 0.01)\,\mathrm{eV\,mol^{-1}}$. Comparing the extracted iodide migration activation energies $E_{A,I}$ to the bromide migration, the iodide migration seems less affected by the ionic liquid, resulting in nearly unchanged activation energies of $E_{A,I,Ref} = (0.88 \pm 0.04)\,\mathrm{eV\,mol^{-1}}$ and $E_{A,I,IL} = (0.91 \pm 0.01)\,\mathrm{eV\,mol^{-1}}$. From these results two conclusions may be drawn:

I) The observed change of activation energy for bromide migration indicates that $BMIMBF_4$ directly impacts the mechanism of the mixing process, i.e., the nature of bromide diffusion. Presumably between or at grain interfaces, at which $BMIMBF_4$ is known to aggregate.[325, 343]

II) As activation energies $E_{A,I}$ for iodide migration between reference and $BMIMBF_4$-containing samples appear similar within error ranges, the nature of iodide migration is expected to be unchanged. Still, an overall increase in mixing rates is extracted under presence of $BMIMBF_4$, indicating that while the diffusion behaviour is similar, the number of migrating iodide ions has increased. A scenario that leads to an increase in migrating iodide ions is an increase in the ionic defect density in the bulk or at grain interfaces during the thermally induced mixing.

Interestingly, the activation energies of $0.49\,\mathrm{eV\,mol^{-1}}$ to $0.93\,\mathrm{eV\,mol^{-1}}$ for bromide and $0.88\,\mathrm{eV\,mol^{-1}}$ to $0.91\,\mathrm{eV\,mol^{-1}}$ for iodide migration are on average higher than

values found in literature. Considering that these literature values were measured either directly in the thin film samples,[298] by halide ion exchange between two thin films pressed together [302] or from simulations in single crystals,[305] I suspect that the looser contact between the grains in the mechanically packed powder samples increases the average activation barrier compared to thin films with grains grown from solution or vacancy diffusion in a single crystal.

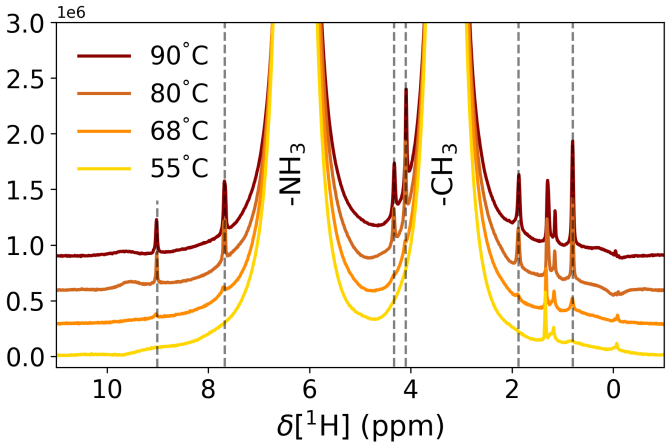

Figure 5.12: ^{1}H NMR spectra of the $BMIMBF_4$ containing physical 1:1 mixture of $MAPbI_3$:$MAPbBr_3$ powder at temperatures between 55 °C to 90 °C. The spectra are shifted in comparison to each other for visibility. The dashed lines mark the evolving resonances of $BMIMBF_4$.

To identify the behavior of $BMIMBF_4$ at elevated temperatures, Helen Grüninger measured the ^{1}H MAS NMR spectra of a $MAPbI_3$:$MAPbBr_3$ mixture with $BMIMBF_4$ at temperatures between 55 °C to 90 °C (Figure 5.12). The ^{1}H MAS NMR spectra are dominated at all temperatures by two resonances related to the ammonium ($-NH_{3+}$) and the methyl group ($-CH_3$) of the methylammonium cation in the perovskite structure at 6.5 ppm and 3.5 ppm, respectively, though elevating the temperature from 55 °C to 90 °C causes narrow resonances to evolve (dashed lines). These ^{1}H resonances are related to the imidazolium cation $BMIM^+$. For temperatures of 55 °C and below, the ionic liquid $BMIMBF_4$ coordinates to the perovskite grain surfaces and retains a solid character,[323] evident by the broad ^{1}H MAS NMR shoulders in the yellow 55 °C curve. At the grain surfaces $BMIMBF_4$ passivates surface defects and trap states,[325] as such hindering ion migration. Above 55 °C the temperature-dependent narrowing of the $BMIMBF_4$-related resonances is attributed to an increase in ionic liquid mobility, which leads to a liquid-like state (averaging of ^{1}H dipolar coupling terms) of $BMIMBF_4$. Consequently, we attribute the acceleration in the thermally induced halide mixing kinetics to the temperature-dependent ionic liquid mobility. As such, the ionic liquid efficiently saturates at low temperatures (e.g. RT) defects at grain boundaries and powder particle surfaces. However, when the temperature is elevated and the mobility of $BMIMBF_4$ increases, the previously saturated defects open up temporarily. It is known that surface defects are a prerequisite for ion exchange and hence facilitate the halide ion diffusion of both iodide and bromide.[303] However, when $BMIMBF_4$ no longer passivates surface defects, the increase in surface defect density does not interfere with the mechanism of the halide ion migration pathway. As a result, the increased surface defect density explains the increased

mixing rates under $BMIMBF_4$ addition, but not the changes in activation energies. Consequently, the twofold increase in activation energies for bromide must be related to another effect. This effect may be related to the bonding strength between the present halide ions and the ions of $BMIMBF_4$. Sanchora et al.[344] showed that in an imidazolium-based ionic liquid containing the super halogen BF_4^-, the imidazolium cation favors hydrogen bonding to halide ions in the order $Cl^- > Br^- > I^-$ instead of the super halogen. For the present $BMIMBF_4$ this preferred bonding to halide ions results in a favored coordination of the $BMIM^+$ cation with the halide ions instead of BF_4^-. Together with the increase in mobility of $BMIM^+$ from ^1H MAS NMR seen earlier this implies that the cation actively shuttles halide ions, as such facilitating halide migration between perovskite grains and across grain boundaries. Furthermore, this explains the more pronounced increase in mixing rates and activation energies for bromide in comparison to iodide with $BMIMBF_4$ addition, since based on Sanchora et al. a stronger interaction of $BMIM^+$ with bromide compared to iodide is expected.

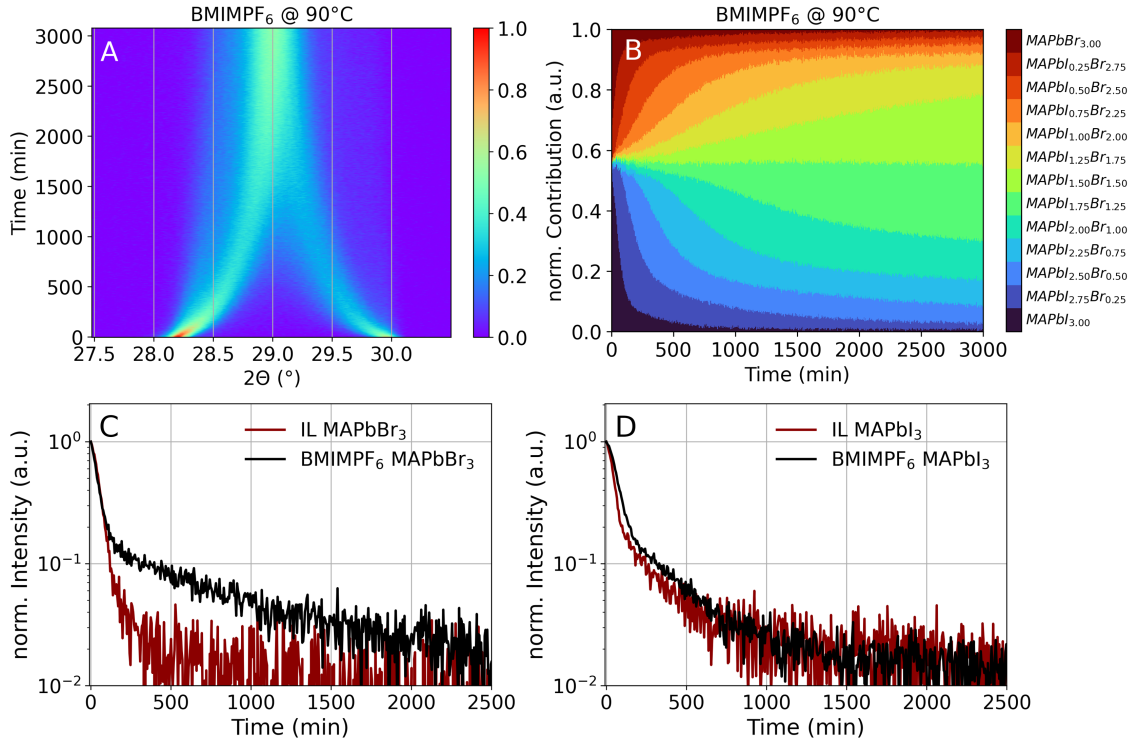

Figure 5.13: (A) Temporal evolution of XRD diffractograms as 2D maps for the cubic (200) $MAPbI_3$ and $MAPbBr_3$ peak positions for 1:1 $MAPbI_3$:$MAPbBr_3$ mixtures with $BMIMPF_6$ for halide mixing at 90 °C. (B) Temporal evolution of normalized halide composition distribution extracted from the halide composition attributed intensities I_i introduced in Eq. 5.2 for the XRD diffractograms in Subfigure A. (C,D) Comparison of the temporal evolution of the normalized intensity attributed to the pure phase of (C) $MAPbBr_3$ and (D) $MAPbI_3$ in mixtures of $MAPbI_3$:$MAPbBr_3$ powders containing $BMIMBF_4$ (IL, red) and $BMIMPF_6$ (black) during thermally induced halide mixing at 90 °C.

To cross-check the proposed mechanism another commonly used imidazolium-based ionic liquid 1-Butyl-3-methylimidazolium hexafluorophosphate($BMIMPF_6$) is added to the parent powders during the synthesis. Parent powders and the respective physical mixtures produced from them are subsequently labeled $BMIMPF_6$. The ionic

liquid $BMIMPF_6$ has a bigger ionic radius of the anion PF_6^- (254 pm) in comparison to the anion BF_4^- (225 pm) in $BMIMBF_4$.[345] Furthermore, while changing the anion the hydrogen bonds between cation and anion are comparable,[346] but in contrast to $BMIMBF_4$, $BMIMPF_6$ is a hydrophobic additive.[347]

By following the same measurements introduced in section 5.1 for the characterization of the parent powders it is ensured that comparable sample morphologies and defect densities are present for the new batch of $BMIMBPF_6$ containing $MAPbI_3$ and $MAPbBr_3$. The results are presented in section 8 in the Appendix in Figure 8.17. From the SEM images in Figure 8.17AB similar powder structures are seen with average pseudoradii of approximately 0.2 µm for $MAPbI_3$ and approximately 0.3 µm for $MAPbBr_3$, equivalent to the IL and Ref parent powders analyzed earlier. From the NQR spectra in Figure 8.17CD the FWHM is extracted as a measure of the defect density. For $MAPbI_3$ a FWHM of 14.0 kHz with a maximum intensity of 5.0e-5 is extracted, and for $MAPbBr_3$ a FWHM of 77.0 kHz and maximum intensity of 1.1e-5. These values are in good agreement with the values presented in section 5.1 indicating that the bulk defect densities in the Ref, IL and $BMIMPF_6$ samples are comparable. Further, PL measurements presented in Figure 8.17EF resulted in Urbach energies for $MAPbI_3$ of $E_U = (14.79 \pm 0.03)$ meV and $E_U = (21.79 \pm 0.08)$ meV for $MAPbBr_3$. For $MAPbI_3$ the extracted Urbach energy is in good agreement with the Ref and IL samples, but a deviation of approximately 0.50 meV is seen for $MAPbBr_3$. This increase in Urbach energy with $BMIMPF_6$ addition might be related to a disorder-induced broadening of the Urbach tail,[328] but in comparison to the disorder-related increases in mixed halide solid solutions resulting in Urbach energies above 90 meV this increase seems negligible.[348] Further, the XRD diffractogram of the 1:1 physical mixture of $BMIMPF_6$-containing parent powders shown in Figure 8.17G have identical peak positions to the IL and Ref containing mixtures presented in Figure 5.4 with no appearance of degradation products related to PbI_2 at 12° and its higher orders.[327] Therefore I conclude that the crystalline morphology and phase purity (in regard to degradation products) between Ref, IL and $BMIMPF_6$ $MAPbI_3$ and $MAPbBr_3$ parent powders are comparable.

After characterization of the $BMIMPF_6$ parent powders and the prepared physical mixtures the thermally induced halide mixing experiments at 90 °C and the in section 5.3 presented analysis approach are repeated. Figure 5.13A shows the temporal evolution of XRD diffractograms as a 2D map. The presented 2D heat map shows a form comparable to the 2D heat map seen for IL containing samples in Figure 5.7, which resulted in fully mixed halide solid solutions. But in the case of $BMIMPF_6$, a broader streak around 29.0° is seen, indicating that a broader distribution of solid solutions is present after equivalent mixing times. The differences in final solid solutions become clearer when comparing the extracted contributions of various solid solutions. The $BMIMPF_6$-containing physical mixture is dominated by a composition mainly consisting of $MAPbI_{1.5}Br_{1.5}$ and $MAPbI_{1.75}Br_{1.25}$ with a tail to I-rich mixed halide compositions after 3000 min. In contrast, Figure 5.8B depicts that for the IL-containing mixture a fully mixed composition of $MAPbI_{1.5}Br_{1.5}$ dominates after 3000 min, with equally distributed amounts of $MAPbI_{1.25}Br_{1.75}$ and $MAPbI_{1.75}Br_{1.25}$. Still, after 3000 min of thermally induced halide mixing both mixtures containing imidazolium-based ionic liquids show significantly stronger halide mixing in comparison to the reference sample presented in Figure 5.7A and Figure 5.8A. The accelerated halide mixing kinetics with $BMIMPF_6$ addition are

further evident from the extracted normalized intensity decays of pure $MAPbBr_3$ and $MAPbI_3$ perovskite phases presented in Figure 5.13CD. The plot in 5.13C shows the intensity decays attributed to $MAPbBr_3$ phase, indicating that while initially both samples decay equally, that after approximately 200 min the Br^- migration seems to be hindered for $BMIMPF_6$. The emerging slope is less steep compared to the IL containing mixture. In contrast, for the decay of the intensity attributed to $MAPbI_3$ phase both imidazolium containing mixtures decay almost equally, if compared to the reference case presented in Figure 5.9.

That for both imidazolium-based ionic liquids accelerated kinetics are observed in comparison to physical mixtures without additives, is indicative of a more general behaviour. I therefore conclude that the addition of imidazolim based ionic liquids, such as $BMIMBF_4$ and $BMIMPF_6$, which are known to be intrinsic ion conductors,[349, 350] accelerate halide migration rates. In combination with a preferred interaction between the imidazolium based cation and Br^- anions,[344] the increase in bromide migration is more pronounced compared to the increase in iodide migration. As the slowest migration rate determines the overall halide mixing rate, accelerated overall mixing is observed in the presence of imidazolium-based ionic liquids.

After investigating the origin of accelerated halide mixing kinetics in this section by analyzing the activation energies for halide migration, by temperature resolved ^1H NMR and by comparative thermally induced mixing experiments with another imidazolium based ionic liquid, the subsequent section is focused on discussing and unifying the previously measured results into a coherent scheme of the mixing process.

5.5 Summary and Discussion

Combining the previously discussed results into a coherent picture, we obtain the following mechanism for halide ion migration under the influence of $BMIMBF_4$: At elevated temperatures the ionic liquid mobility is enhanced, opening up defect-rich areas at grain boundaries and forming a liquid-like transfer channel of $BMIMBF_4$, in which the $BMIM^+$ cation acts as a 'shuttle'. Both the increased surface defect density and the liquid-like transfer channel result in an increased transport of halide ions to neighboring grains and in boosted mixing rates compared to samples without $BMIMBF_4$. Comparable shuttle mechanisms have already been observed for imidazolium-based ILs used as electrolytes in batteries. In these battery systems the IL anions are reported to form complexes with Li^+, transporting Li^+ cations between electrodes.[351] To illustrate the postulated mechanism, Figure 5.14 shows a sketch of how $BMIMBF_4$ enhances the halide migration between neighboring grains of $MAPbBr_3$ and $MAPbI_3$.

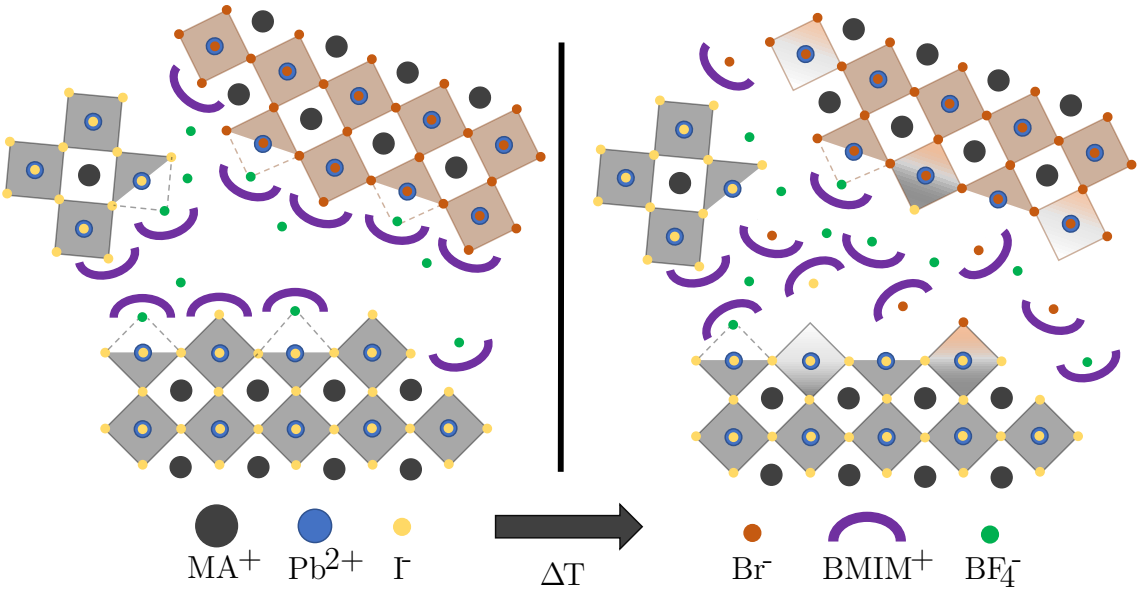

Figure 5.14: Scheme of proposed mechanism of enhanced ion exchange during thermally induced halide mixing, showing the formation of mixed halide perovskite solid solutions. At low temperatures $BMIMBF_4$ retains a solid character at grain boundaries of $MAPbI_3$ and $MAPbBr_3$ and passivates trap states (left). At elevated temperatures the ionic liquid shows increased mobility, while coordinating with I^- and Br^- ions, resulting in accelerated halide mixing kinetics (right). The coordination of $BMIM^+$ with Br^- is favoured in comparison to I^-, which leads to a stronger acceleration of bromide transport in comparison to iodide transport.[344]

However, the deducted effect of $BMIMBF_4$ and $BMIMPF_6$ of enhanced mixing kinetics appears to be in contrast to the literature focused on light-induced phase separation in mixed halide perovskites, in which $BMIMBF_4$ is described to enhance the thermal stability in mixed and single halide perovskite thin film solar cells under illumination, as well as to inhibit halide ion migration in single halide perovskite powder thick films.[322, 323, 352] But in contrast to the aforementioned literature, the presented measurements within this chapter elucidate only the effects of $BMIMBF_4$ on thermally induced halide mixing in the dark without further segregation processes ob-

served under electrical bias[35, 301] or under light irradiation.[127, 296, 297] Furthermore, the results presented here show that the addition of ionic liquids (here $BMIMBF_4$), which are well-known for their high volatility and intrinsic ionic conductivity[349, 350] increases the halide mobility in hybrid perovskites. But this increase in halide mobility does not appear to lead to enhanced halide segregation in mixed halide-perovskite systems under light irradiation at elevated temperatures. On the contrary, literature reports show that the increase in halide mobility seems to enhance the thermal stability.[325] Therefore, I hypothesize that by enhancing the thermally induced halide migration rate, which is more pronounced for bromide as seen from Figure 5.11A, the addition of $BMIMBF_4$ leads to an increase in the total halide mixing rate, which is limited by the slowest halide migration rate. As a consequence, the light-induced demixing rates in excited perovskite domains and the $BMIMBF_4$ enhanced remixing rates in dark domains may equalize, resulting in phase stability of the mixed halide phase. In addition, a mismatch in phase separation and remixing rates is a prerequisite in many models describing halide segregation under light-irradiation.[131, 296, 353, 354] For matching phase separation and remixing rates such models achieve phase stability under light-irradiation. Thus, volatile ionic conductors, such as the ionic liquid $BMIMBF_4$, might be an option to prevent light-induced halide segregation if suitable equilibrium conditions between halide mixing and demixing rates are identified and similar migration rates for the involved halide species are reached. This may be a step to advance the stability of mixed halide perovskite systems, necessary for next-generation tandem solar cells.[294, 295]

In summary, the application of in-situ XRD measurements in combination with ^{1}H NMR spectroscopy allowed me to explore the formation of solid solutions from 1:1 physical mixtures of $MAPbI_3$ and $MAPbBr_3$ with and without addition of the imidazolium-based ionic liquid $BMIMBF_4$. The addition resulted in accelerated halide mixing kinetics, with a preferential increase in bromide kinetics. The results highlight that materials that are reported to hinder ion migration during light-induced phase separation can instead enhance it during the reversed mixing process. Thus, the reported results on the origin of enhanced ion migration may be an important step towards improving the understanding of the underlying stability mechanism of mixed halide perovskites under light irradiation, necessary for further applications in next-generation tandem solar cells.

6 Quantifying Dynamics in Thin Films by GI-XPCS

As shown in the previous chapters a variety of in-situ methods are available to determine the structural and opto-electronic evolution in thin films of lead halide perovskites. But to extract the dynamics in the final or evolving thin films direct methods to measure dynamic phenomena, such as ageing and degradation processes or ionic transport, are scarce. Coherent scattering techniques are the method of choice to directly access these dynamics and their underlying mechanisms. These coherent scattering techniques are directly sensitive to changes of the electron densities in the illuminated coherent volume and thus to e.g. ionic transport and chemical changes during degradation processes. One of these coherent techniques is X-ray photon correlation spectroscopy (XPCS). Applied in transmission geometry it is e.g. used to determine equilibrium and non-equilibrium dynamics in colloidal systems such as gels[248] and suspensions[355], as well as polymeric glass formers.[194] To apply XPCS to thin films the measurements must be carried out in grazing incidence (GI) geometry, allowing the probing of three-dimensional dynamic morphologies in thin films[356] as well as measurements in liquids.[357] In GI geometry the usage of a shallow incident angle leads to an extended beam projection on to the thin film, resulting in enhanced scattered intensity compared to transmission measurements on thin films.[358] In various publications GI-XPCS was used to measure dynamics of thin soft matter systems, such as capillary waves on surfaces and at interfaces or growth mechanisms on various surfaces.[49, 188, 195, 196, 359] These examples choose measurement conditions in which only surface scattering had to be considered, e.g. via the generation of a predominantly reflected signal.[195, 196, 359, 360] However, many questions in thin film science, and especially in thin films of lead halide perovskites, arise due to dynamic processes originating within the bulk of the thin film. These processes can be additionally influenced by the interfaces towards the substrate and their surroundings, resulting in complex dynamics. To examine dynamics arising from the bulk of the film, several different scattering terms, including scattering from reflections, need to be taken into account. These extra scattering terms make the interpretation of GI data in the context of XPCS challenging. Zhang et al.[49] showed that effects known from grazing incidence small angle X-ray scattering (GI-SAXS) need to be accounted for in a GI-XPCS analysis focused on bulk properties. But a thorough approach to quantify these effects in GI-XPCS analysis has not been presented yet.

Hence, as a next step in this thesis an approach to apply GI-XPCS for bulk dynamic measurements is developed. The approach is exemplified for $MAPbI_3$ thin films. To this end, a tool is being developed to measure the intrinsic dynamics that determine the functionality and stability of such thin films. Importantly, this method is not limited to surface-sensitive geometries or kinetic measurements, but can access dynamic phenomena within the bulk of thin films.

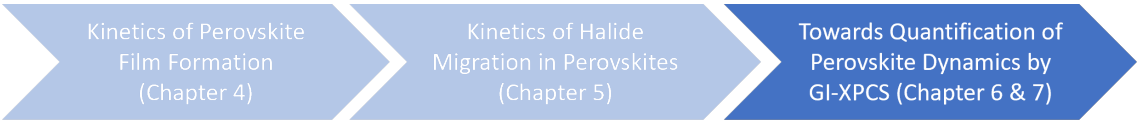

Figure 6.1: Schematic overview of thesis showing the topic of the following chapter: Chapter 6 describes an approach on how to quantify dynamics in the bulk of a lead halide perovskite thin film by GI-XPCS, without including geometrically induced distortions to the extracted dynamics. The approach to identify suitable measurement conditions is exemplified for a one-step processed $MAPbI_3$ thin film.

The present chapter is based on my publication "Effects of the Grazing Incidence Geometry on X-ray Photon Correlation Spectroscopy Measurements", Langmuir, 2023, 39, 23, 8215–8223.[361] In this publication I address the unresolved problem of geometry-related distortions in bulk-sensitive GI-XPCS measurements by combining theoretic calculations on the influence of refractive effects and reflective scattering contributions for a $MAPbI_3$ thin film during a GI-XPCS measurement. The results from the theoretic calculations allow me to identify regions with less distortions within the reciprocal space. To verify my theoretic predictions I take distortion-reduced grazing incidence transmission (GT)-XPCS measurements and compare these with simultaneously measured distorted GI-XPCS measurements. From the comparison of GT-XPCS and GI-XPCS measurements, regions in reciprocal space are identified, which are expected to minimize the GI geometry-related deviations in XPCS. These identified reciprocal space regions are in accordance with my theoretic predictions. My calculations are further used to provide an outlook how various thin film thicknesses, material compositions and experimental parameters can influence the relevant reciprocal space.

The chapter starts with Section 6.1 focusing on the necessary calculations to understand the underlying effects of refraction and reflection in GI and GT geometries for SAXS. Section 6.2 applies the calculation-based considerations to an experiment which is designed to allow the comparison of simultaneous XPCS measurements in GT and GI geometry. The simultaneous approach in measuring XPCS ensures that the same dynamics are measured, but with varying distortions within the detector regions used to capture the experiment. Section 6.3 further discusses additional effects altering extracted dynamics from GI-XPCS measurements and includes these with the earlier results to identify which detector regions and therefore q spaces are scarcely enough influenced by geometry-introduced distortions. The subsequent Section 6.4 applies the derived results to give an outlook, how different materials, film thicknesses and X-ray beam energies influence the identified reciprocal space. The chapter concludes in Section 6.5 with a summary of the results and a short discussion for the general application of bulk-sensitive GI-XPCS.

6.1 Geometrical Effects in bulk-sensitive GI and GT-SAXS Measurements for $MAPbI_3$ Thin Films

As introduced within Section 2.3 the scattering within both GT and GI geometry is well described within the simplified DWBA. But differences occur regarding which first and second-order perturbation terms of scattering-reflection sequences need to be accounted for. In this section an approach on quantifying dominant scattering contributions along the surface-normal scattering direction (q_z) in GT and GI geometry is introduced. The approach focuses on the calculations of two distinct phenomena: I) the non-linear directional change of scattering due to refraction of impinging X-rays and exiting X-ray scattering at interfaces; II) Fresnel coefficient calculations, to identify the strength of scattering signals associated with scattering terms covered within the simplified DWBA. Both calculations are done for a two-slab system of a $MAPbI_3$ thin film placed on silicon.

6.1.1 Influence of Refraction in GT and GI in $MAPbI_3$ Thin Films

When conducting experiments within GT or GI geometry, the intensity distribution on the detector is altered by refraction taking place at interfaces. Although the changes in the refractive index n are small for high energy X-rays when changing from ambient atmosphere to a material ($\Delta n \approx 10^{-6}$),[147] for the low incident angles used for GI-SAXS experiments a significant shift of the scattering signal on the detector is seen. Compared to a transmission SAXS experiment the refraction will shift the position on which scattering from the impinging X-ray beam will reach the detector. This shift due to refraction depends on the ratio between the critical angle of the impinged material and the exit angles of the scattering. Consequently, scattering from various exit angles may reach the same detector pixel. This projection of scattering into the same pixel is equivalent to mixing of scattering from different distinct intrinsic Q values into the same detector q value.

As shown by Liu et al.[161] the difference between intrinsic Q and detector q (defined in Section 2.3) is highly non-linear near the critical angle Θ_c of the thin film for the GI and GT geometry. Importantly, in the small angle scattering regime, the refraction only affects the z-direction and will not alter the shift in the scattering signal on the detector along the horizontal q_r-component. To calculate the shift due to refraction, which reduces the incident angle at the atmosphere/thin film interface, the following cosine form of Snell's law as a function of the critical angle Θ_c of the thin film can be used: $\cos(\alpha_i) = \frac{\cos(\Theta_i)}{\cos(\Theta_c)}$. The nomenclature corresponds to the one introduced in Figure 2.7 in the theoretic introduction, with angles $\Theta_{i/f}$ being external incident and exit angles and $\alpha_{i/f}$ being intrinsic ones, respectively.
Further, refraction needs to be considered when scattered electromagnetic waves travel across the thin film/substrate interface. The second refraction follows the same form of Snell's law but using the critical angle Θ_{Si} of the substrate.

To illustrate the non-linear contribution of refraction[161, 172] to the projection of scattering onto the detector, I calculate the difference between intrinsic Q and detector q as $\Delta q_z = q_z - Q_z$. Hereby Q_z will be calculated using the cosine form of Snell's law for the classical definition of Q_z as introduced above. Four different cases need to be distinguished.

These four cases depend on whether the considered scattering terms of the DWBA depend on Q_{z1} or Q_{z2}, referred to as transmission channel (Tc), respectively reflection channel (Rc) scattering, and in which scattering geometry the scattering experiment takes place, as the measurement geometry influences the number of refraction events. Consequently, the subsequent cases of are distinguished:

I) scattering from the transmission channel Tc in the GT geometry, addressing scattering without reflection events (proportional to the scattering term $|T(\alpha_i)T(\alpha_f)|^2$ $|F(+Q_{z1})|^2$ in the sDWBA, see Section 2.3).
II) scattering from the reflection channel (Rc) in the GT geometry, addressing scattering with a single reflection event (proportional to the scattering term $|R(\alpha_i)T(\alpha_f)|^2$ $|F(+Q_{z2})|^2$ in the sDWBA, see Section 2.3).
III) scattering from the transmission channel (Tc) in the GI geometry, addressing scattering without reflection events or double reflections (proportional to the scattering terms $|T(\alpha_i)T(\alpha_f)|^2|F(+Q_{z1})|^2$ and $|R(\alpha_i)R(\alpha_f)|^2|F(-Q_{z1})|^2$ in the sDWBA, see Section 2.3).
IV) scattering from the reflection channel (Rc) in the GI geometry, addressing scattering with a single reflection event (proportional to the scattering terms $|R(\alpha_i)T(\alpha_f)|^2|F(+Q_{z2})|^2$ and $|T(\alpha_i)R(\alpha_f)|^2|F(-Q_{z2})|^2$ in the sDWBA, see Section 2.3).

Based on the work by Liu et al. 2018[161] and the definitions for detector q and intrinsic Q given in Section 2.3 I can calculate the intrinsic Q_z in terms of external scattering angles and therefore the difference between detector and intrinsic reciprocal space Δq_z. With Snell's law the intrinsic Q_z for the four cases discussed above are:

$$Q_{z,GT,Tc} = k\left(+(\sin^2\Theta_i - \sin^2\Theta_c)^{\frac{1}{2}} - (\sin^2\Theta_f + \sin^2\Theta_{Si} - \sin^2\Theta_c)^{\frac{1}{2}}\right) \quad (6.1a)$$

$$Q_{z,GT,Rc} = k\left(-(\sin^2\Theta_i - \sin^2\Theta_c)^{\frac{1}{2}} + (\sin^2\Theta_f + \sin^2\Theta_{Si} - \sin^2\Theta_c)^{\frac{1}{2}}\right) \quad (6.1b)$$

$$Q_{z,GI,Tc} = k\left(+(\sin^2\Theta_i - \sin^2\Theta_c)^{\frac{1}{2}} + (\sin^2\Theta_f - \sin^2\Theta_c)^{\frac{1}{2}}\right) \quad (6.1c)$$

$$Q_{z,GI,Rc} = k\left(-(\sin^2\Theta_i - \sin^2\Theta_c)^{\frac{1}{2}} + (\sin^2\Theta_f - \sin^2\Theta_c)^{\frac{1}{2}}\right) \quad (6.1d)$$

Depending on these four expressions Figure 6.2 shows a graph of Δq_z as a function of detector q_z for incident angles of $\Theta_i = 0.22°$ (brown lines) and $0.30°$ (blue lines) for the transmission channel Tc (full lines) and reflection channel Rc (dashed lines). The critical angles $\Theta_c = 0.163°$ and $\Theta_{Si} = 0.186°$ used in Eq. (6.1) are calculated from the real part of refraction index n, which is determined by Henke et al.[147] for an X-ray beam energy of 9.65 keV.

Following the curve drawn as a full brown line ($\Theta_i = 0.22°, Tc$) from negative up to positive detector q_z regions (from the GT to the GI regions), first Δq_z increases, followed by an undefined region, followed by a decrease with a subsequent constant value being reached. The lower limit of the undefined region is connected to the substrates critical angle Θ_{Si}, determining the minimal angle under which scattering can exit through the substrate. The upper limit of the undefined region is connected to scattering below the materials critical angle Θ_c, scattering not outcoupling from the material below this angle. Around both limits of the undefined region Δq_z appears non-linear, showing strong increases. Comparing the observations for an incident angle of $\Theta_i = 0.22°, Tc$ (full brown line) to the larger incident angle of

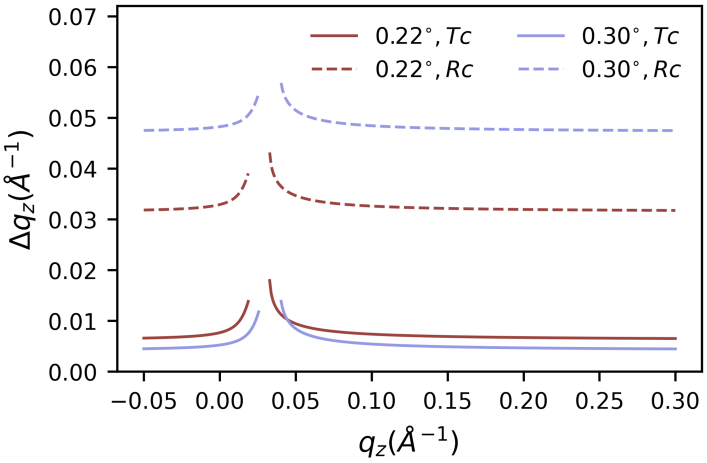

Figure 6.2: The graph shows the difference between detector q_z and intrinsic Q_z ($\Delta q_z = q_z - Q_z$) originating from the refraction at interfaces as a function of detector q_z for incident angles of $\Theta_i = 0.22°$ (brown lines) and $\Theta_i = 0.30°$ (blue lines). Reciprocal q_z values from the transmission channel (Tc, solid) and reflection channel (Rc, dashed) are calculated separately, following Equations 6.1.

$\Theta_i = 0.30°, Tc$ (full blue line) an overall decrease in Δq_z is observed, while the undefined q_z region is shifted to larger q_z values. The shift is related to the larger angle of incidence according to Eq. 2.12. Comparing the calculations of Δq_z for the transmission channel Tc (full lines) to the reflection channel Rc (dashed lines) the overall shape is retained, but a shift to higher Δq_z values is visible, with a higher shift in Δq_z for a higher angle of incidence. This split between Tc and Rc is often seen in monodisperse scattering patterns by splitting distinct scattering features in two.[362] This channel split is known to scale with $2\Theta_i$.[362]

Interpreting the observations from Figure 6.2 it can be seen that regions of non-linear trends for Δq_z exist. For a real XPCS experiment in which the intensity in a Region-of-Interest (ROI) is analyzed this will lead to a mixture of scattering of different intrinsic Q, which originate from the transmission and reflection channel which probe different intrinsic Q respectively. These different intrinsic Q and their length scales may result in different correlation times, which will be present in a single ROI. When analyzing such contribution mixing, the correlation function shape will be altered in comparison to an experiment in which only a single scattering channel is present, such as in a transmission XPCS experiment.

I already identified detector regions in which the impact of refraction is pronounced and non-linear, but want to investigate further how Q_z behaves in the transmission channel Tc and reflection channel Rc. Therefore, I calculated (with focus on the GI region) the absolute of intrinsic Q_z against detector q_z for both Tc and Rc for incident angles of $\Theta_i = 0.22°$ and $\Theta_i = 0.30°$. The result is depicted in Figure 6.3. The plot shows the absolute of the intrinsic Q_z as a function of detector q_z for Tc (full lines) and Rc (dashed lines). Calculations for an incident angle of $\Theta_i = 0.22°$ are shown in brown, for an incident angle of $\Theta_i = 0.30°$ in blue. The black dotted lines at $|Q_z| = 0$ mark the minimal values of $|Q_z|$ and their affiliated detector q_z positions.

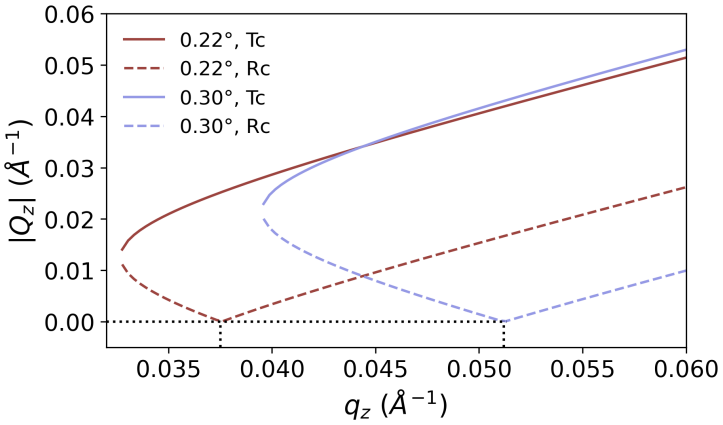

Figure 6.3: Plot of the absolute $|Q_z|$ against q_z for the transmission channel Tc (full lines) and reflection channel Rc (dashed lines) within the GI region above the respective Yoneda positions for incident angles of $\Theta_i = 0.22°$ (brown lines) and $\Theta_i = 0.30°$ (blue lines). The black dotted vertical lines mark the reversal point of decrease in absolute $|Q_z|$ to increase in absolute $|Q_z|$, which coincidences with the respective specular q_z positions for incident angles Θ_i of 0.22° and 0.30°.

From the plot it can be observed that for both incident angles $|Q_z|$ is increasing continuously as a function of q_z in the transmission channel Tc, while for the reflection channel Rc a reduction down to $|Q_z| = 0$ is seen with q_z, followed by an increase in $|Q_z|$ for higher q_z. The minimum values of $|Q_z| = 0$ are reached for the respective expected specular beam positions in q_z. According to Zhang et al. 2019[49] these competing trends of intrinsic $|Q_z|$ between the Yoneda region and the specular beam position can be used to analyze the scaling behaviour of the characteristic decay time τ_0 as a function of q (see Eq. 2.21) in GI-XPCS experiments. They propose to analyze τ_0 as a function of q_r in flat regions of τ_0 as a function of q_z, because in these regions the full dynamics of τ_0 are governed solely by q_r. The reason for this simplified analysis along q_r is that such a mixing of correlation curves associated with countervailing $|Q_z|$ along q_z occurs, that the extracted τ_0 stays constant. They applied their approach to measure the viscosity of confined Polyethyleneglycol in pores via Marker-XPCS of gold nanoparticles. While measurements of this system showed scaling of τ_0 as a function of q attributed to classical diffusion ($\langle r^2 \rangle \propto t$) of the gold nanoparticles for GT-XPCS measurements, the scaling behaviour was in contrast reduced in GI-XPCS measurements, despite extracting the scaling in flat regions of τ_0 as a function of q_z. They further mention that in comparison to the GT-XPCS correlation curves the calculated GI-XPCS correlation curves are best described with a stretched exponential function, while a single exponential is sufficient to extract correlation times from GT-XPCS experiments.

Due to these still existing systematic differences between dynamics in GI and GT, despite the approach of Zhang et al., I propose another necessary consideration to identify valid detector q_z regions with less distorted correlation curves in GI. I propose that also the dominance of the respective scattering channels (Tc and Rc) need consideration. To identify how the amount of scattering from the transmission and reflection channel changes as a function of q_z their respective Fresnel coefficients within the DWBA will be analyzed in the next subsection.

6.1.2 Fresnel Calculations for Reflectivities and Transmissivities in $MAPbI_3$ Thin Films

To describe the intensity distribution on a detector the simplified DWBA was introduced in Section 2.3 (Eq. 2.14) and reasons were given why the simplified DWBA is a good approximation to describe Methylammonium Lead Iodide thin films with its disperse grain size distribution. As shown, the simplified DWBA approximates the intensity I_d at the detector for a particular q_z with the following sum of four terms:

$$\begin{aligned} I_d(q_z) =& |T(\alpha_i)T(\alpha_f)|^2|F(+Q_{z1})|^2 + |T(\alpha_i)R(\alpha_f)|^2|F(-Q_{z2})|^2 + \\ & |R(\alpha_i)T(\alpha_f)|^2|F(+Q_{z2})|^2 + |R(\alpha_i)R(\alpha_f)|^2|F(-Q_{z1})|^2 \end{aligned} \tag{6.2}$$

Herein $Q_{\pm z1}$ and $Q_{\pm z2}$ follows the definition of the intrinsic Q space given in Section 2.3. The terms $T(\alpha_i)$ & $T(\alpha_f)$ and $R(\alpha_i)$ & $R(\alpha_f)$ are the Fresnel transmissivities and Fresnel reflectivities, depending on the incident angles α_i and exit angles α_f. Due to their dependence on the incident and exit angles the Fresnel coefficients are varying as a function of q_z. Furthermore, I_d depends on the the form factor scattering contribution $F(Q)$ at different $\pm Q_{z1}$ and $\pm Q_{z2}$. For a polydisperse system, such as Methylammonium Lead Iodide grains in a thin film with a wide distribution of sizes and forms, the form factor terms are known to decay steadily. Also, such polydisperse systems do not show any distinct features or oscillations along $Q_{z1/2}$ and are known to not decay as fast as simple form factors (e.g. spheres: $F(Q) \propto Q^{-4}$), but decay significantly slower.[363] Therefore, the Fresnel coefficients are a good approximation to quantify the intensity from each simplified DWBA term on the detector for a polydisperse system of Methylammonium Lead Iodide grains.

To calculate the Fresnel coefficients the multilayer matrix formalism approach based on Rauscher et al.[164] and Renaud et al.[364] is used, which is considered the standard method for thin films showing only weak contrast within the thin film. For material systems, which cannot be approximated with the uniform-film approximation used here, other methods need to be considered, such as DWBA variants including multi-layered or graded profiles for thin films.[163, 364] These are for example applied to describe embedded nanostructures in thin films or to describe nanoparticles distributed in an island-like fashion.[163]

In the approach by Rauscher et al.[164] and Renaud et al.[364] the coefficients are calculated for a layered system, in which the influence of a single interface to the impinging wave vector k_0 is considered. From the resulting z-components of the impinging wave vector, single layer reflectivities and transmissivities are deduced. To include the influence of underlying layers, phase interference dependent on layer heights and interface roughness is added to the Fresnel calculations. I implemented this approach to calculate the Fresnel coefficients of a two slab system of Methylammonium Lead Iodide with an incident X-ray energy of 9.65 keV (800 nm height, 10 nm, roughness, $\Theta_c = 0.163°$) on a flat silicon substrate ($\Theta_c = 0.186°$) with an incident angle of $\Theta_i = 0.22°$ and $\Theta_i = 0.30°$. To determine the resulting dominant scattering contribution of the simplified DWBA, I weighted the prefactors of the resulting four DWBA terms against each other and plotted the results against detector q_z for an incident angle 0.22° and an incident angle $\Theta_i = 0.30°$. The result is shown in Figure 6.4 for a q_z range of $-0.005\,\text{Å}^{-1}$ to $0.061\,\text{Å}^{-1}$.

The graph shows the GTSAXS region around $q_z = 0$ below the empty gap. The empty gap arises from inaccessible scattering regions resulting from total reflection of scattering below the substrates critical angle (lower q_z limit) and the sample horizon (higher q_z limit) (see also Figure 2.7 in Section 2.3). For GTSAXS only the two DWBA terms dependent on $|T(\alpha_i)T(\alpha_f)|^2$ and $|R(\alpha_i)T(\alpha_f)|^2$ are present, with the prefactor $|T(\alpha_i)T(\alpha_f)|^2$ becoming more dominant with increasing incident angle. The prefactor $|T(\alpha_i)T(\alpha_f)|^2$ is related to direct scattering described within the Born Approximation (BA),[365] which is used to describe scattering in a transmission geometry. Consequently, with larger incident angles (here: $\Theta_i = 0.30°$) the intensity on the detector approaches the same origin as in a transmission geometry, indicating that GT-XPCS signal will have the same origin as in transmission XPCS for an increased incident angle. This does not hold true for small incident angles, like $\Theta_i = 0.22°$, where the reflection term related to $|R(\alpha_i)T(\alpha_f)|^2$ still contributes in the GT detector region. In contrast, the GISAXS detector region is seen above the empty gap and shows that above the sample horizon and below the Yoneda region[148] (orange line) scattering is dominated by DWBA prefactors $|T(\alpha_i)T(\alpha_f)|^2$ and $|T(\alpha_i)R(\alpha_f)|^2$. Within the Yoneda region all terms are present, but above this region the contribution of the term $|T(\alpha_i)R(\alpha_f)|^2$ is reduced with increasing q_z. For the material system tested here and for q_z values of $0.045\,\text{Å}^{-1}$ for $\Theta_i = 0.22°$ and $0.055\,\text{Å}^{-1}$ for $\Theta_i = 0.30°$, the contributions related to $|R(\alpha_i)R(\alpha_f)|^2$ and $|R(\alpha_i)T(\alpha_f)|^2$ vanish. The weights of the prefactors return their incident angle dependent GTSAXS equivalents, with the BA term (with prefactor $|T(\alpha_i)T(\alpha_f)|^2$) becoming dominant for larger incident angles like $\Theta_i = 0.30°$. This meets the expectation by Lazzari et al.[163] that for high incident and exit angles the BA prefactor becomes dominant in GI geometry.

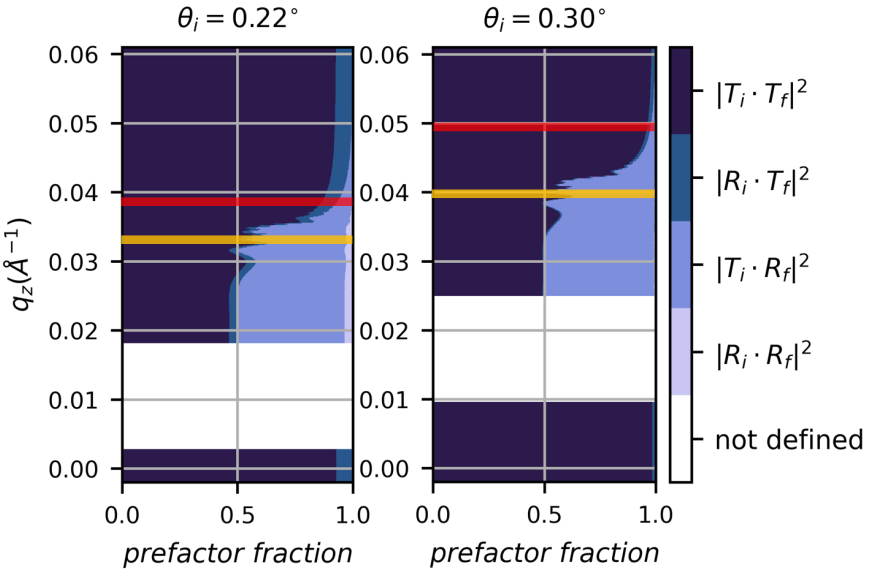

Figure 6.4: Plot of the normalized prefactor fraction of Fresnel coefficients used for intensity calculations in the simplified DWBA for the incident angles $\Theta_i = 0.22°$ ($\Theta_i/\Theta_c = 1.35$) and $\Theta_i = 0.30°$ ($\Theta_i/\Theta_c = 1.84$) as a function of q_z. The reflectivities and transmissivities are calculated for a two-slab system of 800 nm thick $MAPbI_3$ placed on a silicon substrate with varying exit angles Θ_f. The Yoneda and specular positions are marked in orange (Yoneda) and red (specular), respectively.

Combining the information from DWBA prefactors (reflection effects, Figure 6.4) and from nonlinear reciprocal space vector projection (refraction effects, Figure 6.2) allows me to conclude the following points for a comparison of transmission XPCS and XPCS results in grazing incidence geometries.

Firstly: Figure 6.4 shows that for large incident angles ($\Theta_i = 0.30°$) the scattering in the GT region and high q_z GI region is dominated by the BA term and hence approaches the dominant scattering terms of transmission XPCS. While for smaller incident angles scattering contributions from both transmission Tc and reflection channels Rc are mixed on the detector, possibly influencing the shapes of extracted correlation functions. The dominance of BA related scattering does not imply that e.g. correlation times are identical, because on the one hand the absolute q value given by $q = \sqrt{q_r^2 + q_z^2}$ generally differs in GTSAXS where $q_z = 0$ and GISAXS where $q_z > 0$. On the other hand even if the absolute q values for GTSAXS and GISAXS are the same, the origin in reciprocal space is different, as the respective q_z and q_r values differ. As such different dynamics may be probed. The same correlation times are only expected for isotropic dynamics at the same q value, even if the respective q_z and q_r values differ. However, I theorize that for a heterogenuous system with no dominating characteristic length scales, no changes to the nature of the underlying dynamics over the combined q ranges are to be expected. As a result, the dynamics are isotropic and the scaling behavior of correlation times τ as a function of q will be comparable for GT- and GI-XPCS.

Secondly: Figure 6.2 shows that refraction alters the projection of intrinsic Q onto the detector. For higher incident angles the discrepancy between intrinsic Q and detector q is globally reduced for Tc but will still lead to the examination of a different intrinsic Q in transmission XPCS than in GT- and GI-XPCS and to associated changes in the correlation functions when compared to the same detector q in a transmission XPCS experiment. Calculating the influence of refraction allows us to conclude, which detector q values in transmission XPCS and GT-and GI-XPCS are comparable. For the calculated q_z in GI up to $0.06\,\text{Å}^{-1}$ the difference in Δq_z is not yet minimized or as low as in GT-XPCS measured at $q_z = 0$. For q_z below $0.06\,\text{Å}^{-1}$ and when Tc and Rc channels contribute to the detected signal, different intrinsic Q_z values contribute to the recorded intensity within an analyzed ROI in GI-XPCS, influencing the shape of an extracted One-Time correlation function (1TCF) in comparison to GT-XPCS and resulting in expected differences in parameters like exponents and correlation times. This contribution mixing can only be suppressed if solely one of the scattering channels Tc or Rc is contributing.

6.2 Simultaneous GT-GI-XPCS Measurements on $MAPbI_3$ Thin Films

To test the theoretic considerations on the origin of detected intensities and their impact on measured dynamics in GT- and GI-XPCS shown in chapter 6.1 simultaneous GI-GT-XPCS measurements on a $MAPbI_3$ thin film were conducted at the Coherent Hard X-ray (CHX) scattering beamline at NSLS-II, NY (see Section 3.1.2 for the measurement procedure and Section 3.2 for sample preparation).

In order to quantify the expected influence of reflections and refraction, the change in the extracted dynamics is first calculated as a function of q_z. To extract dynamics along q_z the ROIs shown in Figure 8.18BD in the Appendix are used. I applied a single quadratic ROI size of $0.003\,\text{Å}^{-1}$ in the GT region, starting at $q_z = -0.0015\,\text{Å}^{-1}$ and $q_r = 0.0035\,\text{Å}^{-1}$ to catch the unperturbed GT dynamics at $q_z = 0$. For the GI scattering the same ROI size and starting q_r is chosen as for GT, but with a starting $q_z = 0.018\,\text{Å}^{-1}$ for measurements under an angle of incidence of $\Theta_i = 0.22°$ and $q_z = 0.027\,\text{Å}^{-1}$ for measurements under $\Theta_i = 0.30°$. The starting q_r used is necessary to avoid signals from the direct beam within the chosen ROIs, which could result in mixing of homodyne and heterodyne detection schemes.[360] Such detection scheme mixing due to mixing of direct beam intensities and scattered intensities within the same ROI is known to lead to altered forms of the calculated correlation functions. To avoid a detection scheme mixing I calculate the upper limit of where to expect this phenomenon to occur, based on the work of Gutt et al.[360]. The reciprocal length scale in the Fresnel limit up to which homo- and heterodyne mixing occurs is given by $k^2 s$, with $k^2 = \frac{2\pi}{\lambda L_a}$ (with λ being the wavelength and L_a the aperture-sample distance) and s being a measure of the aperture size. In the given measurement geometry with an approximated aperture size of 10 µm and an aperture-sample distance of 1 m this would lead to an upper limit of q space of $0.0005\,\text{Å}^{-1}$, seven times smaller than the lower q limit applied for the ROI in Figure 8.18 in the Appendix.

To extract the dynamic information from the chosen ROIs in Figure 8.18 the approach described in Section 3.1.2 is used. In this method the dynamical information from a XPCS measurement is extracted by fitting of One-Time Correlation Functions (1TCFs) calculated from Two-Time Correlation Functions (2TCFs) with a stretched exponential.[193] To enhance statistics for steady-state dynamics, extracted 1TCFs are averaged over a range of deterioration times $\bar{t}$, where the extracted 1TCFs are invariant. For the data sets shown in this section 1TCFs are averaged over 20 frames, corresponding to 4 s of administered beam. To ensure a full decay of 1TCFs, the 1TCFs are averaged around a chosen deterioration time $\bar{t} = 50\,\text{s}$. Figure 8.19 in the Appendix shows the thus averaged 1TCF extracted from Figure 8.18BD and their respective Kohlrausch-Williams-Watts (KWW) stretched exponential fits. Figure 6.5 depicts the corresponding correlation times τ_0 and the (KWW) exponents γ extracted from the ROIs shown in Figure 8.18BD and the 1TCF in Figure 8.19.

Figure 6.5A shows a jump in correlation times τ_0 when moving from the GT region ($q_z \approx 0.0\,\text{Å}^{-1}$) to the GI region ($q_z > 0.018\,\text{Å}^{-1}$), with higher values of τ_0 for the lower incident angle of $\Theta_i = 0.22°$. The dependence of τ_0 on q_z above the GT region is related to the fact that different length scales are probed, resulting in different correlation times present. For intermediate regions of q_z ($q_z <$ respective Yoneda[148]) flat regions arise (dotted lines in black).

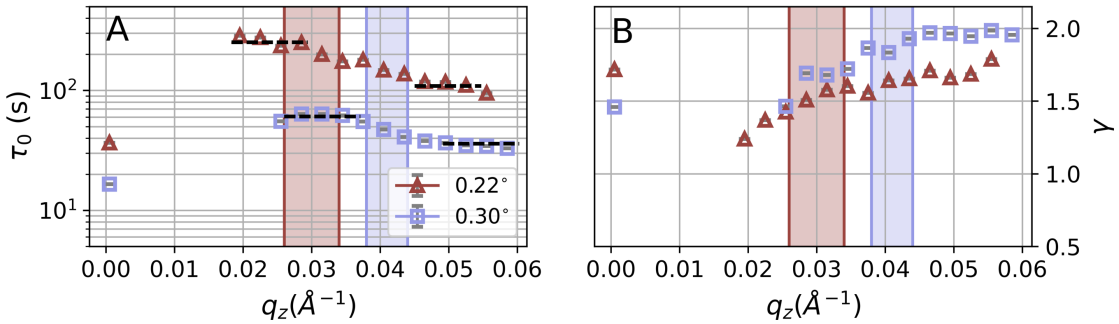

Figure 6.5: (A) Graph of correlation times τ_0 as a function of q_z and (B) KWW exponent γ as a function of q_z extracted from a slot-die coated $MAPbI_3$ thin film in a simultaneous GI-GT-XPCS experiment for two incident angles of $\Theta_i = 0.22°$ (brown) and $\Theta_i = 0.30°$ (blue) at $q_r = 0.0035\,\text{Å}^{-1}$. Error bars are given in gray and are smaller than the marker size. The incident angle-dependent Yoneda regions are marked in the respective colors. Flat regions identified after Zhang et al.[49] are marked as black dotted lines.

Zhang et al.[49] attribute these flat regions in q_z to mixing of scattering signals from the transmission channel Tc and reflection channel Rc originating from different intrinsic Q_z. The overlapping contributions of Tc and Rc scattering signal vary in between the Yoneda region and the specular beam position and roughly cancel each other out due to opposing intrinsic Q_z trends, resulting in flat q_z regions (see Figure 6.3). Within the flat regions most of the scaling of τ_0 as a function of q is governed by the scaling of τ_0 as a function of q_r and hence can be used to analyze the present dynamics in the sample according to Zhang et al.[49].

Figure 6.5B shows the KWW exponent γ as a function of q_z. In the GT region at $q_z \approx 0.0\,\text{Å}^{-1}$ γ values around 1.5 to 1.7 are observed for the applied incident angles. In the GI region γ increases with increasing q_z, from 1.5 up to 2.0 in the GI region ($q_z > 0.018\,\text{Å}^{-1}$) for $\Theta_i = 0.30°$ and an increase from 1.2 up to 1.7 is obtained for $\Theta_i = 0.22°$. Due to the chosen measurement approach of simultaneous GI-GT-XPCS measurements, the probed underlying physical behaviour is expected to be identical in GI and GT geometry. Nevertheless, I observe significant differences between $\gamma_{GT} = 1.7$ ($\Theta_i = 0.22°$, $q_z \approx 0.0\,\text{Å}^{-1}$) in GT and $\gamma_{GI} = 1.2$ ($\Theta_i = 0.22°$, $q_z = 0.018\,\text{Å}^{-1}$) in GI within the same measurement. It is known that γ, which is a descriptor of the sample dynamics, can vary as a function of q. But, the dependence of γ to q does not explain the sharp jump between γ_{GT} and γ_{GI}. Without characteristic length scales within the sample, γ should vary slowly as a function of q.[248] Sharp jumps would only be expected when characteristic length scales are crossed e.g. during structural rearrangements,[248, 366] but in a heterogeneous system of multi-sized crystalline grains no such length scale is dominant. Consequently, the sharp change in γ between GI and GT regions of q_z is attributed to the influence of refraction and multiple reflection and scattering combinations, altering the shape of analyzed 1TCFs. However, the GI data for $\Theta_i = 0.22°$ for $q_z > 0.05\,\text{Å}^{-1}$ reach the value of γ_{GT}. This is in line with the expectations based on the prefactor fractions from Figure 6.4, which show that for high q_z values, the prefactor fractions from the GT region are reached. Although for an incident angle $\Theta_i = 0.22°$ these are not

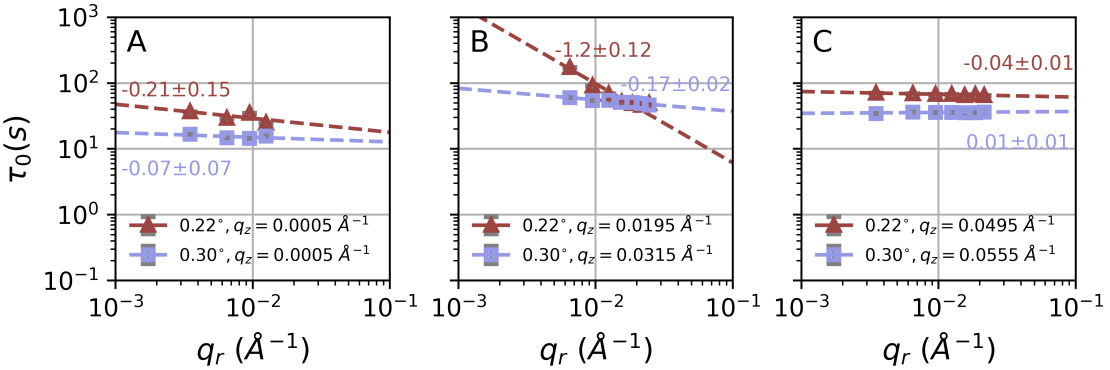

Figure 6.6: The graphs show fit results from the 1TCFs and the resulting comparison of the scaling behavior of the average value of the characteristic decay time τ_0 as a function of q_r between (A) data extracted from the GT region (extracted near $q_z = 0.0\,\text{Å}^{-1}$) , as well as (B) surface and (C) bulk sensitive q_z regions for GI data (for comparison reasons located below and above the respective Yoneda regions). According to Zhang et al.[49] dynamics in the examined GI regions are solely represented by their q_r scaling. Error bars are given in gray and are smaller than the marker size. For an incident angle of 0.22° (brown), scattering stems in all subfigures from Rc and Tc scattering contributions. For an incident angle of 0.30° (blue) subfigures A and C are dominated by scattering from Tc scattering, while contributions from Tc and Rc are present in subfigure B (see Figure 6.4). Numbers above each dashed line mark the slopes of a linear fit in the log-log graph.

dominated by Tc alone as for $\Theta_i = 0.30°$ (possibly explaining the difference between γ_{GT} of $\Theta_i = 0.22°$ and $\Theta_i = 0.30°$), comparable prefactor fractions are nevertheless achieved. In contrast, comparable γ are not achieved for high q_z for $\Theta_i = 0.30°$. I expect that comparable values could be reached for $q_z > 0.06\,\text{Å}^{-1}$, since possibly the influence of the difference between intrinsic Q_z and detector q_z is not yet linear enough (see Figure 6.2). To further analyze the impact of reflection and refraction, the scaling behaviour of τ_0 as a function of q_r is shown for various q_z for incident angles of $\Theta_i = 0.22°$ and $\Theta_i = 0.30°$. The q_z at which τ_0 is examined are chosen as such that the used q_z are within the flat regions of τ as a function of q_z identified via the approach of Zhang et al.[49] (see black dashed lines Figure 6.5) and at $q_z \approx 0$. The ROIs used to calculate the necessary 1TCFs to extract correlation times are shown in Figure 8.18AC and the extracted 1TCFs and their respective stretched exponential fits are shown in Figure 8.20 in the Appendix. The scaling analysis of the extracted τ_0 as a function of q_r are shown in Figure 6.6.

The graph depicting the scaling behaviour for the 3 different q_z regions shows that the scaling behaviour of τ_0 as a function of q_r varies depending on the incident angle and measurement geometry. This is related to the probed dynamics, which the beam induces within the sample. As the beam impinges on the sample ionization and destruction processes of the $MAPbI_3$ thin film are probed. These ionization and destruction processes might be surface-mediated. Hence, analyzed q_z regions related to bulk sensitive measurement conditions (q_z around 0, Figure 6.6A or large incident angle and large exit angles/high q_z, 6.6C) might show a weaker dependence as a function of q_r. In contrast, the more surface-sensitive condition of $\Theta_i = 0.22°$ at

intermediate q_z (below the Yoneda region, Figure 6.6B) might examine the destruction mechanism on the sample surface leading to a stronger scaling as a function of q_r.

As discussed in Section 6.1 the scaling behavior for the decay time τ_0 as a function of q at an incident angle of 0.30° should show comparable scaling dynamics in the GT-SAXS region and in the GISAXS region with large exit angles, here at $q_z > 0.055\,\text{Å}^{-1}$. This results from the fact that the scattering signal in large exit angle detector regions stems from only one DWBA scattering contribution ($|T(\alpha_i)T(\alpha_f)|^2|F(+Q_{z1})|^2$, related to BA scattering). To test if the expected behaviour can be reproduced, the scaling of τ_0 as a function of q_r from the GT data points in Figure 6.6A is projected to q via $q = \sqrt{q_r^2 + q_z^2}$. The projected GT data points and their respective scaling are then compared to the GI data points from Figure 6.5. The result of this comparison is shown in Figure 6.7, in which the GT scaling is visualized by a dashed line. Furthermore, to compare the GT scaling to the GI data points, the GT scaling is shifted as a guide-to-the-eye (dashed-dotted line). The graph shows that the scaling behavior of τ_0 in GT converges with the high q data points (equivalent to high q_z) in GI for $\Theta_i = 0.30°$, but not for $\Theta_i = 0.22°$. Therefore, the plot indicates that the larger the angle of incidence is, the lower the q for which comparable τ_0 scaling as a function of q is reached. This is in accordance with the dominance of the BA term. Consequently, the deviation of the τ_0 scaling behavior for lower q of GI data points in Figure 6.7 can be attributed to the additional DWBA terms resulting in mixing of scattering from the transmission channel Tc and the reflection channel Rc scattering, in addition to the respective non-linear refraction changes.

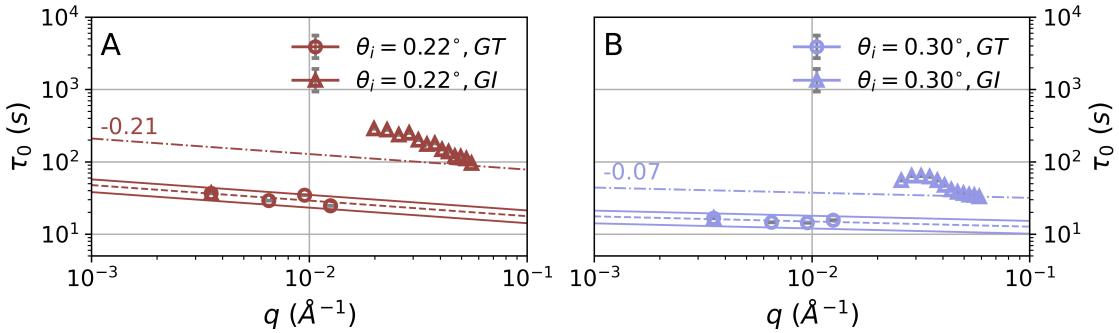

Figure 6.7: The graph shows fit results from 1TCFs and the relevant comparison of correlation times τ_0 as a function of q for extrapolated GT data (circles, taken from GT data points along q_r in Figure 6.6A) and GI data (triangles, taken from GI data points along q_z in Figure 6.5) for (A) $\Theta_i = 0.22°$ (brown) and (B) 0.30° (blue). Error bars are given in gray and are smaller than the marker size. Numbers above dashed lines mark the slopes of a linear fit in the shown log-log graph for GT data. The correlation time τ_0 behaviour is extrapolated from GT data to high q values via the scaling exponent (linear slope). The solid lines are variations to the extrapolated τ_0 by ± 20 % to take into account uncertainties, influencing the refraction within the thin film and altering nominal q_z for the GI data (after Zhang et al.[49]). The dashed-dotted lines are a guide-to-the-eye with the same slope as the dashed lines.

The overarching goal of the simultaneous GI-GT-XPCS measurements and the calculations on refraction and reflection effects is to demonstrate that several regions on the detector can be used to extract comparable dynamics to bulk sensitive

transmission XPCS measurements, while other regions have varying intensities due to refraction and reflection effects. Based on the results from Sections 6.1 and 6.2 the most comparable data to transmission XPCS is extracted from the GT detector region, when using large incident angles. Figure 6.2 shows that in the GT region for an incident angle of 0.30° an offset of correlation times τ_0 in comparison to transmission XPCS occurs. This offset seems to stem from the refraction effect at the thin film surface, resulting in a projection of intrinsic Q to detector q. Furthermore, Figure 6.4 shows that for the same GT region with an incident angle of 0.30° the dominant scattering term is $|T(\alpha_i)T(\alpha_f)|^2|F(+Q_{z1})|^2$, related to BA scattering. Consequently, I do not expect a systematic effect on the stretching exponent γ as a result from the combination of reflection and refraction effects. Further, Figure 6.7 showed that the scaling behaviour for τ_0 as a function of q within the GT region is recovered by GI measurements, when applying high incident angles and high q_z regions, as such measurement conditions result in dominant scattering by the BA term.
Furthermore, Figure 6.3 showed that in between the direct beam and the specular beam position the intrinsic Q_z from the transmission channel Tc and the reflection channel Rc have opposing trends (opposite sign) with increasing detector q_z. From the plot two relevant points are extracted: I) based on Eq. (6.1)c $Q_{z,GI,Tc}$ shows a continuous increase with q_z II) based on Eq. (6.1)d $Q_{z,GI,Rc}$ is decreasing from the Yoneda position up to the specular beam position and increasing above the specular beam position. With these calculations the trend of countervailing q_z for Tc and Rc proposed by Zhang et al.[49] is supported. But contrary to their work, which implied that one should be able to extract the dominant dynamics within the thin film within these regions solely from the scaling of τ_0 as a function of q_r, Figure 6.5 shows that this is not the case and still scaling of τ_0 as a function of q_z exists. However, the scaling of τ_0 as a function of q_z might show unexpected trends. As a consequence, the calculations on the absolute of Q_z as a function of q_z imply that the region to extract meaningful XPCS signals is even further restricted.
In addition, the respective prefactors of the scattering channels Tc and Rc need to be considered to identify q_z ranges in which Tc and Rc prefactors are approximately equal. This allows detector ranges of q_z to be identified in which the intrinsic Q_z are of the same order of magnitude and have opposite signs. The combination of Figure 6.3, indicating that the relevant q_z region must be located below the specular beam position, and Figure 6.4, showing that Tc and Rc prefactors are approximately equal at the Yoneda position, leads to the expectation that flat regions of τ_0 within the Yoneda regions appear. But Figure 6.5 shows that this is not the case for our data set. Consequently, the flat q_z regions identified earlier are false-positives and related to the effect of distortions in GI geometry, which strongly influences the XPCS analysis shown in Figure 6.6B, especially for an intermediate incident angle of 0.22°. For an incident angle of 0.22° Figure 6.6B shows a slope of -1.2 in the double logarithmic presentation of τ_0 as a function of q_r. However, the GT data at $\Theta_i = 0.30°$, closest to a transmission XPCS measurement by the DWBA prefactors, shows a much-reduced slope of -0.07. Such strong deviations of reflection and refraction effects on the correlation times, while probing a comparable dynamic process, makes scaling analysis of correlation times in GI-XPCS data error-prone. Consequently, errors in scaling analysis can be avoided by analyzing Fresnel coefficients and calculate the influence of refraction in GI to identify which q_z regions are suitable for XPCS analysis.

6.3 Additional Geometrical Effects in GI-XPCS

So far in this chapter I have only examined the influence of the DWBA prefactors and the influence of refraction at material interfaces. But other effects might change the 1TCF shape and therefore extracted correlation times in GI-XPCS experiments.

Setup-related q mixing: One group of such effects is related to the measurement geometry and its setup parameters, leading to q mixing in the analysis. The first case of overlap of various q values stems from the finite size of a single detector pixel. I.e. a certain q range is projected together into one pixel, while only the central q value of the pixel is considered for the analysis. To quantify this pixel size related q mixing, the difference $\Delta q_z = q_{z1} - q_{z2}$ is calculated for detector $q_{z1/2}$, based on the given pixel size of 75 µm for an Eiger X 4M at a wavelength $\lambda = 1.285\,\text{Å}$ and an incident angle of 0.30°. The results are depicted in Figure 6.8A and show that the pixel size related effect is approximately constant over the detector within the small angle range of the experiment. Compared to the Δq_z values related to refraction in Figure 6.2 the values related to pixel size are up to 3 orders of magnitude smaller and therefore negligible.
Another setup parameter resulting in q mixing is related to the sample size and the beam footprint projected on it, leading to a range of effective sample-detector distances (SDD). Due to the range in SDDs, with scattering from the upstream sample edge and downstream sample edge reaching different detector pixels, different q_z values are mixed within one detector pixel. The difference in Δq_z is dependent on the exit angle and therefore changes over the detector as a function of q_z. The difference in Δq_z as a function of q_z due to sample size is shown in Figure 6.8B, calculated for a pixel size of 75 µm, a wavelength $\lambda = 1.285\,\text{Å}$, an incident angle of 0.30° and a sample size of 1 cm at a SDD of 13 m. The shift by changes in the SDD through the elongated beam footprint is in most regions of the detector smaller than the effect from mixing of q_z within a single pixel and as such 3 orders of magnitude smaller compared to the Δq_z values related to refraction in Figure 6.2.
A bigger geometrical effect is related to the finite size of the ROIs used for analysis. In the present analysis I applied quadratic ROIs with a length of $0.003\,\text{Å}^{-1}$, introducing q mixing with $\Delta q_z = 0.003\,\text{Å}^{-1}$ on the detector (see Figure 6.8C). Compared to the difference between the Δq_z values seen for the reflection channel Rc and the transmission channel Tc in Figure 6.2, this constant value is still more than one order of magnitude smaller. But if bigger ROIs are chosen, especially if the ROIs are in the highly non-linear region related to the materials critical angle near the Yoneda region, the q mixing due to ROI size, could result in alterations of extracted 1TCFs. The effect can be limited by choosing smaller ROIs along q_z, but hereby the usable photon counts are directly proportional to the ROI size used to calculate 1TCFs. This can limit the reliability of extracted 1TCFs, which bigger ROIs along q_r can compensate for, but introducing a lower resolution along the horizontal direction. For this reason, an optimum combination of illumination duration and ROI size must be found for experiments, depending on the sensitivity of the sample to X-rays, even if this requires complex measurements and analysis approaches.

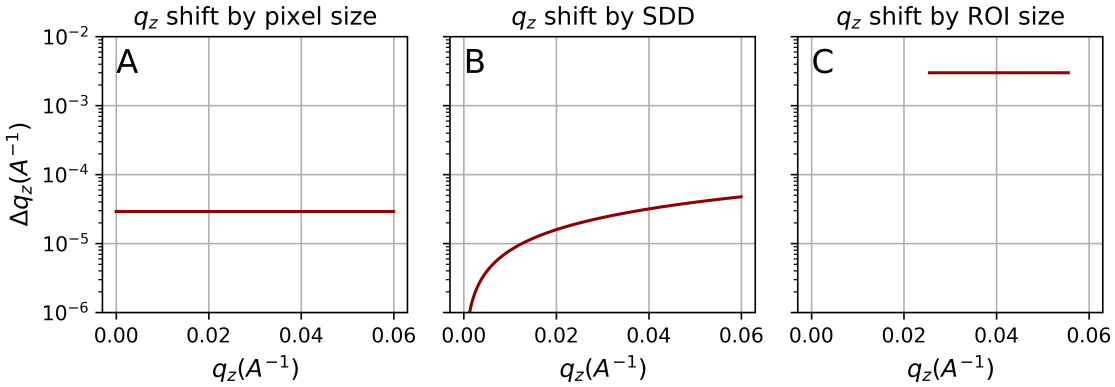

Figure 6.8: The Graph shows a comparison for q mixing as the shift given by $\Delta q_z = q_{z1} - q_{z2}$ (two positions on the detector) for different cases for a fixed incident angle of 0.30°. (A) Difference Δq_z as a function of q_z introduced by single pixel size (Eiger 4M). (B) Difference Δq_z as a function of q_z from the change of SDD at 13 m given by the elongated footprint on a finite sample (1 cm) in GI-geometry projected to an Eiger 4M. (C) Difference Δq_z as a function of q_z given by finite ROI size necessary to evaluate the experiments of the study with sufficient photon statistics.

Homo- and heterodyning: Another effect which may result in altered 1TCF shape was introduced by Gutt et al.[367]. Gutt et al. showed that the wave vector spread $\delta q/q$ related to the coherent properties of the used X-ray beam can have substantial influence on the shape of calculated correlation functions in XPCS experiments. They showed that the contrast factor β might diminish with increasing wave vector spread and if heterodyne mixing occurs, i.e. the occurrence of both first- and second-order correlation functions in the intensity autocorrelation function, might be observed. This is referred to as a detection scheme shift, e.g. from homodyne detection (i.e. correlation of scattered intensity with scattered intensity) to heterodyne detection (i.e. correlation of scattered intensity with e.g. the intensity of the direct beam).[360, 367, 368] The Siegert relation states that between these detection schemes the same dynamics result in correlation times differing by a factor of two.[368] Depending on the system, such a detection scheme shift, introducing heterodyne mixing, is not necessarily obvious. Gutt et al. showed that for a system of overdamped capillary waves, e.g. on a polymer film a continuous detection scheme shift induces a decrease in extracted correlation times τ_0.[367] For the overlap region these are not differing by the expected factor of two. Instead a sum of exponential functions is seen in the transition regime, which shows a stretched exponential behaviour. Consequently, a decrease in correlation times and stretched exponential behaviour may be misinterpreted as a change of the present dynamics, but is in contrast the same dynamics measured within another detection scheme or within the transition region of between a homodyne and a heterodyne detection scheme. Furthermore, the wave vector spread depends on the incident angle Θ_i and exit angle Θ_f due to the projection of coherence length and the projection of the beam size. While Gutt et al. introduced the necessary calculations on wave vector spread for a point detector their results can be generalized to a 2D detector, in which each pixel works as a point detector, with the pixel size working at the equivalent aperture size for a point detector.

Gutt et al.[367] showed that the wave vector spread can be calculated as follows:

$$\delta q_z = 2\pi \sqrt{\frac{2}{\Xi_z^2} + \frac{1}{\Sigma_z^2}\left[1 + \left(\frac{k_0 \Delta a^2}{L_a}\right)^2 \left(1 - \frac{\Sigma_z^2}{\Delta a^2} \frac{L_a sin^2(\Theta_f) + L_b sin^2(\Theta_i)}{L_b}\right)^2\right]} \quad (6.3)$$

$$\delta q_r = 2\pi \sqrt{\frac{2}{\Xi_r^2} + \frac{1}{\Sigma_r^2}\left[1 + \left(\frac{k_0 \Delta a^2}{L_a}\right)^2 \left(1 - \frac{\Sigma_r^2}{\Delta a^2} \frac{L_a + L_b}{L_b}\right)^2\right]} \quad (6.4)$$

With δq_z being the wave vector spread along the beam, δq_r perpendicular to the beam, $\Xi_{z,r}$ being the projected transversal coherence length, $\Sigma_{z,r}$ being the projected beam size and Δa the measure of the incident aperture size. Further, L_a is the aperture-sample distance, L_b the sample-detector distance and $k_0 = 2\pi/\lambda$ the wave number of the incident wavelength. The non-projected coherence length is calculated as $\Xi = \frac{\lambda L_a}{2D}$ with an aperture-sample distance L_a of 1 m, a wavelength λ of 1.285 Å and source size D of 10 µm. Further, the following values were used within the calculations: $\Delta a = 10\,\mu m$, $L_b = 13\,m$, non-projected beam size $\Sigma = 10\,\mu m$. While for Θ_i incident angles of 0.22° and 0.30° are considered. The exit angle Θ_f ranges between 0.0° and 0.68°, taken from the observable angle range at 13 m sample-detector distance for an Eiger X 4M.
The calculated $\delta q_z/q_z$ as a function of q_z are shown in Figure 6.9. The plot shows that with increasing q_z the values of wave vector spread decreases. Further, no wave vector spread above 0.01 is observed. While the wave vector spread δq_z depends directly on the incident and exit angles, δq_r assumes a single value. Thus only the maximum value at the lowest q_r value in our experiments needs consideration. The wave vector spread $\delta q_r/q_r$ at $q_r = 0.0035\,\text{Å}^{-1}$ is 0.0395. As such, the wave vector spread along q_r will dominate the overall wave vector spread. Furthermore, Gutt et al.[367] approximated from simulated correlation functions that changes of the detection scheme from homo- to heterodyne are only expected for values above 0.2. As the values along q_z and q_r are significantly lower than the identified limit of 0.2 by Gutt et al.[367] no heterodyne mixing is expected to be presented in the presented experiments.

Another possibility resulting in heterodyne detection was considered in Section 6.2, when it was calculated if overlap of Fourier components should be expected at the lowest analyzed q values. The calculations based on Gutt et al.[360] showed that no overlap of Fourier components should be expected and consequently a shift to a heterodyne detection scheme (i.e. heterodyne mixing) is not expected within the chosen ROIs. To verify the calculation-based expectations a direct approach to check the experimental data for heterodyne mixing is applied. This can be done by analyzing the contrast factor β extracted from the 1TCFs as a function of q_r. Skihaluridze et al.[369] showed that a detection scheme shift from homo- to heterodyne detection is accompanied by a jump in contrast β. This is related to the nature of heterodyne mixing, which is modulated with a strong elastic signal (direct or reflected beam), while in homodyne mixing the signal is modulated with itself, a weaker quasi-elastic signal. To demonstrate that no sharp jumps in contrast occur the contrast factors β of the data points presented in Figure 6.6 are shown in Figure 6.10. No sharp jumps are present in Figure 6.10 and only gradual change in contrast, i.e. for the GT region, are observed. Consequently, no change from a homo- to a

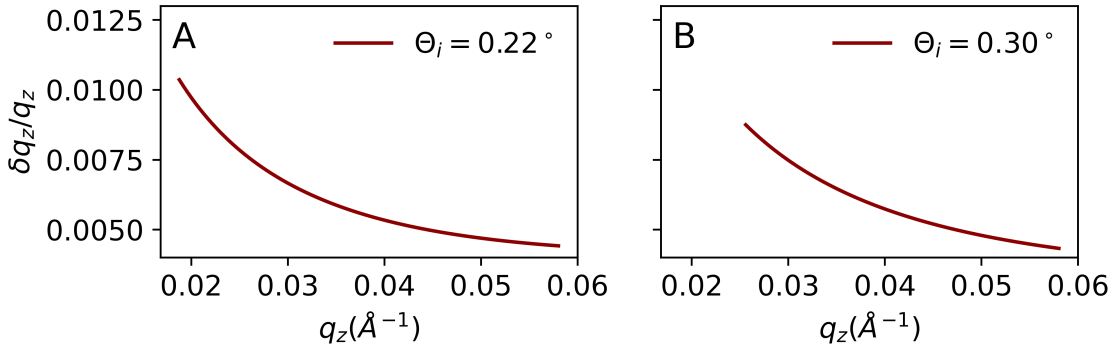

Figure 6.9: The Figure shows the influence of the incident angle to the wave vector spread $\delta q_z/q_z$. (A) Wave vector spread $\delta q_z/q_z$ as a function of q_z starting from the q_z value of the horizon for an incident angle of $\Theta_i = 0.22°$. (B) wave vector spread $\delta q_z/q_z$ as a function of q_z starting from the q_z value of the horizon for an incident angle of $\Theta_i = 0.30°$. Both graphs end at a q_z of $0.059\,\text{Å}^{-1}$ marking the upper limit of the detector used within the experiments shown within the Section 6.2. For the calculation of $\delta q_z/q_z$ see Eq. (6.3).

heterodyne detection scheme is present within the chosen regions of interest (ROIs) used for data analysis. Since the selected ROIs are far enough away from specular reflected X-rays and/or the direct beam the data acquisition take places solely within a homodyne detection scheme.

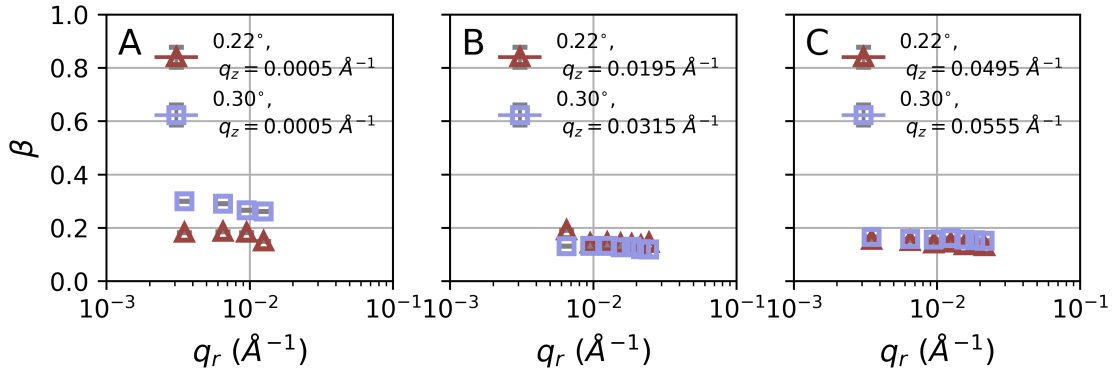

Figure 6.10: The Figure shows the contrast factor β as a function of q_r for the data points shown in Figure 6.6. (A) Contrast factor for data points extracted in GT (extracted near $q_z = 0$) and in (B) surface and (C) bulk sensitive q_z regions for GI data (for comparison reasons located below and above the respective Yoneda regions).

After the well-known effects of partial coherence, resolution and detection scheme mixing are now considered and their influence on the presented experimental data excluded, the distortions to the expected dynamics must be related to the geometrical effects presented in Section 6.1. Hence, suitable regions of analysis can be identified with the presented approach, relying on the calculation of refraction and reflection contributions. But both the reflection contributions and refraction effects alter the

projection of intrinsic scattering on the 2D detector and depend on material properties. The refraction influence can be calculated with knowledge of the critical angle Θ_c of the material, which can be measured in GISAXS experiments or calculated from the materials refractive index.[147] The material dependent Fresnel reflectivities and transmissivities are not as easy to estimate or measure. But if uniform films are used for experiments, meaning that the scattering contrast from structures within the film is significantly smaller than the scattering contrast between the thin film and the ambient atmosphere, these Fresnel coefficients are well approximated by the average film thickness, density and roughness.[163, 246] In this case a two-slab approach for Fresnel coefficient calculations can be applied.[161] Based on this, the most suitable q_z regions for analysis can be determined for a wide range of material systems.

6.4 Generalized Approach to GI-XPCS

To exemplify that the presented approach, on the calculation of reflection and refraction effects, can be generalized it is applied to two different materials (perovskite, polymer) and for a variety of material parameters/experimental conditions (film thickness, incident angle, X-ray energy). This also represents how material-sensitive the presented approach is and that no easy rule-of-thumb should be derived from the selection of calculations presented here.

In a first example the material parameters for the material $MAPbI_3$ that was analyzed earlier are varied. By varying material and experimental conditions, such as the film thickness and the X-ray energy trends in the prefactor faction of the DWBA terms can be identified. Figure 6.11 shows a comparison of the prefactor fraction of the DWBA terms as a function of q_z for film thicknesses of (A,C) 800 nm and (B,D) 20 nm. Furthermore, two different energies are used in the calculations: (A,B) 9.65 keV ($\lambda = 1.285$ Å, comparable to the X-ray energies used for the simultaneous GT-GI-XPCS measurements) and (C,D) of 13.5 keV ($\lambda = 0.918$ Å). In Figure 6.4 the incident angle Θ_i was presented in absolute units, but since the material critical angle Θ_c is energy-dependent it is now presented as a multiple of Θ_i to ensure comparability between the two presented X-ray energies. For the calculations critical angles Θ_c of $\Theta_c(MAPbI_3, 9.65\,\text{keV}) = 0.163°$ and Θ_c ($MAPbI_3$, 13.5 keV) = 0.135° are used, calculated based on Henke et al.[147]. For the calculations presented in this Section of the thesis no roughness to the thin films is included. This should have no influence on the validity of the results, as all Fresnel coefficients are multiplied within the applied matrix formalism calculations by the same decreasing exponential function.[370] Therefore, the exclusion of roughness effects does not change the introduced prefactor fraction presentation due to its inherent weighting.

The figure shows that for the tested material thicknesses and X-ray energies already at an incident angle of $\Theta_i = 1.5\Theta_c$ the BA scattering term becomes dominant. Furthermore, it also shows how sensitive the calculations are towards the exact X-ray energies used. Comparing the top row (X-ray energy = 9.65 keV) and bottom row (X-ray energy = 13.5 keV) the plot further indicates that for a higher X-ray energy already at a small incident angle of $\Theta_i = 1.1\Theta_c$ the BA scattering terms become quickly dominant for q_z above the specular peak position ($> 0.04\,\text{Å}^{-1}$). Further, at the Yoneda position not all DWBA scattering terms are equally present as they are for the lower X-ray energy. As the dominant terms at the Yoneda positions stem solely from the transmission channel Tc for the higher X-ray energy, q mixing

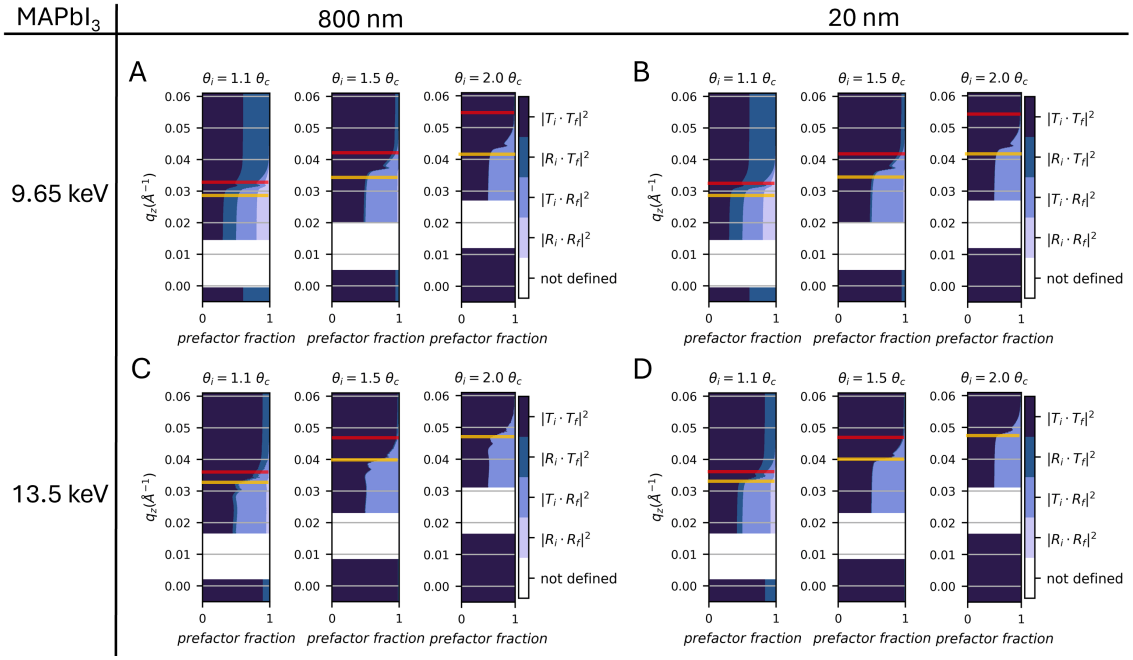

Figure 6.11: Material dependent Fresnel coefficient analysis used for intensity calculations in the simplified DWBA for incident angles Θ_i = 1.1 Θ_c, 1.5 Θ_c and 2.0 Θ_c as a function of q_z for $MAPI_3$. The reflectivities and transmissivities are calculated for a two-slab system of (A,C) 800 nm thick $MAPbI_3$ and (B,D) 20 nm thick $MAPbI_3$ placed on a silicon substrate with varying exit angles Θ_f, which are converted to q_z. Calculations are for X-ray energies of (A,B) of 9.65 keV (λ = 1.285 Å) and (C,D) of 13.5 keV (λ = 0.918 Å). The Yoneda and specular positions are marked in orange (Yoneda) and red (specular), respectively. At 13.5 keV and Θ_i = 2.0 Θ_c the specular position is located above of the calculated q_z range.

will be reduced compared to the lower X-ray energy. Consequently, the results of a scaling analysis as presented in Figure 6.7 would differ. This is explained by the fact that the influence of Δq_z is reduced as only a weak scattering contribution from the reflection channel Rc is expected over the whole detector. In contrast to the change of DWBA term dominance with X-ray energy, the change with material thickness is less significant. The change of thickness from 800 nm to 20 nm mainly plays a role for the prefactor fractions around the Yoneda region but does not significantly influence for which q_z the BA term or the Tc dominate.

To further apply the presented approach for a different material system Figure 6.12 presents comparable calculations for a polymeric thin film of Poly-(3-hexylthiophen-2,5-diyl) (P3HT). Figure 6.12 shows a comparison of the prefactor fraction of the DWBA terms as a function of q_z for film thicknesses of (A,C) 200 nm and (B,D) 20 nm. Furthermore, two different energies are used in the calculations: (A,B) 9.65 keV (λ = 1.285 Å) and (C,D) of 13.5 keV (λ = 0.918 Å). To have comparable incident angle ratios to Figure 6.12 and between X-ray energies the chosen incident angles Θ_i are again presented as multiples of Θ_c. For the calculations the used critical angles Θ_c are Θ_c(P3HT, 9.65 keV) = 0.132° and Θ_c($P3HT_3$, 13.5 keV) = 0.095°, calculated according to Henke et al.[147]. Compared to $MAPbI_3$ presented in Figure 6.11, the critical angles are lower due to the lower electron density of the material.

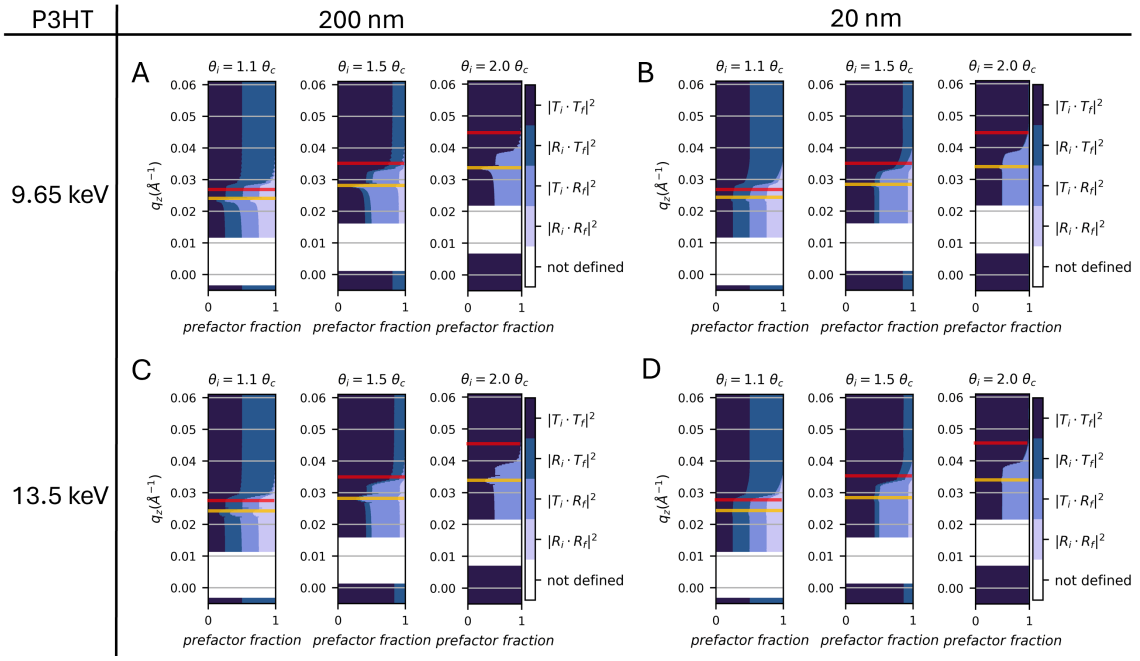

Figure 6.12: Material dependent Fresnel coefficient analysis used for intensity calculations in the simplified DWBA for incident angles Θ_i = 1.1 Θ_c, 1.5 Θ_c and 2.0 Θ_c as a function of q_z for P3HT. The reflectivities and transmissivities are calculated for a two-slab system of (A,C) 200 nm and (B,D) 20 nm thick P3HT placed on a silicon substrate with varying exit angles Θ_f, which are converted to q_z. Calculations are carried out for X-ray energies of (A,B) of 9.65 keV (λ = 1.285 Å) and (C,D) of 13.5 keV (λ = 0.918 Å). The Yoneda and specular positions are marked in orange (Yoneda) and red (specular), respectively.

The figure depicts that for the chosen P3HT thicknesses and X-ray energies an incident angle of $\Theta_i = 1.5\Theta_c$ is not sufficient for the BA scattering term to become dominant. Only with an incident angle of at least $\Theta_i = 2\Theta_c$ the BA scattering term becomes dominant for all analyzed film thicknesses and X-ray energies above their respective specular peak positions. To follow the change in X-ray energies the Figures 6.12A and C and 6.12B and D are compared. The plots indicate that for P3HT the influence of X-ray energies is mainly located around the Yoneda regions, where different ripple-like oscillations along q_z emerge for different X-ray energies. No strong differences in the present scattering terms along q_z with changing X-ray energies are observed. As such, the influence of changing X-ray energy appears to be smaller compared to Figure 6.11 for $MAPbI_3$, as no vanishing of Rc-related scattering can be determined for the low incident angles at 13.5 keV for P3HT. Furthermore, the influence of the layer thickness again shows less significant influences, when compared to the changes seen in Figure 6.11 for $MAPbI_3$. Following the change in thickness in the Figures 6.12A and B and 6.12C and D, the change of thickness from 200 nm to 20 nm mainly plays a role for the prefactor fractions around the Yoneda region but does not significantly influence for which q_z the BA term or the Tc dominate.

Comparing the results of both $MAPbI_3$ and P3HT the necessary incident angle for the BA scattering term to dominate above the specular peak position is different. For $MAPbI_3$ an incident angle of 1.5 Θ_c is sufficient for the BA scattering term to be dominant around the specular beam position, while for P3HT an incident angle of 2.0 Θ_c is necessary. Furthermore, while for the low electron density material (P3HT) no strong dependence of the Fresnel parameters as a function of X-ray energy is observed, this changed for the high electron density material ($MAPbI_3$). This further shows that due to the complexity of the relationship between material parameters and X-ray energy no simple rule-of-thumb can be established. The reason for this change with X-ray energies could be related to X-ray absorption edges of the calculated materials, which alter reflectivity and transmissivity calculations by changes in the absorption coefficient β.[147] For $MAPbI_3$ no absorption edge is located near 9.65 keV, but the Pb(L-III) absorption edge (E = 13.035 keV [147]) is near the energy of 13.5 keV and might relate to the strong influence of X-ray energies seen for $MAPbI_3$. Consequently, one should calculate the dominant scattering terms for specific experiments to identify the lowest angle at which the BA term dominates. This allows for maximization of the overall scattering intensity that decays with increasing incident angle.

6.5 Summary and Discussion

In the current chapter of the thesis, Fresnel reflectivity and transmittivity calculations are discussed to reveal the dominant scattering terms in GI scattering experiments as a function of the incident and exit angle. The Fresnel coefficient calculations are carried out within the framework of the simplified DWBA for bulk sensitive GT and GI scattering, captured on a large 2D detector. The Fresnel coefficient calculations are combined with the calculation of q space distortions due to refraction at material interfaces, which occur for scattering within the grazing incidence geometry. The combination allows me to propose how reflection and refraction leads to mixed intensity signals over a detector, originating from different intrinsic reciprocal vectors and from different scattering terms of the simplified DWBA. The mixed intensity signals alter observed dynamics examined by GI- and GT-XPCS, in contrast to transmission XPCS. By using the combined Fresnel coefficient and refraction calculations q_z regions along the detector could be identified, which should be less distorted in comparison to distortion free transmission XPCS. These expectations on distortion-free and/or distortion-reduced q_z regions are examined by a study of simultaneously taken measurements of GT- and GI-XPCS. The simultaneous measurements allow me to identify regions along q_z and angle of incidence Θ_i from the measurements, which show comparable scattering origin in GI and GT geometry, resulting in comparable extracted dynamics to the non-distorted dynamics from transmission XPCS measurements. Further, the regions in q_z identified within the simultaneous measurements are in accordance with the expectations from the Fresnel coefficient and refraction calculations. The section concludes with calculations identifying the influence of material parameters (film composition and film thickness) and experimental conditions (incident angle and X-ray energy).

The generalized calculations indicate that due to the complexity of the relationship between material parameters and X-ray energy no simple rule-of-thumb can be established to capture the expected behaviour of dominant scattering terms when changing the material composition/film thickness. While Figures 6.11 and 6.12 suggest that for incident angles $\Theta_i = 2\Theta_c$ BA scattering dominance is quickly achieved, the larger incident angles will result in generally reduced scattering intensities captured on the detector at the high q_z values that are necessary. As XPCS in general, and bulk-sensitive GI-XPCS especially is a method sensitive to the photon statistics, this reduced photons at higher incident angles might result in experiments under non-ideal measurement conditions. Consequently, I suggest that for optimizing the photon statistics an as-low-as-possible incident angle is applied to achieve bulk-sensitive GI-XPCS measurements. To achieve these low incident angles the presented approach based on reflection and refraction effects allows me to identify at which incident angles the BA scattering term dominates scattering on the detector. Furthermore, distortion-reduced q_z values can be identified prior to the experiment. This allows the user in real experiments to not only achieve less distorted correlation functions from bulk-sensitive GI-XPCS measurements, but also to optimize the experimental conditions beforehand, saving the valuable commodity of 'beam time'.

7 Identifying Differences in Calculated XPCS and GI-XPCS Experiments

As shown in chapter 6 the quantification of dynamics with GI-XPCS measurements is challenging. The chapter showed that distortions of the extracted dynamics are related to the overlap of scattering channels within the detected 2D scattering data and refractions of the scattering X-rays taking place at film interfaces, leading to a shift between the intrinsic and detector reciprocal space. The chapter furthermore showed that by calculating Fresnel coefficients, distortion reduced detector regions can be identified, in which comparable dynamics to GT-XPCS can be extracted. The GT-XPCS derived dynamics are extracted from scattering which contains fewer reflection contributions and are mainly dominated by scattering described within in the Born Approximation (BA).[161, 246] However, extra reflection contributions are still present within the 2D scattering patterns and as such the extracted decorrelation frequencies are expected to be distorted.[49, 161] Furthermore, the influence of refraction effects is also present both in GT- and GI-XPCS measurements. These refraction effects stem from refraction at thin film or substrate interfaces, which alter the true scattering angles in the film as they emerge from the thin film. This refraction at interfaces results in a non-linear difference between the intrinsic and detector reciprocal space, which may lead to an overlap of the different reflection contributions on the detector as shown in the previous chapter. As only experimental data from two angles of incidence for GI and GT-XPCS experiments could be discussed in the previous chapter, a different approach will now be used to quantify the influence of refraction effects and reflection contributions in GI-XPCS experiments.

To quantify the influence refraction and reflection effect have on extracted dynamics from GI-XPCS data a computational approach to model XPCS and GI-XPCS from molecular dynamics (MD) simulations was derived, as no readily available software/and or python package for such calculations exists to my knowledge and accordingly literature is scarce. In earlier studies, which focus on the modeling of thin film growth processes, the relevant auto-correlation functions for extraction of dynamic properties are calculated from the height-height structure factor.[371, 372] From the height-height structure factors the expected coherent X-ray scattering data is calculated by applying the Distorted Wave Born approximation (DWBA) by following the approach of Sinha and Rauscher.[162, 246] In these studies the height-height structure factors were calculated for self-affine surfaces in linear (Kuramoto-Sivashinsky[373, 374]) and non-linear (Kardar-Parisi-Zhang[375]) growth models. Although the authors could not conclude that the calculated GISAXS intensities are simply proportional to the height-height structure factor, still their respective simulations showed that the intensity auto-correlation functions yield accurate estimates of the surface growth scaling exponents with exceptions at low wavenumbers. Unfortunately, this approach

can only be applied if one is interested in surface growth and therefore in surface-sensitive GI-XPCS at shallow incident angles. Another approach was developed by Mohanty et al..[376] In this work a computational approach to model XPCS from MD simulations was developed, based on two calculations methods.

I) A direct method in which the SAXS intensities are calculated at each reciprocal space vector separately.

II) Calculating the SAXS pattern from the atomic density and its Fourier transformation, in which all reciprocal space vectors are calculated at once.

The authors could show that their simulated speckle pattern reproduces the known properties and relations of experimental liquid transmission XPCS measurements with both calculation approaches.

As the work by Mohanty et al.[376] showed the validity of calculating transmission XPCS 2D data based on MD simulations to extract dynamical properties, within this chapter a comparable approach is derived to calculate GI-XPCS 2D data from MD simulations. The derived approach of calculating GI-XPCS 2D data from real space particle trajectories simulated by MD will be used to quantify the impact of refraction effects and reflection contributions. In contrast to previous studies, the approach presented here not only focuses on modelling surface-sensitive GI-XPCS but also allows for modelling of arbitrary structural factors in bulk materials via MD simulations.

The chapter will start with MD simulations of real space particle trajectories with known dynamics and their quantification in section 7.1.1. The particle trajectories are simulated within LAMMPS[242] und quantified based on the calculated Mean-Square-Displacement. Based on the time-resolved real space particle positions a similar approach to Mohanty et al.[376] is implemented in section 7.1.2, which calculates the transmission 2D scattering pattern from a discrete Fourier transformation of the real space particle positions. The transmission XPCS 2D intensity pattern are used to calculate 1- and 2TCFs. The extracted dynamics from the reciprocal space correlation functions show good comparability to the extracted real space MD dynamics, validating the computational approach taken for transmission XPCS. In a next step the same time resolved particle positions are used to calculate GI-XPCS 2D intensity pattern based on the simplified Distorted wave Born Approximation (sDWBA)[162, 246] in section 7.1.3. The necessary Fresnel coefficients are calculated according to Lazzari and Rauscher.[163, 246] Again 1- and 2TCFs are calculated from the GI-XPCS 2D intensity pattern and their respective dynamics are extracted. The dynamics extracted from the calculated GI-XPCS 2D data show significant deviations from the transmission derived dynamics. In section 7.2 refraction effect corrections are integrated in the sDWBA calculations, so that the reciprocal vectors are calculated within the intrinsic Q space, in which the extracted GI-XPCS dynamics are in good agreement with the transmission XPCS ones. The chapter concludes in section 7.3 with a summary of the results, a comparison to the results derived in chapter 6 and gives an outlook on how a reconstructive approach based on the work of Liu & Yager[161] could be applied for real GI-XPCS experiments.

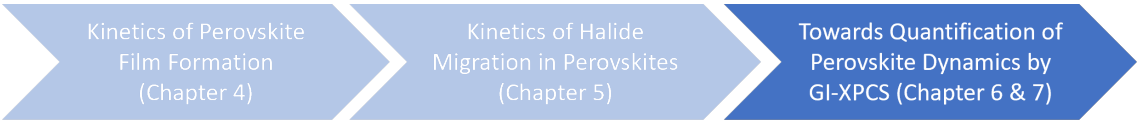

Figure 7.1: Schematic overview of thesis showing the topic of the following chapter: Chapter 7 focuses on a computational approach to calculate XPCS and GI-XPCS 2D scattering pattern from MD simulations to further quantify the impact of refraction and reflection effects introduced in Chapter 6. By a comparison of extracted dynamics between the simulated trajectories and the transmission and grazing incidence scattering pattern the main origin of distortions can be identified.

7.1 Calculation of XPCS and GI-XPCS based on MD Simulations

In this section the dynamics of the motion of a model particle system is extracted, either directly from the simulated particle trajectories, or from calculated XPCS and GI-XPCS 2D data, derived from the simulated particle trajectories. Hereby, the analysis directly from the MD trajectories works as a baseline for subsequent comparisons. The calculation of transmission XPCS 2D data allows me to extract how the real space dynamics from MD are translated to reciprocal space. For the extracted transmission XPCS 2D data the detector and intrinsic Q space are the same, as no refraction effects need to be included for SAXS. After the baseline for reciprocal space dynamics is established the distorted dynamics from calculated GI-XPCS is analyzed. By varying the incident angles within the calculations of GI-XPCS 2D data the influence of refraction effects and reflection contributions (Fresnel coefficients) can be varied. As the calculated GI-XPCS 2D data is based on the same initial MD real space trajectories and the refraction and reflection effects are varied, their influence to the extracted dynamics, i.e. the influence to the scaling of decorrelation frequency with reciprocal vector q and the influence to extracted particle velocities, can be quantified.

7.1.1 Undistorted Dynamics in MD Simulations

To further analyze the effect of the applied scattering geometry in XPCS and GI-XPCS experiments first a dynamical system of particles is simulated via Lammps, a MD simulator.[242] For this a well-understood model system of a liquid-like melt of uniformly sized particles is chosen, in which the particle dynamics in physical systems can range from sub-diffusive to diffusive to super-diffusive and ballistic motion.[377–380] The particle interaction will be taken into account via a Lennard-Jones (LJ) potential, as literature showed that various melts can be described well within a LJ potential.[243–245] The particles start their trajectories from a fcc-structure and equilibrate thermally from the initial fcc occupation. To ensure that the simulated particles and their trajectories show non-divergent equilibrium dynamics, and therefore homogeneous dynamics, a fixed temperature is set for the simulation. The simulation is done in reduced units so that the results, such as travelled distances within extracted particle trajectories, particle sizes, run times, as well as the box size can be rescaled for the calculations of the XPCS and GIXPCS 2D data. The technical details of the MD simulation is presented in section 3.3.

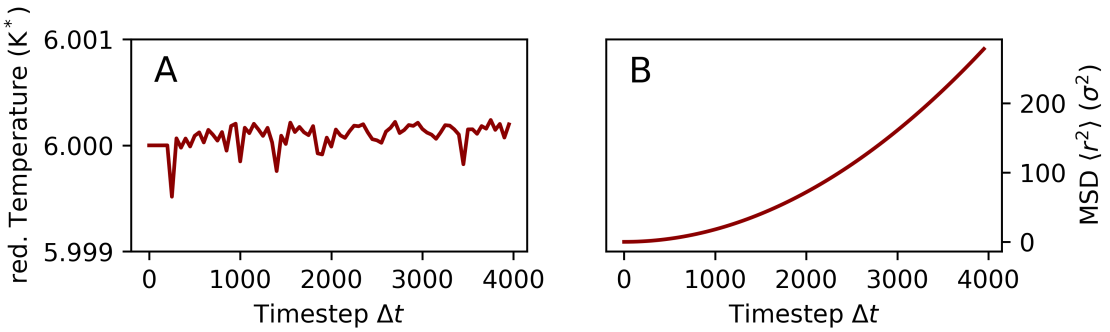

Figure 7.2: (A) LJ-reduced temperature as a function of timestep Δt and (B) LJ-reduced Mean-Square-Displacement (MSD) $\langle r^2 \rangle$ as a function of timestep Δt calculated from particle trajectories (see Section 3.3 for MD model parameters).

To establish a baseline of the simulated dynamics, the trajectories of the simulated particle motions are analyzed and the quality of the simulation ensured. One measure to ensure that the simulated particle motion is not divergent over the simulation is to track the LJ-reduced temperature of the particle ensemble.[242] Figure 7.2A shows the LJ-reduced temperature as a function of the number of simulated timesteps Δt (4000 Δt correspond to a simulation time of 4 τ). The graph shows that the ensemble keeps its temperature of about 6 K^* and the maximum divergence from the simulation temperature is below 0.01 %. This maximum divergence is close to the start of the simulation when the particles are still equilibrating from their initial crystalline fcc structure. As such, when analyzing calculated scattering pattern from the initial crystalline starting structure it must be ensured that no homo- and heterodyne mixing is present due to overlapping intensity signals.[360]

To further ensure that the ensemble of the simulated particle trajectories is valid, the simulations described in Section 3.3 are repeated on a longer time scale (doubled to 8τ), while keeping all other parameters presented in section 3.3 the same. Additionally, the potential, kinetic and total energy of the particle ensemble is extracted from the MD simulation. The results are presented in Figure 8.21 in the Appendix. The figure depicts that the reduced temperature in the second half of the longer simulation is stable and shows comparable statistics. Considering the potential and kinetic energy of the particle ensemble, it can be seen that stable values for the mean value and the standard deviation are also present in the first and second half of the simulation. Furthermore, the kinetic energy of the particle ensemble is about 4 orders of magnitude greater compared to its potential energy, which implies that the system is characterized primarily by ballistic motion. Combining the potential and kinetic energy into the total energy of the simulated particle ensemble it is apparent that also the total energy is non-divergent and that the mean value and standard deviation are stable within the first and second half of the MD simulation.

Extracted from the shorter simulation described in section 3.3 Figure 7.2B shows the Mean-Square-Displacement (MSD) $\langle r^2 \rangle$ with timestep ΔT calculated from the simulated particle ensemble. The non-linear increase with timesteps Δt further supports that no simple diffusive motion is present within the simulated particle ensemble, but a super-diffusive or even ballistic motion.[381] To quantify which kind of

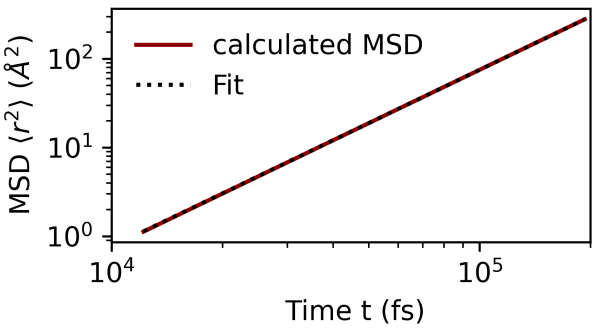

Figure 7.3: Mean-Square-Displacement (MSD) $\langle r^2 \rangle$ as a function of time t scaled from LJ-reduced units (see Figure 7.2B) on a double logarithmic scale. The scaled MSD was modelled with Eq. 7.1 to extract the slope and its scaling exponent.

dynamics are present, the MSD is fitted with an exponential function as follows:

$$\langle r^2 \rangle = m * x^{\alpha} \tag{7.1}$$

in where the MSD $\langle r^2 \rangle$ is described by a slope m and a scaling exponent α. Depending on the scaling exponent it can be determined whether a ballistic motion ($\alpha \approx 2$) or a super-diffusive motion ($1 < \alpha < 2$) is present.[381] As the XPCS simulations in the following subsections are calculated with a real space geometry, i.e. on a detector placed several meters from the simulated scattering centers, the LJ-reduced units are scaled accordingly to real space units. For this each time step is multiplied by 48.88 fs and each σ by 196 Å. The results of the scaled MSD and time are shown in Figure 7.3 on a double logarithmic scale. A fit of the MSD results in a scaling exponent $\alpha = 1.994 \pm 0.001$. As such the simulated motion is best described by a model of ballistic motion.

Based on this type of motion one can extract the velocity v of particle motion from the MSD $\langle r^2 \rangle$. For this Metzler et al.[381] showed that the MSD is described in the case of ballistic motion by the following equation:

$$\langle r^2(t) \rangle = (v \cdot t)^2 \tag{7.2}$$

Based on the slope m derived from the fit shown in Figure 7.3 the velocity can be calculated by taking the square root of m. Resulting in a value of the MD-derived velocity of $v_{MD} = (17.64 \pm 0.59)$ Å/ns.

To further ensure the validity of the presented MD simulations the MD derived velocities and their scaling exponent α are calculated also for the longer MD simulation with a duration of 8τ. The results are presented in Figure 8.22 in the Appendix and show that within a fit for the first half of the duration the results presented in Figure 7.3 and the following analysis based on Metzler et al.[381] are recreated. Slight deviations occur for the second half of the simulation. While the scaling exponent, as a measure of the particle motion, stays the same, the derived velocity changes slightly to a higher $v_{MD} = (18.6 \pm 0.8)$ Å/ns. As expected, a fit over the whole time range results in an intermediate velocity with a slightly higher error, covering both derived values within the error margin. As no significant differences from the first and second half of the simulation occur the dynamics are ensured to be non-divergent.

This is also the case on longer time scales, ensuring that homogeneous equilibrium dynamics are simulated. Going forward the velocity $v_{MD} = (17.64 \pm 0.59)\,\text{Å/ns}$, calculated from the particle ensemble on the short time scale of 4τ, acts as a baseline for further comparisons between MD simulations and the extracted dynamics from calculated XPCS scattering pattern, as the 4τ MD simulations trajectories will be used to calculate 2D scattering patterns.

7.1.2 Undistorted Dynamics by Calculated Transmission XPCS

After the baseline of the simulated dynamics is established and the validity of homogeneous dynamics ensured, the simulated particle positions in time are projected to detector reciprocal space q via the approach described in subsection 3.3. Figure 7.4 shows an example of a calculated 2D scattering pattern of a single timestep of the particle ensemble. The square detector on which the scattering is projected spans a reciprocal space of up to $0.064\,\text{Å}^{-1}$ along q_z and up to $0.032\,\text{Å}^{-1}$ along q_{xy}. The colored regions mark ROIs used for the calculation of 1- and 2TCFs. With 17 ring-like regions, starting at $q = 0.016\,\text{Å}^{-1}$ and a $\Delta q = 0.003\,\text{Å}^{-1}$ the majority of calculated scattering on the detector is used to extract dynamics from the change in the calculated scattering pattern over time. The gaps in the marked ROIs along the q_z and q_{xy} axis are located around square shaped intensity fluctuations. These fluctuations are a result of the simulated box and can be interpreted as direct beam scattering from the box edges, similar in appearance to the streak seen in a GISAXS experiment along the q_z axis. Consequently, to avoid heterodyning within 1- and 2TCF calculations these areas must be avoided.[360]

As mentioned in subsection 7.1.1 initially the particle ensemble equilibrates from a fcc structure, resulting in the highest deviations from the given temperature. As such, the first 300 timesteps will be discarded, to exclude the initial equilibration phase. This equilibration phase was expressed in Figure 7.2A as a flat line in the beginning, followed by the maximum deviation from the simulation temperature. To check if the exclusion of the first 300 timesteps is sufficient to avoid heterogeneities in the extracted dynamics 2TCFs are calculated. The 2TCFs from the ROIs in Figure 7.4 are calculated for a time scale ranging from 300 to 4000 Δt and are shown in Figure 7.5.

The figure shows that for the exemplarily chosen ROIs the 2TCFs show one central diagonal line, whose width narrows from Subfigure A (q = $(0.0160 \pm 0.0015)\,\text{Å}^{-1}$) to Subfigure C (q = $(0.0550 \pm 0.0015)\,\text{Å}^{-1}$). The narrowing indicates that with increasing q, meaning a lower real space distance, the time for the local structure to decorrelate shrinks. Furthermore, the 2TCFs in A,B and C show no avalanche-like behaviour, i.e. disruptions along the diagonal direction. This is indicative of homogeneous dynamics over the whole analyzed timescale. Consequently, the absence of dynamic heterogeneities allows me to calculate 1TCFs by averaging these over the whole simulated timespan, enhancing the available statistics of the resulting 1TCFs $g_2(\tau)$.

The results of the calculated 1TCFs $g_2(\tau)$ with time τ (τ equals number of timesteps multiplied with 48.88 fs) for the ROIs presented in Figure 7.4 is shown in Figure 7.6A. The $g_2(\tau)$ are colored in accordance with the color of the ROIs shown earlier, which the $g_2(\tau)$ were calculated from. All calculated $g_2(\tau)$ decorrelate from a value around 2 to a baseline of 1, with increasing plateau times around 2 (later decorrelation)

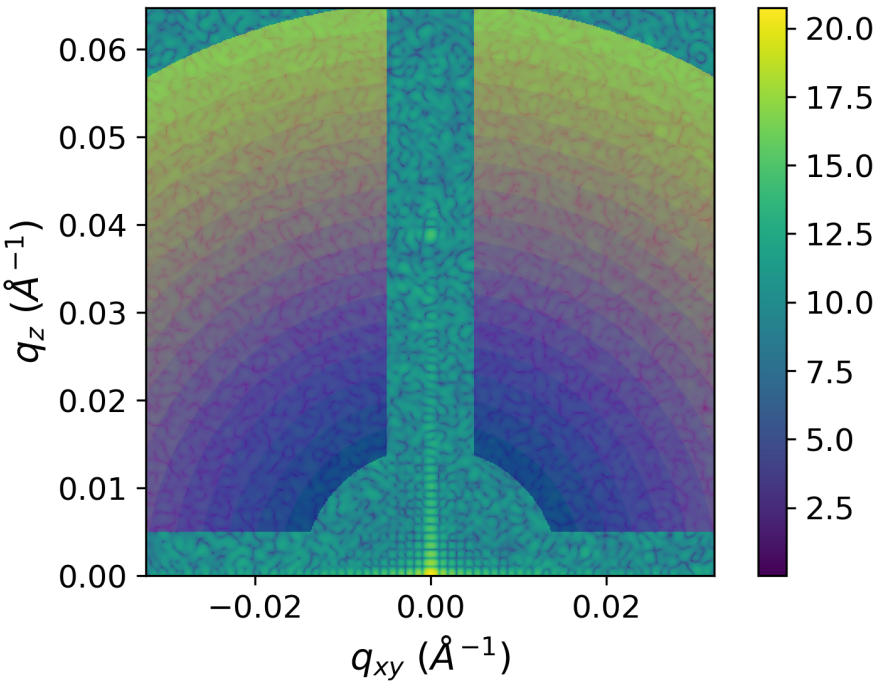

Figure 7.4: Simulated 2D detector image of BA scattering from the MD simulated particle ensemble for a single timestep. The detector image is overlaid with ring-like ROIs located around the direct beam. The marked ROIs are used for the calculation of 2- and 1TCFs. Gaps in the ROIs are necessary to avoid direct beam scattering, which results in heterodyning.

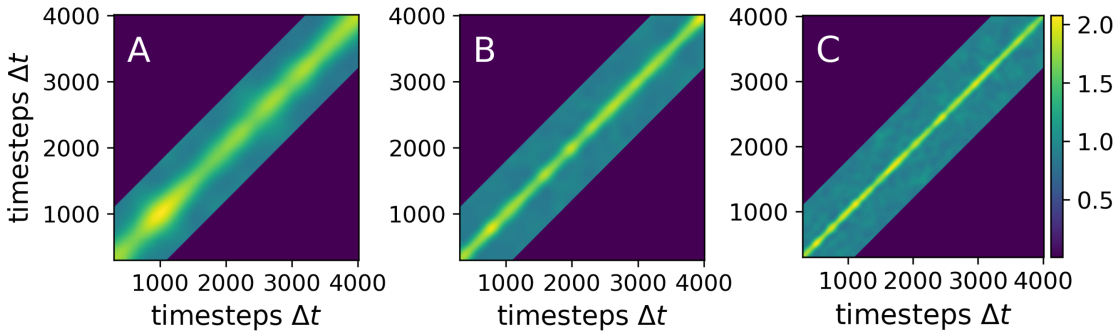

Figure 7.5: 2TCFs calculated for ROIs shown in Figure 7.4 located at (A) q = $(0.0160 \pm 0.0015)\,\text{Å}^{-1}$, (B) q = $(0.0240 \pm 0.0015)\,\text{Å}^{-1}$ and (C) q = $(0.0550 \pm 0.0015)\,\text{Å}^{-1}$. The central line without significant narrowing or widening ('avalanches') over the simulated timesteps indicates that no dynamical heterogeneities are present.

with decreasing q values. The $g_2(\tau)$ were fitted with a stretched exponential function (Eq. 2.21 in Section 2.3) to extract the decorrelation frequency Γ_s, the stretching exponent γ, the contrast factor β and the offset g_∞. The fits to $g_2(\tau)$ are shown as dashed lines in their respective color.

Based on the parameters derived from the fit the $g_2(\tau)$ are normalized by sub-

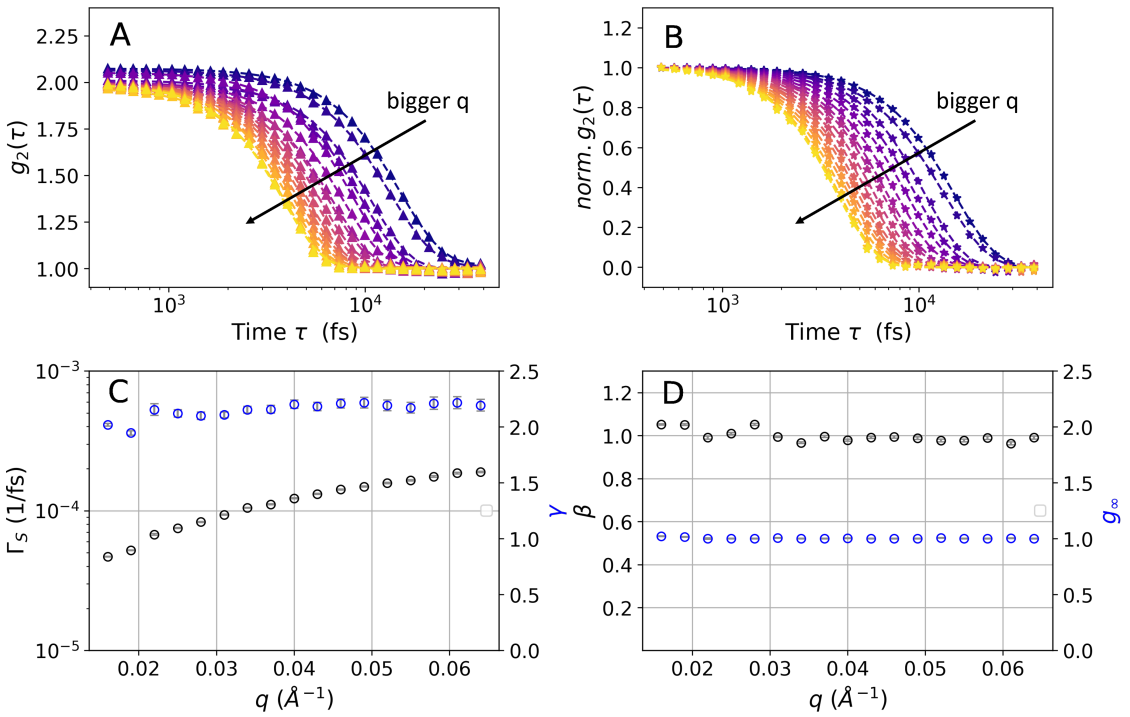

Figure 7.6: (A) 1TCF $g_2(\tau)$ with time τ calculated for ROIs shown in Figure 7.4. The dashed-lines are stretched-exponential fits (Eq. 2.21) to the data. Colors are chosen in accordance with Figure 7.4. (B) Normalized 1TCF $g_2(\tau)$ with time τ, based on the *base* and contrast β values derived from the fits in A. (C) Decorrelation frequency Γ_s (black) and stretching exponent γ (blue) with reciprocal vector q. (D) Contrast factor β (black) and offset g_∞ value (blue) with reciprocal vector q. Error bars are given in the respective colors and are smaller than the marker size.

traction of g_∞ and rescaled based on the contrast factor β, so that the maximum values are set to 1 and decorrelate to 0. The normalized $g_2(\tau)$ with τ are shown in Figure 7.6B. The normalized $g_2(\tau)$ are commonly used to ease the visualization of changes in the decorrelation frequencies Γ_s with q and are especially applied when significant changes in β are observed.[369] In the present case no such sharps jumps in β are observed. Still, the normalized $g_2(\tau)$ allow a better visualization of the clear trend of increasing decorrelation frequency Γ_s with increasing q. This is shown in more detail in Figure 7.6C, which shows the decorrelation frequency Γ_s (black) and stretching exponent γ (blue) as a function of q. One sees that for the whole range of q an increasing decorrelation frequency is observed. This indicates that simple homogeneous dynamics are observed and no altering effects, e.g. deGennes-narrowing [382] is present within the simulated dynamics and q range. Further, the figure shows the stretching exponent γ (blue), which stays slightly above 2 over the whole q range, with an exception in the first two data points. As the respective 1TCFs have the lowest decorrelation frequency, this deviation might be attributed to the absence of a full decay, altering the necessary stretching exponent to fit such a decay. Further fit parameters are presented in Figure 7.6D, showing the contrast factor β (black) and the offset g_∞ (blue). The contrast factor β reaches values around 1. This indicates that for the present simulated experiment full coherence is present. For a physical

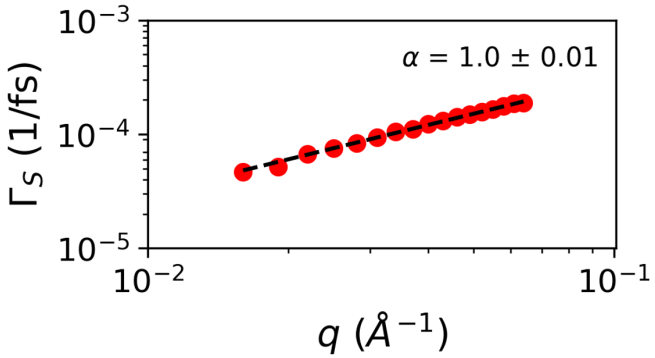

Figure 7.7: Decorrelation Frequency Γ_s as a function of reciprocal vector q on a double logarithmic scale. The data points were modelled based on Eq. 7.1 (black dashed line) to extract the slope and its scaling exponent.

experiment of e.g. overlapping coherence volumes or partial coherent beams, only values below 1 are observed.[361] Furthermore, the stable β value indicates that no heterodyning due to direct beam-related scattering is included in the chosen ROIs, which would result in jumps of β and often in values $>>1$.[369] Analyzing the offset g_∞ also shows values close to 1. This behaviour is indicative of a full decay of the 1TCFs, showing that no secondary dynamics on longer time-scales, outside of the calculated one, are to be expected.

To finish the analysis of the simulated transmission XPCS measurements the behaviour of the decorrelation frequency Γ_s as a function of q is further analyzed. Figure 7.7 shows Γ_s as a function of q on a double logarithmic scale. The decorrelation frequency is fitted to Eq. 7.1 (dashed line) to analyze the scaling of Γ_s as a function of q, resulting in a line. The resulting scaling exponent $\alpha = 1.00 \pm 0.01$, as indicated within the Figure. This linear relation of decorrelation frequency Γ_s and reciprocal vector q indicates that in the calculated XPCS experiment no diffusive, but ballistic motion is extracted as well. This ballistic motion corresponds to the MD results obtained from real space trajectories in section 7.1.1. Furthermore, from the slope m, a comparable velocity to v can be extracted. As this velocity is extracted from the transmission XPCS experiment it will be called v_t. After including a factor of 2π to project the reciprocal space vector to real space, the slope m translates to a velocity of $v_t = (19.27 \pm 0.84)$ Å/ns. Compared to the velocity v_{MD} calculated based on the MSD of simulated real space trajectories, v_t deviates by 8.4 %. This small discrepancy between the velocities derived from the MD simulation (v_{MD}) and the calculated time resolved transmission 2D scattering patterns (v_t) shows that the reciprocal space transmission XPCS calculations are valid and able to reproduce the real space dynamics seen from the MD trajectories. Furthermore, with the extracted velocity from the transmission XPCS calculations a measure for a systematic deviation between the real and reciprocal space is established. This shows that a change in the extraction method is accompanied by a deviation, in the presented case of less than 10 %.

7.1.3 Distorted Dynamics by Calculated GI-XPCS

After the dynamics of the particle ensemble are quantified by extraction from the simulated particle trajectories and by calculated transmission XPCS, their method dependent deviations are used for the subsequent comparison to calculated GI-XPCS. As described in subsection 3.3 the simulated particle positions from MD are projected to detector reciprocal space q via calculations within the sDWBA.[162, 163, 246] For incident angles $\Theta_i = 0.19°$, $0.22°$, $0.30°$, $0.40°$, $0.50°$ and $0.60°$ are chosen. These incident angles are equivalent to $\Theta_i = 1.05$, 1.22, 1.67, 2.22, 2.78 and 3.33 Θ_c. Figure 7.8 shows an example of a calculated 2D scattering pattern of a single timestep of the particle ensemble for $\Theta_i = 0.22°$. The direct beam is located outside the scattering pattern and the lower detector edge around $q_z = 0.02\,\text{Å}^{-1}$ coincides with the sample horizon. The point of highest intensity at $q_{xy} = 0$ and $q_z = 0.039\,\text{Å}^{-1}$ is the specular peak position. Scattering streaks to and from this position are related to the box shape of the simulated particle ensemble and can be interpreted as direct beam scattering from the box edges. A line of enhanced intensity below the specular peak is visible at $q_z = 0.0354\,\text{Å}^{-1}$, which is created by the intensity amplification when the exit angle corresponds to the critical angle (Yoneda).[148] The colored regions mark square-like ROIs used for the calculation of 1- and 2TCFs. The ROI shape is adjusted in comparison to the calculations in Subsection 7.1.2 as the reciprocal vector q is not isotropic anymore and q_{xy} and q_z must be distinguished. To analyze the accessable detector q range 20 ROIs are placed starting at the lower detector boundary at $q_z = 0.0215\,\text{Å}^{-1}$ and $q_{xy} = 0.015\,\text{Å}^{-1}$. Each ROI has a width of $\Delta q_z = 0.003\,\text{Å}^{-1}$ and $\Delta q_{xy} = 0.01\,\text{Å}^{-1}$. The width along q_z is chosen in accordance with the ROI width from the transmission XPCS measurements and the width along q_{xy} is chosen to gather a sufficient number of pixels, so that the calculated 1- and 2TCFs are not dominated by the photon statistics.[247] Moreover, the width and position along q_{xy} are chosen so that no direct beam scattering from the central high intensity streak is used for the correlation calculations. This ensures that no heterodyning takes place and that the calculations are solely within a homodyne detection scheme.[360] Furthermore, for a single ROI located at the height of the specular beam position a high intensity streak is crossing into the chosen ROIs. For this ROI it will be later checked whether heterodyning occurs. In this case the results from the ROI will be discarded for further scaling analysis to ensure that a single homodyne detection scheme is applied.[360]

As established in subsection 7.1.2 the first 300 timesteps are discarded for the calculation of correlation functions, to exclude the initial equilibration phase of the particle ensemble. To check how the changed measurement geometry changes the extracted dynamics, a selection of 2TCFs calculated from the ROIs in Figure 7.8 are presented in Figure 7.9. The shown 2TCFs are located at different q_z (A: $q_z = (0.0215 \pm 0.0015)\,\text{Å}^{-1}$, B: $q_z = (0.0425 \pm 0.0015)\,\text{Å}^{-1}$, C: $q_z = (0.0635 \pm 0.0015)\,\text{Å}^{-1}$), depicting decreasing real space distances. In accordance with Figure 7.5 this leads to smaller outlines of the presented 2TCFs. But in contrast to the transmission 2TCFs the GI 2TCFs don't appear as smooth. The GI 2TCFs show narrowing and/or widening over the simulated time steps. This doesn't lead to complete decorrelations ('avalanches'), which would lead to a checker board-like pattern in the 2TCFs.[383] Still, the narrowing/widening of the 2TCFs indicates that despite the homogeneous nature of the dynamics, as established from the simulated

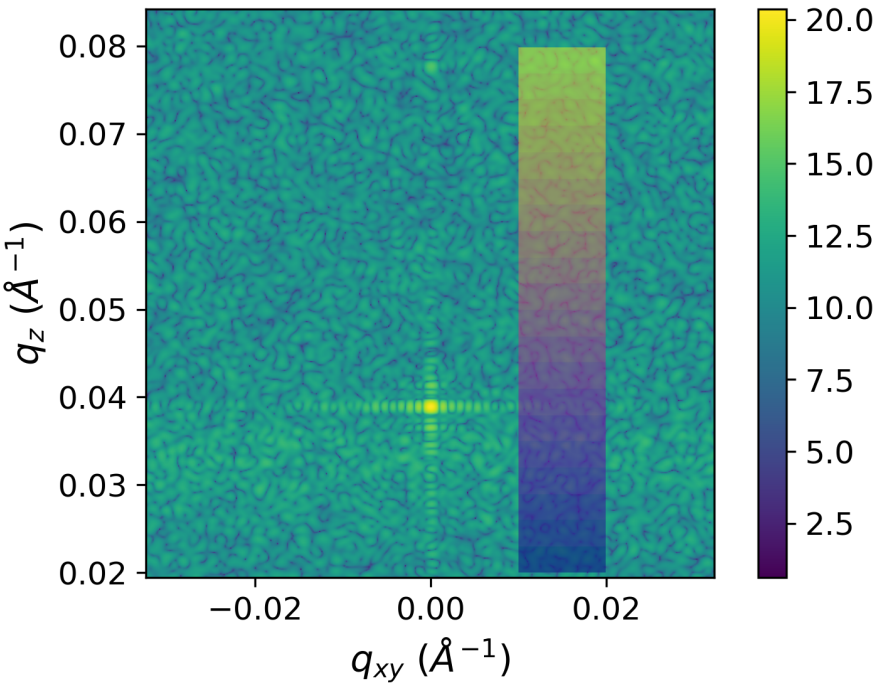

Figure 7.8: Simulated 2D detector image of DWBA scattering in the grazing incidence geometry ($\Theta_i = 0.22°$) from the MD simulated particle ensemble for a single timestep. The detector image is overlaid with square-like ROIs located above the direct beam. The marked ROIs are used for the calculation of 2- and 1TCFs. The ROIs are moved to their respective q_{xy} position to avoid direct beam scattering, which results in heterodyning.

MD trajectories and the respective calculations from transmission XPCS, the same dynamics appear more heterogeneous when calculated in grazing incidence geometry. However, since no complete decorrelations take place, 1TCFs can be calculated as before, by averaging over the whole simulated timespan of timesteps Δt. By taking the average the available statistics of the resulting 1TCFs $g_2(\tau)$ are enhanced and the approach to extract dynamics is kept comparable to section 7.1.2.

The results for the calculated 1TCFs $g_2(\tau)$ as a function of time τ (τ equals number of timesteps multiplied with 48.88 fs) for the ROIs presented in Figure 7.8 are shown in Figure 7.10A. The $g_2(\tau)$ are colored in accordance with the earlier shown color of the ROIs, which the $g_2(\tau)$ were calculated from. Most calculated $g_2(\tau)$ decorrelate from a value around 2 to a baseline of 1, with earlier decorrelation times for increasing q values. A single 1TCF deviates from the trend and shows a decrease from 2.25 to 1.4. This 1TCF correlates to the ROI catching direct beam scattering. All $g_2(\tau)$ were fitted with a stretched exponential function (Eq. 2.21) to extract the decorrelation frequency Γ_s, the stretching exponent γ, the contrast factor β and an offset g_∞. The fits to $g_2(\tau)$ are shown as dashed lines in their respective color.

Based on the parameters extracted from the fit, the $g_2(\tau)$ are normalized by subtraction of g_∞ and rescaled based on the contrast factor β, so that the maximum value is set to 1 and the function decorrelates to 0. The normalized $g_2(\tau)$ as a function of τ are shown in Figure 7.10B. Figure 7.10C shows the decorrelation frequency Γ_s (black) and stretching exponent γ (blue) as a function of q ($q = \sqrt{q_z^2 + q_{xy}^2}$). For the

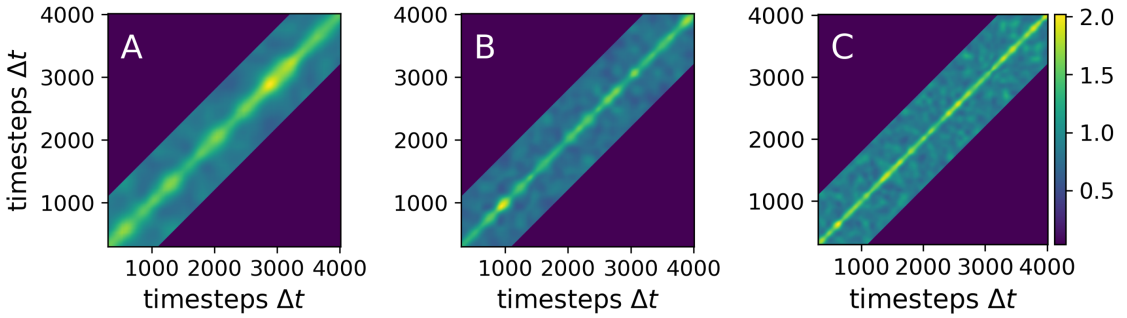

Figure 7.9: 2TCFs calculated for ROIs shown in Figure 7.8 located at $q_{xy} = (0.015 \pm 0.005)\,\text{Å}^{-1}$ and (A) $q_z = (0.0215 \pm 0.0015)\,\text{Å}^{-1}$, (B) $q_z = (0.0425 \pm 0.0015)\,\text{Å}^{-1}$ and (C) $q_z = (0.0635 \pm 0.0015)\,\text{Å}^{-1}$. The outline of the central line shows narrowing and/or widening for A and B, but no full decorrelations ('avalanches') over the simulated timesteps. This behaviour indicates that the present dynamics appear to be not completely homogeneous.

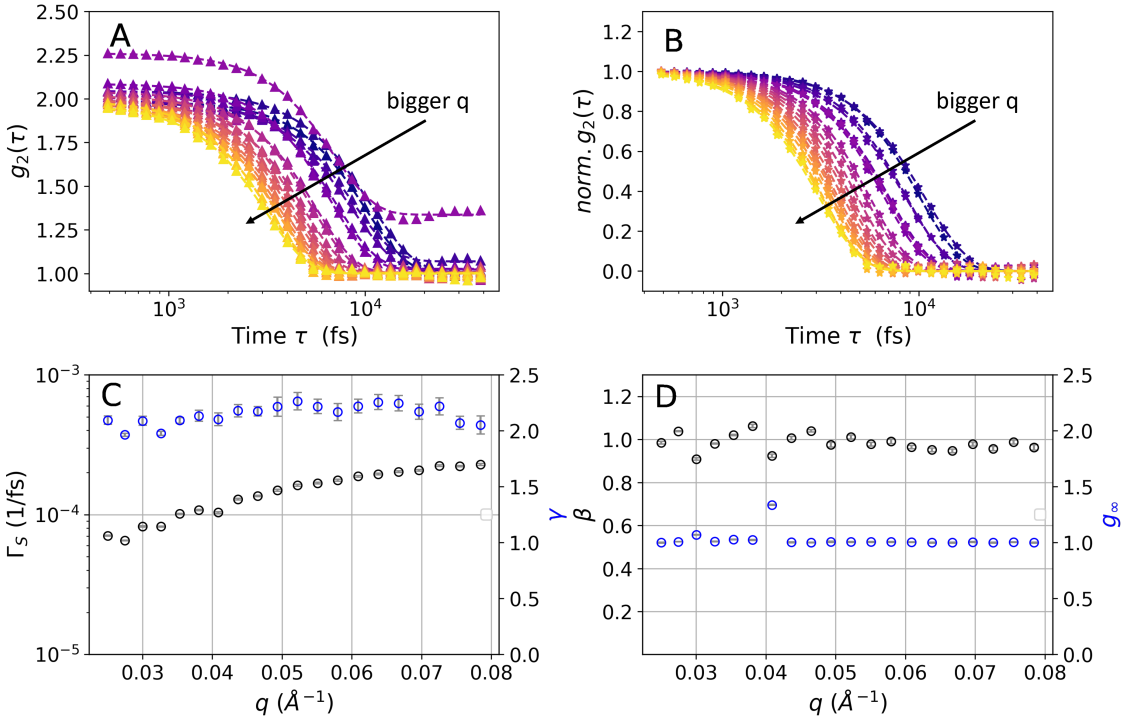

Figure 7.10: (A) 1TCF $g_2(\tau)$ as a function of time τ calculated for ROIs shown in Figure 7.8. The dashed-lines are stretched-exponential fits (Eq. 2.21) to the data. Colors are chosen in accordance with Figure 7.8. (B) Normalized 1TCF $g_2(\tau)$ as a function of time τ, based on the offset g_∞ and contrast β values derived from the fits in A. (C) Decorrelation frequency Γ_s (black) and stretching exponent γ (blue) as a function of reciprocal vector q. (D) Contrast factor β (black) and the offset g_∞ (blue) as a function of reciprocal vector q. Error bars are given in the respective colors and are smaller than the marker size.

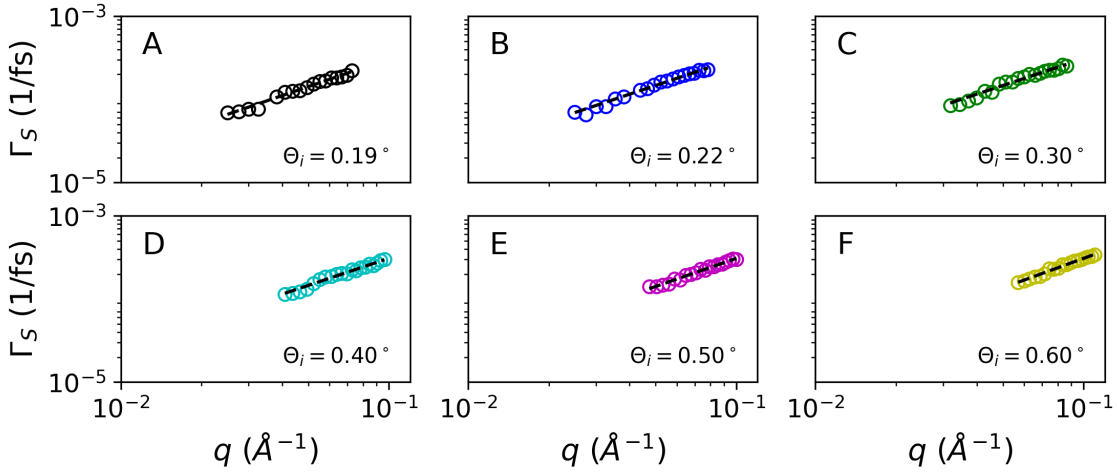

Figure 7.11: Decorrelation Frequency Γ_s as a function of reciprocal vector q on a double logarithmic scale for incident angles Θ_i of (A) 0.19°, (B) 0.22°, (C) 0.30°, (D) 0.40°, (E) 0.50° and (F) 0.60°. The data points are modelled based on Eq. 7.1 (black dashed line) to extract the slope and the respective scaling exponent.

whole range of q an increasing decorrelation frequency Γ_s is observed. In contrast to the 2TCFs showing slightly heterogeneous dynamics this behaviour of Γ_s as a function of q indicates simple homogeneous dynamics and again no altering effects are visible. Such altering effects, e.g. deGennes-narrowing[382], i.e. a significant decrease in Γ_s around a single q value, which corresponds to a maximum of the structure factor $S(q)$, are not present within the simulated dynamics and q range. Further, the figure shows the stretching exponent γ (blue), which remains above 2 over the whole q range. This matches with the results derived earlier from the transmission XPCS simulations.

Figure 7.10D shows the extracted contrast factor β (black) and the offset g_∞ (blue). The contrast factor β reaches values of around 1. This indicates that for the present simulated experiment full coherence is present. Furthermore, the stable β value indicates that no heterodyning due to direct beam-related scattering is included in the chosen ROIs, which would result in jumps of β and in values >1.[369] Analyzing the offset g_∞ shows that in most cases g_∞ reaches values close to 1. This behaviour is indicative of a full decay of the 1TCFs, showing that no secondary dynamics on longer time scales, outside of the calculated one, are expected.[384]

But for a single 1TCF at approximately $q = 0.04\,\text{Å}^{-1}$ no full decorrelation is observed. The ROI at $q = 0.04\,\text{Å}^{-1}$ covers the specular peak reflection line located at $q_z = 0.039\,\text{Å}^{-1}$, associated with scattering due to the finite size of the simulated box in the MD simulation. Further, the corresponding Γ_s value also shows a dip. In combination with the decay starting from 2.25 this indicates, that heterodyning and/or secondary dynamics on longer time scales may be present,[360, 384] despite the fact that no jump in the contrast factor is observed, which might be related to the direct scattering from the finite box size. Consequently, for the further scaling analysis of Γ_s with q this data point will be excluded.

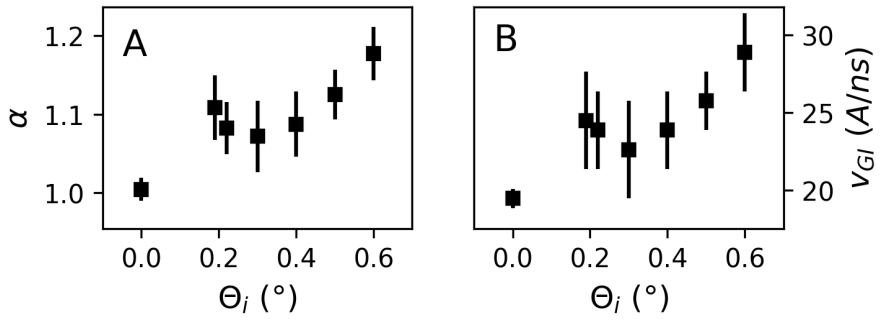

Figure 7.12: (A) Scaling exponent α and (B) velocity v_{GI} as a function of the incident angle Θ_i extracted via Eq. 7.1 from the decorrelation frequency scaling shown in Figure 7.11. Error bars are shown in black. The values shown at $\Theta_i = 0.0°$ are derived from transmission XPCS calculations.

To compare the dynamics derived from GI calculations, comparable scaling analysis of Γ_s as a function of q is performed as in Figure 7.7 depicted. Since GI-XPCS 2D data for Θ_i ranging from 0.19° to 0.60° were calculated, also the scaling analysis is performed for the whole range of incident angles. The decorrelation frequencies are extracted via the approach shown for an incident angle $\Theta_i = 0.22°$ in Figures 7.8 to 7.10. As shown in the example analysis, outliers associated with box scattering around the specular peak position are sorted out based on $g_2(\tau)$ values, contrast factor β and g_∞ values. Figure 7.11 shows the resulting Γ_s as a function of q on a double-logarithmic scale for Θ_i ranging from (A) 0.19° to (F) 0.60°. The angle dependent decorrelation frequencies are fitted to Eq. 7.1 (dashed-line) to analyze the scaling of Γ_s as a function of q, resulting in a line.

Figure 7.12 shows the results for the scaling analysis, with (A) the exponent α and (B) the velocities derived from the slope. As a reference the scaling exponent and velocity derived from the transmission XPCS simulations is shown at 0° incidence. Following the scaling exponent α for all simulations in GI geometry the α values deviate from the expected value of 1, which indicates ballistic motion. Instead values between 1.07 ± 0.05 and 1.18 ± 0.03 are observed. Such scaling exponent would indicate dynamics attributed to hyperdiffusive behaviour,[381] despite the earlier established dynamics of ballistic motion. Further, following the calculated velocities v_{GI} these also deviate from the expected values, ranging from (22.62 ± 3.14) Å/ns up to (28.90 ± 2.51) Å/ns. These deviations correspond to differences from the MD simulation velocity v_{MD} of 28.2 % to 63.8 %, well above the difference of 8.4 % seen for the transmission XPCS result.

As the scaling analysis seems to severely overestimate velocities and scaling exponents derived from GI-XPCS simulations, the need arises to check where the deviations originate from.

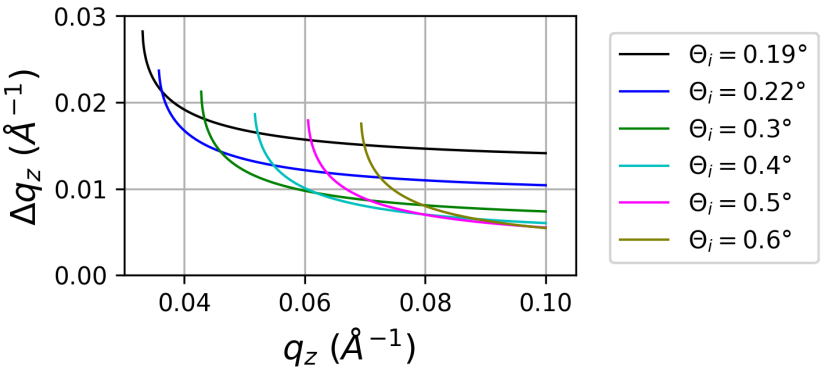

Figure 7.13: Difference between detector q_z and intrinsic Q_z ($\Delta q_z = q_z - Q_z$) originating from the refraction at interfaces vs detector q_z for incident angles of 0.19° to 0.60° for the Transmission channel Tc.

7.2 Origin of Deviations between XPCS and GI-XPCS

As introduced in section 6.1 the intrinsically reciprocal vector Q, under which scattering takes place in a thin film in grazing incidence geometry, is not linearly projected to detector reciprocal space q. This occurs because the magnitude of the change in the refracted component q_z depends on the material critical angle (see Eq. 6.1). The difference between intrinsic Q and detector q can therefore be quantified by calculation of $\Delta q_z = q_z - Q_z$, resulting in two shifts, dependent on the respective scattering channel Rc and Tc. To approximate in which q_z region the strongest deviations are expected, I calculated in Figure 7.13 Δq_z as a function of q_z for the Transmission channel Tc (the more dominant scattering channel, especially for higher incident angles) for the calculated incident angles of 0.19° to 0.60°. The plot shows that for each angle the highest deviations occur around the Yoneda region. At this position the exit angle equals the materials critical angle, resulting in pronounced non-linearities when refraction occurs. Furthermore, the plot shows that at higher q_z the difference Δq_z becomes nearly constant. Interestingly this constant value seems to be nearly the same when the incident angle is sufficiently above the critical angle Θ_c of the material.

Transferring the influence of the non-linearities in Δq_z to the scaling analysis seen in Figure 7.11 for each incident angle, several extracted decorrelation frequencies at lower q values are expected to be underestimated in contrast to their respective counterparts at higher q. Consequently, the underestimation in Γ_s alters the fit, resulting in skewed velocities and scaling exponents. However, despite knowing the difference in Δq_z a correction for this shift is not easy to establish, but the simulations offer the possibility to directly include refraction of scattering vectors to calculate the scattering in its intrinsic reciprocal Q space, which was introduced in Chapter 6, Eq. 6.1.

To transition the GI-XPCS 2D data calculations from detector reciprocal space q to the intrinsic reciprocal space Q, under which scattering takes place within the sample, the refraction of scattering at interfaces has to be included. To include this refraction effects the calculation of the q_z vector under which scattering takes place

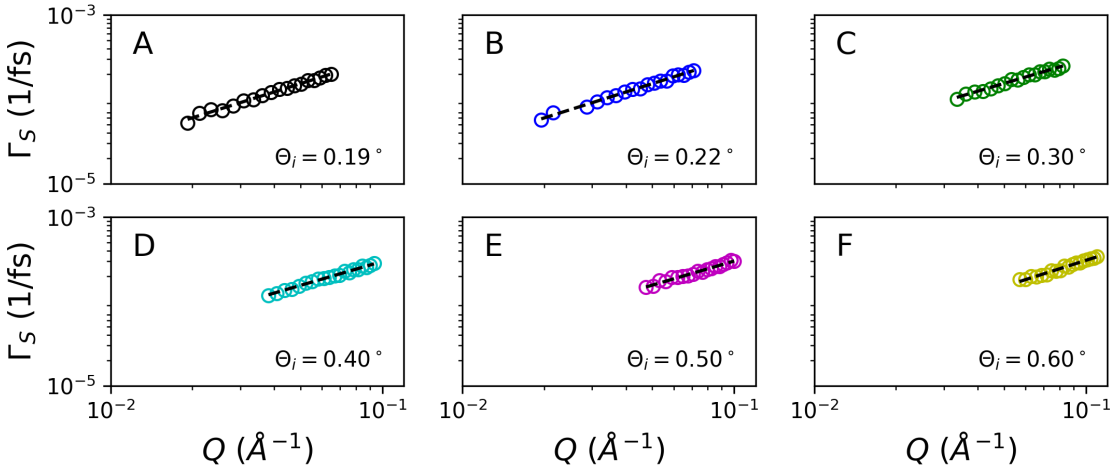

Figure 7.14: Decorrelation Frequency Γ_s as a function of reciprocal intrinsic vector Q on a double logarithmic scale for incident angles Θ_i of (A) 0.19°, (B) 0.22°, (C) 0.30°, (D) 0.40°, (E) 0.50° and (F) 0.60°. The data points were modelled based on Eq. 7.1 (black dashed line) to extract the slope and the respective scaling exponent.

was altered from its classical calculation given in Eq. 2.12 to the formula given in Eq. 6.1. This equation includes refraction at interfaces, which depend on the material's critical angle Θ_c, for both the Transmission and Reflection channel necessary to describe scattering events within the sDWBA. With this alteration of the reciprocal space vectors calculations of q_z the calculations of GI-XPCS 2D data analyzed in section 7.1.3 are repeated. The calculated GI-SAXS images are analyzed with the same approach as introduced in the Figures 7.8 through 7.10. Furthermore, the same incident angle range of 0.19° to 0.60° is calculated and the respective dynamics extracted. The extracted decorrelation frequencies Γ_s as a function of the intrinsic reciprocal vector Q are presented in Figure 7.14. The black dashed lines are scaling fits based on Eq. 7.1. In comparison to Figure 7.11, which was calculated within the detector reciprocal space q, the progression of Γ_s as a function of intrinsic reciprocal space Q appears smoother, without 'bumps', which were seen for several Θ_i in Figure 7.11 (e.g. 0.19° and 0.40° within the first half of the analyzed detector q range). To quantify these observed changes in appearance, the results of the scaling fit are presented in Figure 7.15 on the same y-axis ranges as in Figure 7.12.

Following the exponent α in Figure 7.15A the scaling exponents extracted from the intrinsic Q projections are not continuously overestimated as before. Instead the extracted values for α are now close to the expected value of 1. The maximum difference is seen for $\Theta_i = 0.40°$, which has a value of $\alpha = (0.94 \pm 0.03)$.

Similar behaviour is seen for the extracted velocities v_{GIQ}. Instead of continuously overestimating the velocity the extracted velocities v_{GIQ} are now located close to the expected value of the transmission XPCS calculations v_t. The calculated velocities ranging from $v_{GIQ} = (16.46 \pm 1.27)$ Å/ns up to (20.66 ± 1.55) Å/ns. Thus, some of the calculated velocities, taking into account the associated errors, are now coinciding with the velocity of $v_t = (19.27 \pm 0.84)$ Å/ns derived from the transmission simulations.

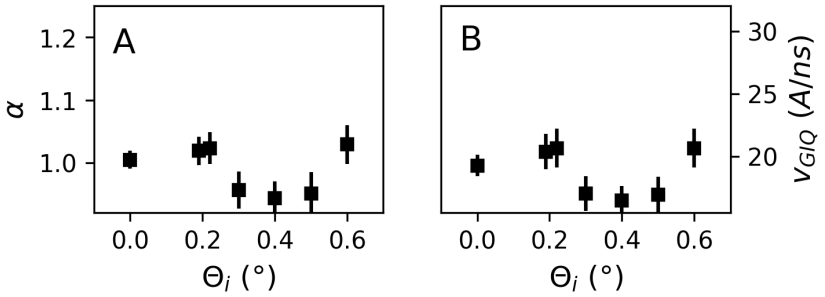

Figure 7.15: (A) Scaling exponent α and (B) velocity v_t as a function of the incident angle Θ_i extracted via Eq. 7.1 from the decorrelation frequency scaling shown in Figure 7.14. Error bars are shown in black. The values shown at $\Theta_i = 0.0°$ are derived from transmission XPCS calculations.

The reduced differences in extracted velocities v_{GIQ} in comparison to the reference values show that by switching to intrinsic Q space the simulations can be improved. Furthermore, the reduction also indicates that refraction effects are a major contributor to the differences seen for the scaling analysis, i.e. the scaling exponent and the extracted velocities. In addition, both scaling analyses in Figure 7.12 depending on q and in 7.15 depending on Q show correlations between α and $v_{GI(Q)}$, in which the positions of the data points respective to the reference are mirrored between α and $v_{GI(Q)}$.

To investigate the cross-dependencies of scaling exponent and velocity, the fits seen in Figure 7.14 were repeated with a global fit model. The global fit model is based on Eq 7.1, but all Γ_s as a function of Q data sets for all incident angles from $\Theta_i = 0.19°$ to $0.60°$ are optimized in parallel to derive a single value for the scaling exponent and the velocity each. The fit is presented in Figure 8.23A in Appendix section 8. With this approach cross dependencies leading to over- and underestimation of fit parameters, based on their respective incident angle Θ_i are eliminated. The fit results in a scaling exponent of $\alpha = (0.99 \pm 0.01)$ and a velocity $v_{GIQ} = (18.72 \pm 0.47)$ Å/ns. This equals a difference in velocities between transmission and globally fitted intrinsic GI calculations of about 2.9 %, but both velocities are comparable within the calculated uncertainties. This means that by applying a global fit, the differences between the velocities derived from the transmission and grazing incidence calculations can be further reduced. To ensure that the global fit for the scaling of Γ_s as a function of Q does not alter the general characteristics of the derived results I applied the same approach for a combined data set of Γ_s as a function of detector q. Thus I check whether the general behaviour of overestimating velocities v_{GI} is captured when the data set is globally fitted. The resulting fit is presented in Figure 8.23B in Appendix section 8. The fit results in a scaling exponent of $\alpha = (1.09 \pm 0.01)$ and a velocity $v_{GI} = (24.02 \pm 0.88)$ Å/ns. Both values are still significantly overestimated compared to the expected values derived from the transmission calculations, as such reproducing the overestimation seen in section 7.1.3. This shows that the global fit approach does not change the general characteristics of the extracted dynamics, but minimizes variances in the extracted data.

7.3 Summary and Discussion

Combining the results from this chapter of the thesis indicates several points for the extracted dynamics from XPCS and GI-XPCS calculations: I) The dynamics extracted from the implemented transmission XPCS calculations are in good agreement with the dynamics from the underlying MD simulations. II) The extracted dynamics from the GI-XPCS calculations in detector reciprocal space q show deviations from the transmission XPCS calculations and the underlying MD simulations, overestimating the expected velocity and scaling exponent, moreover obfuscating the underlying ballistic motion. III) When moving within the GI-XPCS calculations from detector reciprocal space q to intrinsic reciprocal space Q, by including refraction effects, the deviations in the extracted velocity and scaling exponent are significantly reduced. IV) Applying a global fit to extract the GI-XPCS dynamics over all simulated grazing incident angles further equalizes the extracted GI dynamics with its transmission reference. From these four points, several conclusions can be derived and applied to real experiments.

The points (II) and (III) indicate that the observed deviations in extracted dynamics from GI-XPCS calculations can be explained in large parts by refraction effects. As the refraction effects are highly non-linear in their projection on the detector reciprocal space q along the z-direction (see Figure 7.13) this indicates for real GI-XPCS experiments that the ROIs in highly distorted q_z regions should not be included in the analysis. This agrees with the results of the scaling analysis in chapter 6 (Figure 6.7), which also showed that the deviations of decorrelation times extracted from grazing incidence XPCS decrease with increasing q_z and that the highest deviations are visible for intermediate q_z values around the Yoneda region. Unfortunately, these distorted q_z regions around the Yoneda have increased photon statistics in real experiments. While q_z regions above the specular peak position, which have a near-linear dependence between intrinsic and detector reciprocal space, often cannot be evaluated due to the lack of a sufficient number of photons or need elaborate strategies to reduce beam damage within the examined sample to increase the number of scattered photons. This complicates data analysis in real experiments, as q_z regions cannot be easily excluded. Furthermore, point (IV) indicates that even after including refraction effects within the simulations a dependence on the incident angle Θ_i is seen, as concluded from the incident angle-dependent cross-dependencies between fit parameters α and $v_{GI(Q)}$. One possible reason for this dependency is related to the Fresnel coefficient calculations shown in Chapter 6. The calculations showed for different material systems, that especially for low incident angles intermediate q_z regions and even the reciprocal space above the specular peak position are dominated by a superposition of the different sDWBA scattering terms, while in contrast for higher incident angles above the specular peak position scattering from BA scattering dominates. This angle-dependent behaviour is seen for both the detector and intrinsic reciprocal space vector scaling analysis, in which particularly for the q regions below the specular peak position at low incident angles deviations from the linear behaviour are observed. As already shown in points (II) and (III), point (IV) also shows that for bulk-sensitive GI-XPCS experiments the qualitative analysis of q_z regions that are distorted by several scattering terms.

However, if a back calculation can be carried out to generate an undistorted scattering signal, q_z regions dominated by several scattering terms can be analyzed, which has the advantage that high signal intensities are often recorded in these regions. One method to receive undistorted data from GISAXS measurements was presented by Liu & Yager,[161] in which a method was derived to recover an estimate of the true undistorted scattering pattern, based on fitting experimental GISAXS images at multiple incident angles. The undistorted image derived by Liu & Yager is equivalent to the calculated SAXS images in intrinsic reciprocal space Q. As such it is expected to also lead to a significant reduction in dynamical distortions, when used for a XPCS reconstruction. Unfortunately, the 2D data reconstruction method is computation-intensive and dependent on the measurement of several incident angles, to disentangle the scattering channels Tc and Rc. Furthermore, until now the reconstruction method was only applied for well-ordered, static samples. Especially for XPCS measurements in which the structure factor is changing with time, several reconstructions would be necessary, further increasing the necessary computation time. Also, the measurements at several incident angles would need a good reproducibility in time, so that the same changes in structure factor occur at the same time for all measured incident angles. In addition, coherent effects will likely play another role. For example the speckle size needs to be optimized to overlap with the pixel size, to allow for the method to converge in a high-quality reconstruction of the undistorted coherent-scattering and to not split speckles over different detector regions.

However, the advantages of Liu & Yager's method are speculations. So far, no GI-XPCS measurements have been reconstructed in this way in intrinsic reciprocal Q space, because the low photon number and the often limited reproducibility in GI-XPCS measurements makes 2D data reconstruction difficult. Nevertheless, if a dynamic measurement system can be found which offers sufficient photon statistics and is reproducible, this offers the possibility to verify the simulations carried out in this section of the thesis and the proposed effect of reproduced transmission XPCS dynamics can be verified. Furthermore, the analysis on the translation of ballistic motion in a particle melt from transmission to GI-XPCS presented here is of interest for various material systems as ballistic motion, together with diffusive motion, is a cornerstone of the dynamics in condensed matter systems. For example, the ballistic particle motion analyzed here governs phenomena such as active motion by thermophoretic forces[385] or the merging of interfaces during spinodal decomposition in colloidal particle emulsions.[180, 181] The analyses carried out in this chapter thus make it possible to understand some of the fundamental dynamics that are relevant in many condensed matter systems. Consequently, a follow-up project should investigate whether the results extracted here also retain their validity for diffusive motion.

8 Conclusion and Outlook

The work presented in this thesis shows I) that the optoelectronic properties of organic hybrid lead halide perovskites depend strongly on its structure on a broad range of length scales. The thesis further shows II) that the interplay of structures over a wide range of length scales influences the corresponding structural kinetics over the whole length scale range. In addition, the thesis presented III) how coherent scattering methods can be applied to measure the dynamics of structural changes in organic hybrid lead halide perovskite thin films.

From the work in Chapter 4 I can conclude that systematic differences in organic hybrid lead halide perovskite processing routes can be extracted from optoelectronic properties tracked during the processing. By monitoring both the absorption and photoluminescence in-situ during the structure formation process, I could show that a systematic variation in the kinetics of the thin film formation exist and that this variation determines the final film structure. I applied the optoelectronic in-situ approach to compare the film formation during spin and slot-die coating for one-step processing of an organic hybrid lead halide perovskite from solution. Thus, I carried out pioneering work in elucidating the evolution of the optoelectronic properties of organic hybrid lead halide perovskites for two major solution-based processing methods that are currently used in lab and fab. The work further demonstrated that the evolving microscopic and macroscopic perovskite and pre-cursor solvate structures cannot be resolved by a single optical property and that the interdependency of optical properties must be taken into account to follow the processing routes. For example, the initial increase in OD can only be attributed to the formation of pre-cursor solvate structures by the simultaneous measurement of an increase of the scattering LED and an absence of the photoluminescence. However, other effects such as quantum confinement effects and changes in the wet film thickness must also be taken into consideration to fully characterize the recorded optical spectra and attribute the observed spectral features to structural changes within the forming thin films.

The work in Chapter 5 revealed that imidazolium-based ionic liquids lead to enhanced halide migration, when added in a mixture of two different dry-processed organic hybrid lead halide perovskite powders. These ionic liquids are commonly applied to hinder halide migration and enhance the phase-segregation stability of solid solutions of mixed halide perovskites under illumination, but result in an opposing effect when added to a mixture of two organic hybrid lead halide perovskite powders. The accelerated halide migration was investigated by applying different in-situ methods to study the structural rearrangements during thermally induced halide mixing. I used XRD to study the kinetics of halide transport and combined it with PL and NMR measurements from cooperation partners to evaluate the halide transport on different length scales, from the single nuclei environment up to mesoscopic perovskite grains. The combined measurements demonstrated that the addition of imidazolium-based ionic liquids result in halide-specific increases of the halide migration rates

and activation energies for halide transport, equilibrating both. This equilibration in migration rates and activation energies may be a cornerstone of the phase-segregation stability under illumination reported earlier, when fully mixed solid solutions are examined. This is also supported by current theories of segregation, which assume a difference in the activation energies of halide transport and the resulting halide migration rates. Thus my presented work is a step towards understanding the underlying stability mechanism of mixed halide perovskite materials, necessary for the next-generation tandem solar cells.

The work in the Chapters 6 and 7 demonstrated that bulk-sensitive measurements are necessary to further elucidate dynamical processes in organic hybrid lead halide perovskite thin films. The method of GI-XPCS was introduced and I was able to quantify dynamics in thin films, which are prone to misinterpretation of calculated correlation functions. By simultaneous measurements of XPCS in a grazing incidence transmission and grazing incidence geometry, I identified reciprocal space vectors and their respective detector regions with strongly reduced distortions, by combining refractivity with Fresnel coefficient calculations. The distortions were further quantified by MD simulations and subsequent scattering calculations, revealing the origin of the observed distortions. At the same time, the effect of the distortions in GI-XPCS measurements for the fundamental class of the ballistic motion was quantified. With these works I demonstrated that while the interpretation of GI-XPCS for lead halide perovskites thin films is challenging, with the appropriate care during analysis a good measure of undistorted dynamics can be extracted.

Overall, with the work in the present thesis I have contributed to answering relevant scientific questions on the kinetics and dynamics of structural formation processes of organic hybrid lead halide perovskites and identified potential approaches for addressing these questions. The work demonstrated that the identified approaches can be used to elucidate processes such as thin film formation from solution for different processing routes or halide transport in phase-segregated organic hybrid lead halide perovskites. Based on the presented results, I suggest that future studies further focus on in-situ measurements. As organic hybrid lead halide perovskites are highly dynamical, especially their defect chemistry, in-situ investigations will help to address some of the most urgent questions about dynamical processes. For the different presented projects within my thesis I suggest different follow-up projects to address still-open questions.

For example, the work in Chapter 4 can be expanded to explore the still unresolved role of lead solvate states in precursor solutions during thin film formation. These lead solvate states often form before or concurrently with precursor solvate structures, but their exact role for the final morphology and how the various concentration dependent species form dynamically during processing are poorly investigated. To expand knowledge on such lead solvate states, the measurement approach which was demonstrated within the thesis, needs to be altered. This can be achieved by extending the spectral range in the in-situ absorption measurements to the UV-range, i.e. the spectral range in which the lead solvates absorb. With such changes the simultaneous approach of photoluminescence, scattering and absorption can resolve lead solvate states and their dependency on dynamically evolving precursor concentrations, derived from wet film thicknesses. By tackling these initially forming lead solvate states, one of the outstanding challenges of processing of organic hybrid lead halide perovskites from solution can be addressed.

Furthermore, based on the results in Chapter 5 I suggest that future studies address the non-equilibrium conditions in halide migration rates and activation energies and identify the underlying mechanism of phase-segregation and halide mixing. While it is already well known that halide migration depends on grain sizes and is mainly surface-mediated for small grain sizes (order of magnitude of 1 µm) and bulk-mediated for bigger grain sizes, the underlying process leading to the size-dependent mediation change is not understood. I propose that by further analyzing mixed halide lead perovskite systems with in-situ methods on different length scales this knowledge gap can be bridged. This requires identification of suitable phase formation models from which the underlying length scale dependent halide migration and the connected structural formation mechanism can be derived. Possible models describing the halide migration and the connected structural reformation may be e.g. a Johnson-Mehl-Avrami phase transformation, Boltzmann-Matano plane interdiffusion of halides or non-linear recrystallization at connected grain boundaries of differing halide perovskite species. A fundamental understanding of the underlying mechanisms of halide migration is a prerequisite for tackling the still occurring stability problems in solar cells of mixed halide lead perovskites and paving their way for commercialisation.

Moreover, I propose to further apply the GI-XPCS method introduced in Chapters 6 and 7 as an effective means of measuring a wide range of in-situ processes without the distortions that occur without careful data analysis. As the presented approach is bulk-sensitive and can be applied for thin film measurements the opportunity arises to apply it for measurements of depth-dependent processes. Of interest to the lead halide perovskite community are further measurements of processes such as the ionization of perovskite thin films for X-ray detector applications, the characterization of degradation processes in the thin film bulk or to further follow the halide migration in mixed halide perovskites. Here both processes such as thermally induced halide migration or halide migration due to externally applied electrical fields are still of interest. In regards to this a setup for GI-XPCS measurements at beamline 11-ID at the NSLS-II is currently under preparation. For this I devised an atmospherical chamber with X-ray-permeable Kapton windows, which is presented in Figure 8.1. Within the atmospherical chamber a thin film sample can be mounted, on which external electrical fields up to field strengths of $\pm$ 2.5 keV can be applied. The mount for the external electrical field application is devised so that a reciprocal space vector up to $1.4\,\text{Å}^{-1}$ along the surface normal can be measured, allowing for simultaneous GI-XPCS and GI-WAXS measurements. The atmosphere in the chamber can be switched from pure nitrogen or dry air towards adjustable degrees of solvent atmospheres, due to a combination of adjustable mass flow meters and an integrated gas washing bottle. Furthermore, the thin film substrate holder is heatable up to 180 °C and coolable down to −15 °C under RT due to a Peltier element and a water cooling system placed below the copper substrate holder. The copper substrate holder is connected to the chamber via a magnetic suspension system via four arms, which each have a thermal decoupling element made of quartz glass between the suspension arm and the chamber. This mount has the distinct advantage that during heating the thermal expansion of the copper substrate holder is directed away from the sample placed on the substrate holder, as such adjustments to the measurement height of a GI-XPCS experiments are not necessary during e.g. heating cycles. The quartz glass elements further serve as a decoupling element between electrical charges between the chamber casing and the substrate holder. The

proportions of the chamber are devised to allow for simultaneous photoluminescence measurements of the thin films. The combination of photoluminescence with GI-XPCS will allow the simultaneous measurement and observation of optoelectronic and structural properties and may directly allow linking kinetic properties extractable from the photoluminescence and GI-WAXS (e.g. phase transformation rates or halide migration rates) to the dynamical properties of the examined samples. With the plethora of external stimuli, which can be applied in the athmospherical chamber, such a simultaneous measurement approach between GI-XPCS, photoluminescence and GI-WAXS, will be a valuable tool to further study the kinetic and dynamic phenomena covered within the thesis.

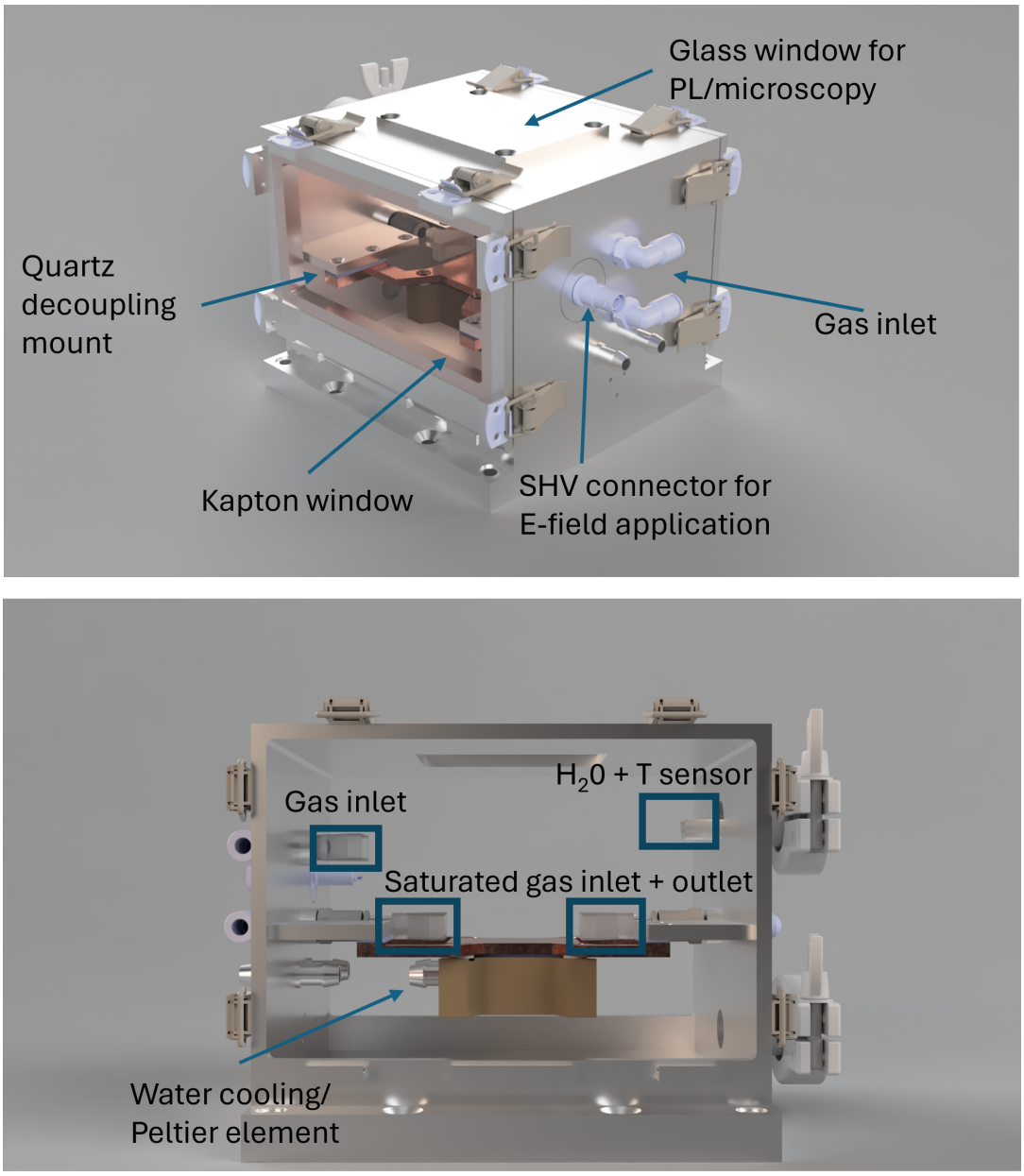

Figure 8.1: 3D rendering of the atmospherical chamber described in Chapter 8. The highlighted features and possible application areas are described within the text.

A. List of Abbreviations

1TCF	One-time correlation function
2TCF	Two-time correlation function
$BMIMBF_4$	1-butyl-3-methyl-imidazolium tetrafluoroborate
$BMIMPF_6$	1-butyl-3-methyl-imidazolium hexafluorophosphate
CB	conduction band
CBM	conduction band minimum
CCD	charged coupled device
DFT	discrete Fourier-transformation
DI	deionized
DMF	dimetyhlformamide
FWHM	full width half maximum
GIWAXS	grazing incidence wide angle X-ray scattering
GISAXS	grazin incidence small angle X-ray scattering
GI-XPCS	grazing incidence X-ray photon correlation spectroscopy
GIXS	grazing incidence X-ray scattering
GTSAXS	grazing incidence transmission small angle X-ray scattering
GT-XPCS	grazing incidence transmission X-ray photon correlation spectroscopy
HOIP	hybrid organic-inorganic perovskite
IL	ionic liquid
KWW	Kohlrausch-Williams-Watts
LED	light-emitting diode
LJ	Lennard-Jones
MABr	methylammonium bromide
MAI	methylammonium iodide
$MAPbBr_3$	methylammonium lead bromide
$MAPbI_3$	methylammonium lead iodide
MD	molecular dynamics
MHP	metal halide perovskite
MSD	mean square displacement
NMR	nuclear magnetic resonance
NQR	nuclear quadrupole resonance
NVE	micro-canonical ensembe
OD	optical density
OM	optical microscopy
P3HT	Poly(3-hexylthiophen-2,5-diyl)
PbI_2	Lead(II) Iodide
$PbBr_2$	Lead(II) bromide
PL	Photoluminescence
PLQE	Photoluminescence quantum efficiency
ROI	region of interest

SDD	sample-detector distance
(s)DWBA	(simplified) distorted wave Born approximation
SEM	scanning electron microscopy
TER	total external reflection
THF	Tetrahydrofuran
UV-Vis	ultraviolet-visible
VB	valence band
VBM	valence band maximum
XPCS	X-ray photon correlation spectroscopy
XRD	X-ray diffraction
ZrO_2	Zirconium(IV) oxide

B. Appendix

Full intensity heat maps of the in-situ optical data for Chapter 4

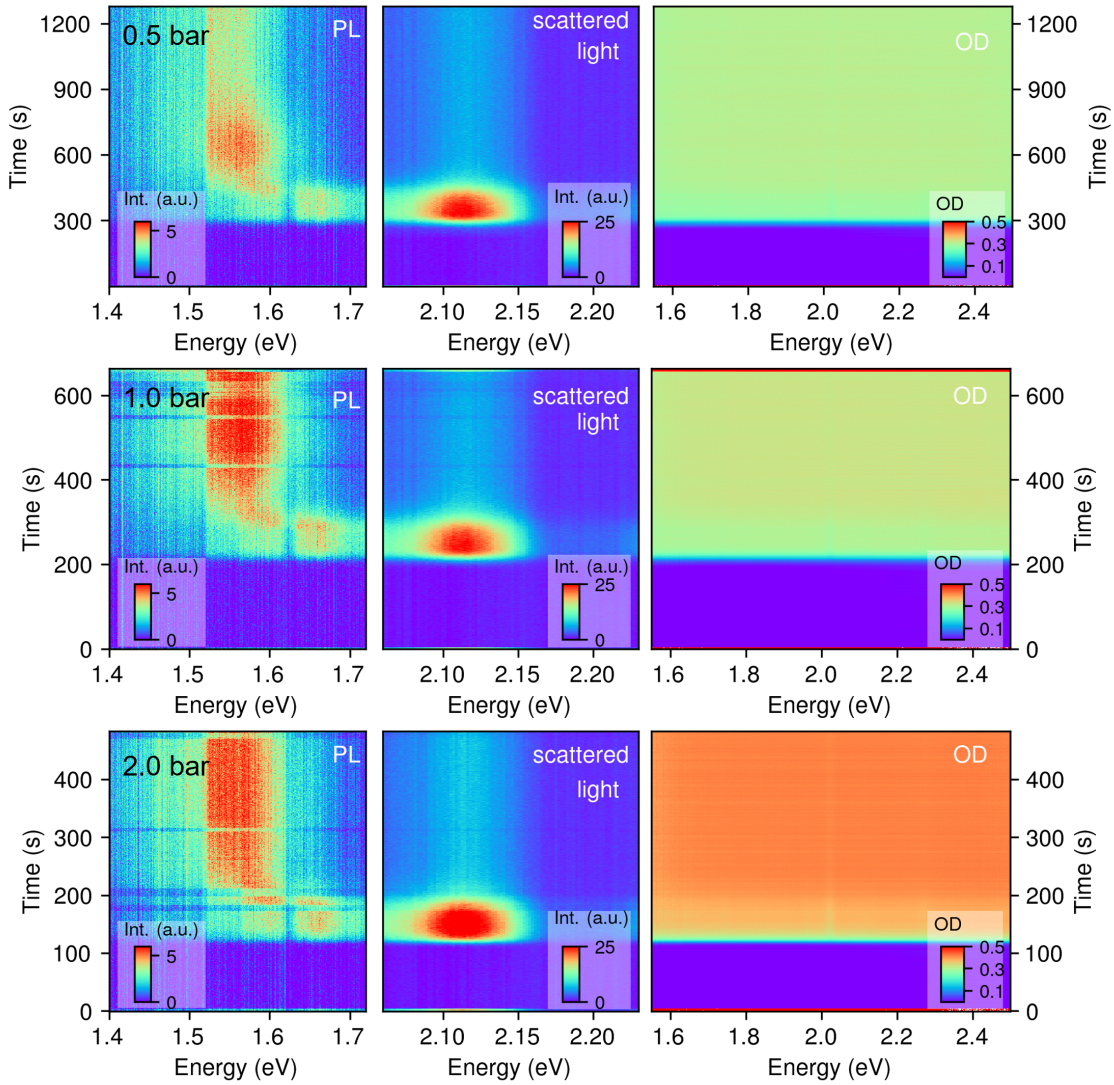

Figure 8.2: 2D intensity maps of the in-situ photoluminescence spectra (PL, left), the in-situ scattered room light spectra (middle) and the in-situ optical density (OD, right) measured during one-step slot-die coating from DMF of $MAPbI_3$ thin films for air-knife pressures between 0.5 bar to 2.0 bar.

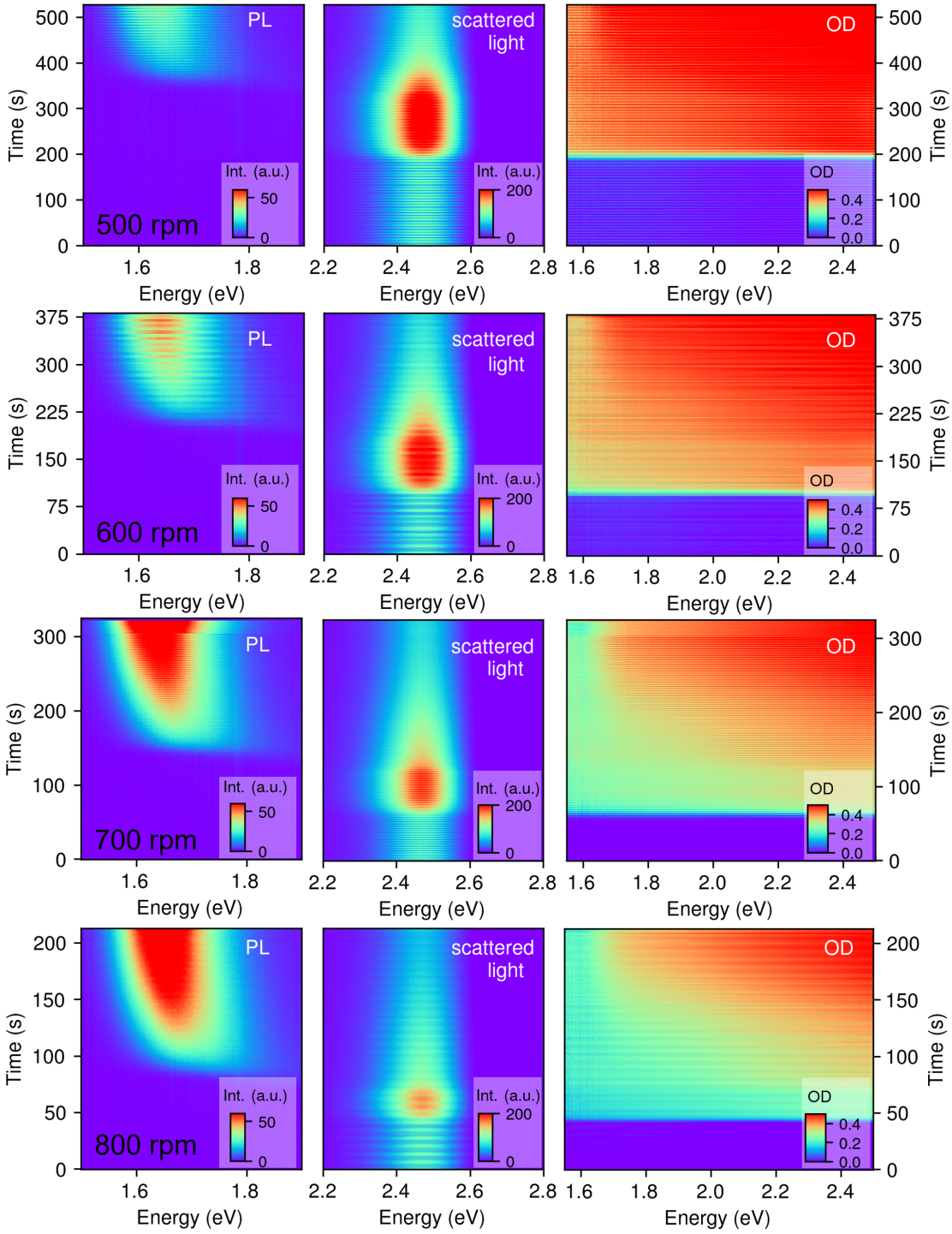

Figure 8.3: 2D intensity maps of the in-situ photoluminescence spectra (PL, left), the in-situ scattered LED light spectra (middle) and the in-situ optical density (OD, right) measured during one-step spin coating from DMF of $MAPbI_3$ thin films for spin speeds from 500 to 800 rpm.

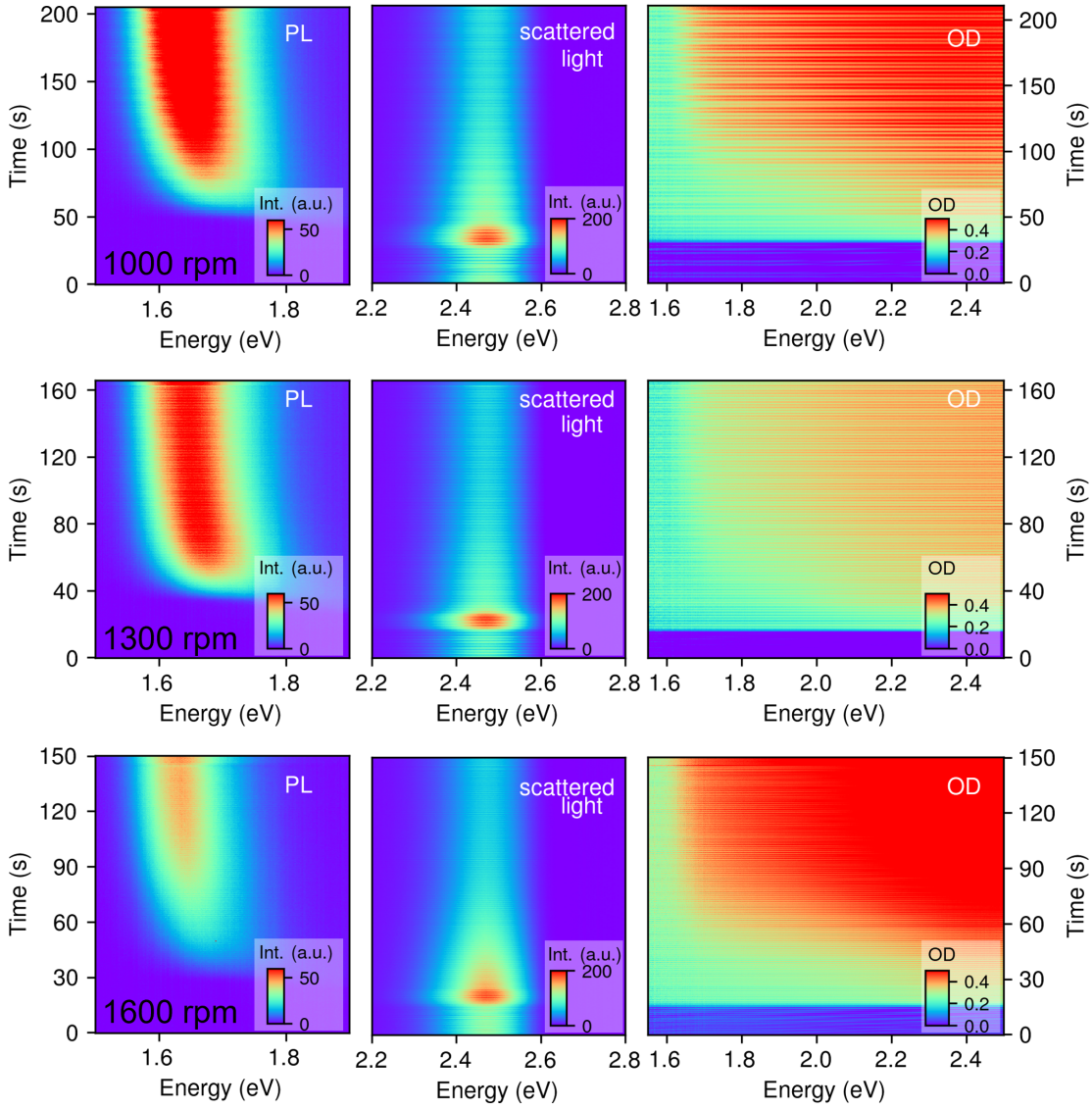

Figure 8.4: 2D intensity maps of the in-situ photoluminescence spectra (PL, left), the in-situ scattered LED light spectra (middle) and the in-situ optical density (OD, right) measured during one-step spin coating from DMF of $MAPbI_3$ thin films for spin speeds from 1000 to 1600 rpm.

Time evolution of the extracted optical parameters of the in-situ optical data for Chapter 4

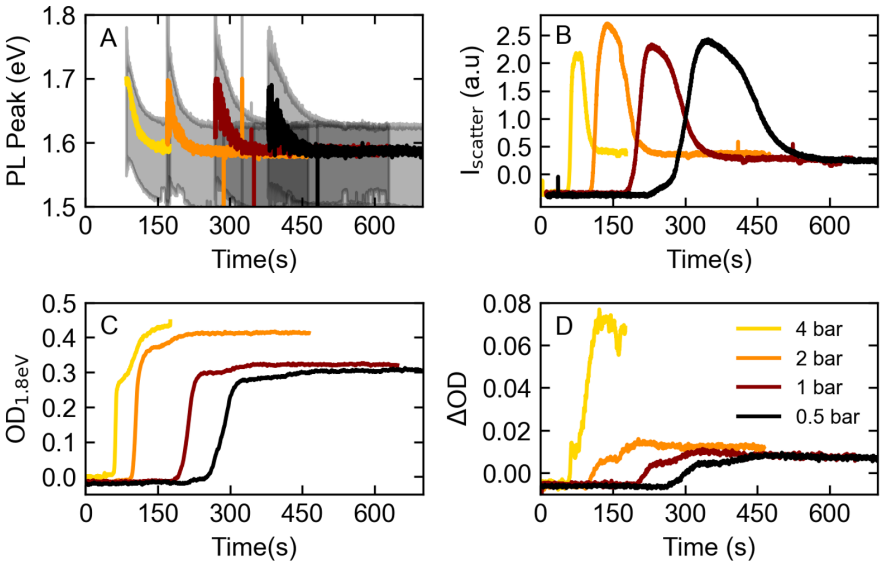

Figure 8.5: A-D: Time evolution of different optical parameters for slot-die coating $MAPbI_3$ from DMF at air-knife pressures ranging from 0.5 bar to 4 bar. A: PL peak position, the grey shaded area indicates the spectral range where the PL intensity is above 1/e of the peak intensity. B: Integrated intensity $I_{Scatter}$ of the scattered light. C: OD at 1.8 eV. D: ΔOD, difference in the OD at 1.8 eV and at 1.575 eV.

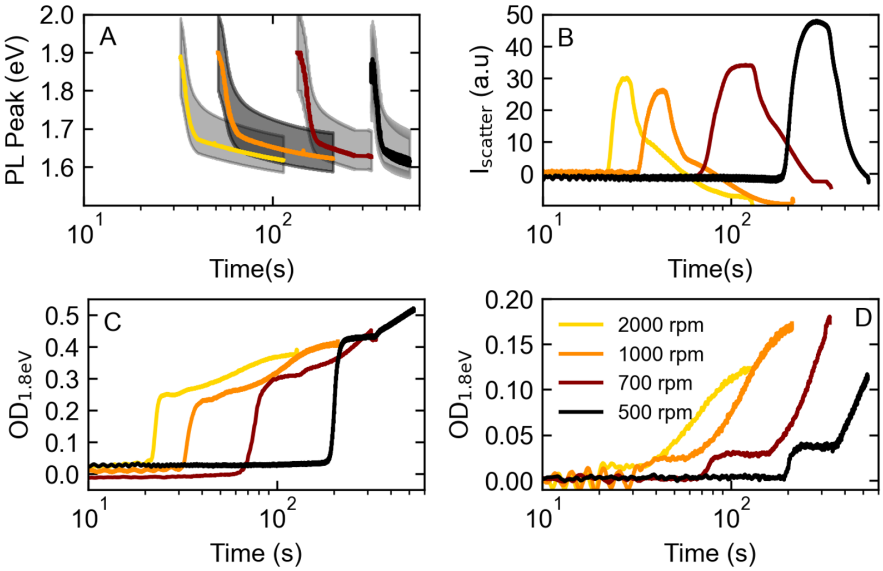

Figure 8.6: A-D: Time evolution of different optical parameters for spin coating $MAPbI_3$ from DMF at spin speeds ranging from 500 to 2000 rpm. A: PL peak position, the grey shaded area indicates the spectral range where the PL intensity is above 1/e of the peak intensity. B: Integrated intensity $I_{Scatter}$ of the scattered light. C: OD at 1.8 eV. D: ΔOD, difference in the OD at 1.8 eV and at 1.575 eV.

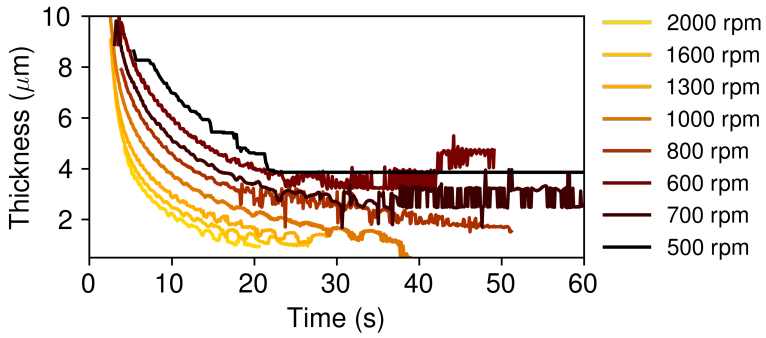

Figure 8.7: Time evolution of the thickness d of the solution layer extracted from the energetical distance ΔE of adjacent maxima in the white light interference modulations for one-step spincoating of $MAPb_3$ from DMF at 500 to 2000 rpm. The plot shows that depending on the spin speed the first discernible thickness ranges from approximately 5 µm to 10 µm and the final thickness from approximately 1 µm to 4 µm.

Overview: Reflected Optical and Scanning Electron Microscopy images of spin and slot-die coated films used in Chapter 4

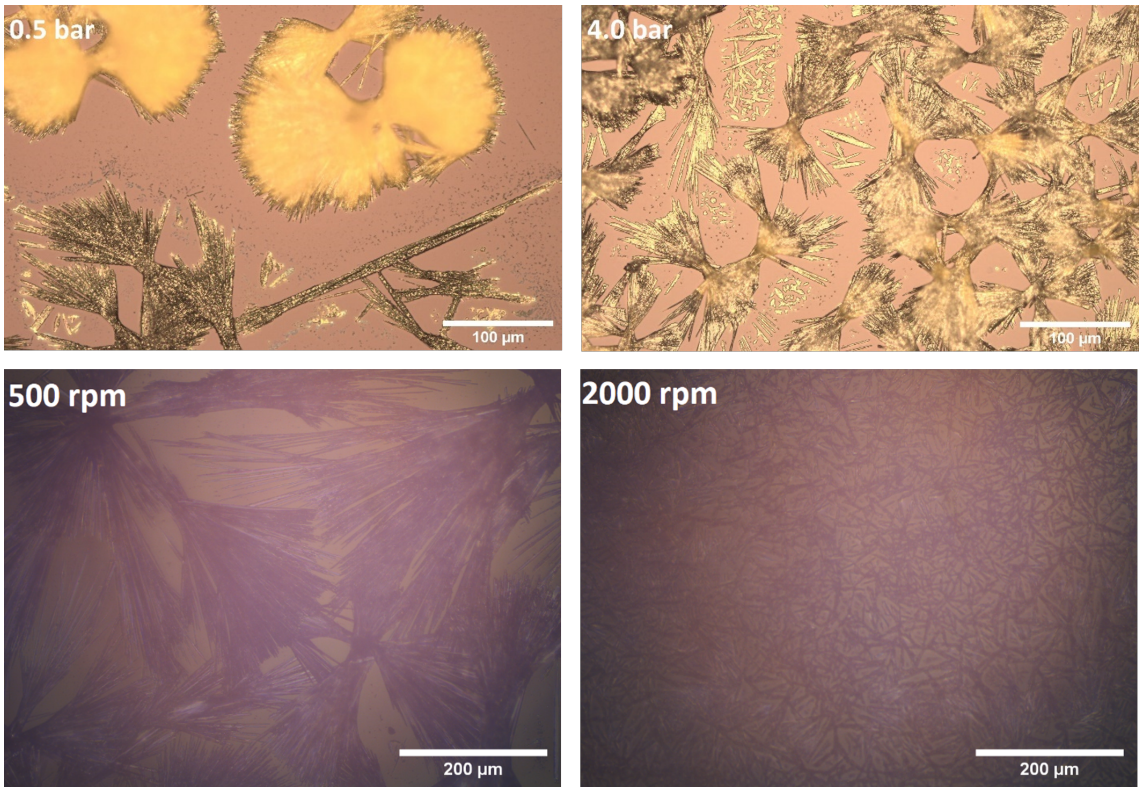

Figure 8.8: Microscopy images (20x) of $MAPbI_3$ thin films processed via one-step slot-die coating (top) from DMF with air-knife pressures of 0.5 bar and 4.0 bar and via spin coating (bottom) with spin speeds of 500 and 2000 rpm. The comparison shows that both in spin and slot-die coating faster drying kinetics lead to a more homogenously covered film with overall smaller needle-like structures.

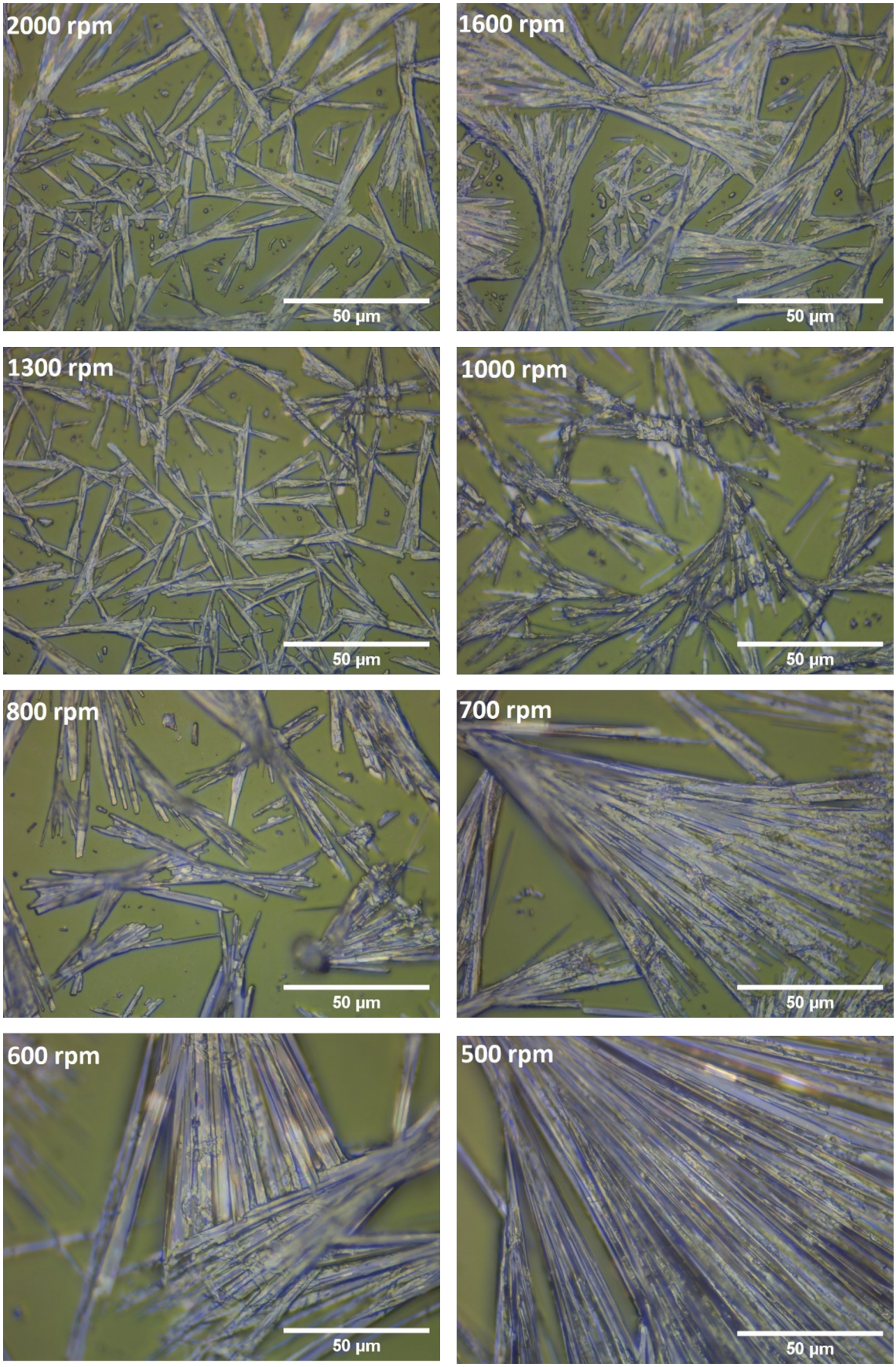

Figure 8.9: Microscopy images (100x) of $MAPbI_3$ thin films processed via one-step spin coating from DMF with spin speeds varyying between 2000 rpm and 500 rpm (see labels). From off-focal plane imaging and off-focus depictions it is evident that with decreasing rpm the height variations and therefore film roughness of the film increase.

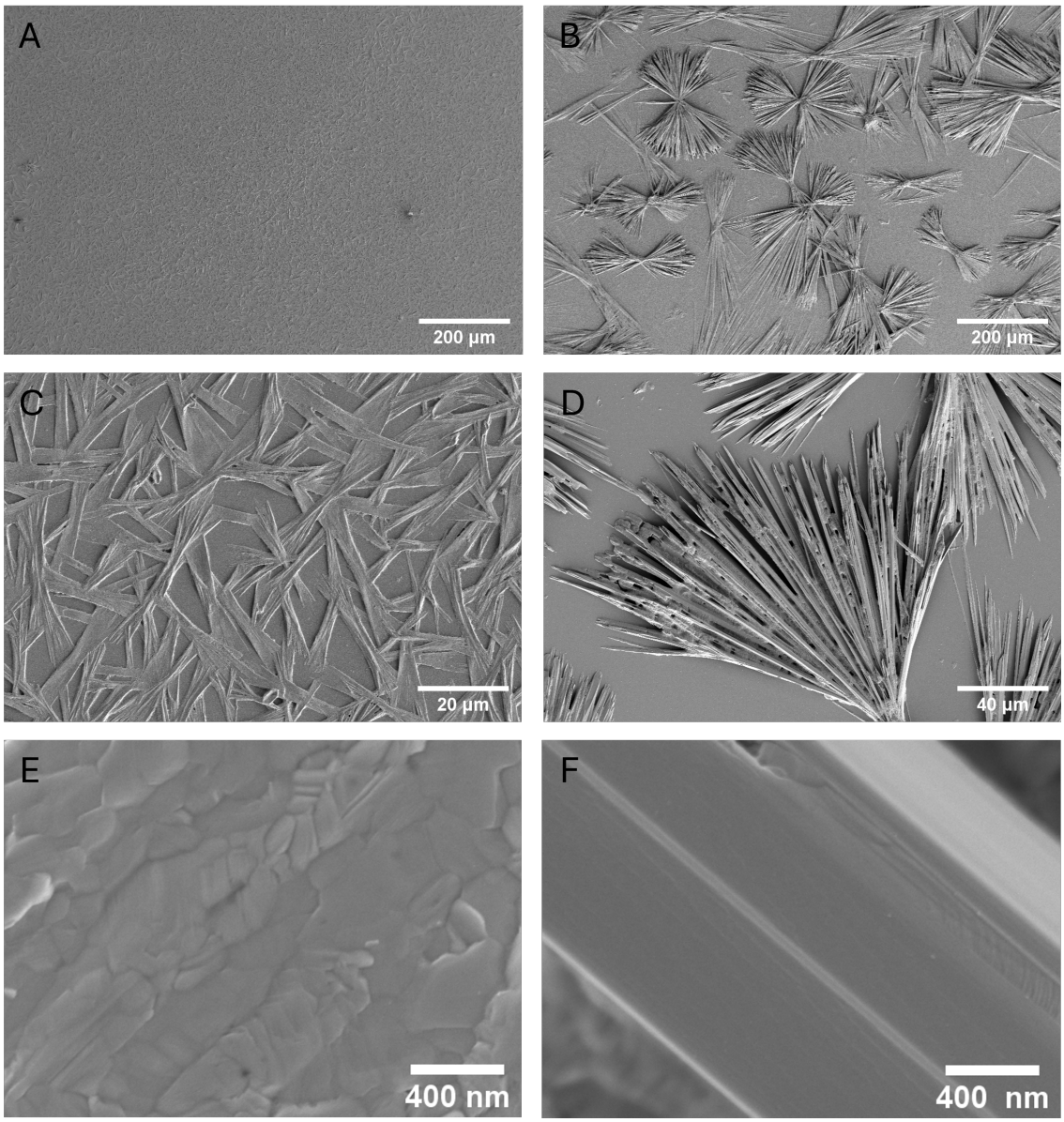

Figure 8.10: Scanning electron microscopy (SEM) images of $MAPbI_3$ thin films processed from DMF via one-step spin coating at 2000 rpm (left column) and dropcasting at an air-knife pressure of 0 bar (right column). The magnification increases from top to bottom: from (A,B) 100x, (C,D) 500x and (E,F) 25.000x. The last row shows that the surface structures of the needles varies between the two processing methods. The solely evaporation dried film (dropcasting) consists of highly crystalline structures with smoother surfaces, while in the case of spin coating the surface appears rougher, indicating a high number of small crystalline grains and their respective grain boundaries.

Exemplary Fitting of time-resolved XRD diffractograms in Chapter 5

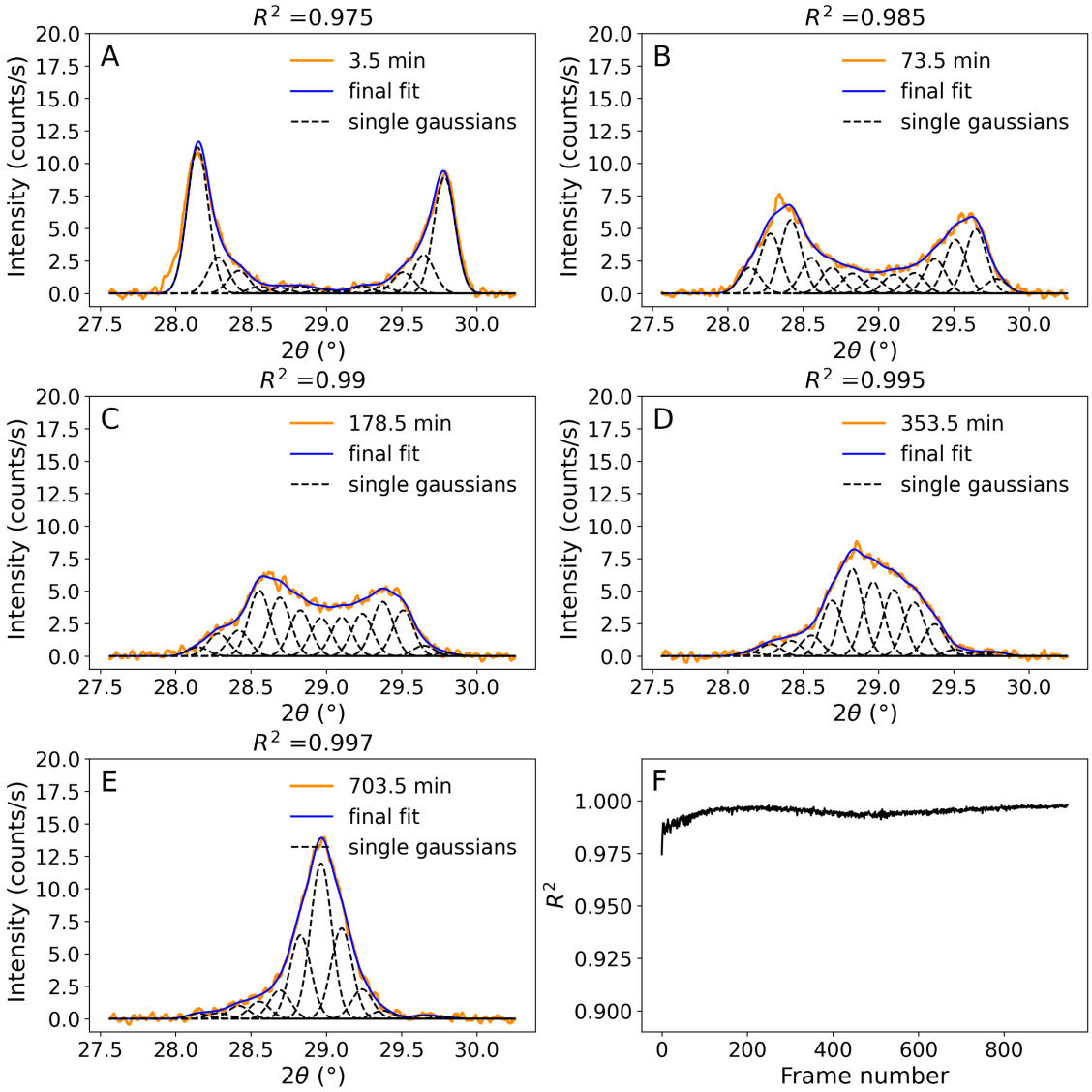

Figure 8.11: A-E) Temporal evolution of 1D XRD diffractograms for the cubic (200) $MAPbI_3$ and $MAPbBr_3$ peak positions for 1:1 $MAPbI_3$:$MAPbBr_3$ showing the initial and final fit based on Eq. 5.2 for halide mixing at 90 °C under BMIMBF4 addition. The retention time at 90 °C is indicated within the labels and R^2-values of model and data are given as subtitles. F) R^2-values as a function of frame number. Each frame is equivalent to one measurement as seen in A-E and took 3.5 min to record.

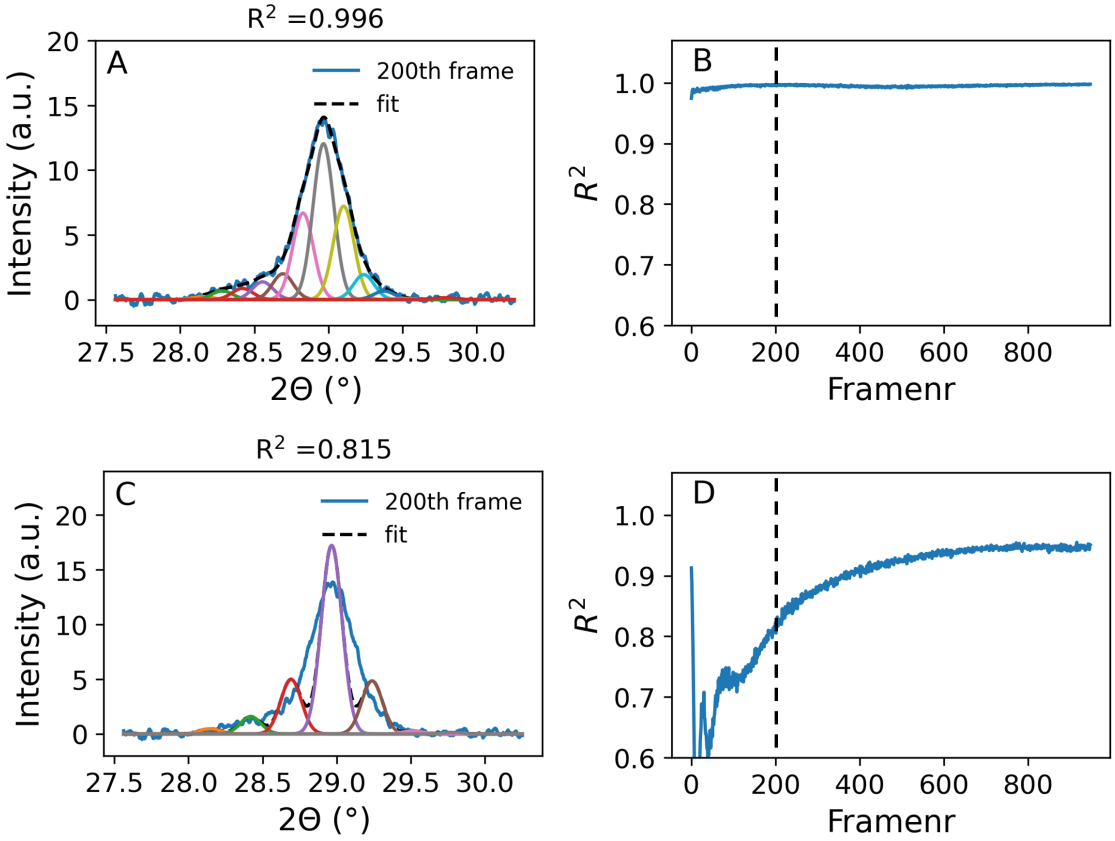

Figure 8.12: (A,C) Exemplary fitting procedure of a pXRD diffractogramm of a $BMIMBF_4$ containing sample processed at 90 °C. The fit is based on (A) 13, respectively (C) 7 equidistantly spaced Gaussians of fixed width. (B,D) Evolution of the coefficient of determination R^2 with frame number for the full mixing experiment fitted with (B) 13 or (D) 7 equidistant Gaussians. The dashed black line marks R^2 for frame number 200, shown in A,C.

XRD diffractograms of thermally induced halide mixing at 75 °C and 60 °C in Chapter 5

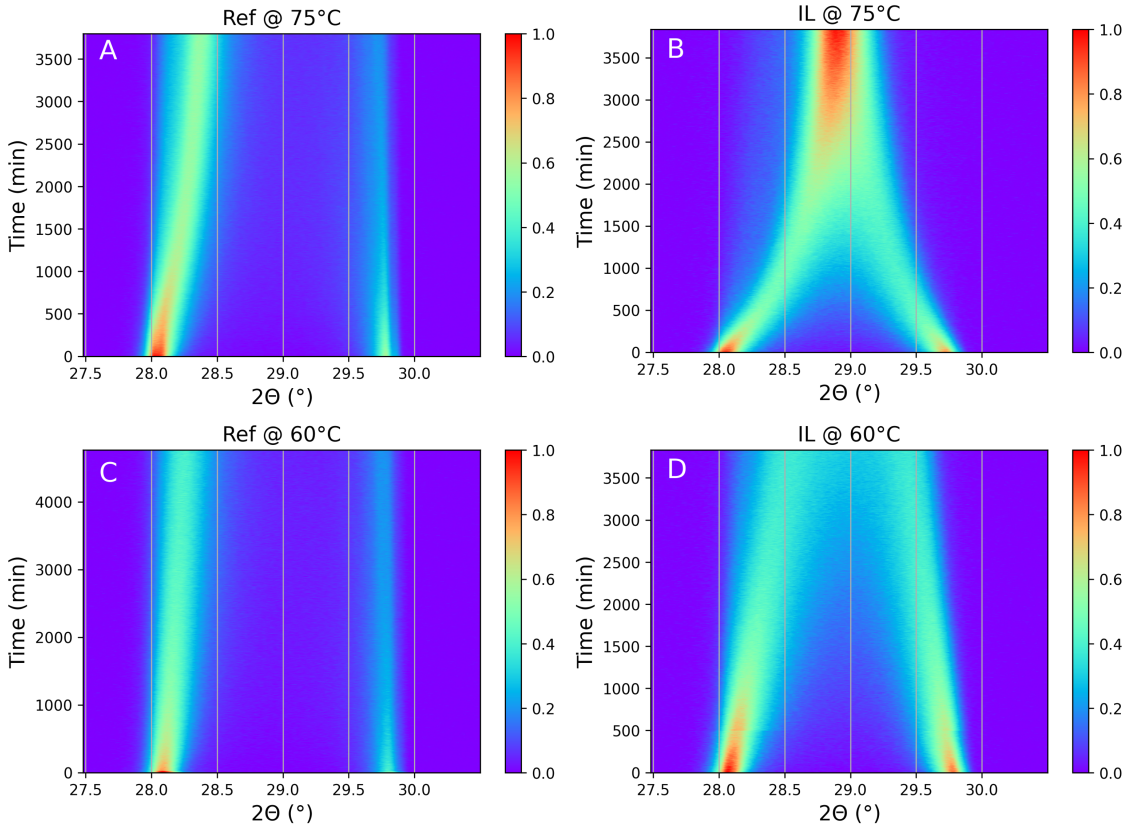

Figure 8.13: Temporal evolution of XRD diffractograms as 2D maps for the cubic (200) $MAPbI_3$ and $MAPbBr_3$ peak positions for 1:1 $MAPbI_3$:$MAPbBr_3$ mixtures (A,C) without (labelled Ref) and (B,D) with $BMIMBF_4$ (labelled IL) for halide mixing at (A,B) 75 °C and (C,D) 60 °C. The color indicates the signal intensities of evolving equivalent phases of differently mixed $MAPbI_{3-x}Br_x$ signals.

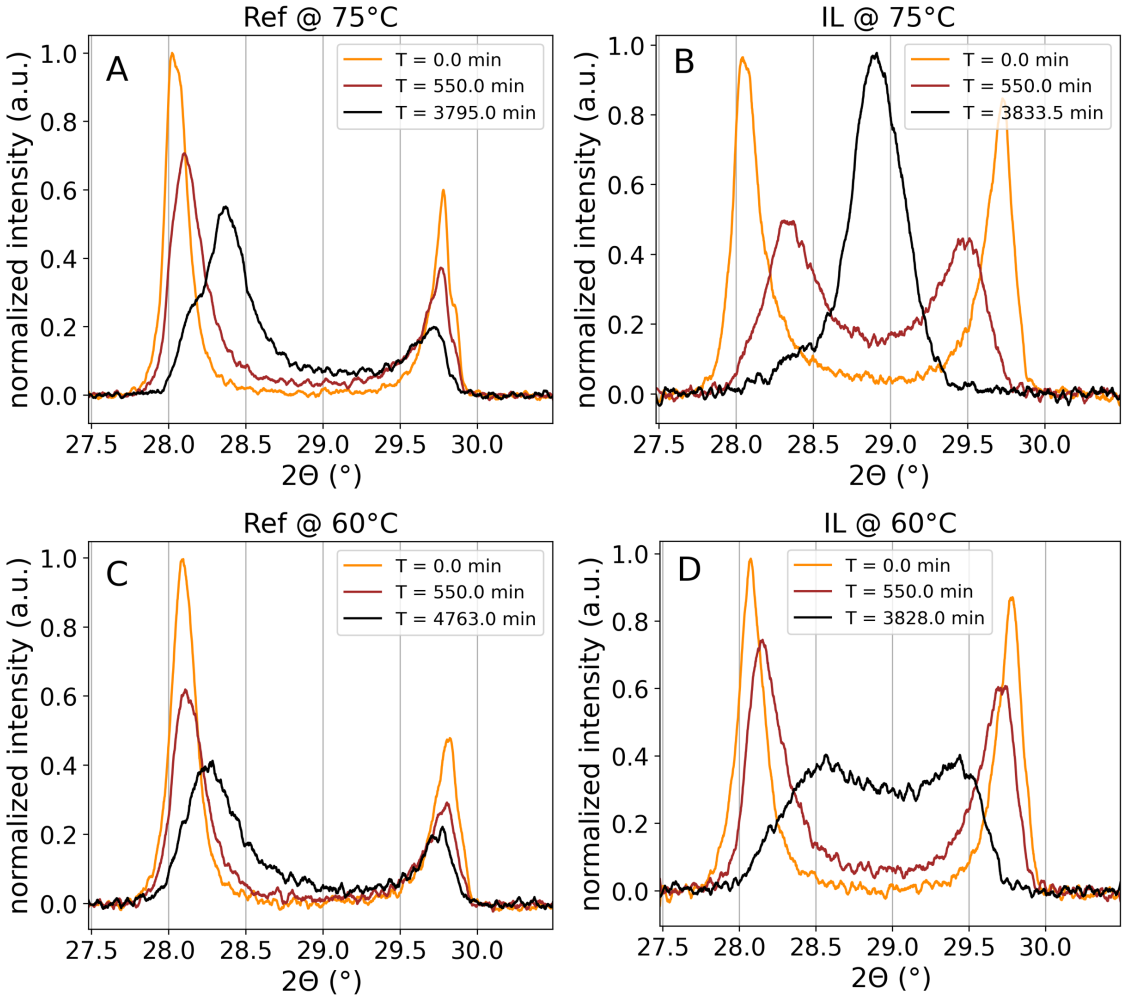

Figure 8.14: Initial, intermediate and final XRD diffractograms for the cubic (200) $MAPbI_3$ and $MAPbBr_3$ peak positions for 1:1 $MAPbI_3$:$MAPbBr_3$ mixtures (A,C) without (labelled Ref) and (B,D) with $BMIMBF_4$ (labelled IL) for halide mixing at (A,B) 75 °C and (C,D) 60 °C extracted from Figure 8.13 for the times indicated in the subfigures. The intensities were normalized to the maximum intensity seen in Figure 8.13.

Extraction of halide kinetics during thermally induced halide mixing from pure parent phase intensity decays in Chapter 5

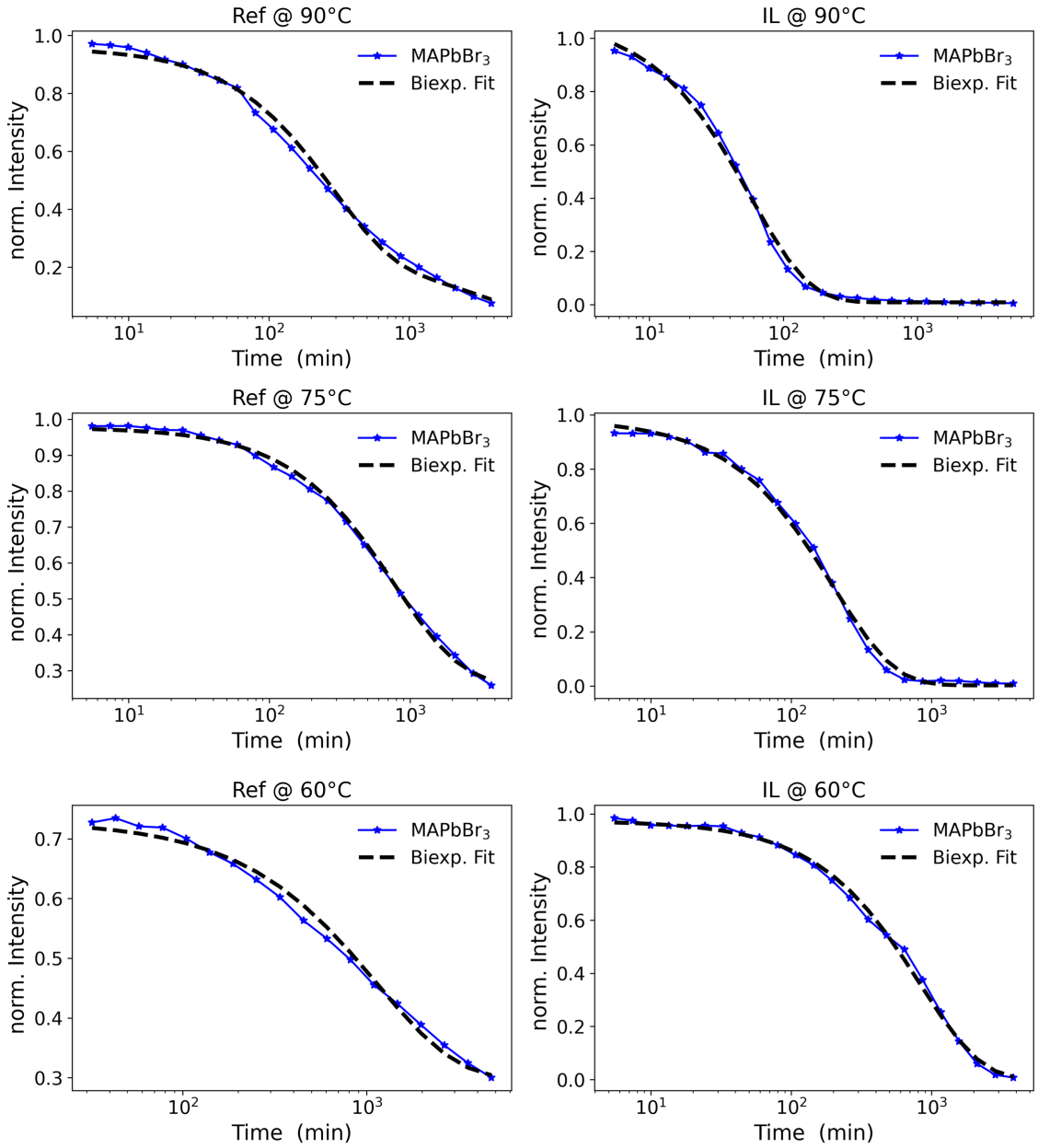

Figure 8.15: Biexponential fit of the following form: $I(t) = A_1 \cdot \exp(-t \cdot k_1) + A_2 \cdot \exp(-t \cdot k_2) + \text{offset}$, applied to the normalized intensity decays of $MAPbBr_3$ phase in physical mixtures of $MAPbI_3$:$MAPbBr_3$ mixtures synthesized without (Ref, left column) and with $BMIMPF_4$ (IL, right column) for mixing experiments at temperatures of 90 °C (top), 75 °C (middle) and 60 °C (bottom). The biexponential fit is marked as a black dashed line. Linear data points in time are resampled to a logarithmic time scale (see Section 5.4).

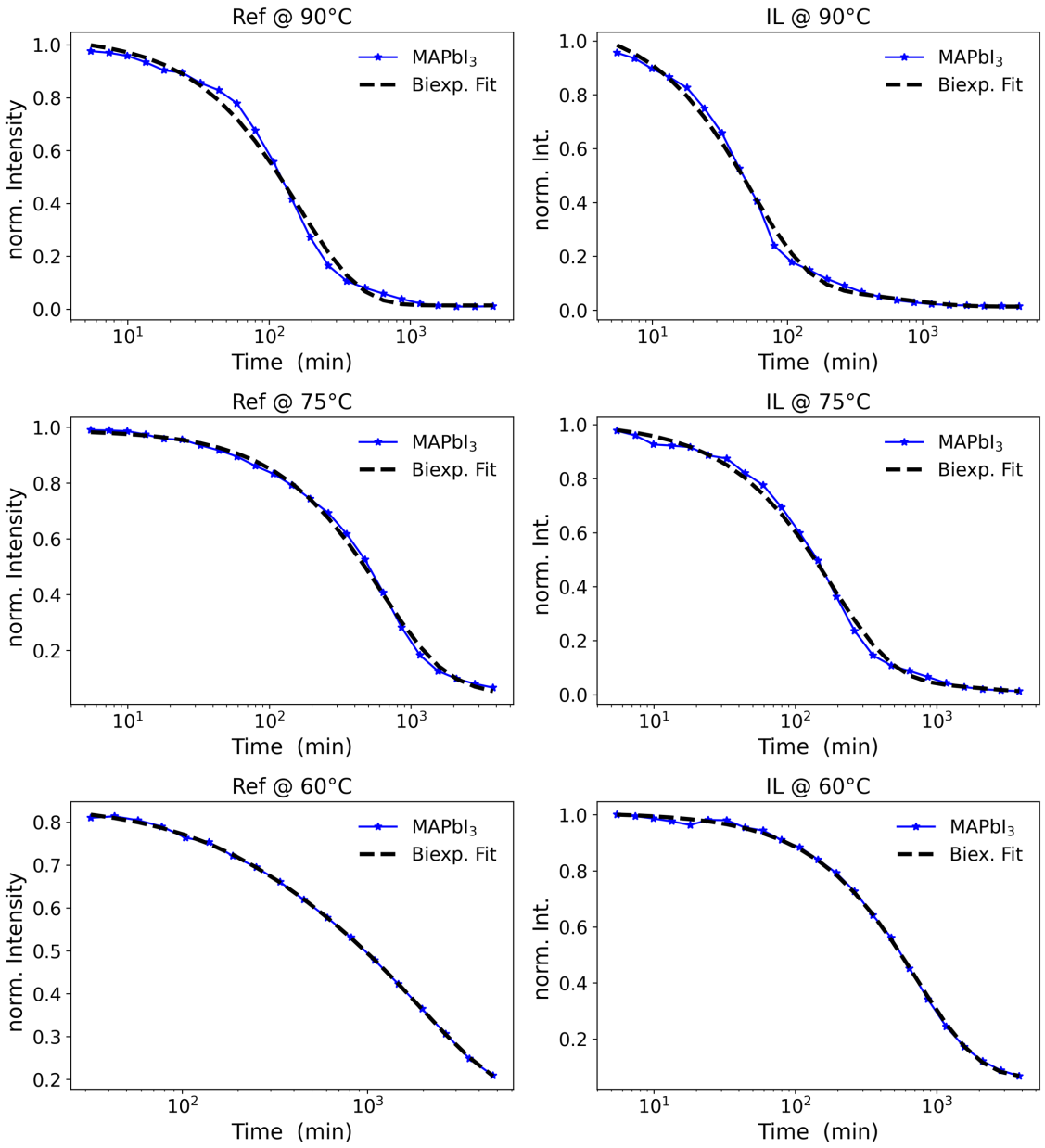

Figure 8.16: Biexponential fit of the following form: $I(t) = A_1 \cdot \exp(-t \cdot k_1) + A_2 \cdot \exp(-t \cdot k_2) + \text{offset}$, applied to the normalized intensity decays of $MAPbBr_3$ phase in physical mixtures of $MAPbI_3$:$MAPbBr_3$ mixtures synthesized without (Ref, left column) and with $BMIMPF_4$ (IL, right column) for mixing experiments at temperatures of 90 °C (top), 75 °C (middle) and 60 °C (bottom). The biexponential fit is marked as a black dashed line. Linear data points in time are resampled to a logarithmic time scale (see Section 5.4).

Ionic Liquid					
T (°C)	A_1	A_2	k_1 (min^{-1})	k_2 (min^{-1})	offset
90	0.949	0.113	1.96e-2	2.76e-3	0.017
75	0.900	0.100	5.80e-3	1.33e-3	0.011
60	0.944	0.000	1.37e-3	—	0.063
Reference					
T (°C)	A_1	A_2	k_1 (min^{-1})	k_2 (min^{-1})	offset
90	0.929	0.088	6.18e-3	6.18e-3	0.014
75	0.552	0.378	1.56e-3	1.56e-3	0.057
60	0.616	0.003	7.52e-4	—	0.199

Table 8.1: Extracted fit parameters of a biexponential fit of the following form: $I(t) = A_1 \cdot \exp(-t \cdot k_1) + A_2 \cdot \exp(-t \cdot k_2) + \text{offset}$, applied to the normalized intensity decays of $MAPbI_3$ phase from Figure 8.16.

Ionic Liquid					
T (°C)	A_1	A_2	k_1 (min^{-1})	k_2 (min^{-1})	offset
90	0.999	0.064	1.82e-2	4.61e-3	0.005
75	0.983	0.000	4.97e-3	3.00e-3	0.002
60	0.974	0.000	1.20e-3	1.14e-4	0.000
Reference					
T (°C)	A_1	A_2	k_1 (min^{-1})	k_2 (min^{-1})	offset
90	0.740	0.200	3.57e-3	2.76e-4	0.019
75	0.661	0.114	1.33e-3	1.46e-4	0.202
60	0.432	0.000	8.74e-4	2.64e-4	0.297

Table 8.2: Extracted fit parameters of a biexponential fit of the following form: $I(t) = A_1 \cdot \exp(-t \cdot k_1) + A_2 \cdot \exp(-t \cdot k_2) + \text{offset}$, applied to the normalized intensity decays of $MAPbBr_3$ phase from Figure 8.15.

Characterization of $MAPbI_3$ and $MAPbBr_3$ parent powders synthesized with $BMIMPF_6$ in Chapter 5

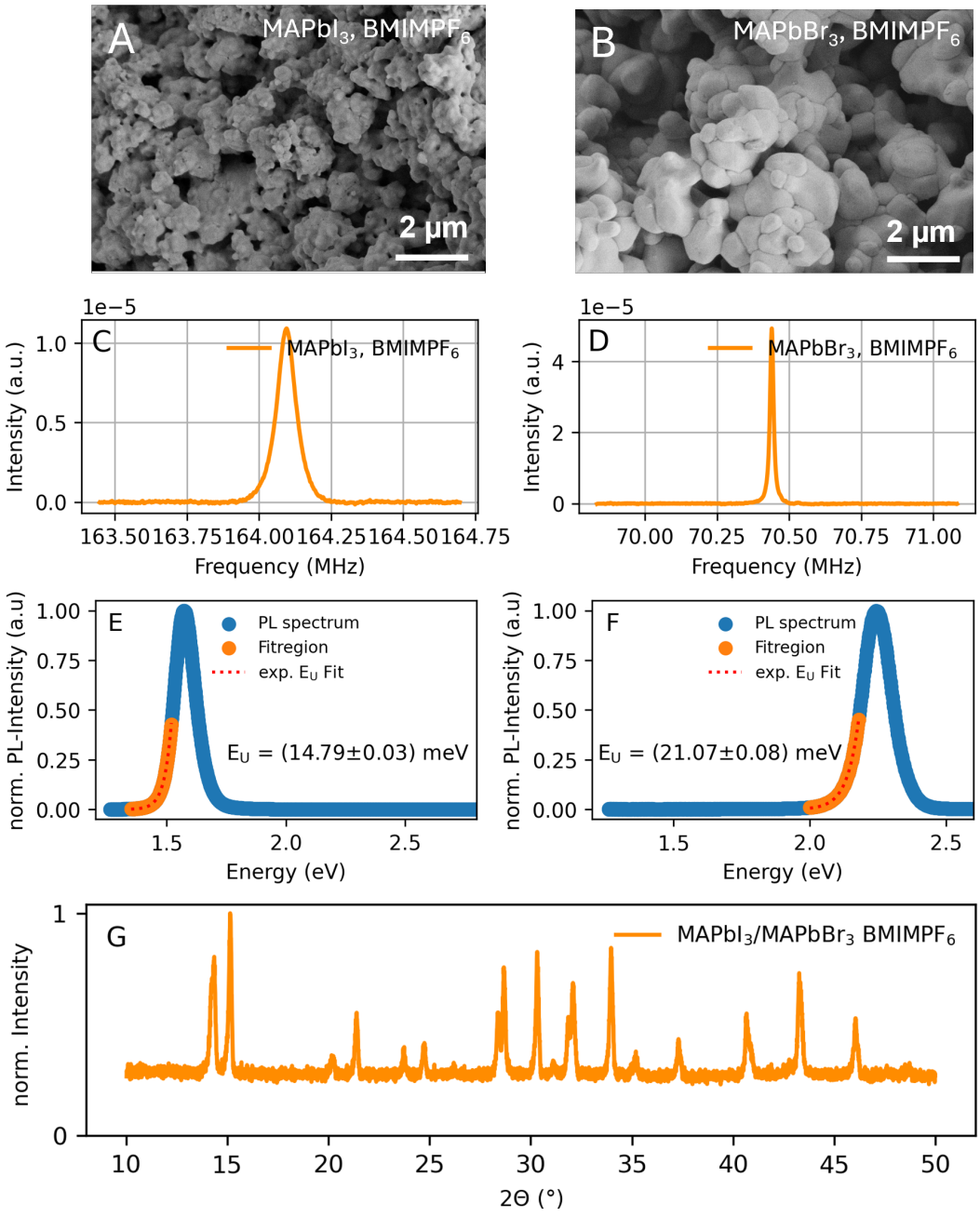

Figure 8.17: Precharacterization of $MAPbI_3$ (left column) and $MAPbBr_3$ phases (right column) synthesized with $BMIMPF_6$. (A,B) SEM images of the neat parent powders. (C) ^{79}Br and (D) ^{127}I NQR spectra of $MAPbI_3$:$MAPbBr_3$ mixtures recorded prior to mixing experiments. ^{127}I NQR spectra were recorded for the equatorial Iodine atoms in the tetragonal $MAPbI_3$ phase at RT due to limitations of the probe to tune to higher frequencies. (E,F) Normalized PL spectra (blue) of parent powders. The fit region (orange), the exponential Urbach fit (red dotted-line) and the extracted Urbach-energy E_U are labelled within the normalized spectra. (G) Normalized pXRD patterns of $MAPbI_3$:$MAPbBr_3$ mixtures at RT prior to mixing experiments.

Simultaneous GT-GI-XPCS measurements of $MAPbI_3$ thin films presented in Chapter 6

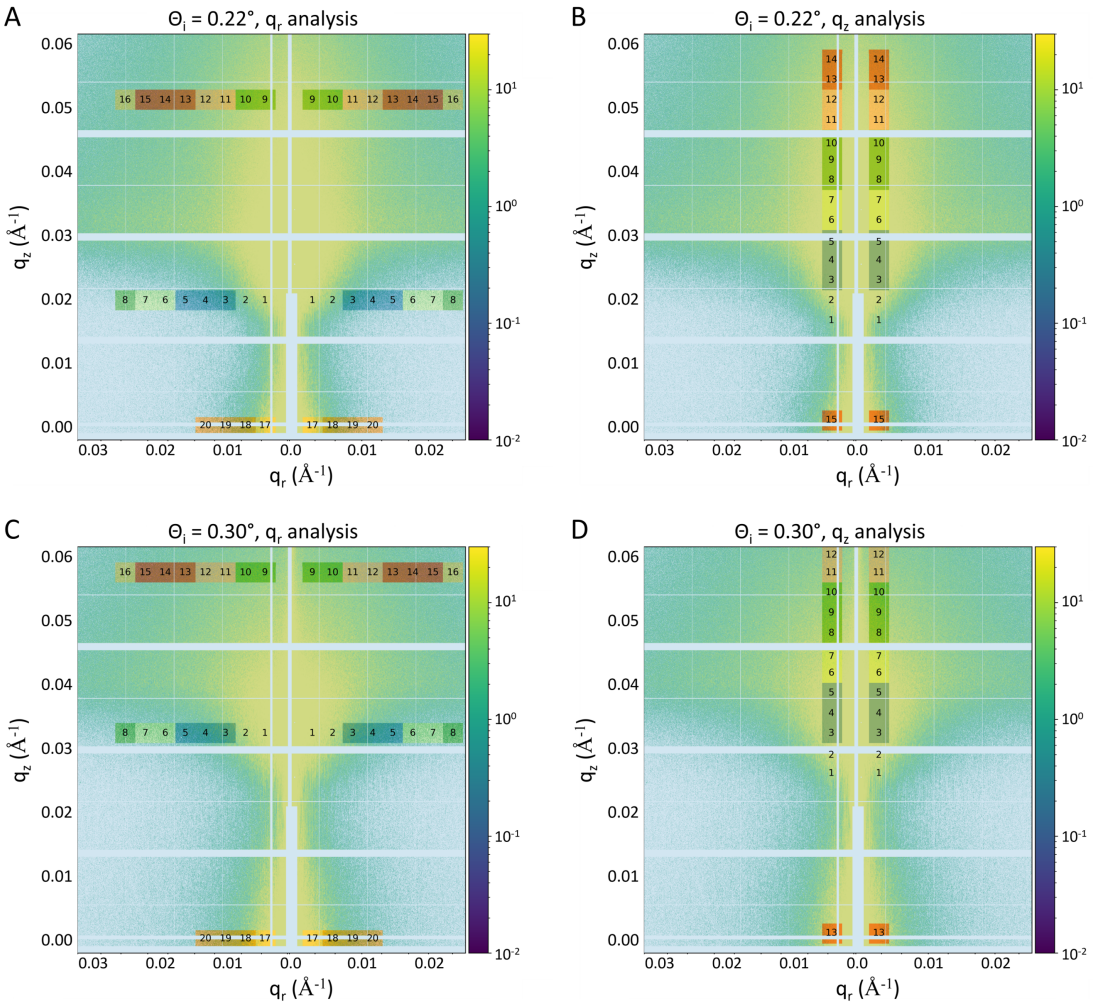

Figure 8.18: The graphic shows averaged intensity pattern of simultaneous GI-GT-XPCS measurements of a $MAPbI_3$ thin film. The colored and numbered regions mark the Regions-of-Interest (ROIs) used within the manuscript for the calculation of 2TCFs. Subgraphs A and B show intensity pattern taken at an angle of incidence of $\Theta_i = 0.22°$. Subgraphs C and D show intensity pattern taken at an angle of incidence of $\Theta_i = 0.30°$. The ROI labelled '1' in subgraph B was not used within the thesis to calculate 1TCFs, as the low number of photons introduced significant errors.

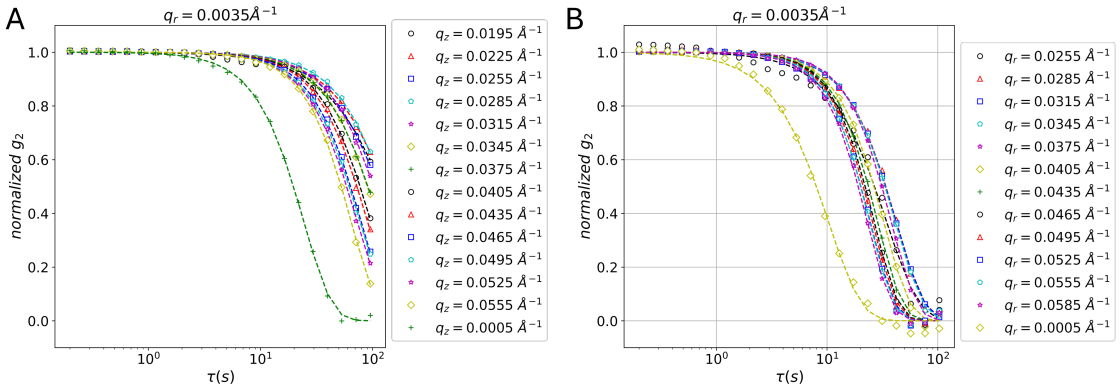

Figure 8.19: The graphs depict normalized 1TCFs and their respective stretched exponential fits extracted from Figure 8.18BD. The left plot (A) shows the extracted 1TCFs from the ROIs presented in Figure 8.18B for an incident angle of $\Theta_i = 0.22°$, while the right graph (B) shows the extracted 1TCFs from the ROIs presented in Figure 8.18D for an incident angle of $\Theta_i = 0.30°$.

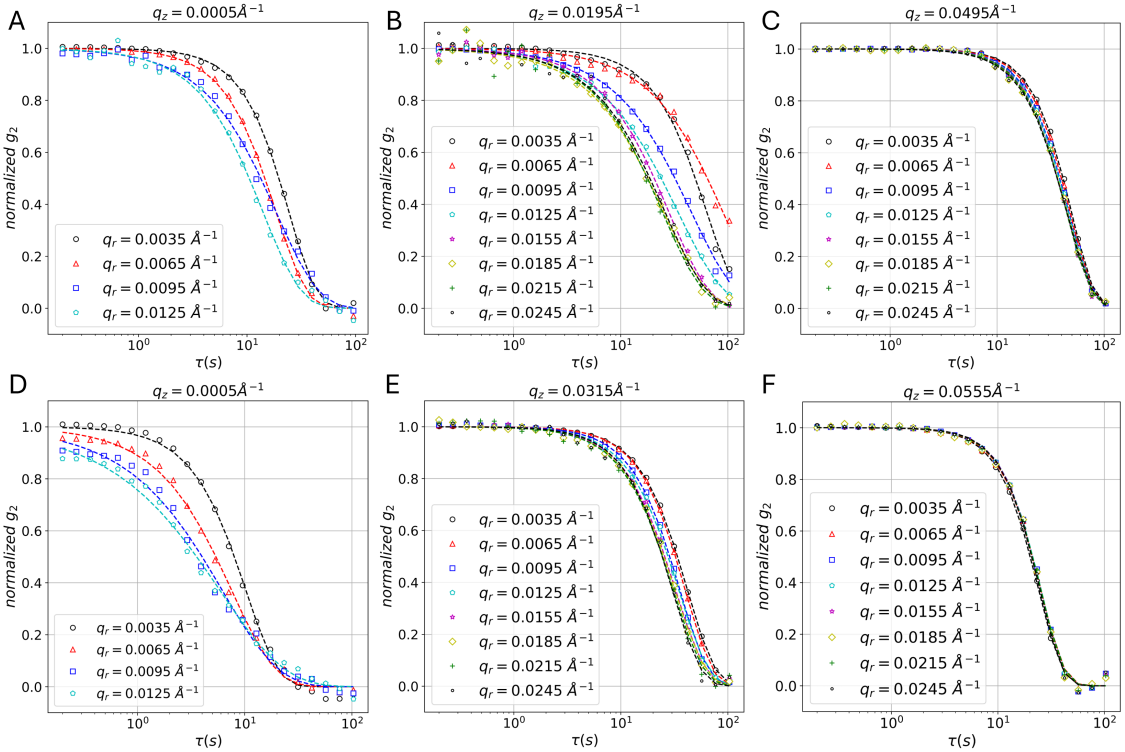

Figure 8.20: The graphs depict normalized 1TCFs and their respective stretched exponential fits extracted from Figure 8.18AC. The top row (ABC) shows the extracted 1TCFs from the ROIs presented in Figure 8.18A for an incident angle of $\Theta_i = 0.22°$ along q_z, while the bottom row (DEF) shows the extracted 1TCFs from the ROIs presented in Figure 8.18C for an incident angle of $\Theta_i = 0.30°$ along q_z.

Statistical analysis of MD simulations presented in Chapter 7

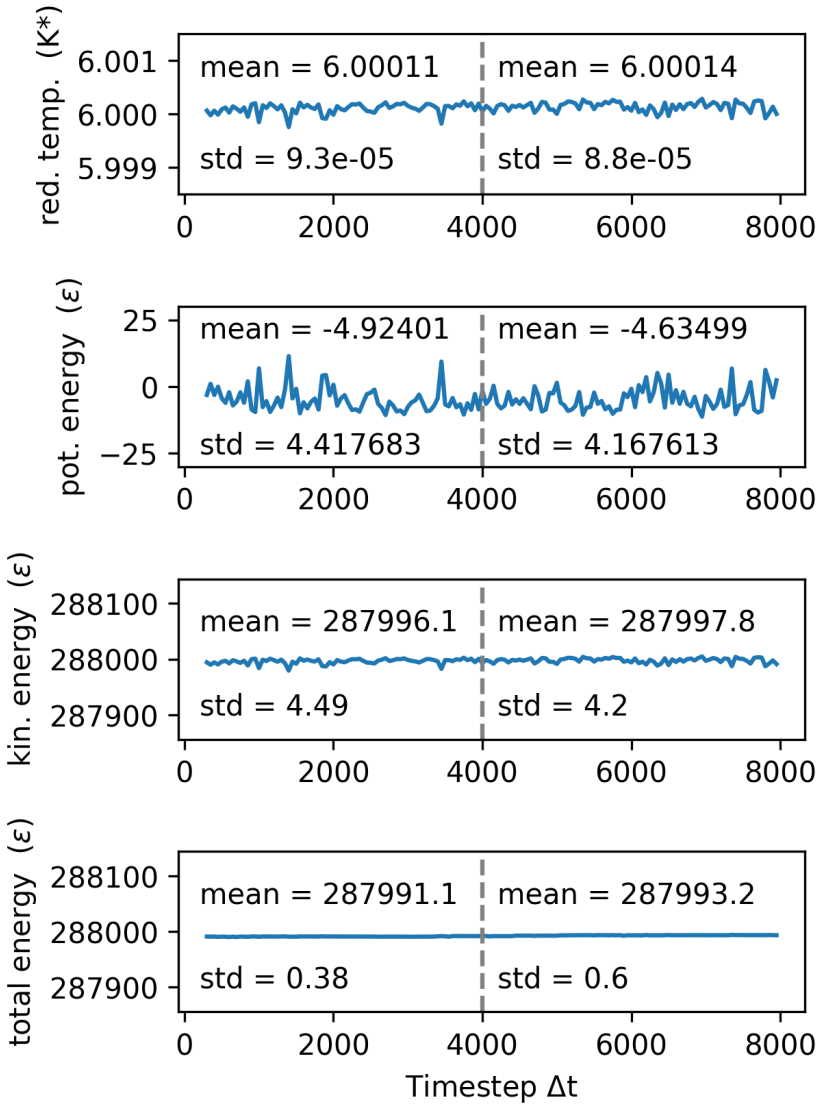

Figure 8.21: The graphic shows the LJ reduced temperature and the LJ reduced potential, kinetic and total energy (top to bottom) as a function of timesteps Δt (blue line) calculated from particle trajectories (see Section 3.3 for MD model parameters) for a doubled time duration of the MD simulation. The gray vertical lines indicate the halfway time of the simulation. Each graph has the mean value (mean) and standard deviation (std) for the first 4000 timesteps ΔT and second 4000 time steps ΔT labelled. The derived mean and std values are well comparable within the first and second half of the MD simulation, indicating that the MD simulation is not diverging with time and that the total energy is conserved.

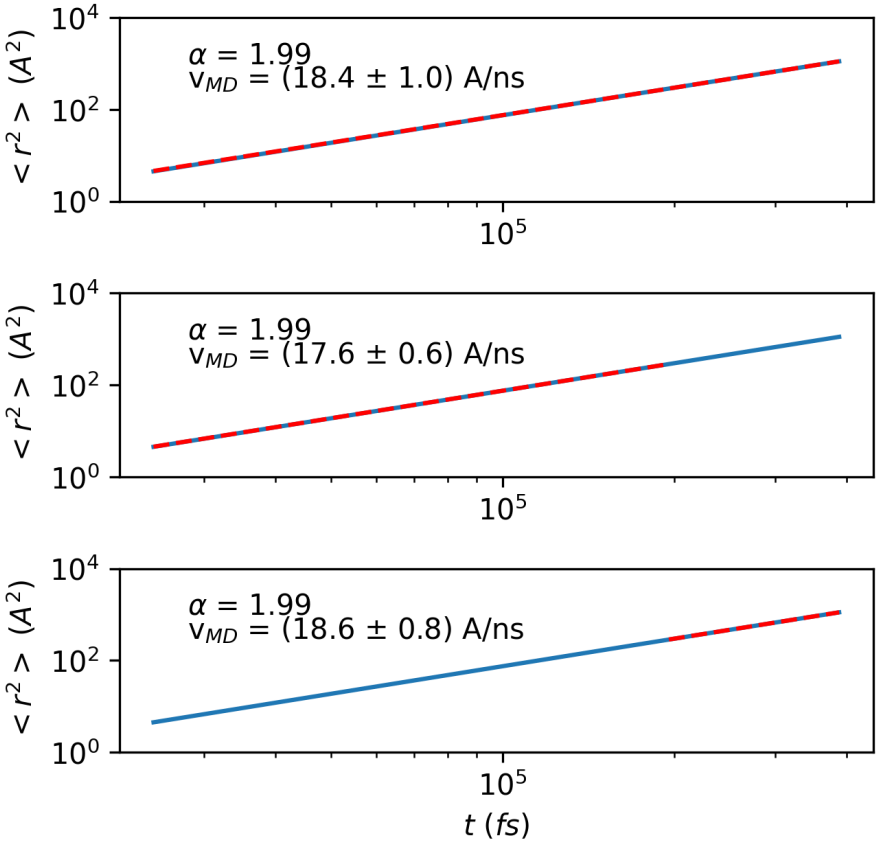

Figure 8.22: Mean-Square-Displacement (MSD) $\langle r^2 \rangle$ (blue line) vs time t scaled from LJ reduced units on a double logarithmic scale. The scaled MSD was modelled with Eq. 7.1 (red dashed line) to extract the slope m and its scaling exponent α for different parts of the simulated trajectories. From top to bottom the fit regions cover the whole time range presented in Figure 8.21, the first half and the second half. The derived values for α and the velocities v_{MD} calculated from m are labelled in each subfigure. All three fits show ballistic motion with comparable velocities within the calculated errors.

Global Fitting of simulated GI-XPCS experiments presented in Chapter 7

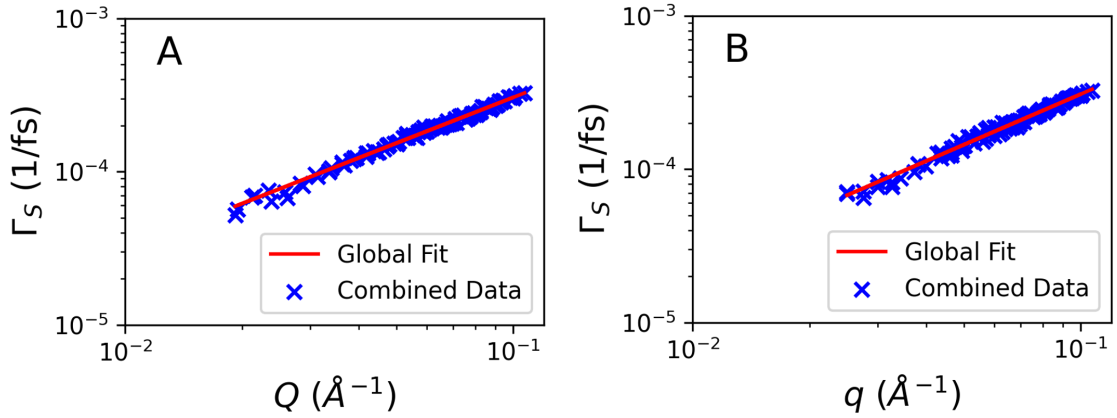

Figure 8.23: The graphic shows the combined data of extracted decorrelation frequencies for (A) refraction-corrected calculated GI-XPCS and (B) classical calculated GI-XPCS and their respective fit. The combined data includes the angles of incidence from 0.19° to 0.60° used in section 7.2 and 7.1.3. The fit results are presented in section 7.2.

C. Bibliography

[1] Fraunhofer ISE (17.05.2023). *Recent Facts about Photovoltaics in Germany*. URL: https://www.ise.fraunhofer.de/en/publications/studies/recent-facts-about-pv-in-germany.html.

[2] United Nations ESCAP (25.02.2021). *Coal Phase Out and Energy Transition Pathways for Asia and the Pacific*. URL: https://www.unescap.org/kp/2021/coal-phase-out-and-energy-transition-pathways-asia-and-pacific.

[3] Khagendra P. Bhandari, Jennifer M. Collier, Randy J. Ellingson, and Defne S. Apul (2015). Energy payback time (EPBT) and energy return on energy invested (EROI) of solar photovoltaic systems: A systematic review and meta-analysis. *Renewable and Sustainable Energy Reviews* **47**, 133–141. DOI: 10.1016/j.rser.2015.02.057.

[4] Hui Li and Wei Zhang (2020). Perovskite Tandem Solar Cells: From Fundamentals to Commercial Deployment. *Chemical reviews* **120** (18), 9835–9950. DOI: 10.1021/acs.chemrev.9b00780.

[5] Niraj N. Lal et al. (2017). Perovskite Tandem Solar Cells. *Advanced Energy Materials* **7** (18). DOI: 10.1002/aenm.201602761.

[6] Colin D. Bailie and Michael D. McGehee (2015). High-efficiency tandem perovskite solar cells. *MRS Bulletin* **40** (8), 681–686. DOI: 10.1557/mrs.2015.167.

[7] National Renewable Energy Lab (1.10.2023). *NREL Best Research Cell Efficiencies Chart*. URL: https://www.nrel.gov/pv/cell-efficiency.html.

[8] Akihiro Kojima, Kenjiro Teshima, Yasuo Shirai, and Tsutomu Miyasaka (2009). Organometal halide perovskites as visible-light sensitizers for photovoltaic cells. *Journal of the American Chemical Society* **131** (17), 6050–6051. DOI: 10.1021/ja809598r.

[9] Saewon Kang et al. (2019). Ultrathin, lightweight and flexible perovskite solar cells with an excellent power-per-weight performance. *Journal of Materials Chemistry A* **7** (3), 1107–1114. DOI: 10.1039/C8TA10585E.

[10] Martin Kaltenbrunner et al. (2015). Flexible high power-per-weight perovskite solar cells with chromium oxide-metal contacts for improved stability in air. *Nature materials* **14** (10), 1032–1039. DOI: 10.1038/nmat4388.

[11] Lei Gao and Qingfeng Yan (2020). Recent Advances in Lead Halide Perovskites for Radiation Detectors. *Solar RRL* **4** (2). DOI: 10.1002/solr.201900210.

[12] Haotong Wei and Jinsong Huang (2019). Halide lead perovskites for ionizing radiation detection. *Nature communications* **10** (1), 1066. DOI: 10.1038/s41467-019-08981-w.

[13] Mykhailo Sytnyk, Sarah Deumel, Sandro Francesco Tedde, Gebhard J. Matt, and Wolfgang Heiss (2019). A perspective on the bright future of metal halide perovskites for X-ray detection. *Applied Physics Letters* **115** (19). DOI: 10.1063/1.5125999.

[14] Sampson Adjokatse, Hong-Hua Fang, and Maria Antonietta Loi (2017). Broadly tunable metal halide perovskites for solid-state light-emission applications. *Materials Today* **20** (8), 413–424. DOI: 10.1016/j.mattod.2017.03.021.

[15] Naresh Kumar Kumawat, Xiao-Ke Liu, Dinesh Kabra, and Feng Gao (2019). Blue perovskite light-emitting diodes: progress, challenges and future directions. *Nanoscale* **11** (5), 2109–2120. DOI: 10.1039/C8NR09885A.

[16] Peipei Du, Liang Gao, and Jiang Tang (2020). Focus on performance of perovskite light-emitting diodes. *Frontiers of optoelectronics* **13** (3), 235–245. DOI: 10.1007/s12200-020-1042-y.

[17] Qing Zhang, Qiuyu Shang, Rui Su, T. Thu Ha Do, and Qihua Xiong (2021). Halide Perovskite Semiconductor Lasers: Materials, Cavity Design, and Low Threshold. *Nano letters* **21** (5), 1903–1914. DOI: 10.1021/acs.nanolett.0c03593.

[18] Lei Wang, Mingqing Yang, Shiyu Zhang, Chunhui Niu, and Yong Lv (2022). Perovskite Random Lasers, Process and Prospects. *Micromachines* **13** (12). DOI: 10.3390/mi13122040.

[19] Lei Lei, Qi Dong, Kenan Gundogdu, and Franky So (2021). Metal Halide Perovskites for Laser Applications. *Advanced Functional Materials* **31** (16). DOI: 10.1002/adfm.202010144.

[20] Itaru Raifuku et al. (2021). Halide perovskite for low–power consumption neuromorphic devices. *EcoMat* **3** (6). DOI: 10.1002/eom2.12142.

[21] Soumitra Satapathi, Kanishka Raj, Yukta, and Mohammad Adil Afroz (2022). Halide-Perovskite-Based Memristor Devices and Their Application in Neuromorphic Computing. *Physical Review Applied* **18** (1). DOI: 10.1103/PhysRevApplied.18.017001.

[22] Keonwon Beom, Zhaoyang Fan, Dawen Li, and Nathan Newman (2022). Halide perovskite based synaptic devices for neuromorphic systems. *Materials Today Physics* **24**, 100667. DOI: 10.1016/j.mtphys.2022.100667.

[23] Hyun Wook Ro et al. (2016). Morphology changes upon scaling a high-efficiency, solution-processed solar cell. *Energy & Environmental Science* **9** (9), 2835–2846. DOI: 10.1039/C6EE01623E.

[24] Yufei Zhong et al. (2018). Blade-Coated Hybrid Perovskite Solar Cells with Efficiency ¿ 17%: An In Situ Investigation. *ACS Energy Letters* **3** (5), 1078–1085. DOI: 10.1021/acsenergylett.8b00428.

[25] Shahriyar Safat Dipta and Ashraf Uddin (2021). Stability Issues of Perovskite Solar Cells: A Critical Review. *Energy Technology* **9** (11). DOI: 10.1002/ente.202100560.

[26] Carolin Rehermann et al. (2020). Origin of Ionic Inhomogeneity in MAPb(IxBr1-x)3 Perovskite Thin Films Revealed by In-Situ Spectroscopy during Spin Coating and Annealing. *ACS applied materials & interfaces* **12** (27), 30343–30352. DOI: 10.1021/acsami.0c05894.

[27] Ziqiu Ren et al. (2023). Advances in Intermediates for the Solution-Processing of Perovskite Films. *CCS Chemistry*, 1–19. DOI: 10.31635/ccschem.023.202302989.

[28] Maged Abdelsamie et al. (2020). Impact of Processing on Structural and Compositional Evolution in Mixed Metal Halide Perovskites during Film Formation. *Advanced Functional Materials* **30** (38), 2001752. DOI: 10.1002/adfm.202001752.

[29] Andrey A. Petrov et al. (2017). Crystal Structure of DMF-Intermediate Phases Uncovers the Link Between CH 3 NH 3 PbI 3 Morphology and Precursor Stoichiometry. *The Journal of Physical Chemistry C* **121** (38), 20739–20743. DOI: 10.1021/acs.jpcc.7b08468.

[30] Lijian Zuo, Zexin Li, and Hongzheng Chen (2023). Ion Migration and Accumulation in Halide Perovskite Solar Cells †. *Chinese Journal of Chemistry* **41** (7), 861–876. DOI: 10.1002/cjoc.202200505.

[31] Yevgeny Rakita, Sidney R. Cohen, Nir Klein Kedem, Gary Hodes, and David Cahen (2015). Mechanical properties of APbX3 (A = Cs or CH3NH3; X= I or Br) perovskite single crystals. *MRS Communications* **5** (4), 623–629. DOI: 10.1557/mrc.2015.69.

[32] Henry J. Snaith et al. (2014). Anomalous Hysteresis in Perovskite Solar Cells. *The journal of physical chemistry letters* **5** (9), 1511–1515. DOI: 10.1021/jz500113x.

[33] Prashant V. Kamat and Masaru Kuno (2021). Halide Ion Migration in Perovskite Nanocrystals and Nanostructures. *Accounts of chemical research* **54** (3), 520–531. DOI: 10.1021/acs.accounts.0c00749.

[34] Alexander J. Knight, Jay B. Patel, Henry J. Snaith, Michael B. Johnston, and Laura M. Herz (2020). Trap States, Electric Fields, and Phase Segregation in Mixed–Halide Perovskite Photovoltaic Devices. *Advanced Energy Materials* **10** (9). DOI: 10.1002/aenm.201903488.

[35] Ian L. Braly et al. (2017). Current-Induced Phase Segregation in Mixed Halide Hybrid Perovskites and its Impact on Two-Terminal Tandem Solar Cell Design. *ACS Energy Letters* **2** (8), 1841–1847. DOI: 10.1021/acsenergylett.7b00525.

[36] Teddy Salim et al. (2015). Perovskite-based solar cells: impact of morphology and device architecture on device performance. *Journal of Materials Chemistry A* **3** (17), 8943–8969. DOI: 10.1039/C4TA05226A.

[37] Naveen Kumar Tailor et al. (2020). Recent progress in morphology optimization in perovskite solar cell. *Journal of Materials Chemistry A* **8** (41), 21356–21386. DOI: 10.1039/D0TA00143K.

[38] Jinxin Li, Basudev Pradhan, Surya Gaur, and Jayan Thomas (2019). Predictions and Strategies Learned from Machine Learning to Develop High–Performing Perovskite Solar Cells. *Advanced Energy Materials* **9** (46). DOI: 10.1002/aenm.201901891.

[39] Michael Saliba et al. (2018). How to Make over 20% Efficient Perovskite Solar Cells in Regular (n–i–p) and Inverted (p–i–n) Architectures. *Chemistry of Materials* **30** (13), 4193–4201. DOI: 10.1021/acs.chemmater.8b00136.

[40] Finn Babbe and Carolin M. Sutter–Fella (2020). Optical Absorption–Based In Situ Characterization of Halide Perovskites. *Advanced Energy Materials* **10** (26). DOI: 10.1002/aenm.201903587.

[41] Klara Suchan, Justus Just, Pascal Becker, Eva L. Unger, and Thomas Unold (2020). Optical in situ monitoring during the synthesis of halide perovskite solar cells reveals formation kinetics and evolution of optoelectronic properties. *Journal of Materials Chemistry A* **8** (20), 10439–10449. DOI: 10.1039/D0TA01237H.

[42] Laura E. Mundt and Laura T. Schelhas (2020). Structural Evolution During Perovskite Crystal Formation and Degradation: In Situ and Operando X–Ray Diffraction Studies. *Advanced Energy Materials* **10** (26), 1903074. DOI: 10.1002/aenm.201903074.

[43] Shivam Singh et al. (2016). Effect of Thermal and Structural Disorder on the Electronic Structure of Hybrid Perovskite Semiconductor CH3NH3PbI3. *The journal of physical chemistry letters* **7** (15), 3014–3021. DOI: 10.1021/acs.jpclett.6b01207.

[44] Fabian Panzer, Cheng Li, Tobias Meier, Anna Köhler, and Sven Huettner (2017). Impact of Structural Dynamics on the Optical Properties of Methylammonium Lead Iodide Perovskites. *Advanced Energy Materials* **7** (16). DOI: 10.1002/aenm.201700286.

[45] Klara Suchan et al. (2023). Multi–Stage Phase–Segregation of Mixed Halide Perovskites under Illumination: A Quantitative Comparison of Experimental Observations and Thermodynamic Models. *Advanced Functional Materials* **33** (3), 2206047. DOI: 10.1002/adfm.202206047.

[46] Minchao Qin, Pok Fung Chan, and Xinhui Lu (2021). A Systematic Review of Metal Halide Perovskite Crystallization and Film Formation Mechanism Unveiled by In Situ GIWAXS. *Advanced materials (Deerfield Beach, Fla.)* **33** (51), e2105290. DOI: 10.1002/adma.202105290.

[47] Alec R. Sandy, Qingteng Zhang, and Laurence B. Lurio (2018). Hard X-Ray Photon Correlation Spectroscopy Methods for Materials Studies. *Annual Review of Materials Research* **48** (1), 167–190. DOI: 10.1146/annurev-matsci-070317-124334.

[48] Robert L. Leheny (2012). XPCS: Nanoscale motion and rheology. *Current Opinion in Colloid & Interface Science* **17** (1), 3–12. DOI: 10.1016/j.cocis.2011.11.002.

[49] Zheng Zhang et al. (2019). Nanoscale viscosity of confined polyethylene oxide. *Physical review. E* **100** (6-1), 062503. DOI: 10.1103/PhysRevE.100.062503.

[50] Luigi Cristofolini (2014). Synchrotron X-ray techniques for the investigation of structures and dynamics in interfacial systems. *Current Opinion in Colloid & Interface Science* **19** (3), 228–241. DOI: 10.1016/j.cocis.2014.03.006.

[51] Gustav Rose (1840). Ueber einige neue Mineralien des Urals. *Journal für Praktische Chemie* **19** (1), 459–468. DOI: 10.1002/prac.18400190179.

[52] A. M. Glazer (1972). The classification of tilted octahedra in perovskites. *Acta Crystallographica Section B Structural Crystallography and Crystal Chemistry* **28** (11), 3384–3392. DOI: 10.1107/S0567740872007976.

[53] M. A. Peña and J. L. Fierro (2001). Chemical structures and performance of perovskite oxides. *Chemical reviews* **101** (7), 1981–2017. DOI: 10.1021/cr980129f.

[54] David A. Egger, Andrew M. Rappe, and Leeor Kronik (2016). Hybrid Organic-Inorganic Perovskites on the Move. *Accounts of chemical research* **49** (3), 573–581. DOI: 10.1021/acs.accounts.5b00540.

[55] Joseph Berry et al. (2015). Hybrid Organic-Inorganic Perovskites (HOIPs): Opportunities and Challenges. *Advanced materials (Deerfield Beach, Fla.)* **27** (35), 5102–5112. DOI: 10.1002/adma.201502294.

[56] Dieter Weber (1978). CH 3 NH 3 SnBr x I 3-x (x = 0-3), ein Sn(II)-System mit kubischer Perowskitstruktur / CH 3 NH 3 SnBr x I 3-x (x = 0-3), a Sn(II)-System with Cubic Perovskite Structure. *Zeitschrift für Naturforschung B* **33** (8), 862–865. DOI: 10.1515/znb-1978-0809.

[57] Dieter Weber (1978). CH 3 NH 3 PbX 3 , ein Pb(II)-System mit kubischer Perowskitstruktur / CH 3 NH 3 PbX 3 , a Pb(II)-System with Cubic Perovskite Structure. *Zeitschrift für Naturforschung B* **33** (12), 1443–1445. DOI: 10.1515/znb-1978-1214.

[58] Yana Vaynzof (2020). The Future of Perovskite Photovoltaics—Thermal Evaporation or Solution Processing? *Advanced Energy Materials* **10** (48), 2003073. DOI: 10.1002/aenm.202003073.

[59] Zhaosheng Hu et al. (2019). A Review on Energy Band–Gap Engineering for Perovskite Photovoltaics. *Solar RRL* **3** (12). DOI: 10.1002/solr.201900304.

[60] Ali Sephar Shikoh and Alexander Polyakov (2020). A Quantitative Analysis of the Research Trends in Perovskite Solar Cells in 2009–2019. *physica status solidi (a)* **217** (23). DOI: 10.1002/pssa.202000441.

[61] Biplav Dahal and Wenzhi Li (2022). Configuration of Methylammonium Lead Iodide Perovskite Solar Cell and its Effect on the Device's Performance: A Review. *Advanced Materials Interfaces* **9** (19). DOI: 10.1002/admi.202200042.

[62] P. S. Whitfield et al. (2016). Structures, Phase Transitions and Tricritical Behavior of the Hybrid Perovskite Methyl Ammonium Lead Iodide. *Scientific reports* **6**, 35685. DOI: 10.1038/srep35685.

[63] Constantinos C. Stoumpos, Christos D. Malliakas, and Mercouri G. Kanatzidis (2013). Semiconducting tin and lead iodide perovskites with organic cations: phase transitions, high mobilities, and near-infrared photoluminescent properties. *Inorganic chemistry* **52** (15), 9019–9038. DOI: 10.1021/ic401215x.

[64] T. Jesper Jacobsson, L. Josef Schwan, Mikael Ottosson, Anders Hagfeldt, and Tomas Edvinsson (2015). Determination of Thermal Expansion Coefficients and Locating the Temperature-Induced Phase Transition in Methylammonium Lead Perovskites Using X-ray Diffraction. *Inorganic chemistry* **54** (22), 10678–10685. DOI: 10.1021/acs.inorgchem.5b01481.

[65] Hua Zhang et al. (2015). Photovoltaic behaviour of lead methylammonium triiodide perovskite solar cells down to 80 K. *Journal of Materials Chemistry A* **3** (22), 11762–11767. DOI: 10.1039/C5TA02206A.

[66] Rebecca L. Milot, Giles E. Eperon, Henry J. Snaith, Michael B. Johnston, and Laura M. Herz (2015). Temperature–Dependent Charge–Carrier Dynamics in CH 3 NH 3 PbI 3 Perovskite Thin Films. *Advanced Functional Materials* **25** (39), 6218–6227. DOI: 10.1002/adfm.201502340.

[67] Md Nadim Ferdous Hoque et al. (2016). Polarization and Dielectric Study of Methylammonium Lead Iodide Thin Film to Reveal its Nonferroelectric Nature under Solar Cell Operating Conditions. *ACS energy letters* **1** (1), 142–149. DOI: 10.1021/acsenergylett.6b00093.

[68] Dehui Li et al. (2016). Size-dependent phase transition in methylammonium lead iodide perovskite microplate crystals. *Nature communications* **7**, 11330. DOI: 10.1038/ncomms11330.

[69] Kwang Jae Lee et al. (2021). Domain–Size–Dependent Residual Stress Governs the Phase–Transition and Photoluminescence Behavior of Methylammonium Lead Iodide. *Advanced Functional Materials* **31** (15). DOI: 10.1002/adfm.202008088.

[70] Dongtao Liu et al. (2021). Strain analysis and engineering in halide perovskite photovoltaics. *Nature materials* **20** (10), 1337–1346. DOI: 10.1038/s41563-021-01097-x.

[71] Ariany Bonadio et al. (2023). Comparing the Cubic and Tetragonal Phases of MAPbI3 at Room Temperature. *Inorganic chemistry* **62** (19), 7533–7544. DOI: 10.1021/acs.inorgchem.3c00874.

[72] Christopher L. Davies et al. (2018). Bimolecular recombination in methylammonium lead triiodide perovskite is an inverse absorption process. *Nature communications* **9** (1), 293. DOI: 10.1038/s41467-017-02670-2.

[73] Laura M. Herz (2017). Charge-Carrier Mobilities in Metal Halide Perovskites: Fundamental Mechanisms and Limits. *ACS energy letters* **2** (7), 1539–1548. DOI: 10.1021/acsenergylett.7b00276.

[74] H. Beck, C. Gehrmann, and D. A. Egger (2019). Structure and binding in halide perovskites: Analysis of static and dynamic effects from dispersion-corrected density functional theory. *APL Materials* **7** (2). DOI: 10.1063/1.5086541.

[75] Adam Jaffe et al. (2016). High-Pressure Single-Crystal Structures of 3D Lead-Halide Hybrid Perovskites and Pressure Effects on their Electronic and Optical Properties. *ACS central science* **2** (4), 201–209. DOI: 10.1021/acscentsci.6b00055.

[76] David A. Egger et al. (2018). What Remains Unexplained about the Properties of Halide Perovskites? *Advanced materials (Deerfield Beach, Fla.)* **30** (20), e1800691. DOI: 10.1002/adma.201800691.

[77] Rudolf Gross and Achim Marx (2012). *Festkörperphysik*. Mathematik, Physik 10-2012. München: Oldenbourg. DOI: 10.1524/9783486714869.

[78] Emmanuel Rosencher and Borge Vinter (2002). *Optoelectronics*. Cambridge and New York: Cambridge University Press. DOI: 25918.

[79] Jacques I. Pankove (1975). *Optical processes in semiconductors*. Unabridged republication, with slight corrections. New York: Dover Publications Inc.

[80] Xi Zhu, Haibin Su, Rudolph A. Marcus, and Maria E. Michel-Beyerle (2014). Computed and Experimental Absorption Spectra of the Perovskite CH3NH3PbI3. *The journal of physical chemistry letters* **5** (17), 3061–3065. DOI: 10.1021/jz501174e.

[81] Edoardo Mosconi, Anna Amat, Md. K. Nazeeruddin, Michael Grätzel, and Filippo DE Angelis (2013). First-Principles Modeling of Mixed Halide Organometal Perovskites for Photovoltaic Applications. *The Journal of Physical Chemistry C* **117** (27), 13902–13913. DOI: 10.1021/jp4048659.

[82] Federico Brivio, Keith T. Butler, Aron Walsh, and Mark van Schilfgaarde (2014). Relativistic quasiparticle self-consistent electronic structure of hybrid halide perovskite photovoltaic absorbers. *Physical Review B* **89** (15). DOI: 10.1103/PhysRevB.89.155204.

[83] Tsutomu Miyasaka (2018). Lead Halide Perovskites in Thin Film Photovoltaics: Background and Perspectives. *Bulletin of the Chemical Society of Japan* **91** (7), 1058–1068. DOI: 10.1246/bcsj.20180071.

[84] M. V. Kurik (1971). Urbach rule. *physica status solidi (a)* **8** (1), 9–45. DOI: 10.1002/pssa.2210080102.

[85] T. Skettrup (1978). Urbach's rule derived from thermal fluctuations in the band-gap energy. *Physical review. B, Condensed matter* **18** (6), 2622–2631. DOI: 10.1103/PhysRevB.18.2622.

[86] Cem Ayik, Ihor Studenyak, Mladen Kranjec, and Mykhailo Kurik (2014). Urbach Rule in Solid State Physics. *International Journal of Optics and Applications* **4** (3), 76–83. DOI: 10.5923/j.optics.20140403.02.

[87] Chujun Zhang et al. (2022). Unraveling Urbach Tail Effects in High-Performance Organic Photovoltaics: Dynamic vs Static Disorder. *ACS energy letters* **7** (6), 1971–1979. DOI: 10.1021/acsenergylett.2c00816.

[88] Franz Urbach (1953). The Long-Wavelength Edge of Photographic Sensitivity and of the Electronic Absorption of Solids. *Physical Review* **92** (5), 1324. DOI: 10.1103/PhysRev.92.1324.

[89] S. R. Johnson and T. Tiedje (1995). Temperature dependence of the Urbach edge in GaAs. *Journal of Applied Physics* **78** (9), 5609–5613. DOI: 10.1063/1.359683.

[90] G. D. Cody, T. Tiedje, B. Abeles, B. Brooks, and Y. Goldstein (1981). Disorder and the Optical-Absorption Edge of Hydrogenated Amorphous Silicon. *Physical Review Letters* **47** (20), 1480–1483. DOI: 10.1103/PhysRevLett.47.1480.

[91] Martin Ledinsky et al. (2019). Temperature Dependence of the Urbach Energy in Lead Iodide Perovskites. *The journal of physical chemistry letters* **10** (6), 1368–1373. DOI: 10.1021/acs.jpclett.9b00138.

[92] Hitoshi Sumi and Yutaka Toyozawa (1971). Urbach-Martienseen Rule and Exciton Trapped Momentarily by Lattice Vibrations. *Journal of the Physical Society of Japan* **31** (2), 342–358. DOI: 10.1143/JPSJ.31.342.

[93] Ivan Pelant (2012). *Luminescence Spectroscopy of Semiconductors*. Oxford: OUP Oxford. URL: http://site.ebrary.com/lib/alltitles/Doc?id=10531073.

[94] Laura M. Herz (2016). Charge-Carrier Dynamics in Organic-Inorganic Metal Halide Perovskites. *Annual review of physical chemistry* **67**, 65–89. DOI: 10.1146/annurev-physchem-040215-112222.

[95] W. van Roosbroeck and W. Shockley (1954). Photon-Radiative Recombination of Electrons and Holes in Germanium. *Physical Review* **94** (6), 1558–1560. DOI: 10.1103/PhysRev.94.1558.

[96] Anna Köhler and Heinz Bässler (2015). *Electronic Processes in Organic Semiconductors*. Wiley. DOI: 10.1002/9783527685172.

[97] Emmanuel Rashba and G. E. Gurgenishvili (1962). Edge absorption theory in semiconductors. *Soviet Physics - Solid state* (4), 759.

[98] C. H. Henry and K. Nassau (1970). Lifetimes of Bound Excitons in CdS. *Physical Review B* **1** (4), 1628–1634. DOI: 10.1103/PhysRevB.1.1628.

[99] Yutaka Toyozawa (2009). *Optical Processes in Solids*. Cambridge University Press. DOI: 10.1017/CBO9780511615085.

[100] Michael A. Reshchikov (2014). Temperature dependence of defect-related photoluminescence in III-V and II-VI semiconductors. *Journal of Applied Physics* **115** (1). DOI: 10.1063/1.4838038.

[101] M. A. Reshchikov and R. Y. Korotkov (2001). Analysis of the temperature and excitation intensity dependencies of photoluminescence in undoped GaN films. *Physical review. B, Condensed matter* **64** (11). DOI: 10.1103/PhysRevB.64.115205.

[102] Stuart Thomson. *Observing Phase Transitions in a Halide Perovskite Using Temperature Dependent Photoluminescence Spectroscopy: AN_P45*. Ed. by Edinburgh Instruments Ltd. URL: https://www.edinst.com/phase-transitions-halide-perovskite/.

[103] Yoshihiko Kanemitsu (2017). Luminescence spectroscopy of lead-halide perovskites: materials properties and application as photovoltaic devices. *Journal of Materials Chemistry C* **5** (14), 3427–3437. DOI: 10.1039/C7TC00669A.

[104] Carlito S. Ponseca et al. (2014). Organometal halide perovskite solar cell materials rationalized: ultrafast charge generation, high and microsecond-long balanced mobilities, and slow recombination. *Journal of the American Chemical Society* **136** (14), 5189–5192. DOI: 10.1021/ja412583t.

[105] Christian Wehrenfennig, Giles E. Eperon, Michael B. Johnston, Henry J. Snaith, and Laura M. Herz (2014). High charge carrier mobilities and lifetimes in organolead trihalide perovskites. *Advanced materials (Deerfield Beach, Fla.)* **26** (10), 1584–1589. DOI: 10.1002/adma.201305172.

[106] Christian Wehrenfennig, Mingzhen Liu, Henry J. Snaith, Michael B. Johnston, and Laura M. Herz (2014). Charge carrier recombination channels in the low-temperature phase of organic-inorganic lead halide perovskite thin films. *APL Materials* **2** (8). DOI: 10.1063/1.4891595.

[107] Quang Le Phuong, Yumi Nakaike, Atsushi Wakamiya, and Yoshihiko Kanemitsu (2016). Free Excitons and Exciton-Phonon Coupling in CH3NH3PbI3 Single Crystals Revealed by Photocurrent and Photoluminescence Measurements at Low Temperatures. *The journal of physical chemistry letters* **7** (23), 4905–4910. DOI: 10.1021/acs.jpclett.6b02432.

[108] Hiba Diab et al. (2016). Narrow Linewidth Excitonic Emission in Organic-Inorganic Lead Iodide Perovskite Single Crystals. *The journal of physical chemistry letters* **7** (24), 5093–5100. DOI: 10.1021/acs.jpclett.6b02261.

[109] Jun Hong Noh, Sang Hyuk Im, Jin Hyuck Heo, Tarak N. Mandal, and Sang Il Seok (2013). Chemical management for colorful, efficient, and stable inorganic-organic hybrid nanostructured solar cells. *Nano letters* **13** (4), 1764–1769. DOI: 10.1021/nl400349b.

[110] Samuel D. Stranks et al. (2013). Electron-hole diffusion lengths exceeding 1 micrometer in an organometal trihalide perovskite absorber. *Science (New York, N.Y.)* **342** (6156), 341–344. DOI: 10.1126/science.1243982.

[111] N. Kitazawa, Y. Watanabe, and Y. Nakamura (2002). Optical properties of CH3NH3PbX3 (X = halogen) and their mixed-halide crystals. *Journal of Materials Science* **37** (17), 3585–3587. DOI: 10.1023/A:1016584519829.

[112] Guichuan Xing et al. (2014). Low-temperature solution-processed wavelength-tunable perovskites for lasing. *Nature materials* **13** (5), 476–480. DOI: 10.1038/nmat3911.

[113] Naresh K. Kumawat et al. (2015). Band Gap Tuning of $CH_3NH_3Pb(Br(1-x)Clx)_3$ Hybrid Perovskite for Blue Electroluminescence. *ACS applied materials & interfaces* **7** (24), 13119–13124. DOI: 10.1021/acsami.5b02159.

[114] Giles E. Eperon et al. (2014). Formamidinium lead trihalide: a broadly tunable perovskite for efficient planar heterojunction solar cells. *Energy Environ. Sci.* **7** (3), 982. DOI: 10.1039/C3EE43822H.

[115] Norman Pellet et al. (2014). Mixed-organic-cation perovskite photovoltaics for enhanced solar-light harvesting. *Angewandte Chemie (International ed. in English)* **53** (12), 3151–3157. DOI: 10.1002/anie.201309361.

[116] Makhsud I. Saidaminov et al. (2016). Perovskite Photodetectors Operating in Both Narrowband and Broadband Regimes. *Advanced materials (Deerfield Beach, Fla.)* **28** (37), 8144–8149. DOI: 10.1002/adma.201601235.

[117] V. M. Goldschmidt (1926). Die Gesetze der Krystallochemie. *Die Naturwissenschaften* **14** (21), 477–485. DOI: 10.1007/BF01507527.

[118] Constantinos C. Stoumpos and Mercouri G. Kanatzidis (2015). The Renaissance of Halide Perovskites and Their Evolution as Emerging Semiconductors. *Accounts of chemical research* **48** (10), 2791–2802. DOI: 10.1021/acs.accounts.5b00229.

[119] Bayrammurad Saparov and David B. Mitzi (2016). Organic-Inorganic Perovskites: Structural Versatility for Functional Materials Design. *Chemical reviews* **116** (7), 4558–4596. DOI: 10.1021/acs.chemrev.5b00715.

[120] Federico Brivio, Alison B. Walker, and Aron Walsh (2013). Structural and electronic properties of hybrid perovskites for high-efficiency thin-film photovoltaics from first-principles. *APL Materials* **1** (4). DOI: 10.1063/1.4824147.

[121] Hui-Seon Kim et al. (2012). Lead iodide perovskite sensitized all-solid-state submicron thin film mesoscopic solar cell with efficiency exceeding 9%. *Scientific reports* **2**, 591. DOI: 10.1038/srep00591.

[122] Ye Yang et al. (2015). Comparison of Recombination Dynamics in CH3NH3PbBr3 and CH3NH3PbI3 Perovskite Films: Influence of Exciton Binding Energy. *The journal of physical chemistry letters* **6** (23), 4688–4692. DOI: 10.1021/acs.jpclett.5b02290.

[123] Giovanni Mannino et al. (2020). Temperature-Dependent Optical Band Gap in CsPbBr3, MAPbBr3, and FAPbBr3 Single Crystals. *The journal of physical chemistry letters* **11** (7), 2490–2496. DOI: 10.1021/acs.jpclett.0c00295.

[124] Paolo Fedeli et al. (2015). Influence of the Synthetic Procedures on the Structural and Optical Properties of Mixed-Halide (Br, I) Perovskite Films. *The Journal of Physical Chemistry C* **119** (37), 21304–21313. DOI: 10.1021/acs.jpcc.5b03923.

[125] Christopher Greve et al. (2023). To Stop or to Shuttle Halides? The Role of an Ionic Liquid in Thermal Halide Mixing of Hybrid Perovskites. *ACS energy letters*, 5041–5049. DOI: 10.1021/acsenergylett.3c01878.

[126] Aurélien M. A. Leguy et al. (2016). Experimental and theoretical optical properties of methylammonium lead halide perovskites. *Nanoscale* **8** (12), 6317–6327. DOI: 10.1039/C5NR05435D.

[127] Eric T. Hoke et al. (2015). Reversible photo-induced trap formation in mixed-halide hybrid perovskites for photovoltaics. *Chemical science* **6** (1), 613–617. DOI: 10.1039/c4sc03141e.

[128] Daniel J. Slotcavage, Hemamala I. Karunadasa, and Michael D. McGehee (2016). Light-Induced Phase Segregation in Halide-Perovskite Absorbers. *ACS Energy Letters* **1** (6), 1199–1205. DOI: 10.1021/acsenergylett.6b00495.

[129] Huichao Zhang et al. (2019). Phase segregation due to ion migration in all-inorganic mixed-halide perovskite nanocrystals. *Nature communications* **10** (1), 1088. DOI: 10.1038/s41467-019-09047-7.

[130] Silvia G. Motti et al. (2021). Phase segregation in mixed-halide perovskites affects charge-carrier dynamics while preserving mobility. *Nature communications* **12** (1), 6955. DOI: 10.1038/s41467-021-26930-4.

[131] Sergiu Draguta et al. (2017). Rationalizing the light-induced phase separation of mixed halide organic-inorganic perovskites. *Nature communications* **8** (1), 200. DOI: 10.1038/s41467-017-00284-2.

[132] Alexander J. Knight et al. (2019). Electronic Traps and Phase Segregation in Lead Mixed-Halide Perovskite. *ACS Energy Letters* **4** (1), 75–84. DOI: 10.1021/acsenergylett.8b02002.

[133] Wanyi Nie et al. (2015). High-efficiency solution-processed perovskite solar cells with millimeter-scale grains. *Science (New York, N.Y.)* **347** (6221), 522–525. DOI: 10.1126/science.aaa0472.

[134] Samuel D. Stranks et al. (2014). Recombination Kinetics in Organic-Inorganic Perovskites: Excitons, Free Charge, and Subgap States. *Physical Review Applied* **2** (3). DOI: 10.1103/PhysRevApplied.2.034007.

[135] Dane W. deQuilettes et al. (2015). Solar cells. Impact of microstructure on local carrier lifetime in perovskite solar cells. *Science (New York, N.Y.)* **348** (6235), 683–686. DOI: 10.1126/science.aaa5333.

[136] Yu Bi et al. (2016). Charge Carrier Lifetimes Exceeding 15 μs in Methylammonium Lead Iodide Single Crystals. *The journal of physical chemistry letters* **7** (5), 923–928. DOI: 10.1021/acs.jpclett.6b00269.

[137] Qingfeng Dong et al. (2015). Solar cells. Electron-hole diffusion lengths 175 μm in solution-grown CH3NH3PbI3 single crystals. *Science (New York, N.Y.)* **347** (6225), 967–970. DOI: 10.1126/science.aaa5760.

[138] Wei Zhang, Giles E. Eperon, and Henry J. Snaith (2016). Metal halide perovskites for energy applications. *Nature Energy* **1** (6). DOI: 10.1038/nenergy.2016.48.

[139] Johanna Siekmann, Sandheep Ravishankar, and Thomas Kirchartz (2021). Apparent Defect Densities in Halide Perovskite Thin Films and Single Crystals. *ACS Energy Letters* **6** (9), 3244–3251. DOI: 10.1021/acsenergylett.1c01449.

[140] Valerio D'Innocenzo et al. (2014). Excitons versus free charges in organo-lead tri-halide perovskites. *Nature communications* **5**, 3586. DOI: 10.1038/ncomms4586.

[141] Weiguang Kong et al. (2015). Characterization of an abnormal photoluminescence behavior upon crystal-phase transition of perovskite CH3NH3PbI3. *Physical chemistry chemical physics : PCCP* **17** (25), 16405–16411. DOI: 10.1039/C5CP02605A.

[142] Anna Osherov et al. (2016). The Impact of Phase Retention on the Structural and Optoelectronic Properties of Metal Halide Perovskites. *Advanced materials (Deerfield Beach, Fla.)* **28** (48), 10757–10763. DOI: 10.1002/adma.201604019.

[143] Alexander Dobrovolsky, Aboma Merdasa, Eva L. Unger, Arkady Yartsev, and Ivan G. Scheblykin (2017). Defect-induced local variation of crystal phase transition temperature in metal-halide perovskites. *Nature communications* **8** (1), 34. DOI: 10.1038/s41467-017-00058-w.

[144] Cheng Zhu et al. (2019). Strain engineering in perovskite solar cells and its impacts on carrier dynamics. *Nature communications* **10** (1), 815. DOI: 10.1038/s41467-019-08507-4.

[145] Erin G. Moloney, Vishal Yeddu, and Makhsud I. Saidaminov (2020). Strain Engineering in Halide Perovskites. *ACS Materials Letters* **2** (11), 1495–1508. DOI: 10.1021/acsmaterialslett.0c00308.

[146] Metin Tolan (1999). *X-ray scattering from soft-matter thin films: Materials science and basic research*. Vol. 148. Springer tracts in modern physics. Berlin u.a.: Springer. URL: https://permalink.obvsg.at/AC02491674.

[147] B. L. Henke, E. M. Gullikson, and J. C. Davis (1993). X-Ray Interactions: Photoabsorption, Scattering, Transmission, and Reflection at E = 50-30,000 eV, Z = 1-92. *Atomic Data and Nuclear Data Tables* **54** (2), 181–342. DOI: 10.1006/adnd.1993.1013.

[148] Y. Yoneda (1963). Anomalous Surface Reflection of X Rays. *Physical Review* **131** (5), 2010–2013.

[149] William H. Bragg and William L. Bragg (1913). The reflection of X-rays by crystals. *Proceedings of the Royal Society of London. Series A, Containing Papers of a Mathematical and Physical Character* **88** (605), 428–438. DOI: 10.1098/rspa.1913.0040.

[150] W. Friedrich, P. Knipping, and M. Laue (1912). Interferenz Erscheinungen bei Röntgen-Strahlen. *Sitzungsber. d. Bayer. Akad. der Wiss.* 311–322.

[151] P. P. Ewald (1969). Introduction to the dynamical theory of X-ray diffraction. *Acta Crystallographica Section A: Crystal Physics, Diffraction, Theoretical and General Crystallography* **25** (1), 103–108. DOI: 10.1107/S0567739469000155.

[152] J. Brentano (1924). Focussing method of crystal powder analysis by X-rays. *Proceedings of the Physical Society of London* **37** (1), 184–193. DOI: 10.1088/1478-7814/37/1/326.

[153] Peter Debye and Paul Scherrer (1916). Interferenz an regellos orientierten Teilchen im Röntgenlicht I. *Physikalische Zeitschrift* (17), 277–283.

[154] Harold P. Klug and Leroy E. Alexander (1974). *X-ray diffraction procedures: For polycrystalline and amorphous materials*. 2. ed. A Wiley-Interscience publication. New York, NY: Wiley.

[155] Uwe Holzwarth and Neil Gibson (2011). The Scherrer equation versus the 'Debye-Scherrer equation'. *Nature nanotechnology* **6** (9), 534. DOI: 10.1038/nnano.2011.145.

[156] Paul Pistor, Juliane Borchert, Wolfgang Fränzel, René Csuk, and Roland Scheer (2014). Monitoring the Phase Formation of Coevaporated Lead Halide Perovskite Thin Films by in Situ X-ray Diffraction. *The journal of physical chemistry letters* **5** (19), 3308–3312. DOI: 10.1021/jz5017312.

[157] Yongbo Yuan et al. (2016). Electric–Field–Driven Reversible Conversion Between Methylammonium Lead Triiodide Perovskites and Lead Iodide at Elevated Temperatures. *Advanced Energy Materials* **6** (2). DOI: 10.1002/aenm.201501803.

[158] Alexander J. Knight et al. (2021). Halide Segregation in Mixed-Halide Perovskites: Influence of A-Site Cations. *ACS Energy Letters* **6** (2), 799–808. DOI: 10.1021/acsenergylett.0c02475.

[159] Paul F. Fewster and Norman L. Andrew (1998). Strain analysis by X-ray diffraction. *Thin Solid Films* **319** (1-2), 1–8. DOI: 10.1016/S0040-6090(97)01099-7.

[160] Julian A. Steele et al. (2023). How to GIWAXS: Grazing Incidence Wide Angle X–Ray Scattering Applied to Metal Halide Perovskite Thin Films. *Advanced Energy Materials* **13** (27). DOI: 10.1002/aenm.202300760.

[161] Jiliang Liu and Kevin G. Yager (2018). Unwarping GISAXS data. *IUCrJ* **5** (Pt 6), 737–752. DOI: 10.1107/S2052252518012058.

[162] S. K. Sinha, E. B. Sirota, S. Garoff, and H. B. Stanley (1988). X-ray and neutron scattering from rough surfaces. *Physical review. B, Condensed matter* **38** (4), 2297–2311. DOI: 10.1103/PhysRevB.38.2297.

[163] Rémi Lazzari, Frédéric Leroy, and Gilles Renaud (2007). Grazing-incidence small-angle x-ray scattering from dense packing of islands on surfaces: Development of distorted wave Born approximation and correlation between particle sizes and spacing. *Physical Review B* **76** (12). DOI: 10.1103/PhysRevB.76.125411.

[164] Markus Rauscher et al. (1999). Grazing incidence small angle x-ray scattering from free-standing nanostructures. *Journal of Applied Physics* **86** (12), 6763–6769. DOI: 10.1063/1.371724.

[165] Gilles Renaud, Rémi Lazzari, and Frédéric Leroy (2009). Probing surface and interface morphology with Grazing Incidence Small Angle X-Ray Scattering. *Surface Science Reports* **64** (8), 255–380. DOI: 10.1016/j.surfrep.2009.07.002.

[166] Byeongdu Lee et al. (2005). Structural Analysis of Block Copolymer Thin Films with Grazing Incidence Small-Angle X-ray Scattering. *Macromolecules* **38** (10), 4311–4323. DOI: 10.1021/ma047562d.

[167] K. Omote, Y. Ito, and S. Kawamura (2003). Small angle x-ray scattering for measuring pore-size distributions in porous low-κ films. *Applied Physics Letters* **82** (4), 544–546. DOI: 10.1063/1.1539546.

[168] Byeongdu Lee et al. (2005). Ultralow-k nanoporous organosilicate dielectric films imprinted with dendritic spheres. *Nature materials* **4** (2), 147–151. DOI: 10.1038/nmat1291.

[169] Rémi Lazzari (2002). IsGISAXS : a program for grazing-incidence small-angle X-ray scattering analysis of supported islands. *Journal of Applied Crystallography* **35** (4), 406–421. DOI: 10.1107/S0021889802006088.

[170] Gennady Pospelov et al. (2020). BornAgain: software for simulating and fitting grazing-incidence small-angle scattering. *Journal of Applied Crystallography* **53** (Pt 1), 262–276. DOI: 10.1107/S1600576719016789.

[171] Slim T. Chourou, Abhinav Sarje, Xiaoye S. Li, Elaine R. Chan, and Alexander Hexemer (2013). HipGISAXS : a high-performance computing code for simulating grazing-incidence X-ray scattering data. *Journal of Applied Crystallography* **46** (6), 1781–1795. DOI: 10.1107/S0021889813025843.

[172] Xinhui Lu, Kevin G. Yager, Danvers Johnston, Charles T. Black, and Benjamin M. Ocko (2013). Grazing-incidence transmission X-ray scattering: surface scattering in the Born approximation. *Journal of Applied Crystallography* **46** (1), 165–172. DOI: 10.1107/S0021889812047887.

[173] Qin Hu et al. (2017). In situ dynamic observations of perovskite crystallisation and microstructure evolution intermediated from PbI64- cage nanoparticles. *Nature communications* **8**, 15688. DOI: 10.1038/ncomms15688.

[174] Jinli Yang, Braden D. Siempelkamp, Dianyi Liu, and Timothy L. Kelly (2015). Investigation of CH3NH3PbI3 degradation rates and mechanisms in controlled humidity environments using in situ techniques. *ACS nano* **9** (2), 1955–1963. DOI: 10.1021/nn506864k.

[175] Paulo Ernesto Marchezi et al. (2020). Degradation mechanisms in mixed-cation and mixed-halide Cs x FA 1−x Pb(Br y I 1−y) 3 perovskite films under ambient conditions. *Journal of Materials Chemistry A* **8** (18), 9302–9312. DOI: 10.1039/D0TA01201G.

[176] Vladimir Held et al. (2022). Evolution of Structure and Optoelectronic Properties During Halide Perovskite Vapor Deposition. *The journal of physical chemistry letters* **13** (51), 11905–11912. DOI: 10.1021/acs.jpclett.2c03422.

[177] Edwin La Pineda De O, Noura Alhazmi, Stephen J. Ebbens, and Alan D. F. Dunbar (2021). Influence of Additives on the In Situ Crystallization Dynamics of Methyl Ammonium Lead Halide Perovskites. *ACS Applied Energy Materials* **4** (2), 1398–1409. DOI: 10.1021/acsaem.0c02625.

[178] Sunil K. Sinha, Zhang Jiang, and Laurence B. Lurio (2014). X-ray photon correlation spectroscopy studies of surfaces and thin films. *Advanced materials (Deerfield Beach, Fla.)* **26** (46), 7764–7785. DOI: 10.1002/adma.201401094.

[179] A. Malik et al. (1998). Coherent X-Ray Study of Fluctuations during Domain Coarsening. *Physical Review Letters* **81** (26), 5832–5835. DOI: 10.1103/PhysRevLett.81.5832.

[180] E. M. Herzig, K. A. White, A. B. Schofield, W. C. K. Poon, and P. S. Clegg (2007). Bicontinuous emulsions stabilized solely by colloidal particles. *Nature materials* **6** (12), 966–971. DOI: 10.1038/nmat2055.

[181] E. M. Herzig et al. (2009). Dynamics of a colloid-stabilized cream. *Physical review. E, Statistical, nonlinear, and soft matter physics* **79** (1 Pt 1), 011405. DOI: 10.1103/PhysRevE.79.011405.

[182] Mark Sutton (2008). A review of X-ray intensity fluctuation spectroscopy. *Comptes Rendus Physique* **9** (5-6), 657–667. DOI: 10.1016/j.crhy.2007.04.008.

[183] M. Sutton et al. (1991). Observation of speckle by diffraction with coherent X-rays. *Nature* **352** (6336), 608–610. DOI: 10.1038/352608a0.

[184] P. N. Pusey and W. van Megen (1989). Dynamic light scattering by non-ergodic media. *Physica A: Statistical Mechanics and its Applications* **157** (2), 705–741. DOI: 10.1016/0378-4371(89)90063-0.

[185] Fivos Perakis and Christian Gutt (2020). Towards molecular movies with X-ray photon correlation spectroscopy. *Physical chemistry chemical physics : PCCP* **22** (35), 19443–19453. DOI: 10.1039/D0CP03551C.

[186] Theyencheri Narayanan (2024). Recent advances in synchrotron scattering methods for probing the structure and dynamics of colloids. *Advances in colloid and interface science* **325**, 103114. DOI: 10.1016/j.cis.2024.103114.

[187] Taiki Hoshino, Yasushi Okamoto, Atsushi Yamamoto, and Hiroyasu Masunaga (2023). Dynamic behaviours of epoxy resin thin films during the curing process. *Soft matter* **19** (18), 3267–3272. DOI: 10.1039/D2SM01500E.

[188] Naisheng Jiang, Maya K. Endoh, and Tadanori Koga (2013). 'Marker' grazing-incidence X-ray photon correlation spectroscopy: a new tool to peer into the interfaces of nanoconfined polymer thin films. *Polymer Journal* **45** (1), 26–33. DOI: 10.1038/pj.2012.184.

[189] Xiaozhi Zhang et al. (2024). Local step-flow dynamics in thin film growth with desorption. *Physical Review Materials* **8** (3). DOI: 10.1103/PhysRevMaterials.8.033403.

[190] Peco Myint et al. (2024). Coherent X-ray Spectroscopy Elucidates Nanoscale Dynamics of Plasma-Enhanced Thin-Film Growth. *ACS nano* **18** (3), 1982–1994. DOI: 10.1021/acsnano.3c07619.

[191] Anders Madsen, Robert L. Leheny, Hongyu Guo, Michael Sprung, and Orsolya Czakkel (2010). Beyond simple exponential correlation functions and equilibrium dynamics in x-ray photon correlation spectroscopy. *New Journal of Physics* **12** (5), 055001. DOI: 10.1088/1367-2630/12/5/055001.

[192] Peter Lindner, ed. (2006). *Neutrons, X-rays and light: Scattering methods applied to soft condensed matter*. Transferred to digital print. North-Holland delta series. Amsterdam: Elsevier.

[193] Graham Williams and David C. Watts (1970). Non-symmetrical dielectric relaxation behaviour arising from a simple empirical decay function. *Transactions of the Faraday Society* **66**, 80. DOI: 10.1039/TF9706600080.

[194] H. Conrad et al. (2015). Correlated heterogeneous dynamics in glass-forming polymers. *Physical review. E, Statistical, nonlinear, and soft matter physics* **91** (4), 042309. DOI: 10.1103/PhysRevE.91.042309.

[195] Davide Orsi et al. (2015). 2D dynamical arrest transition in a mixed nanoparticle-phospholipid layer studied in real and momentum spaces. *Scientific reports* **5**, 17930. DOI: 10.1038/srep17930.

[196] Federico Amadei et al. (2020). Ion-Mediated Cross-linking of Biopolymers Confined at Liquid/Liquid Interfaces Probed by In Situ High-Energy Grazing Incidence X-ray Photon Correlation Spectroscopy. *The journal of physical chemistry. B* **124** (40), 8937–8942. DOI: 10.1021/acs.jpcb.0c07056.

[197] Frédéric Livet et al. (2002). Statics and kinetics of the ordering transition in the AuAgZn2 alloy. *Physical review. B, Condensed matter* **66** (13). DOI: 10.1103/PhysRevB.66.134108.

[198] Andrei Fluerasu, Mark Sutton, and Eric M. Dufresne (2005). X-ray intensity fluctuation spectroscopy studies on phase-ordering systems. *Physical Review Letters* **94** (5), 055501. DOI: 10.1103/PhysRevLett.94.055501.

[199] K. Ludwig et al. (2005). X-ray intensity fluctuation spectroscopy studies of ordering kinetics in a Cu-Pd alloy. *Physical Review B* **72** (14). DOI: 10.1103/PhysRevB.72.144201.

[200] Laura Piveteau, Viktoriia Morad, and Maksym V. Kovalenko (2020). Solid-State NMR and NQR Spectroscopy of Lead-Halide Perovskite Materials. *Journal of the American Chemical Society* **142** (46), 19413–19437. DOI: 10.1021/jacs.0c07338.

[201] Wouter M. J. Franssen and Arno P. M. Kentgens (2019). Solid-state NMR of hybrid halide perovskites. *Solid state nuclear magnetic resonance* **100**, 36–44. DOI: 10.1016/j.ssnmr.2019.03.005.

[202] Koji Yamada et al. (2018). Static and Dynamic Structures of Perovskite Halides ABX3 (B = Pb, Sn) and Their Characteristic Semiconducting Properties by a Hückel Analytical Calculation. *Bulletin of the Chemical Society of Japan* **91** (8), 1196–1204. DOI: 10.1246/bcsj.20180068.

[203] Qiang Xu, Taro Eguchi, Hirokazu Nakayama, Nobuo Nakamura, and Michihiko Kishita (1991). Molecular Motions and Phase Transitions in Solid CH 3 NH 3 PbX 3 (X = C1, Br, I) as Studied by NMR and NQR. *Zeitschrift für Naturforschung A* **46** (3), 240–246. DOI: 10.1515/zna-1991-0305.

[204] Alessandro Senocrate et al. (2017). The Nature of Ion Conduction in Methylammonium Lead Iodide: A Multimethod Approach. *Angewandte Chemie (International ed. in English)* **56** (27), 7755–7759. DOI: 10.1002/anie.201701724.

[205] Alessandro Senocrate and Joachim Maier (2019). Solid-State Ionics of Hybrid Halide Perovskites. *Journal of the American Chemical Society* **141** (21), 8382–8396. DOI: 10.1021/jacs.8b13594.

[206] K. Hentschel (1996). Die Entdeckung des Zeeman–Effekts: als Beispiel für das komplexe Wechselspiel von wissenschaftlichen Instrumenten, Experimenten und Theorie. *Physikalische Blätter* **52** (12), 1232–1235. DOI: 10.1002/phbl.19960521209.

[207] Melinda J. Duer (2004). *Introduction to solid-state NMR spectroscopy*. First published. Oxford et al.: Blackwell Publishing and Blackwell Science.

[208] Malcolm H. Levitt (2008). *Spin dynamics: Basics of nuclear magnetic resonance*. 2. ed. Chichester: Wiley. URL: http://www.loc.gov/catdir/enhancements/fy0826/2007022146-d.html.

[209] Edward Raymond Andrew (1981). Magic angle spinning in solid state n.m.r. spectroscopy. *Philosophical Transactions of the Royal Society of London. Series A, Mathematical and Physical Sciences* **299** (1452), 505–520. DOI: 10.1098/rsta.1981.0032.

[210] John C. Lindon (2016). *Encyclopedia of Spectroscopy and Spectrometry*. San Diego: Elsevier Science. URL: https://ebookcentral.proquest.com/lib/kxp/detail.action?docID=4723162.

[211] Cory M. Widdifield, Rebecca P. Chapman, and David L. Bryce (2009). Chapter 5 Chlorine, Bromine, and Iodine Solid-State NMR Spectroscopy. In: vol. 66. Annual Reports on NMR Spectroscopy. Elsevier, 195–326. DOI: 10.1016/S0066-4103(08)00405-5.

[212] Patrick M.J. Szell and David L. Bryce (2015). Recent Advances in Chlorine, Bromine, and Iodine Solid-State NMR Spectroscopy. In: vol. 84. Annual Reports on NMR Spectroscopy. Elsevier, 115–162. DOI: 10.1016/bs.arnmr.2014.10.002.

[213] J. A. S. Smith (1971). Nuclear quadrupole resonance spectroscopy. General principles. *Journal of Chemical Education* **48** (1), 39. DOI: 10.1021/ed048p39.

[214] Bryan A. Rosales et al. (2017). Lead Halide Perovskites: Challenges and Opportunities in Advanced Synthesis and Spectroscopy. *ACS energy letters* **2** (4), 906–914. DOI: 10.1021/acsenergylett.6b00674.

[215] Bryan A. Rosales et al. (2016). Persistent Dopants and Phase Segregation in Organolead Mixed-Halide Perovskites. *Chemistry of Materials* **28** (19), 6848–6859. DOI: 10.1021/acs.chemmater.6b01874.

[216] Abhoy Karmakar et al. (2018). Mechanochemical Synthesis of Methylammonium Lead Mixed–Halide Perovskites: Unraveling the Solid-Solution Behavior Using Solid-State NMR. *Chemistry of Materials* **30** (7), 2309–2321. DOI: 10.1021/acs.chemmater.7b05209.

[217] Abdelrahman M. Askar et al. (2018). Composition-Tunable Formamidinium Lead Mixed Halide Perovskites via Solvent-Free Mechanochemical Synthesis: Decoding the Pb Environments Using Solid-State NMR Spectroscopy. *The journal of physical chemistry letters* **9** (10), 2671–2677. DOI: 10.1021/acs.jpclett.8b01084.

[218] Abdelrahman M. Askar, Guy M. Bernard, Benjamin Wiltshire, Karthik Shankar, and Vladimir K. Michaelis (2017). Multinuclear Magnetic Resonance Tracking of Hydro, Thermal, and Hydrothermal Decomposition of CH 3 NH 3 PbI 3. *The Journal of Physical Chemistry C* **121** (2), 1013–1024. DOI: 10.1021/acs.jpcc.6b10865.

[219] Dominik J. Kubicki et al. (2017). Phase Segregation in Cs-, Rb- and K-Doped Mixed-Cation (MA) x (FA) 1– x PbI 3 Hybrid Perovskites from Solid-State NMR. *Journal of the American Chemical Society* **139** (40), 14173–14180. DOI: 10.1021/jacs.7b07223.

[220] Claire Roiland et al. (2016). Multinuclear NMR as a tool for studying local order and dynamics in CH3NH3PbX3 (X = Cl, Br, I) hybrid perovskites. *Physical chemistry chemical physics : PCCP* **18** (39), 27133–27142. DOI: 10.1039/C6CP02947G.

[221] Douglas H. Fabini et al. (2017). Universal Dynamics of Molecular Reorientation in Hybrid Lead Iodide Perovskites. *Journal of the American Chemical Society* **139** (46), 16875–16884. DOI: 10.1021/jacs.7b09536.

[222] Artem A. Bakulin et al. (2015). Real-Time Observation of Organic Cation Reorientation in Methylammonium Lead Iodide Perovskites. *The journal of physical chemistry letters* **6** (18), 3663–3669. DOI: 10.1021/acs.jpclett.5b01555.

[223] Tom Baikie et al. (2015). A combined single crystal neutron/X-ray diffraction and solid-state nuclear magnetic resonance study of the hybrid perovskites CH 3 NH 3 PbX 3 (X = I, Br and Cl). *Journal of Materials Chemistry A* **3** (17), 9298–9307. DOI: 10.1039/C5TA01125F.

[224] Fei Zhang et al. (2020). Advances in two-dimensional organic–inorganic hybrid perovskites. *Energy Environ. Sci.* **13** (4), 1154–1186. DOI: 10.1039/C9EE03757H.

[225] Matthew D. Smith, Bridget A. Connor, and Hemamala I. Karunadasa (2019). Tuning the Luminescence of Layered Halide Perovskites. *Chemical reviews* **119** (5), 3104–3139. DOI: 10.1021/acs.chemrev.8b00477.

[226] Dominik J. Kubicki et al. (2018). Phase Segregation in Potassium-Doped Lead Halide Perovskites from 39K Solid-State NMR at 21.1 T. *Journal of the American Chemical Society* **140** (23), 7232–7238. DOI: 10.1021/jacs.8b03191.

[227] Dominik J. Kubicki et al. (2018). Formation of Stable Mixed Guanidinium-Methylammonium Phases with Exceptionally Long Carrier Lifetimes for High-Efficiency Lead Iodide-Based Perovskite Photovoltaics. *Journal of the American Chemical Society* **140** (9), 3345–3351. DOI: 10.1021/jacs.7b12860.

[228] Anwar Q. Alanazi et al. (2019). Atomic-Level Microstructure of Efficient Formamidinium-Based Perovskite Solar Cells Stabilized by 5-Ammonium Valeric Acid Iodide Revealed by Multinuclear and Two-Dimensional Solid-State NMR. *Journal of the American Chemical Society* **141** (44), 17659–17669. DOI: 10.1021/jacs.9b07381.

[229] Mohammad Mahdi Tavakoli et al. (2018). Addition of adamantylammonium iodide to hole transport layers enables highly efficient and electroluminescent perovskite solar cells. *Energy Environ. Sci.* **11** (11), 3310–3320. DOI: 10.1039/C8EE02404A.

[230] Dongqin Bi et al. (2018). Multifunctional molecular modulators for perovskite solar cells with over 20% efficiency and high operational stability. *Nature communications* **9** (1), 4482. DOI: 10.1038/s41467-018-06709-w.

[231] M. Hidaka, Y. Okamoto, and Y. Zikumaru (1983). Structural Phase Transition of CsPbCl3 below Room Temperature. *physica status solidi (a)* **79** (1), 263–269. DOI: 10.1002/pssa.2210790129.

[232] Nico Leupold et al. (2023). How Methylammonium Iodide Reactant Size Affects Morphology and Defect Properties of Mechanochemically Synthesized MAPbI 3 Powder. *European Journal of Inorganic Chemistry* **26** (8). DOI: 10.1002/ejic.202200736.

[233] Wouter M. J. Franssen, Sverre G. D. van Es, Rıza Dervişoğlu, Gilles A. de Wijs, and Arno P. M. Kentgens (2017). Symmetry, Dynamics, and Defects in Methylammonium Lead Halide Perovskites. *The journal of physical chemistry letters* **8** (1), 61–66. DOI: 10.1021/acs.jpclett.6b02542.

[234] Shiqing Bi et al. (2019). Halogen bonding reduces intrinsic traps and enhances charge mobilities in halide perovskite solar cells. *Journal of Materials Chemistry A* **7** (12), 6840–6848. DOI: 10.1039/C8TA11835C.

[235] Antonio Abate et al. (2014). Supramolecular halogen bond passivation of organic-inorganic halide perovskite solar cells. *Nano letters* **14** (6), 3247–3254. DOI: 10.1021/nl500627x.

[236] Marco A. Ruiz-Preciado et al. (2020). Supramolecular Modulation of Hybrid Perovskite Solar Cells via Bifunctional Halogen Bonding Revealed by Two-Dimensional 19F Solid-State NMR Spectroscopy. *Journal of the American Chemical Society* **142** (3), 1645–1654. DOI: 10.1021/jacs.9b13701.

[237] Johannes Schindelin et al. (2012). Fiji: an open-source platform for biological-image analysis. *Nature methods* **9** (7), 676–682. DOI: 10.1038/nmeth.2019.

[238] Michael Buchhorn, Stefan Wedler, and Fabian Panzer (2018). Setup to Study the in Situ Evolution of Both Photoluminescence and Absorption during the Processing of Organic or Hybrid Semiconductors. *The journal of physical chemistry. A* **122** (46), 9115–9122. DOI: 10.1021/acs.jpca.8b07495.

[239] Sameera K. Abeykoon et al. (2016). Software tools for X-ray photon correlation and X-ray speckle visibility spectroscopy. In: *2016 New York Scientific Data Summit (NYSDS)*. IEEE, 1–10. DOI: 10.1109/NYSDS.2016.7747815.

[240] Nico Leupold et al. (2019). High Versatility and Stability of Mechanochemically Synthesized Halide Perovskite Powders for Optoelectronic Devices. *ACS applied materials & interfaces* **11** (33), 30259–30268. DOI: 10.1021/acsami.9b09160.

[241] Stephan Pröller et al. (2017). Note: Setup for chemical atmospheric control during in situ grazing incidence X-ray scattering of printed thin films. *The Review of scientific instruments* **88** (6), 066101. DOI: 10.1063/1.4984130.

[242] Aidan P. Thompson et al. (2022). LAMMPS - a flexible simulation tool for particle-based materials modeling at the atomic, meso, and continuum scales. *Computer Physics Communications* **271**, 108171. DOI: 10.1016/j.cpc.2021.108171.

[243] Yong Qin and Kristen A. Fichthorn (2003). Molecular-dynamics simulation of forces between nanoparticles in a Lennard-Jones liquid. *The Journal of chemical physics* **119** (18), 9745–9754. DOI: 10.1063/1.1615493.

[244] Ethan A. Mastny and Juan J. DE Pablo (2007). Melting line of the Lennard-Jones system, infinite size, and full potential. *The Journal of chemical physics* **127** (10), 104504. DOI: 10.1063/1.2753149.

[245] van Sang, Vo van Hoang, and Nguyen Thi Thuy Hang (2013). Molecular dynamics simulation of melting of fcc Lennard-Jones nanoparticles. *The European Physical Journal D* **67** (3). DOI: 10.1140/epjd/e2013-30584-9.

[246] M. Rauscher, T. Salditt, and H. Spohn (1995). Small-angle x-ray scattering under grazing incidence: The cross section in the distorted-wave Born approximation. *Physical review. B, Condensed matter* **52** (23), 16855–16863. DOI: 10.1103/PhysRevB.52.16855.

[247] D. Lumma, L. B. Lurio, S. G. J. Mochrie, and M. Sutton (2000). Area detector based photon correlation in the regime of short data batches: Data reduction for dynamic x-ray scattering. *Review of Scientific Instruments* **71** (9), 3274–3289. DOI: 10.1063/1.1287637.

[248] Andrei Fluerasu, Abdellatif Moussaïd, Anders Madsen, and Andrew Schofield (2007). Slow dynamics and aging in colloidal gels studied by x-ray photon correlation spectroscopy. *Physical review. E, Statistical, nonlinear, and soft matter physics* **76** (1 Pt 1), 010401. DOI: 10.1103/PhysRevE.76.010401.

[249] Seong Sik Shin et al. (2017). Colloidally prepared La-doped BaSnO3 electrodes for efficient, photostable perovskite solar cells. *Science (New York, N.Y.)* **356** (6334), 167–171. DOI: 10.1126/science.aam6620.

[250] Dae-Yong Son et al. (2016). Self-formed grain boundary healing layer for highly efficient CH3NH3PbI3 perovskite solar cells. *Nature Energy* **1** (7). DOI: 10.1038/nenergy.2016.81.

[251] Woon Seok Yang et al. (2015). High-performance photovoltaic perovskite layers fabricated through intramolecular exchange. *Science (New York, N.Y.)* **348** (6240), 1234–1237. DOI: 10.1126/science.aaa9272.

[252] Yehao Deng et al. (2015). Scalable fabrication of efficient organolead trihalide perovskite solar cells with doctor-bladed active layers. *Energy & Environmental Science* **8** (5), 1544–1550. DOI: 10.1039/C4EE03907F.

[253] Yaron Tidhar et al. (2014). Crystallization of methyl ammonium lead halide perovskites: implications for photovoltaic applications. *Journal of the American Chemical Society* **136** (38), 13249–13256. DOI: 10.1021/ja505556s.

[254] Patrick Wai-Keung Fong et al. (2021). Printing High-Efficiency Perovskite Solar Cells in High-Humidity Ambient Environment-An In Situ Guided Investigation. *Advanced science (Weinheim, Baden-Wurttemberg, Germany)* **8** (6), 2003359. DOI: 10.1002/advs.202003359.

[255] Patrick Wai-Keung Fong and Gang Li (2021). The Challenge of Ambient Air–Processed Organometallic Halide Perovskite: Technology Transfer From Spin Coating to Meniscus Blade Coating of Perovskite Thin Films. *Frontiers in Materials* **8**. DOI: 10.3389/fmats.2021.635224.

[256] Min–cheol Kim et al. (2021). Advanced Characterization Techniques for Overcoming Challenges of Perovskite Solar Cell Materials. *Advanced Energy Materials* **11** (15), 2001753. DOI: 10.1002/aenm.202001753.

[257] Ke Meng et al. (2018). In Situ Real-Time Study of the Dynamic Formation and Conversion Processes of Metal Halide Perovskite Films. *Advanced materials (Deerfield Beach, Fla.)* **30** (11). DOI: 10.1002/adma.201706401.

[258] Sehyun Lee et al. (2020). In situ study of the film formation mechanism of organic–inorganic hybrid perovskite solar cells: controlling the solvate phase using an additive system. *Journal of Materials Chemistry A* **8** (16), 7695–7703. DOI: 10.1039/D0TA00048E.

[259] Oliver Filonik et al. (2019). Evolution of Perovskite Crystallization in Printed Mesoscopic Perovskite Solar Cells. *Energy Technology* **7** (10), 1900343. DOI: 10.1002/ente.201900343.

[260] Dounya Barrit et al. (2019). Impact of the Solvation State of Lead Iodide on Its Two–Step Conversion to MAPbI 3 : An In Situ Investigation. *Advanced Functional Materials* **29** (47), 1807544. DOI: 10.1002/adfm.201807544.

[261] Kelly S. Wilson and Cathy Y. Wong (2018). In Situ Measurement of Exciton Dynamics During Thin-Film Formation Using Single-Shot Transient Absorption. *The journal of physical chemistry. A* **122** (31), 6438–6444. DOI: 10.1021/acs.jpca.8b06248.

[262] Yue-Min Xie et al. (2018). Direct observation of cation-exchange in liquid-to-solid phase transformation in FA 1−x MA x PbI 3 based perovskite solar cells. *Journal of Materials Chemistry A* **6** (19), 9081–9088. DOI: 10.1039/C8TA01642A.

[263] Karsten Bruening et al. (2018). Scalable Fabrication of Perovskite Solar Cells to Meet Climate Targets. *Joule* **2** (11), 2464–2476. DOI: 10.1016/j.joule.2018.09.014.

[264] Konstantin Schötz and Fabian Panzer (2021). Using In Situ Optical Spectroscopy to Elucidate Film Formation of Metal Halide Perovskites. *The journal of physical chemistry. A* **125** (11), 2209–2225. DOI: 10.1021/acs.jpca.0c10765.

[265] Seul-Gi Kim et al. (2021). How antisolvent miscibility affects perovskite film wrinkling and photovoltaic properties. *Nature communications* **12** (1), 1554. DOI: 10.1038/s41467-021-21803-2.

[266] Carolin M. Sutter–Fella (2021). The Value of Watching How Materials Grow: A Multimodal Case Study on Halide Perovskites. *Advanced Energy Materials* **11** (17), 2003534. DOI: 10.1002/aenm.202003534.

[267] Simon Biberger et al. (2022). How the ionic liquid BMIMBF 4 influences the formation and optoelectronic properties of MAPbI 3 thin films. *Journal of Materials Chemistry A* **10** (35), 18038–18049. DOI: 10.1039/D2TA04448J.

[268] Maged Abdelsamie et al. (2021). Mechanism of Additive-Assisted Room-Temperature Processing of Metal Halide Perovskite Thin Films. *ACS applied materials & interfaces* **13** (11), 13212–13225. DOI: 10.1021/acsami.0c22630.

[269] Tze–Bin Song et al. (2020). Revealing the Dynamics of Hybrid Metal Halide Perovskite Formation via Multimodal In Situ Probes. *Advanced Functional Materials* **30** (6), 1908337. DOI: 10.1002/adfm.201908337.

[270] Alexander D. Taylor et al. (2021). A general approach to high-efficiency perovskite solar cells by any antisolvent. *Nature communications* **12** (1), 1878. DOI: 10.1038/s41467-021-22049-8.

[271] Kuan Liu et al. (2020). Zwitterionic-Surfactant-Assisted Room-Temperature Coating of Efficient Perovskite Solar Cells. *Joule* **4** (11), 2404–2425. DOI: 10.1016/j.joule.2020.09.011.

[272] Nam Joong Jeon et al. (2014). Solvent engineering for high-performance inorganic-organic hybrid perovskite solar cells. *Nature materials* **13** (9), 897–903. DOI: 10.1038/nmat4014.

[273] Yulia Galagan (2020). Perovskite solar cells from lab to fab: the main challenges to access the market. *Oxford Open Materials Science* **1** (1). DOI: 10.1093/oxfmat/itaa007.

[274] Ming-Chun Tang et al. (2020). Ambient blade coating of mixed cation, mixed halide perovskites without dripping: in situ investigation and highly efficient solar cells. *Journal of Materials Chemistry A* **8** (3), 1095–1104. DOI: 10.1039/C9TA12890E.

[275] Konstantin Schötz et al. (2021). Understanding Differences in the Crystallization Kinetics between One–Step Slot–Die Coating and Spin Coating of MAPbI 3 Using Multimodal In Situ Optical Spectroscopy. *Advanced Optical Materials* **9** (21), 2101161. DOI: 10.1002/adom.202101161.

[276] Mihirsinh Chauhan et al. (2020). Investigating two-step MAPbI 3 thin film formation during spin coating by simultaneous in situ absorption and photoluminescence spectroscopy. *Journal of Materials Chemistry A* **8** (10), 5086–5094. DOI: 10.1039/C9TA12409H.

[277] H. E. W. Jenkins and A. Francis (1937). *Fundamentals of Optics*. New York: Tata McGraw-Hill Education.

[278] Rahim Munir et al. (2017). Hybrid Perovskite Thin-Film Photovoltaics: In Situ Diagnostics and Importance of the Precursor Solvate Phases. *Advanced materials (Deerfield Beach, Fla.)* **29** (2). DOI: 10.1002/adma.201604113.

[279] J. C. Manifacier, J. Gasiot, and J. P. Fillard (1976). A simple method for the determination of the optical constants n, k and the thickness of a weakly absorbing thin film. *Journal of Physics E: Scientific Instruments* **9** (11), 1002–1004. DOI: 10.1088/0022-3735/9/11/032.

[280] (2003). *CRC handbook of chemistry and physics: A ready-reference book of chemical and physical data*. 84th ed. Boca Raton: CRC Press.

[281] Yuxi Tian and Ivan G. Scheblykin (2015). Artifacts in Absorption Measurements of Organometal Halide Perovskite Materials: What Are the Real Spectra? *The journal of physical chemistry letters* **6** (17), 3466–3470. DOI: 10.1021/acs.jpclett.5b01406.

[282] Timothy W. Crothers et al. (2017). Photon Reabsorption Masks Intrinsic Bimolecular Charge-Carrier Recombination in CH3NH3PbI3 Perovskite. *Nano letters* **17** (9), 5782–5789. DOI: 10.1021/acs.nanolett.7b02834.

[283] Stepan Demchyshyn et al. (2017). Confining metal-halide perovskites in nanoporous thin films. *Science advances* **3** (8), e1700738. DOI: 10.1126/sciadv.1700738.

[284] Loredana Protesescu et al. (2015). Nanocrystals of Cesium Lead Halide Perovskites ($CsPbX_3$, X = Cl, Br, and I): Novel Optoelectronic Materials Showing Bright Emission with Wide Color Gamut. *Nano letters* **15** (6), 3692–3696. DOI: 10.1021/nl5048779.

[285] Lili Wang et al. (2017). Scalable Ligand-Mediated Transport Synthesis of Organic-Inorganic Hybrid Perovskite Nanocrystals with Resolved Electronic Structure and Ultrafast Dynamics. *ACS nano* **11** (3), 2689–2696. DOI: 10.1021/acsnano.6b07574.

[286] Victor Malgras, Joel Henzie, Toshiaki Takei, and Yusuke Yamauchi (2017). Hybrid methylammonium lead halide perovskite nanocrystals confined in gyroidal silica templates. *Chemical communications (Cambridge, England)* **53** (15), 2359–2362. DOI: 10.1039/c6cc10245j.

[287] Elizabeth S. Parrott et al. (2019). Growth modes and quantum confinement in ultrathin vapour-deposited MAPbI3 films. *Nanoscale* **11** (30), 14276–14284. DOI: 10.1039/c9nr04104d.

[288] Yosuke Kayanuma. Quantum-size effects of interacting electrons and holes in semiconductor microcrystals with spherical shape.

[289] Dmitry N. Dirin et al. (2016). Harnessing Defect-Tolerance at the Nanoscale: Highly Luminescent Lead Halide Perovskite Nanocrystals in Mesoporous Silica Matrixes. *Nano letters* **16** (9), 5866–5874. DOI: 10.1021/acs.nanolett.6b02688.

[290] Mingcong Wang et al. (2021). Impact of Photoluminescence Reabsorption in Metal–Halide Perovskite Solar Cells. *Solar RRL*, 2100029. DOI: 10.1002/solr.202100029.

[291] Yahui Li et al. (2017). In Situ Observation of Crystallization of Methylammonium Lead Iodide Perovskite from Microdroplets. *Small (Weinheim an der Bergstrasse, Germany)* **13** (26). DOI: 10.1002/smll.201604125.

[292] Yicheng Zhao et al. (2018). Perovskite seeding growth of formamidinium-lead-iodide-based perovskites for efficient and stable solar cells. *Nature communications* **9** (1), 1607. DOI: 10.1038/s41467-018-04029-7.

[293] Yu-Hao Deng, Zhen-Qian Yang, and Ren-Min Ma (2020). Growth of centimeter-scale perovskite single-crystalline thin film via surface engineering. *Nano convergence* **7** (1), 25. DOI: 10.1186/s40580-020-00236-5.

[294] David P. McMeekin et al. (2016). A mixed-cation lead mixed-halide perovskite absorber for tandem solar cells. *Science (New York, N.Y.)* **351** (6269), 151–155. DOI: 10.1126/science.aad5845.

[295] Jixian Xu et al. (2020). Triple-halide wide-band gap perovskites with suppressed phase segregation for efficient tandems. *Science (New York, N.Y.)* **367** (6482), 1097–1104. DOI: 10.1126/science.aaz5074.

[296] Seog Joon Yoon, Masaru Kuno, and Prashant V. Kamat (2017). Shift Happens . How Halide Ion Defects Influence Photoinduced Segregation in Mixed Halide Perovskites. *ACS Energy Letters* **2** (7), 1507–1514. DOI: 10.1021/acsenergylett.7b00357.

[297] Gabriel C. Halford et al. (2022). Structural Dynamics of Metal Halide Perovskites during Photoinduced Halide Segregation. *ACS applied materials & interfaces* **14** (3), 4335–4343. DOI: 10.1021/acsami.1c22854.

[298] Tor Elmelund, Brian Seger, Masaru Kuno, and Prashant V. Kamat (2020). How Interplay between Photo and Thermal Activation Dictates Halide Ion Segregation in Mixed Halide Perovskites. *ACS Energy Letters* **5** (1), 56–63. DOI: 10.1021/acsenergylett.9b02265.

[299] Danil W. Boukhvalov et al. (2020). Thermal Effects and Halide Mixing of Hybrid Perovskites: MD and XPS Studies. *The journal of physical chemistry. A* **124** (1), 135–140. DOI: 10.1021/acs.jpca.9b09653.

[300] Adam D. Wright, Jay B. Patel, Michael B. Johnston, and Laura M. Herz (2023). Temperature-Dependent Reversal of Phase Segregation in Mixed-Halide Perovskites. *Advanced materials (Deerfield Beach, Fla.)* e2210834. DOI: 10.1002/adma.202210834.

[301] Yuze Lin et al. (2018). Excess charge-carrier induced instability of hybrid perovskites. *Nature communications* **9** (1), 4981. DOI: 10.1038/s41467-018-07438-w.

[302] Tor Elmelund, Rebecca A. Scheidt, Brian Seger, and Prashant V. Kamat (2019). Bidirectional Halide Ion Exchange in Paired Lead Halide Perovskite Films with Thermal Activation. *ACS Energy Letters* **4** (8), 1961–1969. DOI: 10.1021/acsenergylett.9b01280.

[303] Hyunhwa Lee et al. (2023). In Situ Observation of Photoinduced Halide Segregation in Mixed Halide Perovskite. *ACS Applied Energy Materials* **6** (3), 1565–1574. DOI: 10.1021/acsaem.2c03438.

[304] Alex J. Barker et al. (2017). Defect-Assisted Photoinduced Halide Segregation in Mixed-Halide Perovskite Thin Films. *ACS Energy Letters* **2** (6), 1416–1424. DOI: 10.1021/acsenergylett.7b00282.

[305] Jon M. Azpiroz, Edoardo Mosconi, Juan Bisquert, and Filippo DE Angelis (2015). Defect migration in methylammonium lead iodide and its role in perovskite solar cell operation. *Energy & Environmental Science* **8** (7), 2118–2127. DOI: 10.1039/C5EE01265A.

[306] Cheng Li, Antonio Guerrero, Sven Huettner, and Juan Bisquert (2018). Unravelling the role of vacancies in lead halide perovskite through electrical switching of photoluminescence. *Nature communications* **9** (1), 5113. DOI: 10.1038/s41467-018-07571-6.

[307] Yicheng Zhao et al. (2020). Strain-activated light-induced halide segregation in mixed-halide perovskite solids. *Nature communications* **11** (1), 6328. DOI: 10.1038/s41467-020-20066-7.

[308] Lucie McGovern, Moritz H. Futscher, Loreta A. Muscarella, and Bruno Ehrler (2020). Understanding the Stability of MAPbBr3 versus MAPbI3: Suppression of Methylammonium Migration and Reduction of Halide Migration. *The journal of physical chemistry letters* **11** (17), 7127–7132. DOI: 10.1021/acs.jpclett.0c01822.

[309] Christopher Eames et al. (2015). Ionic transport in hybrid lead iodide perovskite solar cells. *Nature communications* **6**, 7497. DOI: 10.1038/ncomms8497.

[310] Hsinhan Tsai et al. (2018). Light-induced lattice expansion leads to high-efficiency perovskite solar cells. *Science (New York, N.Y.)* **360** (6384), 67–70. DOI: 10.1126/science.aap8671.

[311] Connor G. Bischak et al. (2017). Origin of Reversible Photoinduced Phase Separation in Hybrid Perovskites. *Nano letters* **17** (2), 1028–1033. DOI: 10.1021/acs.nanolett.6b04453.

[312] Mojtaba Abdi-Jalebi et al. (2018). Maximizing and stabilizing luminescence from halide perovskites with potassium passivation. *Nature* **555** (7697), 497–501. DOI: 10.1038/nature25989.

[313] Yong Wang et al. (2019). Thermodynamically stabilized β-CsPbI3-based perovskite solar cells with efficiencies 18. *Science (New York, N.Y.)* **365** (6453), 591–595. DOI: 10.1126/science.aav8680.

[314] Yongping Fu et al. (2017). Stabilization of the Metastable Lead Iodide Perovskite Phase via Surface Functionalization. *Nano letters* **17** (7), 4405–4414. DOI: 10.1021/acs.nanolett.7b01500.

[315] Dan Liu et al. (2019). A polar-hydrophobic ionic liquid induces grain growth and stabilization in halide perovskites. *Chemical communications (Cambridge, England)* **55** (74), 11059–11062. DOI: 10.1039/c9cc05490a.

[316] Jue Wang et al. (2019). Halide perovskite based on hydrophobic ionic liquid for stability improving and its application in high-efficient photovoltaic cell. *Electrochimica Acta* **303**, 133–139. DOI: 10.1016/j.electacta.2019.02.071.

[317] Peng Chen et al. (2018). Global Control of CH 3 NH 3 PbI 3 Formation with Multifunctional Ionic Liquid for Perovskite Hybrid Photovoltaics. *The Journal of Physical Chemistry C* **122** (20), 10699–10705. DOI: 10.1021/acs.jpcc.8b01026.

[318] Yangyang Wan et al. (2016). Ionic liquid-assisted perovskite crystal film growth for high performance planar heterojunction perovskite solar cells. *RSC Advances* **6** (100), 97848–97852. DOI: 10.1039/C6RA24616H.

[319] Lei Gu et al. (2022). Designing Ionic Liquids as the Solvent for Efficient and Stable Perovskite Solar Cells. *ACS applied materials & interfaces*. DOI: 10.1021/acsami.1c21035.

[320] Weijing Chu, Junyou Yang, Qinghui Jiang, Xin Li, and Jiwu Xin (2018). Enhancement of photovoltaic performance of flexible perovskite solar cells by means of ionic liquid interface modification in a low temperature all solution process. *Applied Surface Science* **440**, 1116–1122. DOI: 10.1016/j.apsusc.2018.01.310.

[321] Meng Li et al. (2018). Interface Modification by Ionic Liquid: A Promising Candidate for Indoor Light Harvesting and Stability Improvement of Planar Perovskite Solar Cells. *Advanced Energy Materials* **8** (24), 1801509. DOI: 10.1002/aenm.201801509.

[322] Xu Huang, Heng Guo, Kai Wang, and Xiaobo Liu (2017). Ionic liquid induced surface trap-state passivation for efficient perovskite hybrid solar cells. *Organic Electronics* **41**, 42–48. DOI: 10.1016/j.orgel.2016.11.031.

[323] Philipp Ramming et al. (2021). Suppressed ion migration in powder-based perovskite thick films using an ionic liquid. *Journal of Materials Chemistry C* **9** (35), 11827–11837. DOI: 10.1039/D1TC01554K.

[324] Xueqing Zheng et al. (2020). Enhanced thermal stability of inverted perovskite solar cells by interface modification and additive strategy. *RSC advances* **10** (31), 18400–18406. DOI: 10.1039/d0ra03238g.

[325] Sai Bai et al. (2019). Planar perovskite solar cells with long-term stability using ionic liquid additives. *Nature* **571** (7764), 245–250. DOI: 10.1038/s41586-019-1357-2.

[326] Hobeom Kim, Jaekeun Lim, Muhammad Sohail, and Mohammad Khaja Nazeeruddin (2022). Superhalogen Passivation for Efficient and Stable Perovskite Solar Cells. *Solar RRL* **6** (7), 2200013. DOI: 10.1002/solr.202200013.

[327] Rajendra Kumar Gunasekaran et al. (2018). Revealing the Self-Degradation Mechanisms in Methylammonium Lead Iodide Perovskites in Dark and Vacuum. *Chemphyschem : a European journal of chemical physics and physical chemistry* **19** (12), 1507–1513. DOI: 10.1002/cphc.201800002.

[328] Stefaan DE Wolf et al. (2014). Organometallic Halide Perovskites: Sharp Optical Absorption Edge and Its Relation to Photovoltaic Performance. *The journal of physical chemistry letters* **5** (6), 1035–1039. DOI: 10.1021/jz500279b.

[329] Kostas Fykouras et al. (2023). Disorder to order: how halide mixing in MAPbI 3− x Br x perovskites restricts MA dynamics. *Journal of Materials Chemistry A* **11** (9), 4587–4597. DOI: 10.1039/D2TA09069D.

[330] Yuiga Nakamura et al. (2020). Crystal Systems and Lattice Parameters of CH3NH3Pb(I1-xBrx)3 Determined Using Single Crystals: Validity of Vegard's Law. *Inorganic chemistry* **59** (10), 6709–6716. DOI: 10.1021/acs.inorgchem.9b03421.

[331] G.K Williamson and W.H Hall (1953). X-ray line broadening from filed aluminium and wolfram. *Acta Metallurgica* **1** (1), 22–31. DOI: 10.1016/0001-6160(53)90006-6.

[332] Tianyi Huang et al. (2021). Performance-limiting formation dynamics in mixed-halide perovskites. *Science advances* **7** (46), eabj1799. DOI: 10.1126/sciadv.abj1799.

[333] Th. H. DE Keijser, J. I. Langford, E. J. Mittemeijer, and A. B. P. Vogels (1982). Use of the Voigt function in a single-line method for the analysis of X-ray diffraction line broadening. *Journal of Applied Crystallography* **15** (3), 308–314. DOI: 10.1107/S0021889882012035.

[334] Jingjing Zhao et al. (2017). Strained hybrid perovskite thin films and their impact on the intrinsic stability of perovskite solar cells. *Science advances* **3** (11), eaao5616. DOI: 10.1126/sciadv.aao5616.

[335] Peter Atkins and Julio DE Paula (2005). *Thermodynamics and kinetics*. 8th ed. Vol. v. 1. Physical chemistry. New York: W.H. Freeman and Co.

[336] Jongseob Kim, Sung-Hoon Lee, Jung Hoon Lee, and Ki-Ha Hong (2014). The Role of Intrinsic Defects in Methylammonium Lead Iodide Perovskite. *The journal of physical chemistry letters* **5** (8), 1312–1317. DOI: 10.1021/jz500370k.

[337] Yuchuan Shao et al. (2016). Grain boundary dominated ion migration in polycrystalline organic–inorganic halide perovskite films. *Energy Environ. Sci.* **9** (5), 1752–1759. DOI: 10.1039/c6ee00413j.

[338] Daniele Meggiolaro, Edoardo Mosconi, and Filippo DE Angelis (2019). Formation of Surface Defects Dominates Ion Migration in Lead-Halide Perovskites. *ACS Energy Letters* **4** (3), 779–785. DOI: 10.1021/acsenergylett.9b00247.

[339] Sebastian Reichert et al. (2020). Probing the ionic defect landscape in halide perovskite solar cells. *Nature communications* **11** (1), 6098. DOI: 10.1038/s41467-020-19769-8.

[340] Lucie McGovern, Isabel Koschany, Gianluca Grimaldi, Loreta A. Muscarella, and Bruno Ehrler (2021). Grain Size Influences Activation Energy and Migration Pathways in MAPbBr3 Perovskite Solar Cells. *The journal of physical chemistry letters* **12** (9), 2423–2428. DOI: 10.1021/acs.jpclett.1c00205.

[341] Dane W. deQuilettes et al. (2016). Photo-induced halide redistribution in organic-inorganic perovskite films. *Nature communications* **7**, 11683. DOI: 10.1038/ncomms11683.

[342] D. C. Johnston (2006). Stretched exponential relaxation arising from a continuous sum of exponential decays. *Physical Review B* **74** (18). DOI: 10.1103/PhysRevB.74.184430.

[343] Ran Yin et al. (2021). Dual-Interface Modification with BMIMPF 6 for High-Efficiency and Stable Carbon-Based CsPbI 2 Br Perovskite Solar Cells. *ACS Applied Energy Materials* **4** (9), 9294–9303. DOI: 10.1021/acsaem.1c01521.

[344] Paridhi Sanchora, Deepak K. Pandey, Debkumar Rana, Arnulf Materny, and Dheeraj K. Singh (2019). Impact of Size and Electronegativity of Halide Anions on Hydrogen Bonds and Properties of 1-Ethyl-3-methylimidazolium-Based Ionic Liquids. *The journal of physical chemistry. A* **123** (23), 4948–4963. DOI: 10.1021/acs.jpca.9b04116.

[345] Li Sun et al. (2022). Ionic Liquid–Based Redox Active Electrolytes for Supercapacitors. *Advanced Functional Materials* **32** (27). DOI: 10.1002/adfm.202203611.

[346] Kun Dong et al. (2012). Understanding structures and hydrogen bonds of ionic liquids at the electronic level. *The journal of physical chemistry. B* **116** (3), 1007–1017. DOI: 10.1021/jp205435u.

[347] J. C. Del Valle, F. García Blanco, and J. Catalán (2015). Empirical parameters for solvent acidity, basicity, dipolarity, and polarizability of the ionic liquids BMIMBF4 and BMIMPF6. *The journal of physical chemistry. B* **119** (13), 4683–4692. DOI: 10.1021/jp511154h.

[348] Aditya Sadhanala et al. (2014). Preparation of Single-Phase Films of CH3NH3Pb(I1-xBrx)3 with Sharp Optical Band Edges. *The journal of physical chemistry letters* **5** (15), 2501–2505. DOI: 10.1021/jz501332v.

[349] Maria Assunta Navarra (2013). Ionic liquids as safe electrolyte components for Li-metal and Li-ion batteries. *MRS Bulletin* **38** (7), 548–553. DOI: 10.1557/mrs.2013.152.

[350] Douglas R. MacFarlane et al. (2014). Energy applications of ionic liquids. *Energy Environ. Sci.* **7** (1), 232–250. DOI: 10.1039/C3EE42099J.

[351] M. Gouverneur, F. Schmidt, and M. Schönhoff (2018). Negative effective Li transference numbers in Li salt/ionic liquid mixtures: does Li drift in the "Wrong" direction? *Physical chemistry chemical physics : PCCP* **20** (11), 7470–7478. DOI: 10.1039/C7CP08580J.

[352] Yachao Du et al. (2022). Ionic Liquid Treatment for Highest-Efficiency Ambient Printed Stable All-Inorganic CsPbI3 Perovskite Solar Cells. *Advanced materials (Deerfield Beach, Fla.)* **34** (10), e2106750. DOI: 10.1002/adma.202106750.

[353] Zehua Chen, Geert Brocks, Shuxia Tao, and Peter A. Bobbert (2021). Unified theory for light-induced halide segregation in mixed halide perovskites. *Nature communications* **12** (1), 2687. DOI: 10.1038/s41467-021-23008-z.

[354] Anthony Ruth et al. (2018). Vacancy-Mediated Anion Photosegregation Kinetics in Mixed Halide Hybrid Perovskites: Coupled Kinetic Monte Carlo and Optical Measurements. *ACS Energy Letters* **3** (10), 2321–2328. DOI: 10.1021/acsenergylett.8b01369.

[355] Davide Orsi et al. (2012). Dynamics in dense hard-sphere colloidal suspensions. *Physical review. E, Statistical, nonlinear, and soft matter physics* **85** (1 Pt 1), 011402. DOI: 10.1103/PhysRevE.85.011402.

[356] Alexander Hexemer and Peter Müller-Buschbaum (2015). Advanced grazing-incidence techniques for modern soft-matter materials analysis. *IUCrJ* **2** (Pt 1), 106–125. DOI: 10.1107/S2052252514024178.

[357] Stephan Pröller et al. (2016). Following the Morphology Formation In Situ in Printed Active Layers for Organic Solar Cells. *Advanced Energy Materials* **6** (1), 1501580. DOI: 10.1002/aenm.201501580.

[358] Detlef-M Smilgies (2009). Scherrer grain-size analysis adapted to grazing-incidence scattering with area detectors. *Journal of applied crystallography* **42** (Pt 6), 1030–1034. DOI: 10.1107/S0021889809040126.

[359] Randall L. Headrick et al. (2019). Coherent X-ray measurement of step-flow propagation during growth on polycrystalline thin film surfaces. *Nature communications* **10** (1), 2638. DOI: 10.1038/s41467-019-10629-8.

[360] C. Gutt et al. (2003). Observation of heterodyne mixing in surface x-ray photon correlation spectroscopy experiments. *Physical Review Letters* **91** (7), 076104. DOI: 10.1103/PhysRevLett.91.076104.

[361] Christopher R. Greve et al. (2023). Effects of the Grazing Incidence Geometry on X-ray Photon Correlation Spectroscopy Measurements. *Langmuir : the ACS journal of surfaces and colloids* **39** (23), 8215–8223. DOI: 10.1021/acs.langmuir.3c00669.

[362] Roland Resel et al. (2016). Multiple scattering in grazing-incidence X-ray diffraction: impact on lattice-constant determination in thin films. *Journal of synchrotron radiation* **23** (Pt 3), 729–734. DOI: 10.1107/S1600577516003672.

[363] Reidar Lund, Lutz Willner, and Dieter Richter (2013). Kinetics of Block Copolymer Micelles Studied by Small-Angle Scattering Methods. In: *Controlled Polymerization and Polymeric Structures*. Ed. by Akihiro Abe, Kwang-Sup Lee, L. Leibler, and Shiro Kobayashi. Vol. 259. Advances in Polymer Science. Cham: Springer International Publishing, 51–158. DOI: 10.1007/12{\textunderscore}2012{\textunderscore}204.

[364] Gilles Renaud, Rémi Lazzari, and Frédéric Leroy (2009). Probing surface and interface morphology with Grazing Incidence Small Angle X-Ray Scattering. *Surface Science Reports* **64** (8), 255–380. DOI: 10.1016/j.surfrep.2009.07.002.

[365] Leon Van Hove (1954). Correlations in Space and Time and Born Approximation Scattering in Systems of Interacting Particles. *Physical Review* **95** (1), 249–262.

[366] Michael Widera and Uwe Klemradt (2015). Non-equilibrium processes in martensitic phase transformations by X-ray photon correlation spectroscopy. *MRS Proceedings* **1754**, 141–146. DOI: 10.1557/opl.2015.637.

[367] C. Gutt, T. Ghaderi, M. Tolan, S. K. Sinha, and G. Grübel (2008). Effects of partial coherence on correlation functions measured by x-ray photon correlation spectroscopy. *Physical Review B* **77** (9). DOI: 10.1103/PhysRevB.77.094133.

[368] F. Livet et al. (2007). Homodyne and heterodyne X-ray photon correlation spectroscopy: latex particles and elastomers. *Journal of Applied Crystallography* **40** (s1), s38–s42. DOI: 10.1107/S0021889807003561.

[369] Irakli Sikharulidze, Igor P. Dolbnya, Anders Madsen, and Wim H. de Jeu (2005). X-ray photon correlation spectroscopy in a reflection geometry: coherence and resolution. *Optics Communications* **247** (1-3), 111–124. DOI: 10.1016/j.optcom.2004.11.044.

[370] L. Névot and P. Croce (1980). Caractérisation des surfaces par réflexion rasante de rayons X. Application à l'étude du polissage de quelques verres silicates. *Revue de Physique Appliquée* **15** (3), 761–779. DOI: 10.1051/rphysap:01980001503076100.

[371] Mahsa Mokhtarzadeh and Karl F. Ludwig (2017). Simulations of Co-GISAXS during kinetic roughening of growth surfaces. *Journal of synchrotron radiation* **24** (Pt 6), 1187–1194. DOI: 10.1107/S1600577517011924.

[372] Chenyu Wang et al. (2022). Early stage growth of amorphous thin film: Average kinetics, nanoscale dynamics, and pressure dependence. *Physical Review Materials* **6** (4). DOI: 10.1103/PhysRevMaterials.6.045601.

[373] D. M. Michelson and G. I. Sivashinsky (1977). Nonlinear analysis of hydrodynamic instability in laminar flames—II. Numerical experiments. *Acta Astronautica* **4** (11-12), 1207–1221. DOI: 10.1016/0094-5765(77)90097-2.

[374] Y. Kuramoto and T. Tsuzuki (1975). On the Formation of Dissipative Structures in Reaction-Diffusion Systems: Reductive Perturbation Approach. *Progress of Theoretical Physics* **54** (3), 687–699. DOI: 10.1143/PTP.54.687.

[375] M. Kardar, G. Parisi, and Y. C. Zhang (1986). Dynamic scaling of growing interfaces. *Physical review letters* **56** (9), 889–892. DOI: 10.1103/PhysRevLett.56.889.

[376] Shaswat Mohanty, Christopher B. Cooper, Hui Wang, Mengning Liang, and Wei Cai (2022). Computational approaches to model X-ray photon correlation spectroscopy from molecular dynamics. *Modelling and Simulation in Materials Science and Engineering* **30** (7), 075004. DOI: 10.1088/1361-651X/ac860c.

[377] K. Kremer, G. S. Grest, and M. O. Robbins (1987). Dynamics of supercooled liquids interacting with a repulsive Yukawa potential. *Journal of Physics A: Mathematical and General* **20** (3), L181–L187. DOI: 10.1088/0305-4470/20/3/012.

[378] M. J. Sánchez-Miranda et al. (2015). Transition from diffusive to subdiffusive motion in colloidal liquids. *Soft matter* **11** (4), 655–658. DOI: 10.1039/C4SM02078B.

[379] Jan Plagge and Claus Heussinger (2013). Melting a granular glass by cooling. *Physical Review Letters* **110** (7), 078001. DOI: 10.1103/PhysRevLett.110.078001.

[380] V. V. Brazhkin, Yu. D. Fomin, A. G. Lyapin, V. N. Ryzhov, and K. Trachenko (2012). Universal crossover of liquid dynamics in supercritical region. *JETP Letters* **95** (3), 164–169. DOI: 10.1134/S0021364012030034.

[381] Ralf Metzler and Joseph Klafter (2004). The restaurant at the end of the random walk: recent developments in the description of anomalous transport by fractional dynamics. *Journal of Physics A: Mathematical and General* **37** (31), R161–R208. DOI: 10.1088/0305-4470/37/31/R01.

[382] Peco Myint et al. (2021). de Gennes Narrowing and Relationship between Structure and Dynamics in Self-Organized Ion-Beam Nanopatterning. *Physical review letters* **126** (1), 016101. DOI: 10.1103/PhysRevLett.126.016101.

[383] L. Müller et al. (2011). Slow aging dynamics and avalanches in a gold-cadmium alloy investigated by x-ray photon correlation spectroscopy. *Physical review letters* **107** (10), 105701. DOI: 10.1103/PhysRevLett.107.105701.

[384] Bradley Frieberg, Jenny Kim, Suresh Narayanan, and Peter F. Green (2013). Surface Layer Dynamics in Miscible Polymer Blends. *ACS macro letters* **2** (5), 388–392. DOI: 10.1021/mz400104p.

[385] Hong-Ren Jiang, Natsuhiko Yoshinaga, and Masaki Sano (2010). Active motion of a Janus particle by self-thermophoresis in a defocused laser beam. *Physical Review Letters* **105** (26), 268302. DOI: 10.1103/PhysRevLett.105.268302.

D. List of Publications

Publications related to the dissertation

- C. Greve, P. Ramming, M. Griesbach, N. Leupold, R. Moos, A. Köhler, E. M. Herzig, F. Panzer, H. Grüninger, 'To Stop or to Shuttle Halides? The Role of an Ionic Liquid in Thermal Halide Mixing of Hybrid Perovskites', *ACS Energy Letters* 2023, 8, 12, 5041-5049. DOI: 10.1021/acsenergylett.3c01878

- C. R. Greve, M. Kuhn, F. Eller, M. A. Buchhorn, A. Hexemer, G. Freychet, L. Wiegart, E. M. Herzig, 'Effects of the Grazing Incidence Geometry on X-ray Photon Correlation Spectroscopy Measurements', *Langmuir* 2023, 39, 23, 8215-8223. DOI: 10.1021/acs.langmuir.3c00669

- K. Schötz, C. Greve, A. Langen, H. Gorter, I. Dogan, Y. Galagan, A. JJM van Breemen, G. H. Gelinck, E. M. Herzig, F. Panzer, 'Understanding Differences in the Crystallization Kinetics between One-Step Slot-Die Coating and Spin Coating of $MAPbI_3$ Using Multimodal In Situ Optical Spectroscopy', *Advanced Optical Materials* 2021, 21, 2101161. DOI: 10.1002/adom.202101161

- C. Greve, E. M. Herzig, 'Effects of Grazing Incidence Geometries on X-Ray Photon Correlation Spectroscopy Simulations', *manuscript in preparation*

Further publications

- M. Kutter, A. Hilgert, M. Maier, M. Schilling, **C. Greve**, R. Loukrakpam, W. Hagemeier, A. Rosin, M. Muggli, E. M. Herzig, R. Zeis, T. Böhm, T. Gerdes, C. Roth, 'LiF@PFSA-based Composite Membranes for PEM Fuel Cells at Intermediate Temperature Conditions', *in submission at Membranes*

  - SAXS measurements were used to analyze the microstructure and the effect of water uptake on the LiF@PFSA-based composite membranes in either a dry or static wet state. A discernible shift in the ionomer peak position to higher q with LiF(m)-doping under dry conditions indicates an interaction between the additive particles and the sulfonic acid groups of PFSA. Under wet conditions, both membranes swell as expected and therefore form larger tunnel-like structures in the fully hydrated status, which is represented in a shift of the ionomer peak position to a smaller q. The results supported other water uptake measurements within the manuscript and indicate that the hygroscopic lithium fluoride nanoparticles can increase water uptake and retention.

- P.-E. Jan, H.-C. Liang, R.-W. Cheng, **C. R. Greve**, C.-L. Chang, H.-L. Lai, P.-W. Chiu, S.-Y. Sun, Y.-L. Li, E. M. Herzig, H.-H. Chou, H.-W. Lin, 'Molecular Design Strategy of Meta-Substituted Aromatic Organic Halides in Zero-Lead-Release Halide Perovskites with Efficient Waterproof Light Emission', *in submission at Advanced Functional Materials*

  - GIWAXS measurements and data analysis of quasi 2.5D Ruddlesden-Popper and 3D lead halide perovskite thin films. The comparative GIWAXS study between the newly synthesised 4PhMA cation and the already established OA and PEA cations and a α-$FAPbI_3$ reference film revealed that 4PhMA addition results in comparatively higher α-$FAPbI_3$ phase stability, high orientation parallel and perpendicular to the substrate and also higher perovskite phase stability against humidity, ambient conditions and water immersion.

- P.-T. Lai, C.-Y. Chen, H.-C. Lin, B.-Y. Chuang, K.-H. Kuo, **C. R. Greve**, T.-K. Su, G.-H. Tan, C.-F. Li, S.-W. Huang, K.-Y. Hsiao, E. M. Herzig, M.-Y. Lu, Y.-C. Huang, K.-T. Wong, H.-W. Lin, 'Harnessing 2D Ruddlesden–Popper Perovskite with Polar Organic Cation for Ultrasensitive Multibit Nonvolatile Transistor-Type Photomemristors', *ACS nano*, 2024, 17, 24, 25552-25564. DOI: 10.1021/acsnano.3c09595

  - GIWAXS measurements and data analysis of 2D Ruddlesden-Popper lead perovskites. A comparative study of 3 different A-side cations could deduce that the newly synthesized EATPCN resulted in a highly isotropic crystal orientation with small crystal sizes. Further, a pi-pi-stacking distance could be resolved well fitting with consecutive theoretical simulations, but mismatching to the classical Pb-Pb octahedra distance, resulting in disorder. The resolved disordered nature and comparatively smaller crystal size of the $(EATPCN)_2PbI_4$ layers explain why the newly synthesised EATPCN cation works excellent as a photomemristor, as the disordered nature and small crystal sizes are morphological advantages for indefinite electron trapping, resulting in an almost zero-decay nonvolatile property.

- M. Kutter, **C. Greve**, M. Maier, M. Schilling, A. Mauel, A. Hilgert, H. Hoffmann, W. Hagemeier, A. Rosin, M. Muggli, R. Zeis, J. Senker, T. Böhm, E. M. Herzig, T. Gerdes, C. Roth, 'Recycling of perfluorosulfonic acid-based membranes and their Re-application in PEM fuel cells', *Journal of Membrane Science* 2024, 693, 122370. DOI: 10.1016/j.memsci.2023.122370

  - SAXS/WAXS measurements and data analysis of neat and recycled perfluorosulfonic acid-based membranes for the application in Polymer electrolyte membrane fuel cells. The SAXS measurements could resolve an increased water uptake after the recycling process by determination of a diminsihing crystalline order in conjunction with an increased water-domain spacing.

- S. F. Winterstein, A. F. Privalov, **C. Greve**, R. Siegel, B. Pötzschner, M. Bettermann, L. Adolph, J. Timm, R. Marschall, E. A. Rössler, E. M. Herzig, M. Vogel, J. Senker,'Ultrafast Proton Conduction in an Aqueous Electrolyte Confined in Adamantane-like Micropores of a Sulfonated, Aromatic Framework', *Journal of the American Chemical Society* 2023, 145, 50, 27563-27575. DOI: 10.1021/jacs.3c09257

  – WAXS measurements and analysis of a nanoporous hydrated sulfonated aromatic frameworks with various degrees of sulfonation. The measurements resolved the average distribution of sulfonated regions within the framework and lead to a reasonable explanation for the preferential immobilization of water molecules for a sulfonation degree of 0.5 and the resulting lower activation barriers (EA $\approx$ 35 kJ/mol) for the charge transport in this case.

- S. Biberger, N. Leupold, C. Witt, **C. Greve**, P. Markus, P. Ramming, D. Lukas, K. Schötz, F.-J. Kahle, C. Zhu, G. Papastavrou, A. Köhler, E. M. Herzig, R. Moos, F. Panzer, 'First of Their Kind: Solar Cells with a Dry-Processed Perovskite Absorber Layer via Powder Aerosol Deposition and Hot-Pressing', *Solar RRL* 2023, 7, 16, 2300261. DOI: 10.1002/solr.202300261

  – GIWAXS measurements and analysis of powder-deposited $MAPbI_3$ thin films for untreated and hot-pressed thin films. The measurements revealed a change in preferred crystalline orientation of the tetragonal unit cells within the thin film after hot-pressing. Furthermore, an increase in crystallite size and a deformation of the unit cells after the hot-pressing treatment were identified, well reflecting the differences seen in the optoeletronic properties.

- T. Weller, J. Timm, L. Deilmann, T. S. Doerr, **C. Greve**, A. S. Cherevan, P. A. Beaucage, U. B. Wiesner, E. M. Herzig, D. Eder, R. Marschall, 'Effects of periodic pore ordering on photocatalytic hydrogen generation with mesoporous semiconductor oxides', *Small Structures* 2023, 4, 6, 2200184. DOI: 10.1002/sstr.202200184

  – Powder SAXS measurements and analysis of crystalline and 3D continuous mesoporous quaternary $CsTaWO_6$ semiconductors. The analysis resolved the increase in long-range mesoscale order for lower precursor concentrations in conjunction with bigger pore sizes. Furthermore, the analysis established that for higher calcination temperatures similar lattice parameters are obvserved, while the long-rang order is significantly reduced.

- C. Wöpke, C.Göhler, M. Saladina, X. Du, L. Nian, **C. Greve**, C. Zhu, K. M Yallum, Y. J. Hofstetter, D. Becker-Koch, N. Li, T. Heumüller, I. Milekhin, D. RT Zahn, C. J. Brabec, N. Banerji, Y. Vaynzof, E. M. Herzig, R. CI MacKenzie, C. Deibel, 'Traps and transport resistance are the next frontiers for stable non-fullerene acceptor solar cells', *Nature Communications* 2022, 13, 1, 3786. DOI: 10.1038/s41467-022-31326-z

  - GIWAXS measurements and analysis of PM6, Y6 and PM6:Y6 blend thin films with and without an ageing treatment on various substrates to study degradation effects. The analysis revealed that interlayers of ZnO reduce aggregation and the formation of bigger crystalline domains. Furthermore, the measurements showed in PM6 thin films an increase in paracrystalline disorder for the π-π-stacking. In PM6:Y6 blends the increase in disorder of the π-π-stacking in unison with the increase in the amount of lamellar stacking implies that the lamellar stacking is enhanced at the cost of the π-π-stacking quality.

- V. Dudko, R. L. Timmins, O. Khoruzhenko, M. Röhrl, **C. Greve**, S. Rosenfeldt, T. Tammelin, S. Agarwal, E. M. Herzig, J. Breu, 'Spontaneous delamination of affordable natural vermiculite as a high barrier filler for biodegradable food packaging', *Materials Advances* 2022, 3, 24, 9052-9062. DOI: 10.1039/D2MA00734G

  - Solution SAXS measurements of vermiculite nanosheets and vermiculite nanosheets + PLA in γ-BL showed no changes in the (001) sheet stacking distance. The measurements resolved that the addition of PLA does not compromise the colloidal stability of the nanaosheet suspension.

E. Acknowledgements

Retrospectively, my time as a doctoral student has flown by and yet it has also accompanied my life to date for quite some time. I would therefore like to take this opportunity to thank everyone who supported me during my doctorate and in the creation of this thesis.

First of all, I would like to thank Prof. Dr Eva M. Herzig for the opportunity to carry out this work at her chair and for supervising my thesis. Thank you also for allowing me to help set up your chair after you moved to Bayreuth and for always having an open ear for me and any ideas I had. Thank you also for my participation in various conferences and workshops. I have truly enjoyed the past years at your chair, which have been a lot of fun.

Special thanks also go to Dr. habil Fabian Panzer and Dr. Helen Grüninger, who initiated two of my doctoral projects and shared their scientific and technical knowledge with me during them. Thank you for stimulating discussions and successful collaborations!

I would like to thank Irene Bauer, Christina Gräbner and Frank Schirmer for their constant support and willingness to help with any problems that arose. Thank you for keeping everything running and functioning, be it in chemistry, electrics or administration. I would also like to thank everyone in the secretariat. Many thanks to Michalea Fischer and Laura Schwarze for preventing us from drowning in paper and (mostly) not having to deal with administrative matters ourselves. I would also like to thank Thomas Dabisch for the fact that one can always come by to borrow equipment to test a spontaneous idea and never leave your workshop without a coffee and a word of encouragement!

I also want to thank all my collaborators for the (mostly) nice collaborations, especially the co-authors of major works contributing to my thesis, Dr. Konstantin Schötz and Philipp Ramming. Thank you all for the successful scientic exchange and the works that resulted from these exchanges. Without you the beautiful works wouldn't have been possible.

Of course, I would also like to thank everyone who contributed to a great working atmosphere and mood. Many thanks to everyone from my working group, but also to Anna Köhler's chair, with whom I was also able to share the office during various renovations. I am very happy that I have had the opportunity to spend so much time with you. It is a shame that Corona has stolen quite a lot of our social time by cancelling conferences and the wonderful barbecues we would have had. Special thanks go to Meike Kuhn, who I was not only lucky to supervise in her Master's thesis, but who also became a great colleague afterwards. Thank you for

accompanying me during my many office moves with your positive manner and good scientific discussions!

I want to thank all my friends in and out of Bayreuth for all the fun times and evenings full of deep talks, nonsense and raiding. I hope we stay in touch when new parts of our lifes start.

Of course, I would especially like to thank my parents and my family for their unconditional support during my studies and doctorate. I appreciated and still appreciate the opportunities and chances you opened up for me. I know that I always have a sympathetic ear when I have problems and I am very grateful for that! Even if enquiries about when I will finally be finished could be a little less frequent.

Finally, my biggest thanks go to my girlfriend Lisa, who accompanied me throughout my entire promotion. Thank you for your unwavering support and your understanding when weekends before beam times became optional and sometimes I had to work late into the night on a revision. Also thank you for your tetris arts, when packaging lab equipment and setups for beam times. You truly made sure that I was able to find relaxation and balance even in stressful times. I love you and look forward to our years to come!

So long, and thanks for all the fish!

F. Eidesstattliche Versicherung

Hiermit versichere ich an Eides statt, dass ich die vorliegende Arbeit selbstständig verfasst und keine anderen als die von mir angegebenen Quellen und Hilfsmittel verwendet habe.

Weiterhin erkläre ich, dass ich die Hilfe von gewerblichen Promotionsberatern bzw. -vermittlern oder ähnlichen Dienstleistern weder bisher in Anspruch genommen habe, noch künftig in Anspruch nehmen werde.

Zusätzlich erkläre ich hiermit, dass ich keinerlei frühere Promotionsversuche unternommen habe.

Bayreuth, den

Unterschrift